R-14-26

# Future evolution of groundwater composition at Forsmark during an extended temperate period

Steven Joyce, Hannah Woollard, AMEC

Niko Marsic, Magnus Sidborn, Kemakta Konsult AB

January 2015

**Svensk Kärnbränslehantering AB**
Swedish Nuclear Fuel
and Waste Management Co

Box 250, SE-101 24 Stockholm
Phone +46 8 459 84 00

ISSN 1402-3091
**SKB R-14-26**
ID 1416908

January 2015

# Future evolution of groundwater composition at Forsmark during an extended temperate period

Steven Joyce, Hannah Woollard, AMEC

Niko Marsic, Magnus Sidborn, Kemakta Konsult AB

# Abstract

As part of the SR-Site safety assessment to support the license application for a spent nuclear fuel repository at Forsmark, groundwater flow and transport calculations were carried out to model the evolution of groundwater composition with time over the temperate climate period from 8000 BC to 12,000 AD. Geochemical calculations were carried out based on the groundwater compositions exported from the groundwater flow and transport models at selected times and locations. The results of these calculations were used to assess the impact on safety functions related to the geochemical conditions, particularly salinity, pH and redox conditions.

Additional climate cases were also considered for SR-Site, but not used for the hydrogeological modelling. One of these is the global warming case, which considers the effects of a temperate climate period that extends to around 60,000 AD. One implication of this case is that the repository site would be exposed to an extended period of meteoric water infiltration. The potential consequence of this is that the more dilute and more oxidising meteoric water could penetrate to repository depth during the extended temperate climate period.

The work reported here carries out groundwater flow, transport and geochemical calculations for the global warming case to assess the impact on groundwater composition within the repository site. The methodology used is similar to SR-Site, but uses a new capability to couple the geochemical calculations with the groundwater flow and transport calculations. Additional cases are also considered with different geochemical reactions that represent either an updated understanding of the site geochemistry or the implications of a more dilute composition for the infiltrating meteoric water.

The results of this work show that the geochemical environment of the site changes little beyond the temperate climate period considered for SR-Site and hardly at all beyond 20,000 AD. The salinity of the groundwater is governed by the low permeability of the bedrock, rock matrix diffusion and the relatively shallow and slow circulation of groundwater. The chemical reactions influence concentrations of reactive species, the calculated pH and redox potential. In particular, the redox reactions considered maintain reducing conditions at repository depth, even with infiltration at the ground surface of meteoric water with a relatively high redox potential. The geochemical safety functions used for SR-Site are met for all of the cases throughout the time period considered.

# Contents

# 1 Introduction

## 1.1 Background

The license application submitted by SKB for a spent nuclear fuel repository at Forsmark is supported by the SR-Site safety assessment to demonstrate the long-term safety of the proposed repository (SKB 2011). One part of SR-Site was groundwater flow and transport modelling of the repository site during the operational phase (Svensson and Follin 2010) and during the post-closure phase. Modelling of the post-closure phase was divided into a temperate climate period (Joyce et al. 2010) and a periglacial and glacial climate period (Vidstrand et al. 2010).

One aspect of the temperate climate period modelling was to calculate the evolution of groundwater composition for the time span 8000 BC to 12,000 AD. This corresponds to the current Holocene period that started at the end of the Weichselian glaciation, but is also taken to represent future inter-glacial periods. The interval from 8000 BC to around 1000 AD corresponds to a time when the Forsmark site was submerged. The subsequent interval up to 12,000 AD corresponds to a period when the site is above sea level and the shoreline is retreating due to post-glacial land rise. The reference glacial cycle (SKB 2010) predicts that the Holocene period will continue to 9000 AD, corresponding to the first occurrence of permafrost. The reference glacial cycle corresponds to the SR-Site base case. A simplified reference glacial cycle (SKB 2010) was also defined for groundwater modelling purposes which defined the end of the temperate climate period as 10,000 AD.

The groundwater composition at selected times was exported from the flow and transport models and used to carry out geochemical calculations (Salas et al. 2010). These calculations determined the concentrations of chemical species, the pH and the redox potential from equilibration with one of two sets of minerals at selected locations. There was no feedback from the geochemical calculations to the flow and transport calculations, i.e. it was a one-way decoupled approach.

Additional climate cases were also considered for SR-Site (SKB 2010), but not included in the groundwater modelling. One such case is the global warming case, which describes a future climate development influenced by both natural climate variability and the possibility of global warming attributed directly or indirectly to human activity. The global warming case predicts that temperate conditions will dominate until around 60,000 AD. This will expose the Forsmark site to an extended period of meteoric water infiltration, which will have implications for groundwater composition and the associated safety functions (particularly those related to salinity, pH and redox conditions).

## 1.2 Scope

The work described here models the evolution of groundwater composition during the extended temperate period associated with the global warming climate case. The time span considered is from 8000 BC to 60,000 AD. The modelling includes the coupled effects of groundwater flow, transport and chemical reactions. The work is based on the regional-scale modelling methodology described in Joyce et al. (2010) and the geochemical calculations described in Salas et al. (2010). However, an approach is adopted which tightly integrates the calculations of flow, transport and chemistry.

A number of cases are simulated, each considering a different set of geochemical reactions, as follows:

Case 1. No chemical reactions, i.e. the groundwater composition is determined only by groundwater flow and transport.

Case 2. Equilibration of groundwater with calcite, quartz and amorphous iron (II) sulphide. This is the “base case” from Salas et al. (2010) for the situation with significant activity of sulphate-reducing bacteria. However, the hydroxyapatite reactions are not included as they are not deemed relevant to this work.

Case 3. Equilibration of groundwater with calcite, quartz and iron (III) oxyhydroxide. This is the “base case” from Salas et al. (2010) for the situation where the redox state is not affected by sulphate-reducing bacteria. Again, the hydroxyapatite reactions are not included.

Case 4. Equilibration of groundwater with calcite, quartz, amorphous iron (II) sulphide, kaolinite, albite, and K-feldspar. This case represents an updated understanding of the site mineralogy relative to SR-Site. The additional reactions and thermodynamic data relative to Case 2 are described in detail in Auqué et al. (2006).

Case 5. As Case 2, but with a more dilute composition for meteoric water.

## 1.3 Report structure

This report is structured as follows:

- Section 1 provides background information to set the work into context.
- Section 2 describes the concepts and methodology used for this study.
- Section 3 describes the numerical modelling.
- Section 4 presents the results.
- Section 5 presents the conclusions.

# 2 Concepts and methodology

## 2.1 Conceptual model

The Forsmark site consists of fractured crystalline rock overlain with Quaternary deposits. Based on the characteristics of the geology, the rock was sub-divided into rock domains (SKB 2008), as shown in Figure 2-1. The repository itself is located in a so-called tectonic lens in which the bedrock is less affected by ductile deformation within surrounding belts of high ductile strain. The upper 200 m of the bedrock is characterised by an increased intensity of sub-horizontal to gently dipping fractures and sheet-joints forming a shallow bedrock aquifer. Below this is sparsely fractured bedrock of low permeability. The intensity of fractures generally decreases with increasing depth.

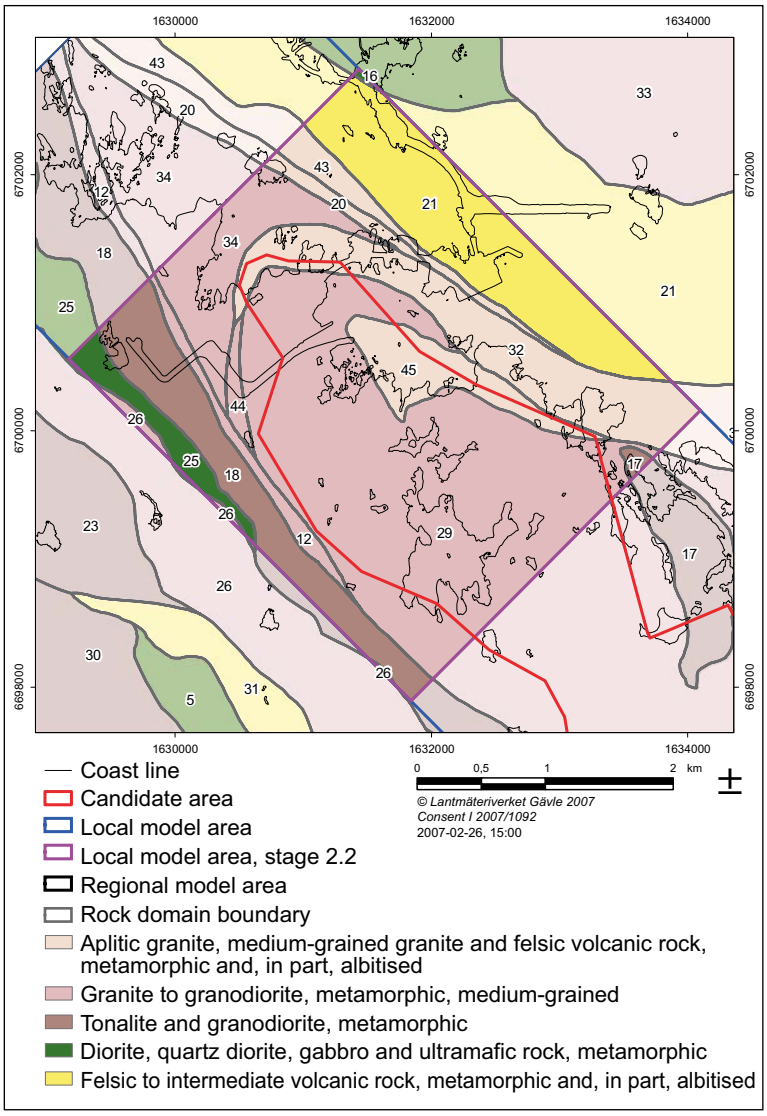


***Figure 2-1.*** *Illustrations of the rock domains at the surface of the local model areas for Forsmark. (SKB 2008).*

A conceptual model of the site hydrogeology was developed during the site-descriptive modelling (SDM), culminating in SDM-Site (SKB 2008), serving as a basis for the SR-Site safety assessment (SKB 2011). The conceptual model describes three hydraulic domains:

- HCD (Hydraulic Conductor Domain) representing deformation zones.
- HRD (Hydraulic Rock mass Domain) representing the less fractured bedrock in between the deformation zones.
- HSD (Hydraulic Soil Domain) representing the regolith (Quaternary deposits).

These domains are illustrated in Figure 2-2.

### 2.1.1 Hydraulic Conductor Domain (HCD)

The deformation zones forming the HCD are defined as structures where there is a concentration of brittle, ductile or combined brittle and ductile deformation. They are envisaged as being composed of swarms of smaller fractures. Each deformation zone structure is characterised by a transmissivity and thickness. Analysis of the site data identified a depth trend for the deformation zone transmissivities, which decrease with increasing depth. An initial deterministic model of the HCD was devised with a uniform horizontal transmissivity (Figure 2-3: top). However, variants were also produced that introduced stochastic horizontal variability, conditioned on borehole measurements, to provide both statistical properties (mean, standard deviation, depth trend) and deterministic values at the borehole intercepts with deformation zones (Figure 2-3: bottom).

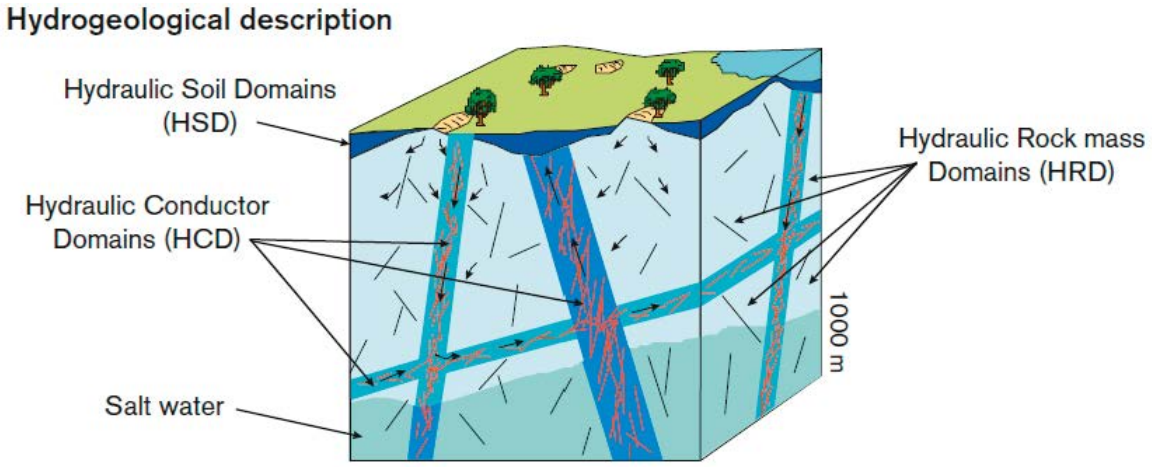


***Figure 2-2.*** *Schematic diagram showing the division of the crystalline bedrock and the regolith (Quaternary deposits) into three hydraulic domains, HCD, HRD and HSD. Figure 3-2 in Rhén et al. (2003).*

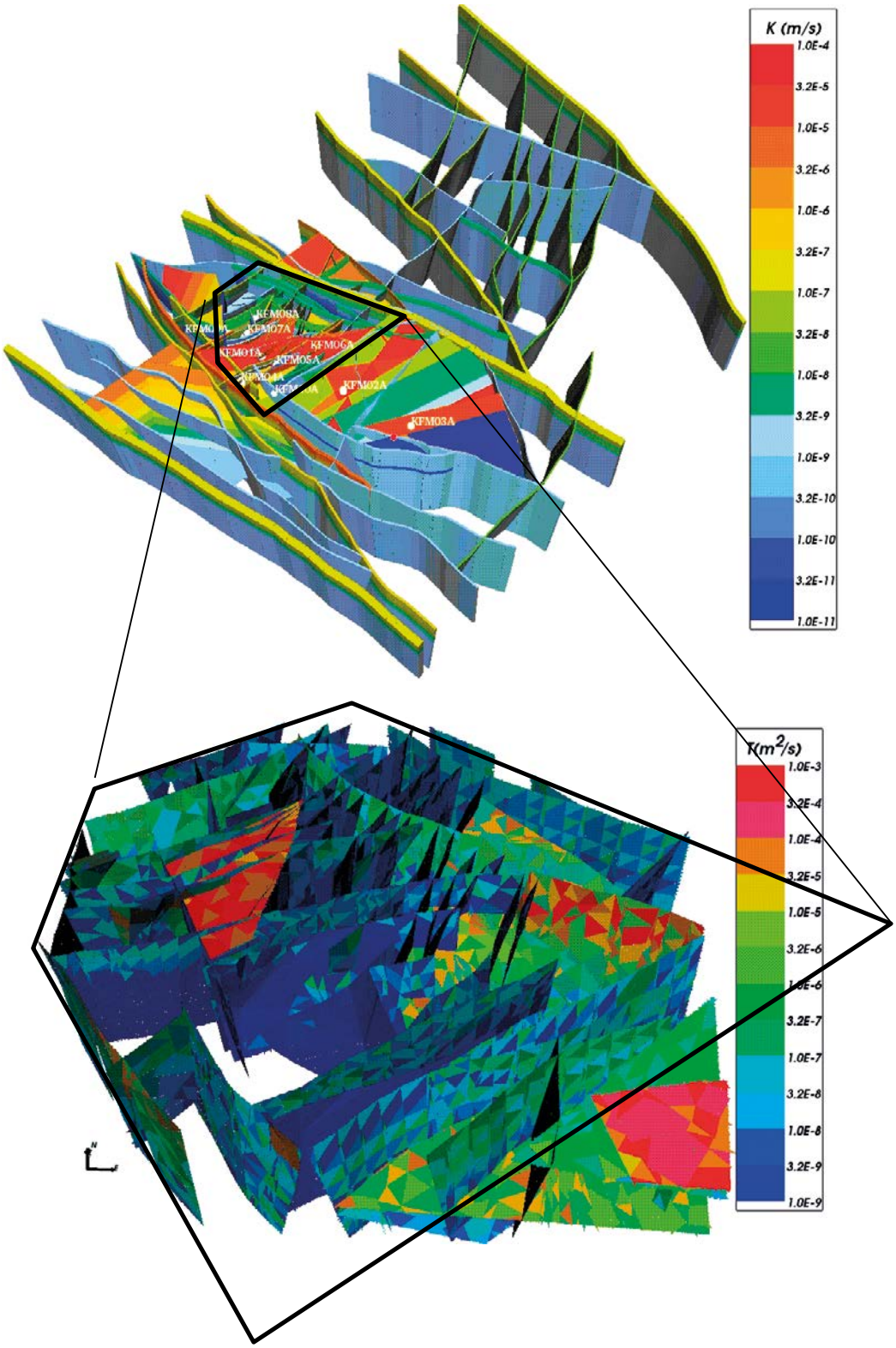


***Figure 2-3.*** *Property model of the deformation zones. Top: Regional scale deformation zones with deterministic properties, represented as volumes to show their assigned width and coloured by hydraulic conductivity. Bottom: Visualisation of one stochastic realisation of the deformation zones that occur inside the local model domain, represented as surfaces and coloured by transmissivity. Adapted from Follin (2008).*

### 2.1.2 Hydraulic Rock mass Domain (HRD)

The fractured bedrock between the deformation zones was divided into a number of fracture domains, characterised by fracture properties and location. These fracture domains were denoted FFM01 to FFM06 and are shown schematically in Figure 2-4 to Figure 2-6. Fracture domain FFM06 has a similar structural context to FFM01 and so these two fracture domains were merged. There was insufficient data to fully describe FFM04 and FFM05 and so their properties were characterised by analogy to FFM03. Due to the depth trend in fracture intensity in Forsmark, the FFM01/06 domain was divided into three depth zones (above –200 m, –200 m to –400 m and below –400 m elevation). The FFM03, FFM04 and FFM05 domains were divided into two depth zones (above and below –400 m elevation). The FFM02 domain is only defined for the upper bedrock and so has a single depth zone. Additionally, fractures were divided by orientation into four sub-vertical fracture sets (NS, NE, NW, EW) and one sub-horizontal fracture set (HZ). A process of analysis and calibration allowed a parameterisation of a hydrogeological discrete fracture network (Hydro-DFN) to be produced. This assumed a power-law relationship between intensity and fracture size:

$$f(r) = \frac{k_r r_0^{\,k_r}}{r^{k_r+1}} \tag{2-1}$$

where $r_0$ and $k_r$ are the location parameter and the shape parameter, respectively. Additionally, a semi-correlated relationship between fracture size and transmissivity was used for the hydro-geological base case:

$$\log(T) = \log\left(a\, r^{b}\right) + \sigma_{\log(T)}\, N[0,1] \tag{2-2}$$

where $T$ is the fracture transmissivity, $r$ is the fracture radius, $a$ and $b$ are constants and $N[0,1]$ denotes a normally distributed random deviate with a mean equal to zero and a standard deviation of 1. The parameters defining the Hydro-DFN for each fracture domain in the candidate area are given in Table 2-1. Outside the candidate area, limited borehole data only allowed an approximate parameterisation of the bedrock properties, as shown in Table 2-2.

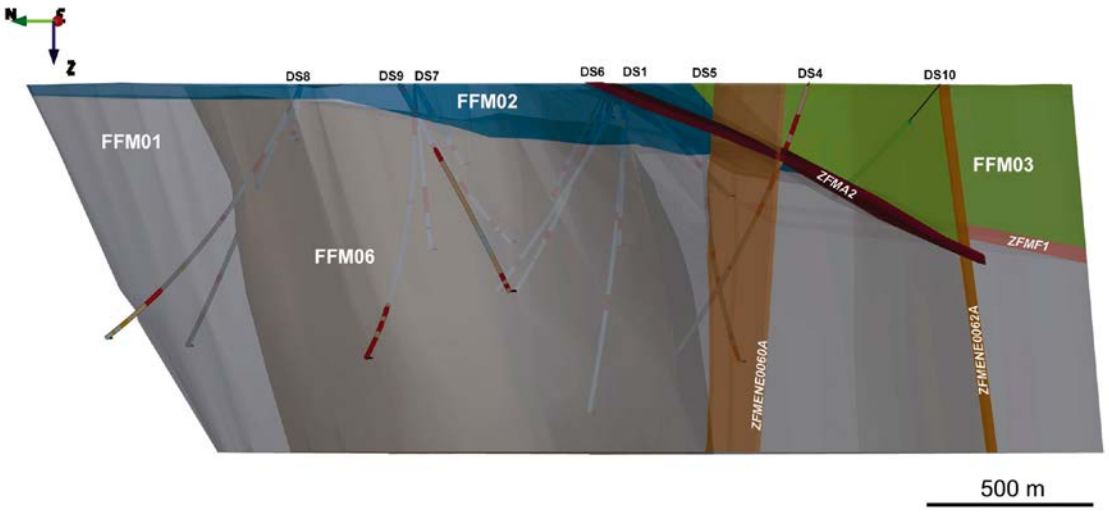


***Figure 2-4.*** *Three-dimensional representation of the fracture domain model, viewed towards ENE. Fracture domains FFM01, FFM02, FFM03 and FFM06 are coloured grey, dark grey, blue and green, respectively. The gently dipping and sub-horizontal zones A2 and F1 as well as the steeply dipping deformation zones ENE0060A and ENE0062A are also shown. (Follin 2008).*

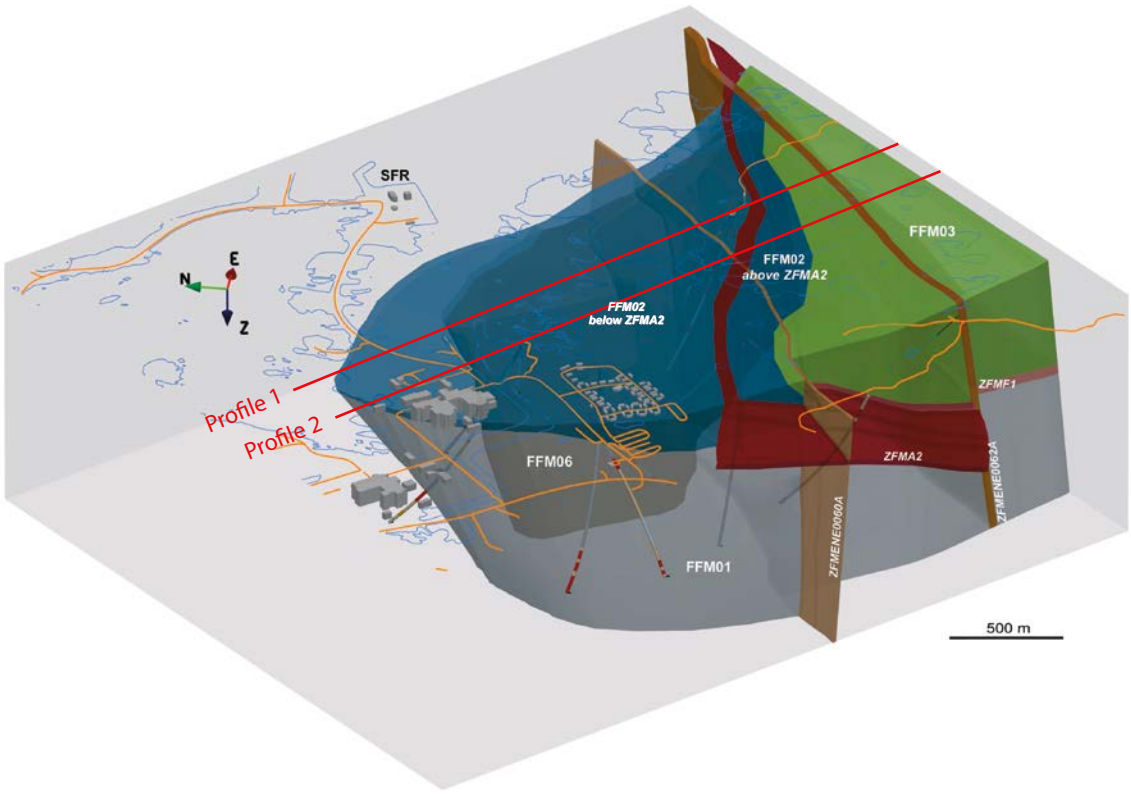


***Figure 2-5.*** *Three-dimensional view towards ENE showing the relationship between deformation zone A2 (red) and fracture domain FFM02 (blue). Profile 1 and 2 are shown as cross-sections in Figure 2-6. (Follin 2008).*

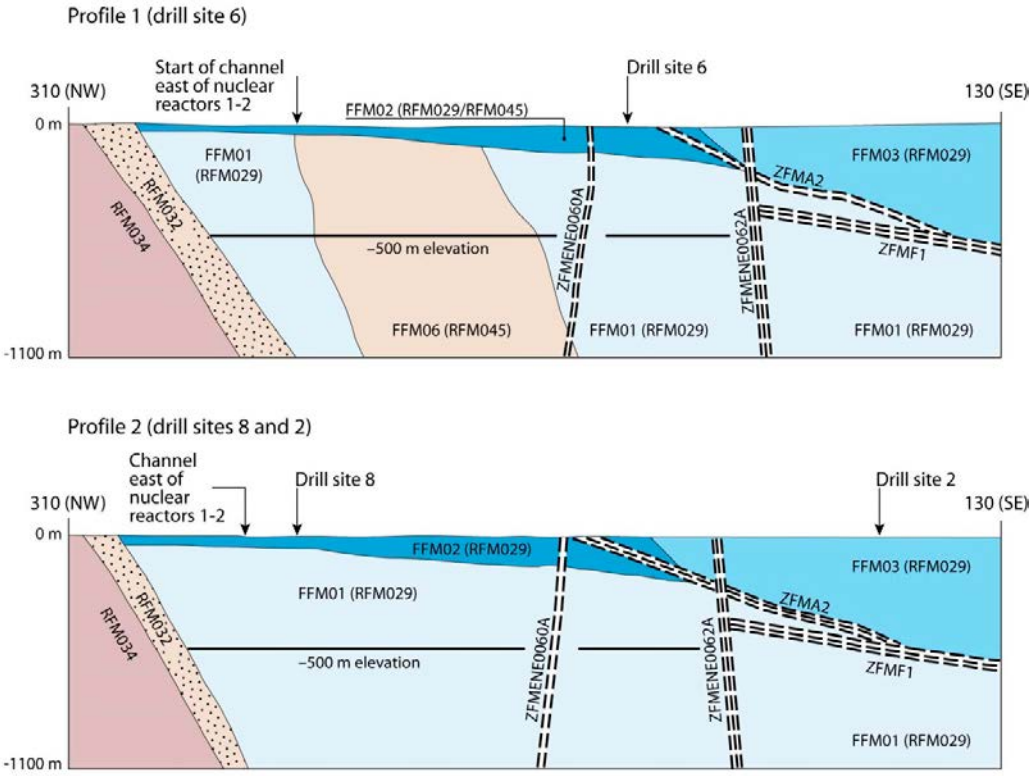


***Figure 2-6.*** *Simplified profiles in a NW-SE direction that pass through the target volume. The locations of the profiles are shown in Figure 2-5. The key fracture domains, FFM01, –02 and –06, for a final repository at Forsmark occur in the footwall of zones A2 (gently dipping) and F1 (sub-horizontal). The major steeply dipping zones ENE0060A and ENE0062A are also included in the profiles. Figure 5-1 in Olofsson et al. (2007).*

**Table 2-1. Hydrogeological DFN parameters for the semi-correlated transmissivity model of each fracture domain with depth dependency. Combined from Tables C-1 to C-3 in Follin (2008).**

| Fracture domain (m RHB 70) | Fracture set name | Orientation set pole: (trend, plunge), conc. | Size model, power-law ($r_0$, $k_r$) (m, –) | Intensity, ($P_{32}$), valid size interval: ($r_0$, 564 m) ($m^2/m^3$) | Parameter values for the transmissivity model shown in Equation 2-2 $T$ ($m^2s^{-1}$) |
|---|---|---|---|---|---|
| FFM01 FFM06 > –200 | NS | (292, 1) 17.8 | (0.038, 2.50) | 0.073 | ($a$, $b$, $\sigma$) = (6.3 × $10^{-9}$, 1.3, 1.0) |
| | NE | (326, 2) 14.3 | (0.038, 2.70) | 0.319 | |
| | NW | (60, 6) 12.9 | (0.038, 3.10) | 0.107 | |
| | EW | (15, 2) 14.0 | (0.038, 3.10) | 0.088 | |
| | HZ | (5, 86) 15.2 | (0.038, 2.38) | 0.543 | |
| FFM01 FFM06 –200 to –400 | NS | As above | As above | 0.142 | ($a$, $b$, $\sigma$) = (1.3 × $10^{-9}$, 0.5, 1.0) |
| | NE | As above | As above | 0.345 | |
| | NW | As above | As above | 0.133 | |
| | EW | As above | As above | 0.081 | |
| | HZ | As above | As above | 0.316 | |
| FFM01 FFM06 < –400 | NS | As above | As above | 0.094 | ($a$, $b$, $\sigma$) = (5.3 × $10^{-11}$, 0.5, 1.0) |
| | NE | As above | As above | 0.163 | |
| | NW | As above | As above | 0.098 | |
| | EW | As above | As above | 0.039 | |
| | HZ | As above | As above | 0.141 | |
| FFM02 > –200 | NS | (83, 10) 16.9 | (0.038, 2.75) | 0.342 | ($a$, $b$, $\sigma$) = (9.0 × $10^{-9}$, 0.7, 1.0) |
| | NE | (143, 9) 11.7 | (0.038, 2.62) | 0.752 | |
| | NW | (51, 15) 12.1 | (0.038, 3.20) | 0.335 | |
| | EW | (12, 0) 13.3 | (0.038, 3.40) | 0.156 | |
| | HZ | (71, 87) 20.4 | (0.038, 2.58) | 1.582 | |
| FFM03 FFM04 FFM05 > –400 | NS | (292, 1) 17.8 | (0.038, 2.60) | 0.091 | ($a$, $b$, $\sigma$) = (1.3 × $10^{-8}$, 0.4, 0.8) |
| | NE | (326, 2) 14.3 | (0.038, 2.50) | 0.253 | |
| | NW | (60, 6) 12.9 | (0.038, 2.55) | 0.258 | |
| | EW | (15, 2) 14.0 | (0.038, 2.40) | 0.097 | |
| | HZ | (5, 86) 15.2 | (0.038, 2.55) | 0.397 | |
| FFM03 FFM04 FFM05 < –400 | NS | As above | As above | 0.102 | ($a$, $b$, $\sigma$) = (1.8× $10^{-8}$, 0.3, 0.5) |
| | NE | As above | As above | 0.247 | |
| | NW | As above | As above | 0.103 | |
| | EW | As above | As above | 0.068 | |
| | HZ | As above | As above | 0.250 | |

**Table 2-2. Homogeneous and isotropic hydraulic properties used for the HRD outside the candidate area (Follin et al. 2007b).**

| Elevation (m RHB 70) | Hydraulic conductivity (m/s) | Kinematic porosity (–) |
|---|---|---|
| > –200 | 1×$10^{-7}$ | 1×$10^{-5}$ |
| –200 to –400 | 1×$10^{-8}$ | 1×$10^{-5}$ |
| < –400 | 3×$10^{-9}$ | 1×$10^{-5}$ |

### 2.1.3 Hydraulic Soil Domain

The regolith at Forsmark was deposited during the Quaternary period and so is generally known as Quaternary deposits. The conceptual model of the HSD consists of nine layers (L1–L3 and Z1–Z6) of varying extents and thicknesses as shown in Figure 2-7. A description of each layer is given in Table 2-3. Suggested hydraulic properties from the SDM for groundwater flow modelling are given in Table 2-4 and Table 2-5.

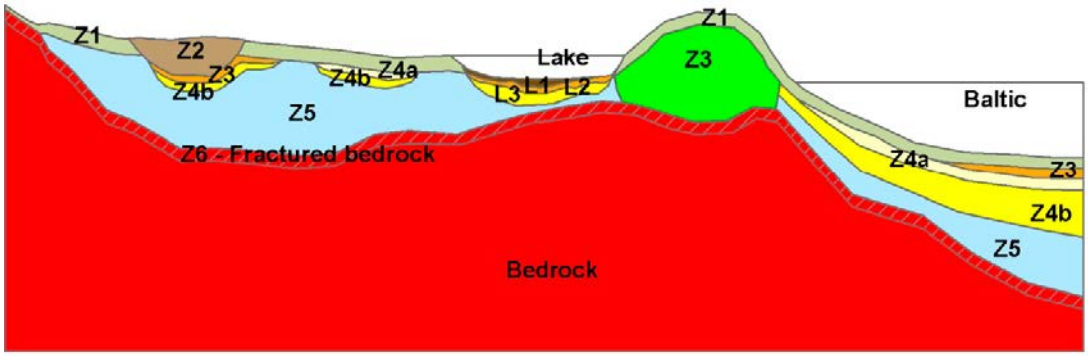


***Figure 2-7.*** *Conceptual model for the layering of Quaternary deposits at Forsmark (Hedenström et al. 2008).*

**Table 2-3. Names and definitions of Quaternary deposits (Hedenström et al. 2008).**

| Layer | Description and comments |
|---|---|
| L1 | Layer consisting of different kinds of gyttja/mud/clay or peat. Interpolated from input data, thickness will therefore vary. |
| L2 | Layer consisting of sand and gravel. Interpolated from input data, thickness will therefore vary. |
| L3 | Layer consisting of different clays (glacial and postglacial). Interpolated from input data, thickness will therefore vary. |
| Z1 | Surface affected layer present all over the model, except where peat is found and under lakes with lenses. Thickness is 0.10 m on bedrock outcrops, 0.60 m elsewhere. If total regolith thickness is less than 0.60 m, Z1 will have the same thickness as the total, i.e. in those areas only Z1 will exist. |
| Z2 | Surface layer consisting of peat. Zero thickness in the sea. Always overlies by Z3. |
| Z3 | Middle layer of sediments. Only found where surface layers are other than till, clay or peat. |
| Z4a | Middle layer consisting of postglacial clay. Always overlies by Z4b. |
| Z4b | Middle layer of glacial clay. |
| Z5 | Corresponds to a layer of till. The bottom of layer Z5 corresponds to the bedrock surface. |
| Z6 | Upper part of the bedrock. Fractured rock. Constant thickness of 0.5 m. Calculated as an offset from Z5. |

**Table 2-4. Values of the saturated hydraulic conductivity of the Quaternary deposits suggested for groundwater flow modelling in SDM stage 2.2 (Bosson et al. 2008).**

| Layer | ***K*** **[m/s] of layers with several types of Quaternary deposits** | | | | | |
|---|---|---|---|---|---|---|
| | **Fine till** | **Coarse till** | **Gyttja** | **Clay** | **Sand** | **Peat** |
| L1 | – | – | $3 \times 10^{-7}$ | – | – | < 0.6 m depth: $1 \times 10^{-6}$ |
| Z1 | $3 \times 10^{-5}$ | $3 \times 10^{-5}$ | – | $1 \times 10^{-6}$ | $1.5 \times 10^{-4}$ | > 0.6 m depth: $3 \times 10^{-7}$ |
| Z5 | $1 \times 10^{-7}$ | $1.5 \times 10^{-6}$ | – | – | – | – |
| | ***K*** **[m/s] of layers with one type of Quaternary deposits** | | | | | |
| L2 | $3 \times 10^{-4}$ | | | | | |
| L3 | < 0.6 m depth: $1 \times 10^{-6}$ ; > 0.6 m depth: $1.5 \times 10^{-8}$ | | | | | |
| Z2 | $3 \times 10^{-7}$ | | | | | |
| Z3 | $1.5 \times 10^{-4}$ | | | | | |
| Z4 | $1.5 \times 10^{-8}$ | | | | | |

**Table 2-5. Values of the total porosity and the specific yield of the Quaternary deposits suggested for groundwater flow modelling in SDM stage 2.2 (Bosson et al. 2008).**

| Layer | Total porosity [–] and specific yield [–] of layers with several types of Quaternary deposits | | | | | |
|---|---|---|---|---|---|---|
| | Fine till | Coarse till | Gyttja | Clay | Sand | Peat |
| L1 | – | – | 0.50 / 0.03 | – | – | 0.60 / 0.20 |
| Z1 | 0.35 / 0.15 | 0.35 / 0.15 | – | 0.55 / 0.05 | 0.35 / 0.20 | 0.40 / 0.05 |
| Z5 | 0.25 / 0.03 | 0.25 / 0.05 | – | – | – | – |
| | Total porosity [–] and specific yield [–] of layers with one type of Quaternary deposits | | | | | |
| L2 | 0.35 / 0.20 | | | | | |
| L3 | 0.55 / 0.05 | | | | | |
| Z2 | 0.40 / 0.05 | | | | | |
| Z3 | 0.35 / 0.20 | | | | | |
| Z4 | 0.45 / 0.03 | | | | | |

### 2.1.4 Hydrogeochemistry

A hydrogeochemical conceptual understanding of the Forsmark site has been constructed from a combination of site measurements and hydrogeochemical modelling (Auqué et al. 2006, Laaksoharju et al. 2008, Salas et al. 2010, Smellie et al. 2008). This conceptual model describes the composition and chemistry of groundwater in the bedrock and the overlying regolith. The main geochemical parameters of concern in the safety assessment for the repository are also discussed in detail in, e.g. Salas et al. (2010) and SKB (2011), and are not further elaborated upon here.

The groundwater composition is a result of the geology and hydrogeological history of the site over a number of glacial cycles. During the current Holocene period, the site has been subject to deglaciation associated with infiltration of dilute glacial water, followed by a period of submersion below the Littorina Sea, leading to an infiltration of brackish water. Land rise caused by post-glacial isostatic rebound led to the emergence of the site above the sea from around 900 AD. Following this, the parts of the site above sea level were subject to infiltration of meteoric water, which will continue until the next permafrost/glacial period.

Most of the groundwater flow at Forsmark is above an elevation of –200 m, with horizontal flows dominating due to the presence of sub-horizontal sheet joints and gently dipping deformation zones. The decrease in fracture intensity with depth and the anisotropy in the hydraulic properties of the bedrock inhibit the penetration of groundwater from the surface to depth. Penetration of waters (aqueous solutions) infiltrating through the ground surface is further inhibited by the retardation effects of rock matrix diffusion and by buoyancy effects caused by the presence of water with higher salinity at depth. These effects give a shallow and slow circulation of groundwater, leading to slow mixing and long residence times of groundwater at depth.

The current groundwater composition in the upper bedrock (above –200 m elevation) is predominantly meteoric in origin or is a mixture of meteoric and Littorina/Baltic Sea water. The presence of limestone within the Quaternary deposits and biological activity has led to a relatively high pH and high calcium and bicarbonate concentrations in the groundwater (Laaksoharju et al. 2008).

At intermediate depths (–200 to –600 m elevation) the current groundwater composition in the footwall bedrock is predominantly a mixture of old meteoric, glacial and deep saline water. In the hanging wall bedrock at these depths, however, Littorina Sea water is more prevalent, leading to relatively high sulphate and magnesium concentrations. The pH of the bedrock at these depths is primarily determined by reactions involving the precipitation or dissolution of calcite, although other reactions have an influence. The redox conditions are reducing and may be controlled by the precipitation of amorphous iron (II) sulphides linked to the activity of sulphate-reducing bacteria.

At greater depths (below –600 m elevation) the salinity increases as deep saline water predominates. The dissolved sulphide concentrations also increase with depth and the geochemical environment is consistent with reducing conditions.

The geochemical conceptual model assumes that the groundwater composition is determined primarily by a mixing of waters of different origins, driven by groundwater flow and transport processes. However, chemical reactions are required to explain the concentrations of some species and the pH and redox conditions. These reactions are with fracture-filling minerals and with rock forming minerals. The selected minerals for SR-Site are those present at Forsmark as fracture fillings with fast kinetics compared to the time intervals considered (calcite and iron (III) oxyhydroxides) or those that appear to be in equilibrium with current groundwaters (quartz, hydroxyapatite and amorphous iron (II) monosulphides). Iron (III) oxyhydroxide and amorphous iron (II) monosulphides are two alternatives, where the former represents a system which is not affected by sulphate-reducing bacteria and the latter a situation in which there is significant activity of sulphate-reducing bacteria (Salas et al. 2010). Additional minerals (albite, kaolinite, and K-feldspar) are included in a case study (Case 4). These minerals are chosen to represent the current understanding of the mineralogy at the site. The representation is discussed and the choice is motivated in e.g. Auqué et al. (2006). There are however large uncertainties regarding e.g. the thermodynamic data for these additional minerals. Furthermore, the additional aluminosilicates in Case 4 are known to react slowly under the geochemical conditions considered. These are reasons to consider the results of Case 4 with caution, as will be further pointed out throughout the report. The selected minerals in all modelled cases are assumed to be in equilibrium with the groundwater at all locations and times. In addition, it is assumed that these minerals are present in sufficient quantity such that they cannot be depleted.

## 2.2 Methods and tools

The modelling reported here was carried out using ConnectFlow version 10.5 (AMEC 2013a, b, c). ConnectFlow is a suite of groundwater flow and transport software that is able to represent rock using continuous porous medium (CPM), discrete fracture network (DFN), or combined CPM/DFN concepts. An equivalent continuous porous medium (ECPM) concept based on upscaled DFN properties is also available. The modelling carried out for this study uses CPM and ECPM representations. The main concepts and methods used for this work are summarised in the following sections. Further details can be found in Joyce et al. (2010, 2015), Hartley and Joyce (2013) and AMEC (2013a, b, c).

### 2.2.1 Discrete fracture network (DFN) representation

The DFN concept is very useful since it naturally reflects the individual flow conduits in fractured rock and the available field data. The properties of the network are usually characterised in terms of:

- Spatial distribution (e.g. Poisson, fractal, clustered around points or lineaments).
- Fracture intensity (and its spatial variation).
- Fracture sets distinguished by orientation.
- Fracture size (e.g. log-normal, power-law distributions).
- Transmissivity-size relationships.

The properties of each fracture are primarily:

- Size.
- Orientation (strike and dip).
- Transmissivity (and possibly spatial variability within the fracture).
- Transport aperture.
- Storativity.

In ConnectFlow, fractures are usually rectangular, but may be right-angled triangles where a complex surface has been triangulated into many pieces (e.g. for a deformation zone). For stochastic fractures, the properties are sampled from probability distribution functions (PDFs) specified for each fracture set. The properties may be sampled independently or correlated with other properties.

### 2.2.2 Continuous porous medium (CPM) representation

CPM models are considered appropriate for certain types of rock, in which flow is predominantly through an interconnected network of pores in the rock matrix, such as for many sandstones, or for soils and unconsolidated deposits. The model assumes continuity in three dimensions and hence a high degree of connectivity between points in the modelling domain. Connectivity is only reduced when very low conductivity layers or flow barriers are incorporated in the model. The flow through such domains is modelled by Darcy's law, which relates specific discharge (Darcy flux) to the driving force, i.e. the pressure gradient and/or buoyancy force.

The CPM representation is less useful for fractured rocks as it can only represent bulk properties over large volumes. However, it can be of use for regions of a model where there is limited data available on fracturing and it is appropriate to use generic rock properties, e.g. in rock mass volumes far away from the repository host rock.

### 2.2.3 Equivalent continuous porous medium (ECPM) representation

In order to assess the implications of a discrete fracture network for flow and transport on the regional-scale, it is often necessary for practical reasons to convert the DFN model to an ECPM model with appropriate properties. The resulting parameters are a directional hydraulic conductivity tensor, fracture kinematic porosity and other transport properties (such as the fracture surface area per unit volume). In ConnectFlow, a flux-based upscaling method is used that requires several flow calculations through a DFN model in different directions (Hartley and Joyce 2013, Jackson et al. 2000).

### 2.2.4 Implicit fracture zones (IFZ)

The properties of large deterministic structures, such as deformation zones, in CPM or ECPM models can be represented in ConnectFlow using the implicit fracture zone (IFZ) method. This approach combines the properties of each cell in the model that is intersected by a structure with the corresponding properties of the intersecting structure, taking the volume of the cell occupied by the structure and its orientation into account (Hartley and Joyce 2013). The result of this process is to produce a spatial distribution of cell properties (hydraulic conductivity tensor, porosity and flow wetted surface) that represent the combined influence of both the deterministic structures and bedrock stochastic fractures.

### 2.2.5 Groundwater flow

Groundwater flow in a CPM or ECPM model in ConnectFlow is expressed in terms of Darcy's law

$$\mathbf{q} = -\frac{k}{\mu} \cdot (\nabla P - \rho \mathbf{g}) \tag{2-3}$$

and the equation for conservation of mass

$$\frac{\partial(\phi_f \rho)}{\partial t} + \nabla \cdot (\rho \mathbf{q}) = 0 \tag{2-4}$$

where

- $\mathbf{q}$ is the specific discharge (or Darcy flux) [m/s],
- $k$ is the equivalent permeability tensor due to the fractures carrying the flow [$m^2$],
- $\mu$ is the groundwater viscosity [kg/m/s],
- $P$ is the (total) pressure in the groundwater [$N/m^2$],
- $\rho$ is the groundwater density [$kg/m^3$],
- $\mathbf{g}$ is the gravitational acceleration [$m/s^2$],
- $t$ is the time [s],
- $\phi_f$ is the kinematic porosity due to the fractures carrying the flow [–].

In general, the density and viscosity of the groundwater depend on temperature, pressure and total salinity. Temperature and salinity are in turn transported by the groundwater. When the variations in temperature or solute concentration are large enough to produce significant changes in density or viscosity, it is necessary to couple the solution of the groundwater flow problem to that of the heat or solute transport problem. For this study, transport of heat is not included.

### 2.2.6 Solute transport

ConnectFlow calculates solute transport using the advection-dispersion equation

$$\frac{\partial(\phi_f \rho c)}{\partial t} + \nabla \cdot (\rho \mathbf{q} c) = \nabla \cdot (\phi_f \rho D \cdot \nabla c) \qquad (2\text{-}5)$$

where

- $c$ is the solute mass fraction in the groundwater flowing through the fractures [–],
- $D$ is the (effective) dispersion tensor [$m^2/s$].

For a single transported component, Equations (2-3), (2-4) and (2-5) can be solved in ConnectFlow as a coupled set of equations. However, for the transport of many components it is not usually practicable to solve the full set of coupled equations simultaneously. In this case, sequential iteration can be used as an operator splitting method to decouple the equations and solve each groundwater flow and transport equation separately within each time step. Multiple iterations of the sequence of equations can be carried out for increased accuracy at the expense of computational time, but normally a single iteration is sufficient for a system that is evolving slowly relative to the time step size.

### 2.2.7 Rock matrix diffusion (RMD)

Rock matrix diffusion (RMD) is the process of migration of solutes from fractured rock into the less mobile water within the rock matrix over long time periods. The rock matrix diffusion method used for the ConnectFlow modelling in SR-Site is not compatible with the calculation of chemical reactions, so a newer method based on a finite volume approach has been used for this study (Joyce et al. 2015). This method divides the rock matrix into separate elements and calculates the transport of components from one element to the next at each time step before carrying out chemical reactions.

### 2.2.8 Hydrogeochemical calculations

ConnectFlow is able to combine groundwater flow and transport calculations with geochemical calculations (reactive transport) (Joyce et al. 2015). At each time step, the mass fractions of components are updated based on the results of chemical reaction calculations carried out at equilibrium. The chemical reactions are calculated by the iPhreeqc software library (Charlton and Parkhurst 2011), which encapsulates and provides access to the widely used PHREEQC geochemical software (Parkhurst and Appelo 1999). The data produced by iPhreeqc are used to calculate the mass fractions of components for the next time step in ConnectFlow. Figure 2-8 shows a flow diagram describing the reactive transport system in ConnectFlow. Chemical reactions are calculated for both the fractures and the rock matrix.

The chemical calculations are based on a set of thermodynamic constraints defined in a separate database. The thermodynamic database used here is basically the same as the one used in the SR-Site calculations performed by Salas et al. (2010) (i.e. SKBdoc 1261302 ver 3.0). Additional equilibrium constraints with mineral phases FeS(ppt), hematite, albite, K-feldspar, and kaolinite have been added to the database to include the reactions considered in this study. The mineral reactions considered are,

- Quartz: $SiO_2 + H_2O = Si(OH)_4$ , logK = –3.746.
- Calcite: $CaCO_3 + H^+ = Ca^{2+} + HCO_3^-$ , logK = 1.849.
- FeS(ppt): $FeS + H^+ = Fe^{2+} + HS^-$ , logK = –3.00.
- Hematite: $Fe(OH)_3 + 3H^+ = Fe^{3+} + 3H_2O$ , logK = –1.10.
- Albite: $NaAlSi_3O_8 + 8H_2O = Al(OH)_4^- + 3Si(OH)_4 + Na^+$ , logK = –19.98.
- K-feldspar: $KAlSi_3O_8 + 8H_2O = Al(OH)_4^- + 3Si(OH)_4 + K^+$ , logK = –22.62.
- Kaolinite: $Al_2Si_2O_5(OH)_4 + 7H_2O = 2Al(OH)_4^- + 2H^+ + 2Si(OH)_4$ , logK = –37.3.

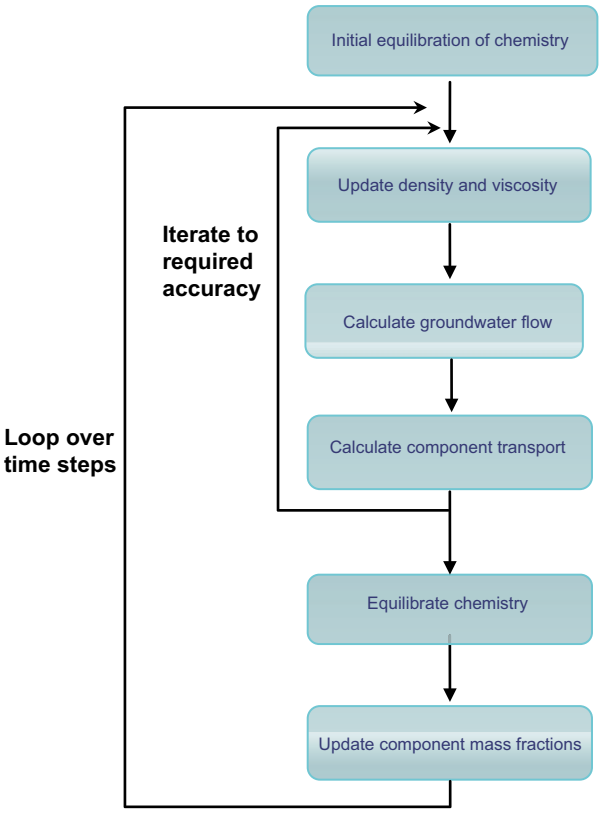


***Figure 2-8.*** *Flow diagram of reactive transport within ConnectFlow.*

The mineral reaction formulae and their corresponding equilibrium constants that were not included in the thermodynamic database used within SR-Site (SKBdoc 1261302 ver 3.0) are listed in the PhreeqC format in Table 2-6. See Parkhurst and Appelo (1999) for details on the input format. These database entries correspond to the recommendations made in e.g. Auqué et al. (2006, Appendix A), where also the rationale behind the choice of reactions and thermodynamic constants is explained in more detail.

**Table 2-6. Additions to the thermodynamic database used in SR-Site (Salas et al. 2010). Reaction formulae and equilibrium constants are given in PhreeqC format (see Parkhurst and Appelo (1999) for details). For details on the choice of reactions and thermodynamic constants, see Auqué et al. (2006).**

| |
|---|
| Albite<br>NaAlSi3O8 + 8H2O = Al(OH)4– + 3Si(OH)4 + Na+<br>log_k –19.98<br>–analytic –5,429.59545 –0.81939 293,813.48663 1,966.59164 –17,577,933.12184 |
| K-feldspar<br>KAlSi3O8 + 8H2O = Al(OH)4– + 3Si(OH)4 + K+<br>log_k –22.62<br>–analytic –5,701.00975 –0.87173 304,836.7864 2,069.03705 –18,119,139.36096 |
| Fe(OH)3(hematite_grenthe)<br>Fe(OH)3 + 3 H+ = Fe+3 + 3 H2O<br>log_k –1.1 |
| FeS(ppt)<br>FeS + H+ = Fe+2 + HS–<br>log_k –3.00 |
| Kaolinite_Grimaud<br>Al2Si2O5(OH)4 + 7H2O = 2Al(OH)4– + 2H+ + 2Si(OH)4<br>log_k –37.3 |

# 3 Modelling

## 3.1 Model description

The models used in this study are based on the regional-scale model of the hydrogeological base case used for the SR-Site temperate climate period modelling (Joyce et al. 2010). The only changes have been to support reactive transport modelling and to extend the simulated period to 60,000 AD. The main features of the models are summarised in the following sections.

### 3.1.1 Model grid

The model grid is approximately 15 km by 10 km in horizontal extent and extends from the ground surface to a depth of 1.2 km. The upstream boundaries of the model correspond to significant surface water divides and the downstream boundary represents the furthest shoreline position reached during the temperate period (Follin et al. 2007a). A local area is defined around the repository, approximately 3.3 km square. Within the local area the grid cells are 20 m square horizontally. Outside the local area the grid cells are a constant 100 m square horizontally. There are around one million finite elements in the model in total. Internal boundary conditions ensure continuity of pressure and flow where there are discontinuities in the grid at the boundaries of the local area. The cells are approximately cubes, except in the soil domain, where a 1 m vertical cell size is used. The upper layers of the model are also mapped to the surface topography which causes some adjustment of cell height.

### 3.1.2 Hydraulic properties

The model uses an equivalent porous medium (ECPM) representation, whose hydraulic properties are derived from the upscaling of a discrete fracture network (DFN) representing the Hydraulic Rock mass Domain (HRD), combined with the application of deformation zone and sheet joint properties using the implicit fracture zone method (IFZ), as described in Section 2.1.4. The Hydraulic Soil Domain (HSD) is represented by four 1 m deep layers. The vertical and horizontal components of the HSD hydraulic conductivity are different, i.e. the hydraulic conductivity is anisotropic. The horizontal component of the conductivity tensor is based on the arithmetic mean of the hydraulic properties of the original stratigraphy, whereas the vertical component is based on its harmonic mean.

The ECPM model used for this study is derived from the first realisation of the DFN for the HRD and the deterministic (with a depth trend) deformation zone model (referred to as $r_0$ in Joyce et al. (2010)).

### 3.1.3 Initial condition and boundary conditions

The initial condition and the boundary conditions are equivalent to those used for the SR-site temperate period regional-scale model (Joyce et al. 2010), which are the same as those used for the "Alternative Case" palaeohydrogeology model in Follin et al. (2007a). The initial groundwater composition and that of recharging groundwater is specified in terms of fractions of reference waters, which are then converted to an equivalent representation in terms of mass fractions of individual components within ConnectFlow. The composition of each reference water is shown in Table 3-1. The fraction of each reference water used in the initial condition varies according to depth and rock domain, as shown in Figure 3-1.

The boundary conditions for the sides of the model specify zero flux of water and zero flux of solute. The boundary condition on the bottom of the model specifies zero flux of water and the mass fractions of the solutes are held constant at their initial values. The top surface boundary condition leads to recharge or discharge of water depending on the calculated head relative to the ground surface elevation (taking land rise, the depth of the sea and the salinity of the sea into account). The composition of infiltrating water through the top boundary varies over time, consisting of Glacial water at early times, followed by Littorina Sea water for parts of the surface below the sea and then meteoric water for land areas above sea level.

**Table 3-1. Reference water compositions.**

| | Deep Saline | Littorina | Altered Meteoric | Glacial | Old Meteoric | Dilute Meteoric |
|---|---|---|---|---|---|---|
| pH | 8.000 | 7.951 | 7.314 | 9.300 | 8.500 | 7.030 |
| pe | –4.449 | –4.422 | 0.554 | –5.260 | –4.925 | 0.456 |
| **Component mass fractions (kg/kgs)** | | | | | | |
| Al | $1.854 \cdot 10^{-10}$ | $8.662 \cdot 10^{-9}$ | $2.081 \cdot 10^{-9}$ | $1.404 \cdot 10^{-7}$ | $2.465 \cdot 10^{-8}$ | $4.000 \cdot 10^{-8}$ |
| Br | $3.081 \cdot 10^{-4}$ | $2.222 \cdot 10^{-5}$ | $5.722 \cdot 10^{-7}$ | 0.000 | $5.720 \cdot 10^{-7}$ | 0.000 |
| C | $4.099 \cdot 10^{-7}$ | $1.932 \cdot 10^{-5}$ | $8.678 \cdot 10^{-5}$ | $1.023 \cdot 10^{-6}$ | $6.268 \cdot 10^{-6}$ | $5.490 \cdot 10^{-5}$ |
| Ca | $1.837 \cdot 10^{-2}$ | $1.532 \cdot 10^{-4}$ | $1.883 \cdot 10^{-5}$ | $2.878 \cdot 10^{-6}$ | $4.743 \cdot 10^{-5}$ | $9.290 \cdot 10^{-5}$ |
| Cl | $4.494 \cdot 10^{-2}$ | $6.506 \cdot 10^{-3}$ | $1.811 \cdot 10^{-4}$ | $4.999 \cdot 10^{-7}$ | $1.810 \cdot 10^{-4}$ | $4.400 \cdot 10^{-6}$ |
| F | $1.524 \cdot 10^{-6}$ | $4.903 \cdot 10^{-7}$ | $1.601 \cdot 10^{-6}$ | 0.000 | $1.600 \cdot 10^{-6}$ | 0.000 |
| Fe | $1.308 \cdot 10^{-8}$ | $4.562 \cdot 10^{-7}$ | $1.001 \cdot 10^{-7}$ | $4.469 \cdot 10^{-8}$ | $4.880 \cdot 10^{-10}$ | $1.400 \cdot 10^{-7}$ |
| K | $2.983 \cdot 10^{-5}$ | $1.341 \cdot 10^{-4}$ | $5.603 \cdot 10^{-6}$ | $4.000 \cdot 10^{-7}$ | $5.600 \cdot 10^{-6}$ | $1.560 \cdot 10^{-6}$ |
| Li | $4.419 \cdot 10^{-6}$ | $7.007 \cdot 10^{-8}$ | $1.401 \cdot 10^{-8}$ | 0.000 | $1.400 \cdot 10^{-8}$ | 0.000 |
| Mg | $2.019 \cdot 10^{-6}$ | $4.482 \cdot 10^{-4}$ | $7.503 \cdot 10^{-6}$ | $9.999 \cdot 10^{-8}$ | $7.501 \cdot 10^{-6}$ | $4.200 \cdot 10^{-6}$ |
| Na | $8.108 \cdot 10^{-3}$ | $3.676 \cdot 10^{-3}$ | $2.741 \cdot 10^{-4}$ | $1.700 \cdot 10^{-7}$ | $2.741 \cdot 10^{-4}$ | $6.000 \cdot 10^{-6}$ |
| S | $2.975 \cdot 10^{-6}$ | $2.975 \cdot 10^{-4}$ | $2.839 \cdot 10^{-5}$ | $1.701 \cdot 10^{-7}$ | $2.838 \cdot 10^{-5}$ | $3.330 \cdot 10^{-6}$ |
| Si | $2.295 \cdot 10^{-6}$ | $3.560 \cdot 10^{-6}$ | $3.767 \cdot 10^{-6}$ | $4.676 \cdot 10^{-6}$ | $3.919 \cdot 10^{-6}$ | $4.350 \cdot 10^{-6}$ |
| Sr | $3.209 \cdot 10^{-4}$ | $2.682 \cdot 10^{-6}$ | $3.801 \cdot 10^{-7}$ | 0.000 | $3.801 \cdot 10^{-7}$ | 0.000 |

### 3.1.4 Solute transport

Calculations of variable density groundwater flow and solute transport are carried out for the simulation period of 8000 BC to 60,000 AD in constant 20 year time steps (for consistency with SR-Site). An efficient multi-component sequential iteration method is used to transport each component individually and decouple the transport and flow calculations within each individual time step, although changes in flow, composition and fluid density affect conditions in the next time step. For those cases involving chemical reactions, the reactions are calculated at each time step. For reasons of efficiency, chemical reactions are only calculated at locations where the mass fraction of any component has changed by at least 2% since the last time chemical reactions were calculated at that location. The 2% calculation threshold was chosen based on scoping simulations to provide good efficiency without impacting the quality of the results.

A finite volume implementation of the rock matrix diffusion method is used for this study, which also allows equilibration of chemical species to occur in the rock matrix. Five rock matrix cells, which increase linearly in size with distance from the fracture, are used for each model grid cell.

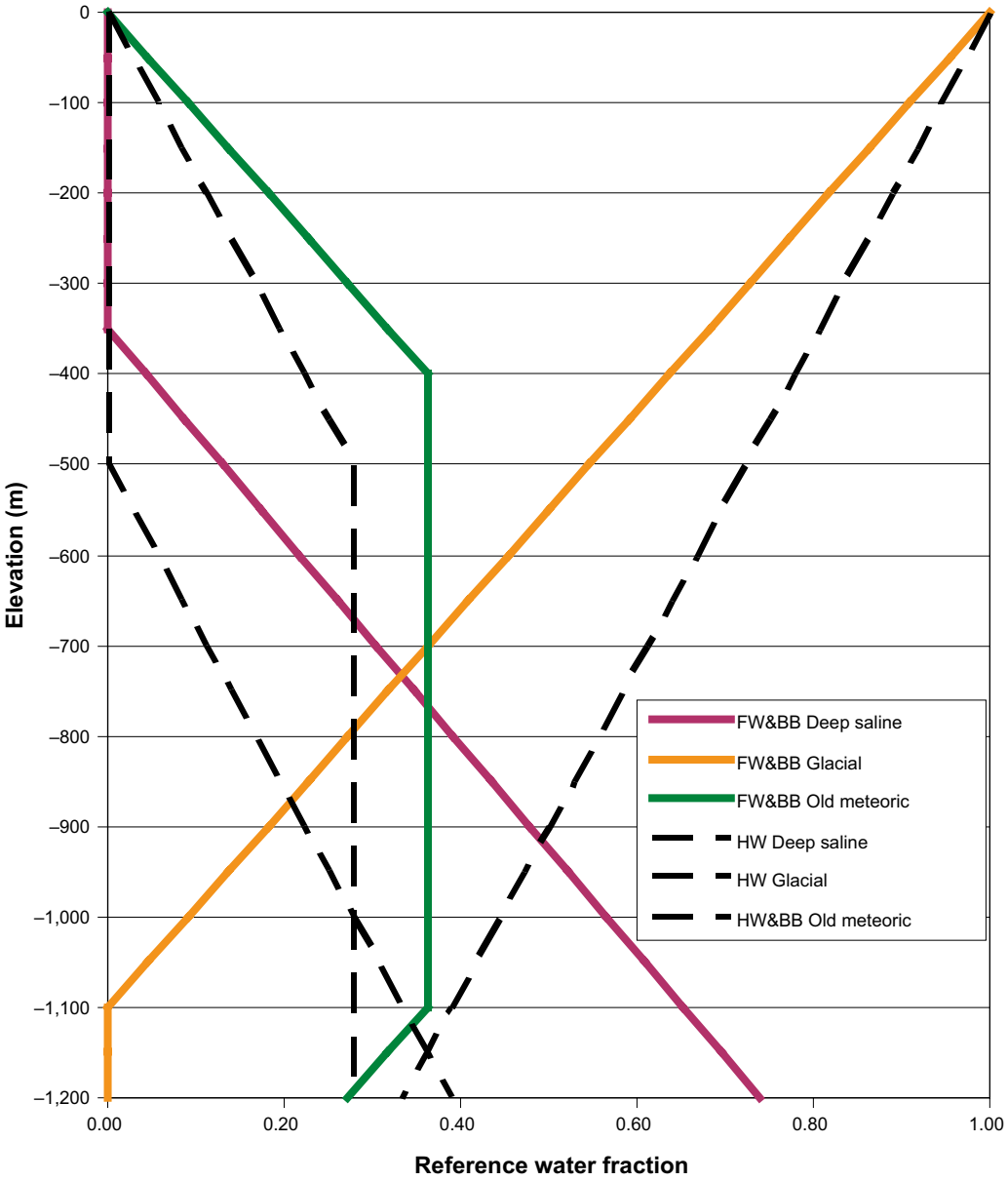


***Figure 3-1.*** *The initial fraction of each reference water as a function of depth in the footwall and border borehole regions (FW&BB) of deformation zone A2 and the hanging wall (HW) bedrock of deformation zone A2. Figure 3-63 (Alternative Case) in Follin et al. (2007a).*

## 3.2 Model cases

A number of cases are considered, as listed below. These cases are the same as those used for SR-Site or explore some of the uncertainties in the geochemical reactions that may occur at the Forsmark site. Case 1 includes no chemical reactions and simply transports the chemical components. Cases 2 to 5 include chemical reactions with different mineral phases. Case 2 and Case 3 correspond to reactions used for SR-Site (Salas et al. 2010). Case 4 includes a more comprehensive set of equilibrium mineral phases with an aim to be more representative with respect to the current understanding of the mineralogy at the Forsmark site. The choice of mineral phases for Case 4 is based on the recommendations in Auqué et al. (2006). Dissolution and precipitation of aluminosilicates in particular are known to be slow processes, and these reactions are therefore often modelled under kinetic constraints. The thermodynamic data of the additional minerals in Case 4 (see Section 2.2.8 and Auqué et al. 2006), and in particular the solubility data for aluminosilicates (albite), may further involve large uncertainties, e.g. depending on a variable degree of crystal order/disorder. The reactions of these minerals are thus difficult to represent accurately in reactive transport models, and model results should be considered with

caution. In this report, one model case with these minerals included at local equilibrium is justified with respect to the scope of the calculations, which is to evaluate the long-term effects of extended temperate conditions and also the sensitivity of the results for a range of geochemical conditions. The results of Case 4, and in particular the equilibrium approach of aluminosilicates, can be considered to be an unlikely yet thermodynamically permissible example of such conditions. Case 5 is similar to Case 2 but includes a more dilute meteoric water (Dilute Meteoric water in Table 3-1) as compared to the other cases, infiltrating at the top boundary for land areas above sea level. Equilibrium conditions are assumed for all chemical reactions, and an initial amount of 10.0 moles of each mineral per kilogram of water (the PHREEQC default) is specified that allows for both dissolution and precipitation.

Case 1. No chemical reactions, i.e. the groundwater composition will be determined only by groundwater flow and transport.

Case 2. Equilibration of groundwater with calcite, quartz and amorphous iron (II) sulphide. This is the "base case" from Salas et al. (2010) for the situation with significant activity of sulphate-reducing bacteria. However, the hydroxyapatite reactions are not included as they are not deemed relevant to this work.

Case 3. Equilibration of groundwater with calcite, quartz and iron (III) oxyhydroxide. This is the "base case" from Salas et al. (2010) for the situation where the redox state is not affected by sulphate-reducing bacteria. Again, the hydroxyapatite reactions are not included.

Case 4. Equilibration of groundwater with calcite, quartz, amorphous iron (II) sulphide, kaolinite, albite, and K-feldspar. This case represents an updated understanding of the site mineralogy relative to SR-Site. The additional reactions and thermodynamic data relative to Case 2 are described in detail in Auqué et al. (2006).

Case 5. As Case 2, but with a more dilute composition for meteoric water. This can be considered a bounding case for dilute water infiltration.

In each of the cases where chemical reactions are included, the reference waters are initially equilibrated with the mineral phases and charge balanced. The equilibration reactions with these minerals are then repeated for each time step using the updated compositions from the transport calculations.

# 4 Results

## 4.1 Presentation of results

Results are presented to illustrate the evolution of the groundwater composition and chemical conditions within the proposed repository volume and in the wider regional context during an extended period of temperate climate conditions. The results are given at a number of times during the extended temperate climate period to illustrate the evolution over that period. The interval between selected times is smaller at earlier times when the site is evolving more quickly. The 2000 AD, 3000 AD, 5000 AD and 9000 AD times correspond to those selected for the SR-Site temperate period (Joyce et al. 2010) and used in Salas et al. (2010). The 20,000 AD, 30,000 AD, 40,000 AD and 60,000 AD times correspond to the later part of the extended temperate climate period. Up to 9000 AD the shoreline is retreating due to land rise until it reaches the boundary of the regional model and the Baltic Sea salinity is reducing. Beyond 9000 AD the model is unchanging apart from continued infiltration of meteoric water.

For each case, box and whisker plots show the statistical distribution of pH, Eh and total molalities (in moles per kilogram of water, mol/$kg_w$) of selected solution species sampled on a regular grid of points within the repository volume between elevations –490 m and –450 m. This grid consists of 65,237 points with a spacing of 10 m vertically. Horizontally, the points reside within a domain with the following corner coordinates (1630620, 6701170); (1633370, 6701170); (1633370, 6698900); (1630620, 6698900) (as used in Salas et al. 2010). The statistical measures are the median, the 25$^{th}$ and 75$^{th}$ percentiles, the mean and the 5$^{th}$ and 95$^{th}$ percentiles.

For each case, the pH, pe and mass fractions (in kilograms per kilogram of solution, kg/$kg_s$) of selected solution species at the deposition hole locations are presented visually on a representation of the repository layout by dots coloured by the magnitude of the quantity. Each dot corresponds to the centre of a deposition hole. These plots show the variation in each quantity across the repository for each selected time.

For each case, the regional evolution of the groundwater composition is visualised as a set of slices through the model coloured by pH, pe or the mass fractions (in kilograms per kilogram of solution, kg/$kg_s$) of selected solution species. Three slices are shown; a horizontal slice at repository depth and two vertical slices, one in the direction NW-SE and one in the direction SW-NE through the centre of the repository area. In these plots the repository structures are shown to provide context, however they are not included in the model. For slices at 2000 AD, 3000 AD, 5000 AD and 9000 AD the shoreline is also presented.

A consistent value range is used for each quantity presented to allow easy comparison between the cases and between the times considered.

## 4.2 Case 1 – No chemical reactions

Since this case involves no chemical reactions, the changes in groundwater composition over time are the result of the transport and mixing of reference waters, although this is done in terms of the individual components of the reference waters. For the temperate climate period at repository depth this is the gradual replacement of mainly Littorina water with Altered Meteoric water. This leads to a reduction in salinity and an increase in the concentration of bicarbonate.

### 4.2.1 TDS and sum of cations

Figure 4-1 and Figure 4-2 show the statistical distribution of total dissolved solids (TDS) and the sum of cation charge molalities for Case 1. The plots are closely related, with the sum of cation charge molalities plot showing the same trend as the TDS plot. As expected, both TDS and the sum of cation charge molalities decrease gradually over time due to the infiltration of the more dilute Altered Meteoric water, levelling out at around 20,000 AD. Below an elevation of –400 m, the rock

in FFM01 is very sparsely fractured and the fracture network is poorly connected, leading to very low flows in the repository volume. Most of the flow in the repository area is above an elevation of -200 m, with horizontal flows dominating due to the presence of sub-horizontal sheet joints and gently dipping deformation zones. This depth dependence of fracture intensity and the anisotropy in the hydraulic properties of the host rock inhibit the penetration of groundwater from the surface to the repository. Penetration of dilute water is further delayed by the retardation effects of rock matrix diffusion and by buoyancy effects caused by the presence of water with higher salinity at or below repository depth. The high salinity at depth is maintained by the fixed composition boundary condition on the bottom surface of the model, which is consistent with the site conceptual understanding and prevents the replacement of saline water with dilute water over very long time periods. These effects limit the changes in groundwater composition caused by penetration of Altered Meteoric water beyond 20,000 AD.

At 9000 AD the 5$^{th}$ percentile for TDS within the repository volume is $1.39 \cdot 10^3$ mg/kg$_w$ and at 60,000 AD it is $1.10 \cdot 10^3$ mg/kg$_w$. This is consistent with the results for the simplified calculation of the penetration of dilute water presented in Figure 10-32 of SKB (2011), where 1% of deposition hole locations experience salinity below 1 g/L at 10,000 AD and 2% of locations at 60,000 AD.

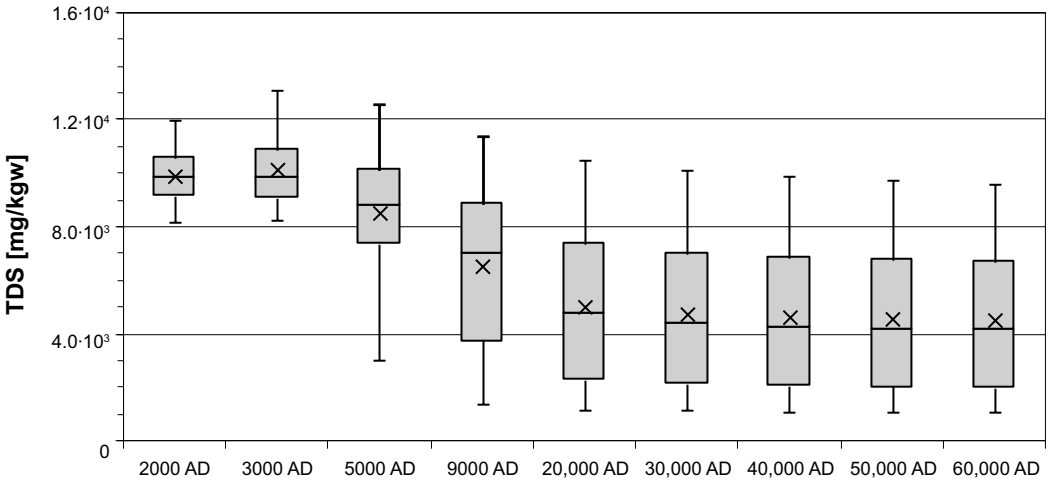


***Figure 4-1.*** *Box and whisker plot showing the statistical distribution of TDS for Case 1 on a regular grid of points within the repository volume between elevations –490 m and –450 m. The statistical measures are the median, the 25$^{th}$ and 75$^{th}$ percentiles (box), the mean (cross) and the 5$^{th}$ and 95$^{th}$ percentiles (whiskers).*

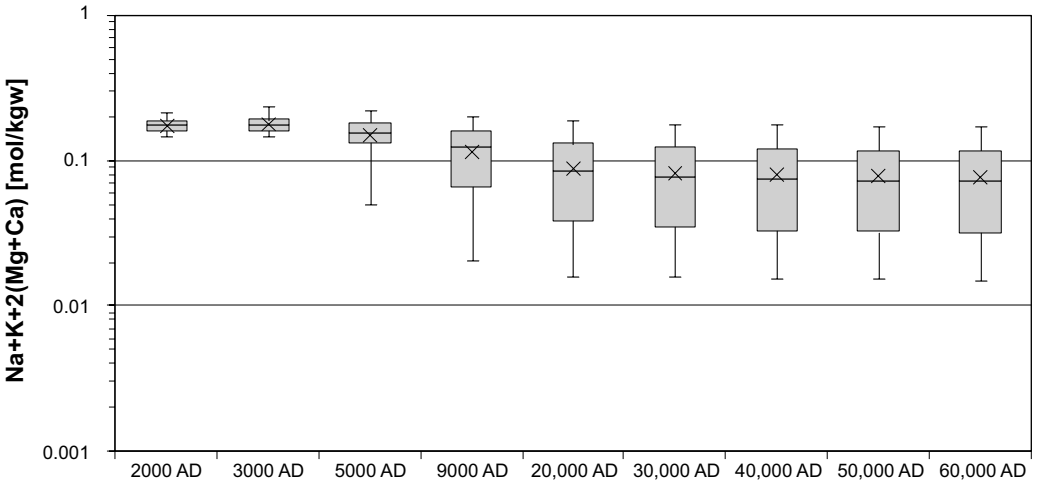


***Figure 4-2.*** *Box and whisker plot showing the statistical distribution of the sum of cation charges (Na+K+2(Mg+Ca)) molalities for Case 1 on a regular grid of points within the repository volume between elevations –490 m and –450 m. The statistical measures are the median, the 25th and 75th percentiles (box), the mean (cross) and the 5th and 95th percentiles (whiskers).*

### 4.2.2 Inorganic carbon

Figure 4-3, Figure 4-4, Figure 4-5 and Figure 4-6 show the change in total inorganic carbon over time. The box and whisker plot (Figure 4-3) shows total inorganic carbon rising over time, but then levelling off. The images in Figure 4-4 and Figure 4-5 show that the infiltration of carbon varies spatially around the deposition holes due to the structural controls and heterogeneity imposed by the underlying fracture system and deformation zones. Again, there is little change after 20,000 AD. The increase in total inorganic carbon mass fractions over time is due to higher concentrations of bicarbonate present in the infiltrating Altered Meteoric water relative to the other waters.

Figure 4-6 shows the evolution of total inorganic carbon over time across the model. On the horizontal slice at the elevation of the repository, total inorganic carbon can be seen increasing in a north easterly direction over time, i.e. towards the retreating shoreline. As in the statistical and deposition hole plots, the changes in the images after 20,000 AD are negligible compared to the changes seen at earlier times.

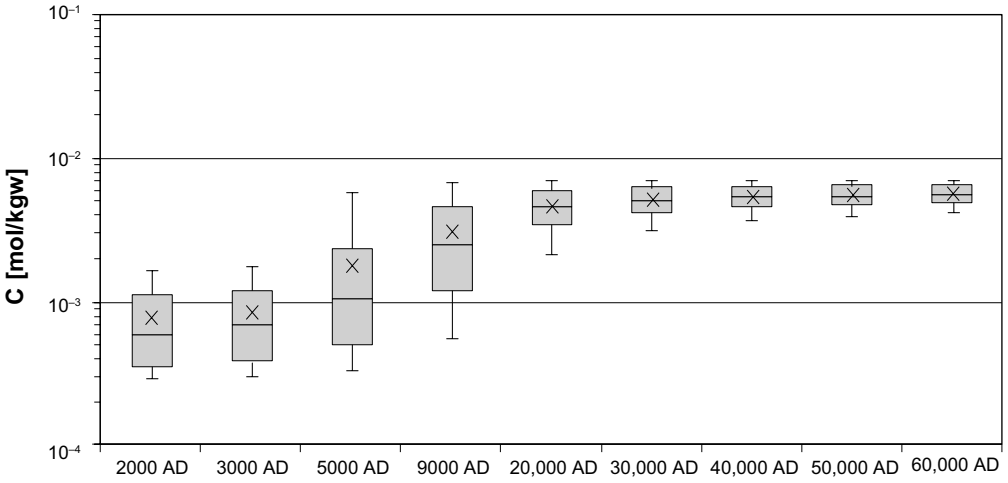


***Figure 4-3.*** *Box and whisker plot showing the statistical distribution of total inorganic carbon molalities for Case 1 on a regular grid of points within the repository volume between elevations –490 m and –450 m. The statistical measures are the median, the 25th and 75th percentiles (box), the mean (cross) and the 5th and 95th percentiles (whiskers).*

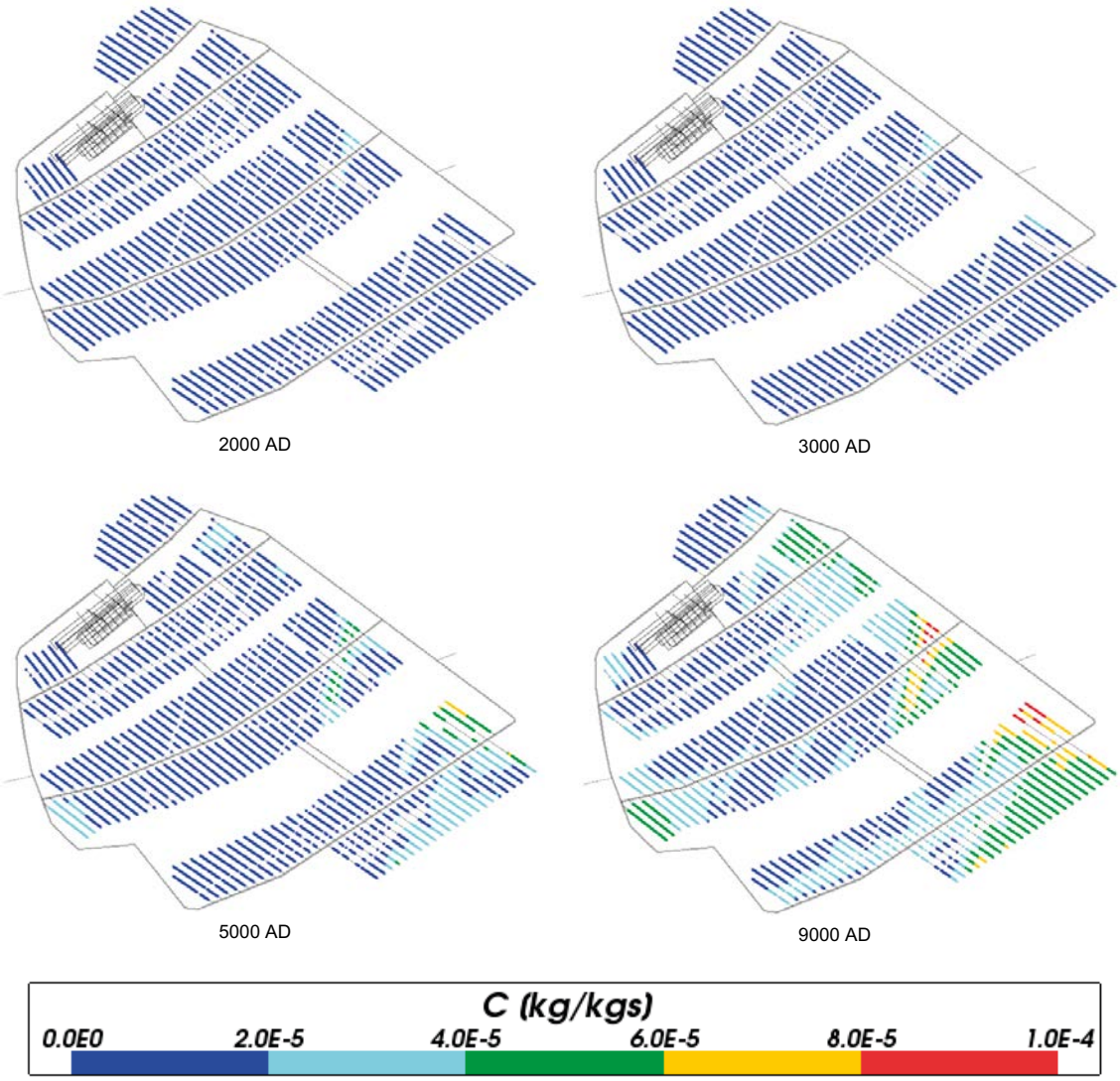


***Figure 4-4.*** *Total inorganic carbon mass fractions for Case 1 at deposition hole locations for time periods 2000 AD to 9000 AD.*

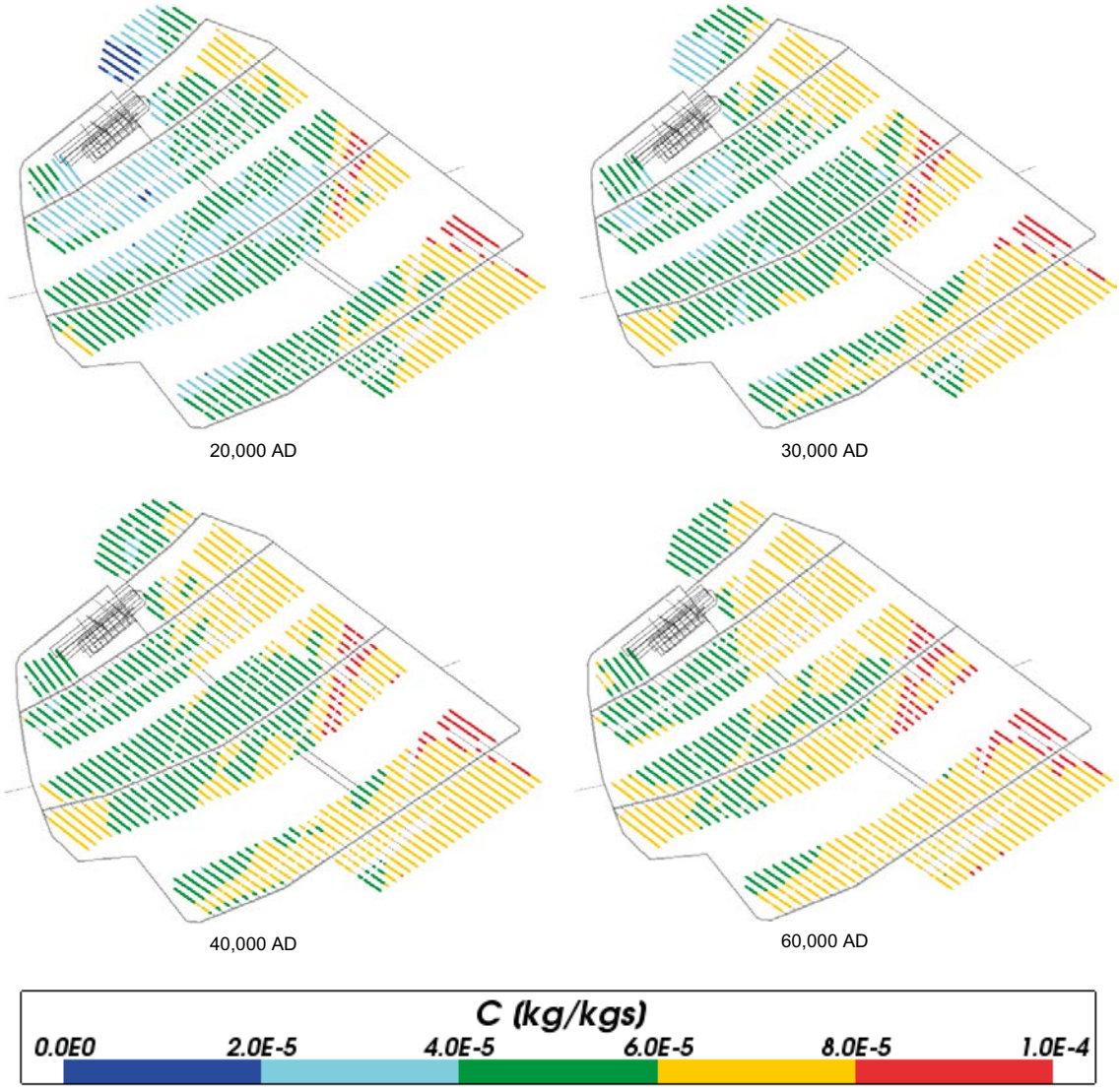


***Figure 4-5.*** *Total inorganic carbon mass fractions for Case 1 at deposition hole locations for time periods 20,000 AD to 60,000 AD.*

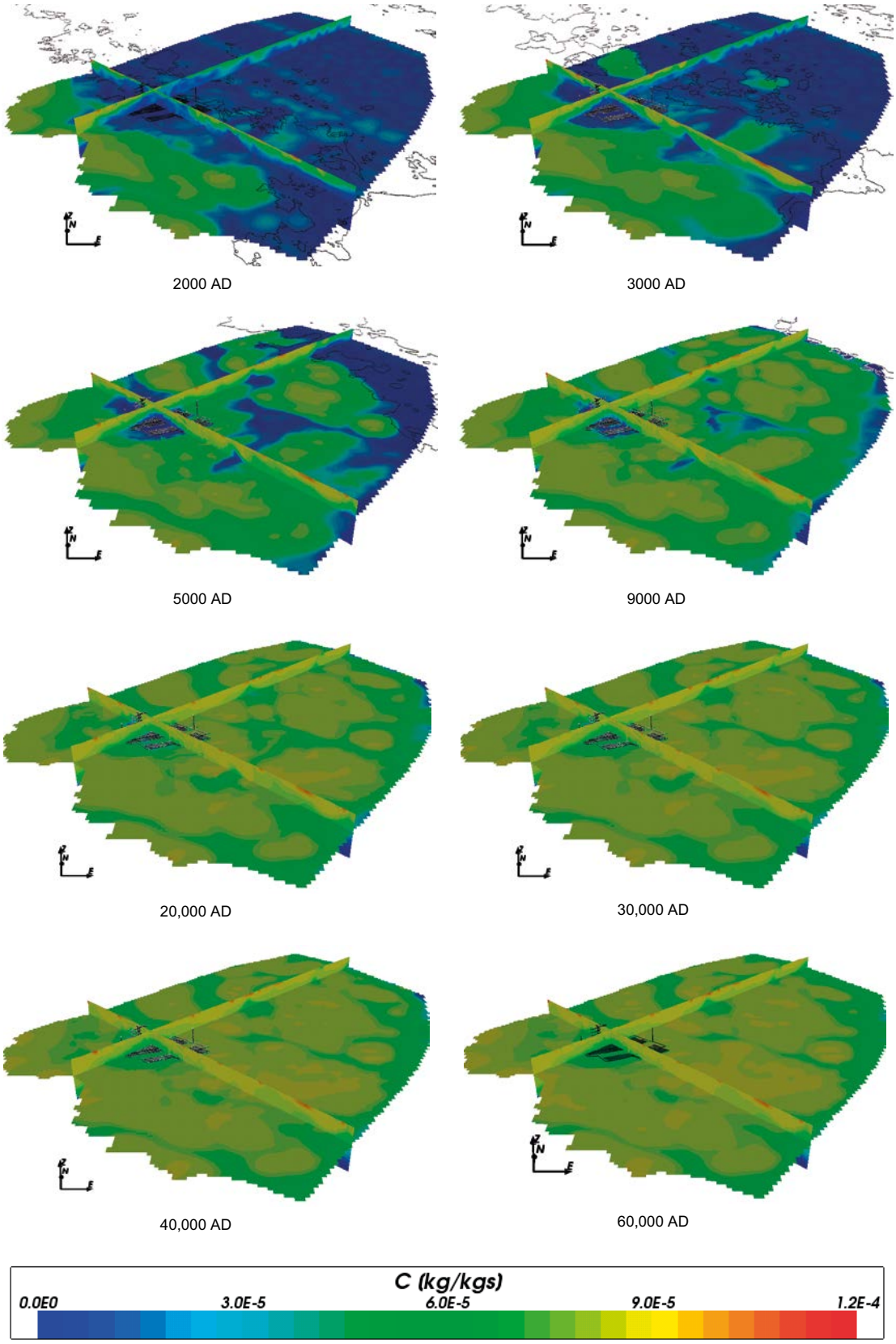


***Figure 4-6.*** *Total inorganic carbon mass fractions on regional scale slices through the repository volume for Case 1 for time periods 2000 AD to 60,000 AD.*

### 4.2.3 Calcium

Figure 4-7, Figure 4-8, Figure 4-9 and Figure 4-10 show the plots for total calcium. For this species, the box and whisker plot (Figure 4-7) shows a slight decrease in calcium over time, however there is little change to the whiskers of the plot, showing that the spread of values stays reasonably constant over time. Figure 4-8 and Figure 4-9 show the change in the spatial distribution of calcium across the deposition hole locations over time, with the calcium mass fractions generally decreasing, although there is a brief increase in one area at 3000 AD. There is little change in the spatial distribution of calcium with time at later times. The decrease in calcium mass fractions over time is due to the lower concentration of calcium in the infiltrating Altered Meteoric water compared to the Littorina water it is replacing.

The regional evolution of calcium is shown in Figure 4-10. At early times the amount of calcium is decreasing with time. After 20,000 AD the majority of the regional area is low in calcium, with occasional high spots around the edges of the model. Higher values of calcium are also seen at depth in the vertical slices (associated with Deep Saline water).

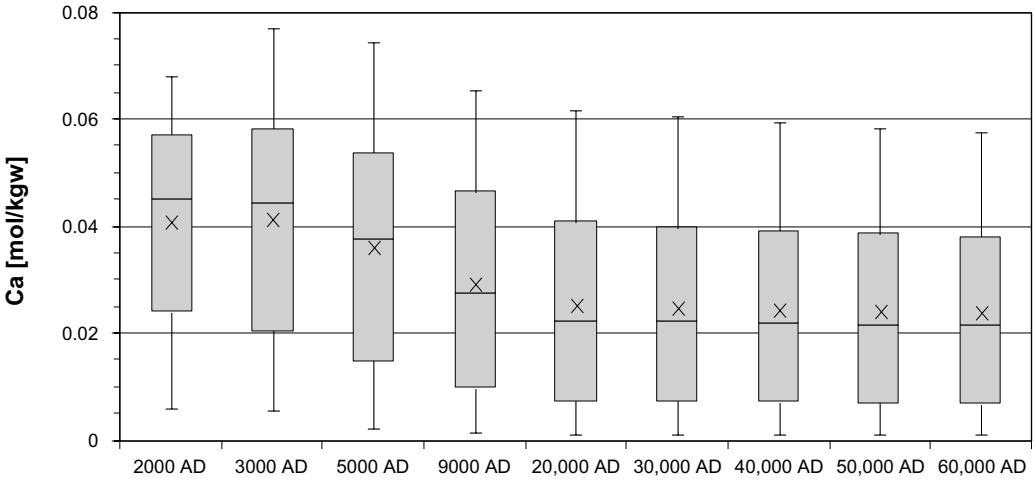


***Figure 4-7.*** *Box and whisker plot showing the statistical distribution of total calcium molalities for Case 1 on a regular grid of points within the repository volume between elevations –490 m and –450 m. The statistical measures are the median, the 25$^{th}$ and 75$^{th}$ percentiles (box), the mean (cross) and the 5$^{th}$ and 95$^{th}$ percentiles (whiskers).*

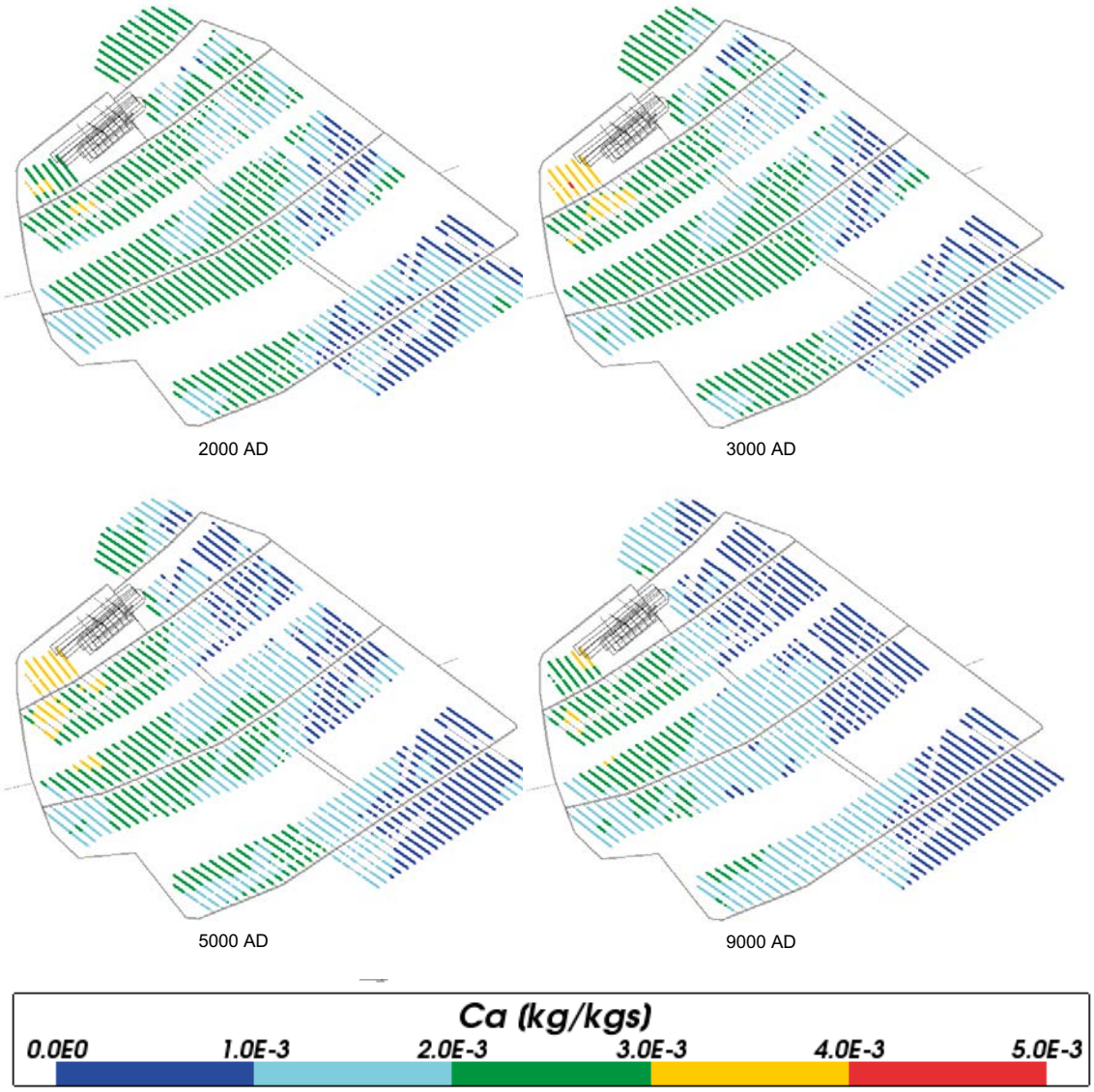


***Figure 4-8.*** *Total calcium mass fractions for Case 1 at deposition hole locations for time periods 2000 AD to 9000 AD.*

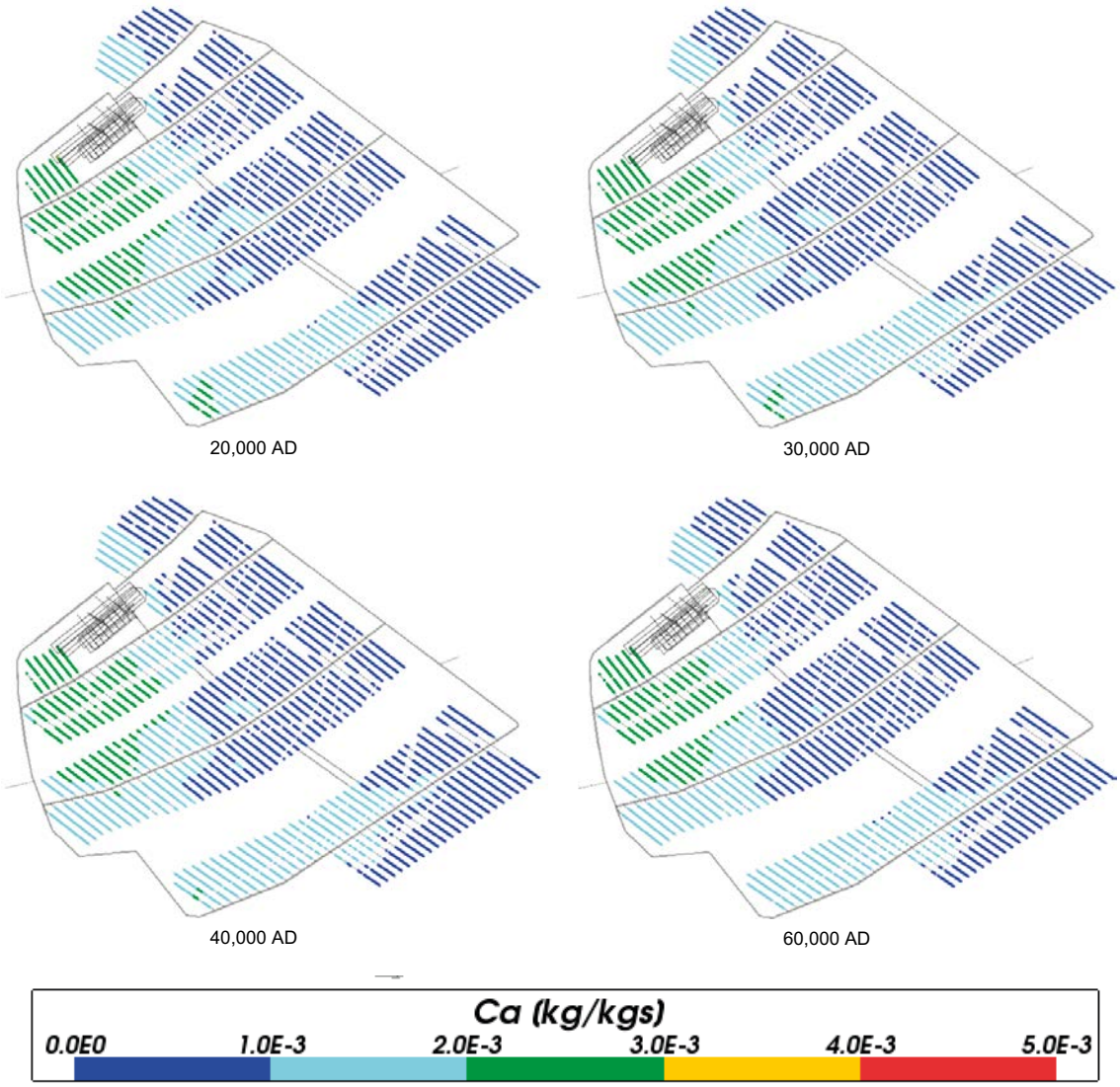


***Figure 4-9.*** *Total calcium mass fractions for Case 1 at deposition hole locations for time periods 20,000 AD to 60,000 AD.*

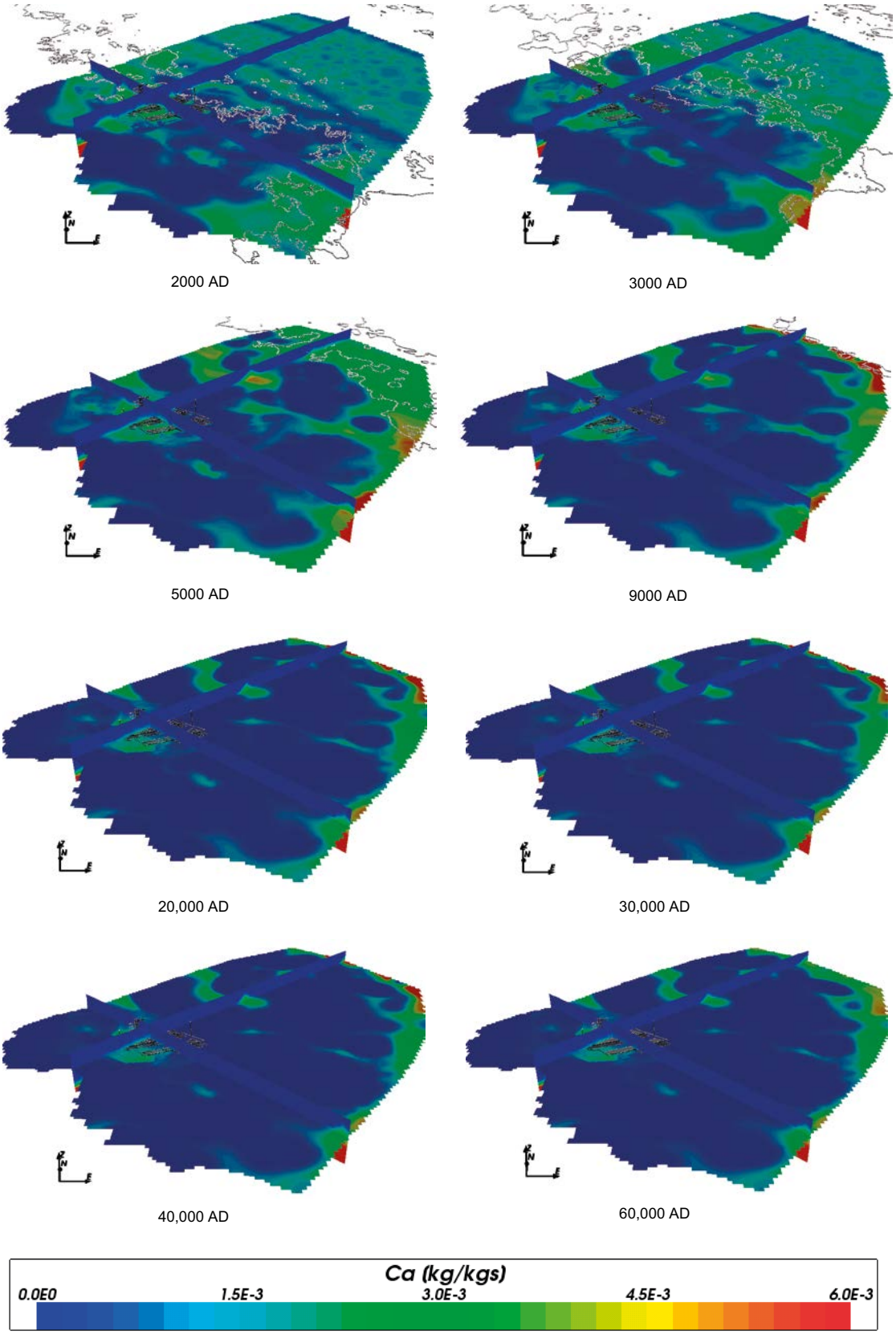


***Figure 4-10.*** *Total calcium mass fractions on regional scale slices through the repository volume for Case 1 for time periods 20,000 AD to 60,000 AD.*

### 4.2.4 Chloride

The change in chloride levels over time is shown in Figure 4-11 to Figure 4-14. The box and whisker plot demonstrates that the amount of chloride decreases over time, again levelling off at approximately 20,000 AD. This is confirmed by the deposition hole colour changes seen in Figure 4-12 and Figure 4-13.

The regional evolution of chloride over the time period modelled (Figure 4-14) is similar to that of calcium, with the value of chloride decreasing over time and responding to a north easterly regional flow.

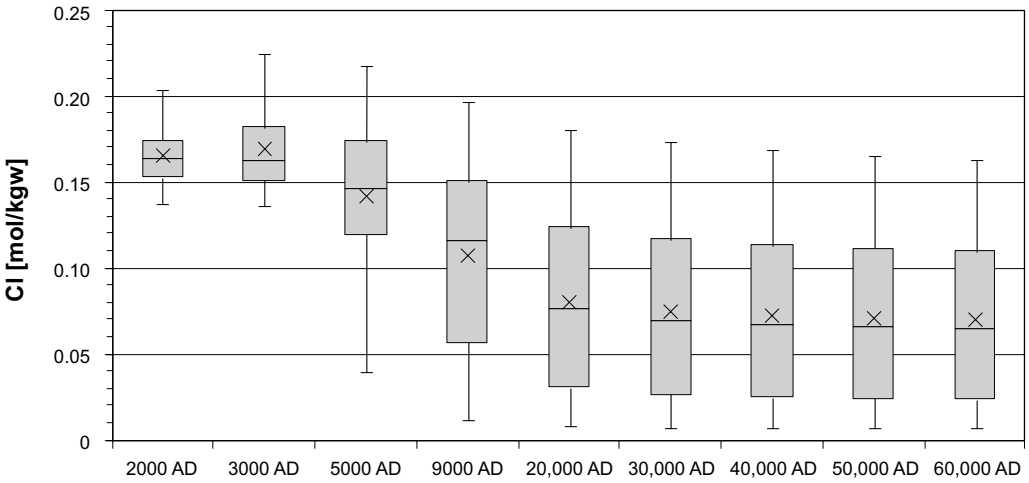


***Figure 4-11.*** *Box and whisker plot showing the statistical distribution of total chloride molalities for Case 1 on a regular grid of points within the repository volume between elevations –490 m and –450 m. The statistical measures are the median, the 25$^{th}$ and 75$^{th}$ percentiles (box), the mean (cross) and the 5$^{th}$ and 95$^{th}$ percentiles (whiskers).*

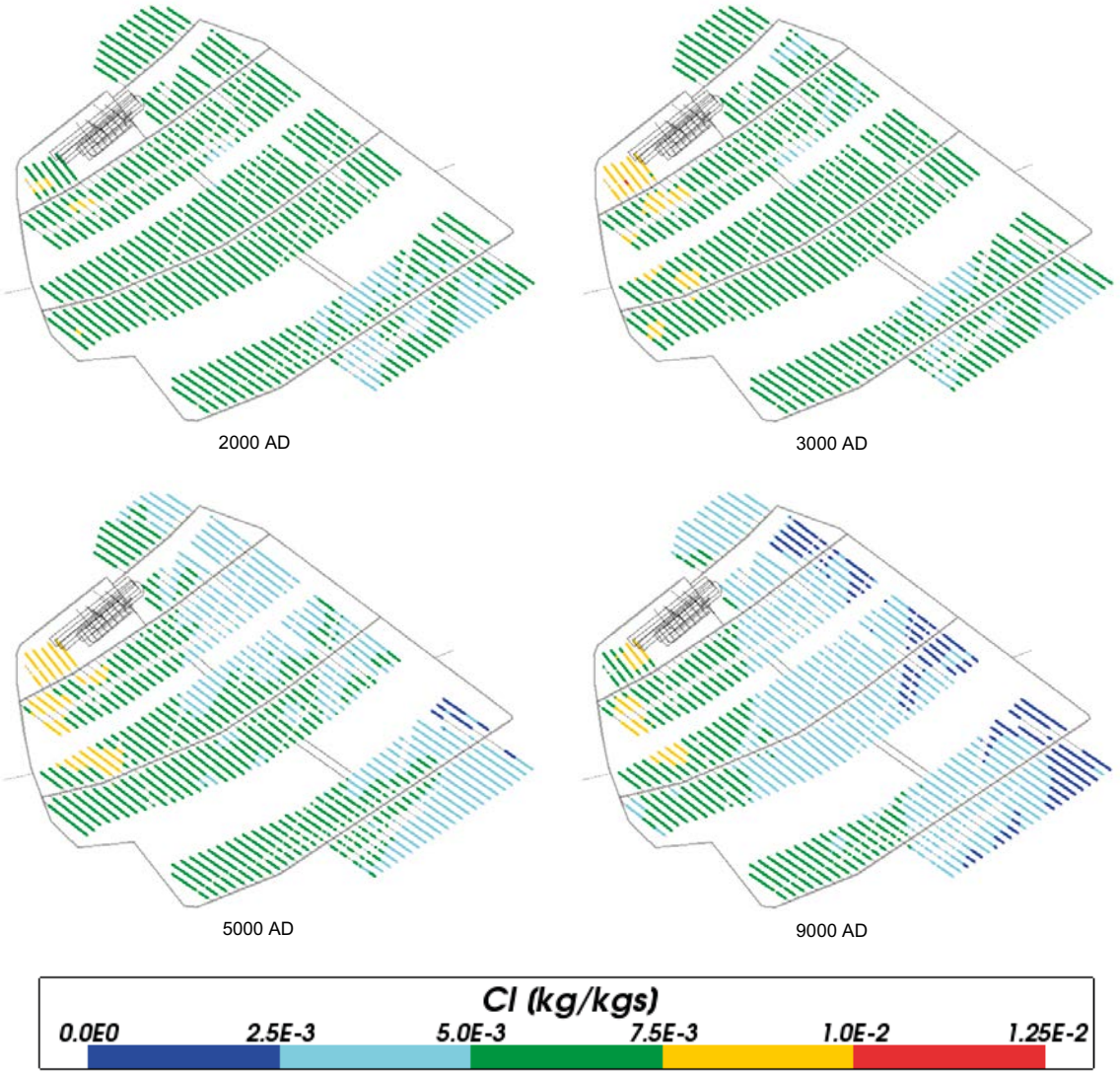


***Figure 4-12.*** *Total chloride mass fractions for Case 1 at deposition hole locations for time periods 2000 AD to 9000 AD.*

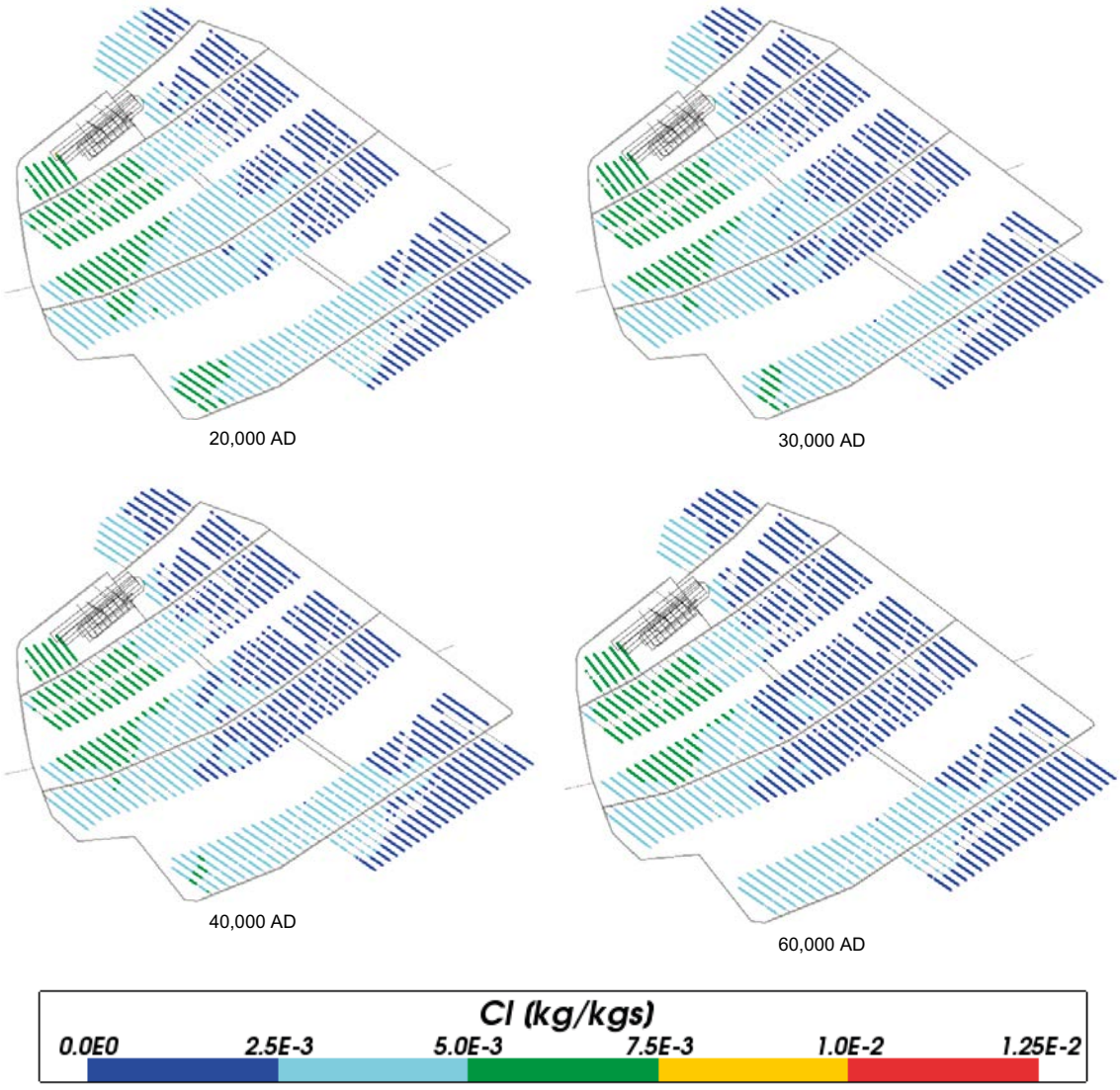


***Figure 4-13.*** *Total chloride mass fractions for Case 1 at deposition hole locations for time periods 20,000 AD to 60,000 AD.*

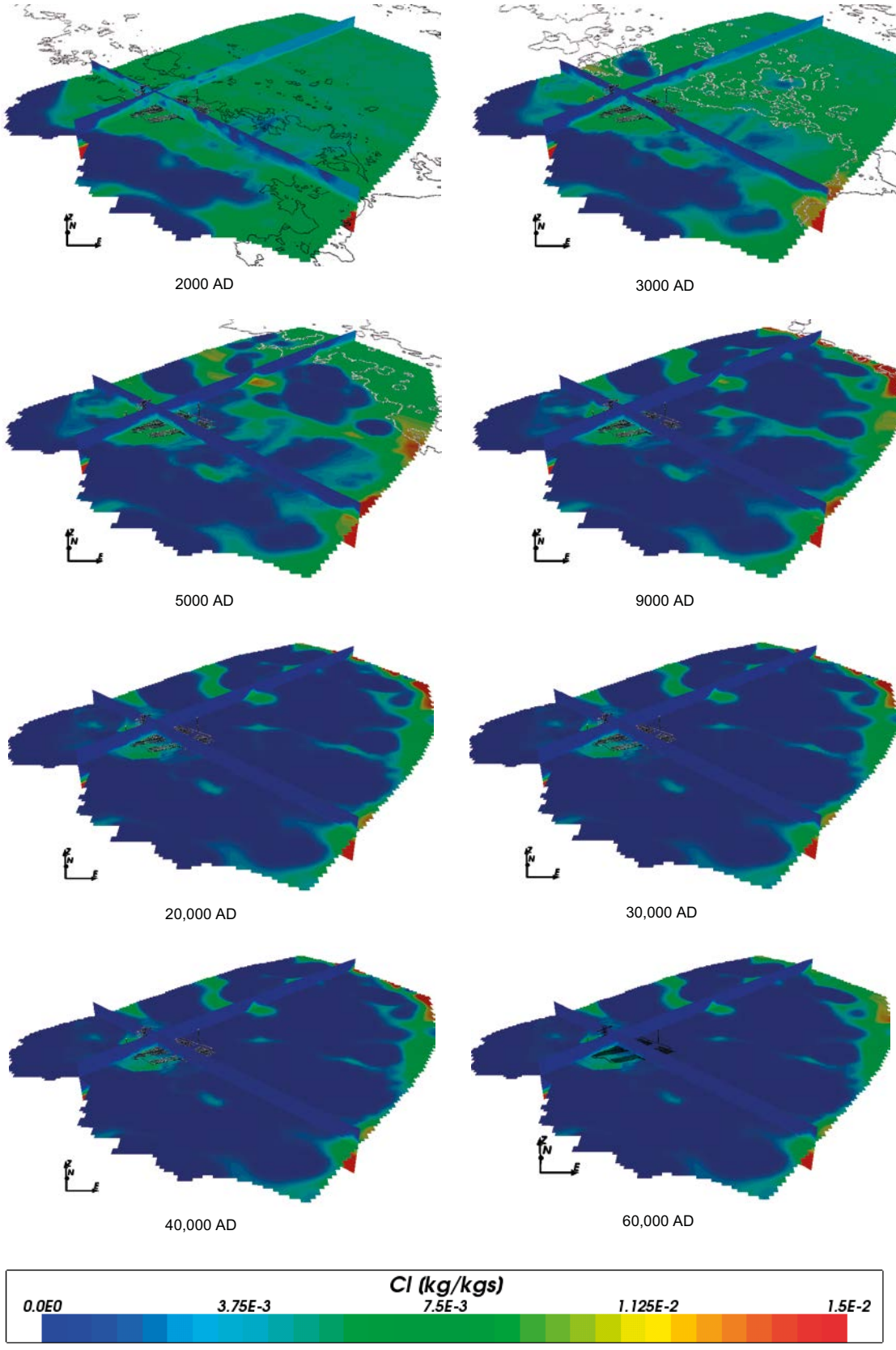


***Figure 4-14.*** *Total chloride mass fractions on regional scale slices through the repository volume for Case 1 for time periods 2000 AD to 60,000 AD.*

### 4.2.5 Iron

The range for Figure 4-15, the box and whisker plot for the concentration of iron in the repository area, has been chosen to be consistent with the range used in the other cases. As iron remains comparatively low in Case 1, where no chemical calculations are completed, little change over time is seen. Similarly Figure 4-16 and Figure 4-17 show no variation in colouring around the deposition holes across the time periods, as any change in iron for Case 1 is insignificant compared to other cases.

As with the other plots, the concentration of iron across the model region (Figure 4-18) is low compared to the concentration of iron seen in other cases, so any change over time is not apparent.

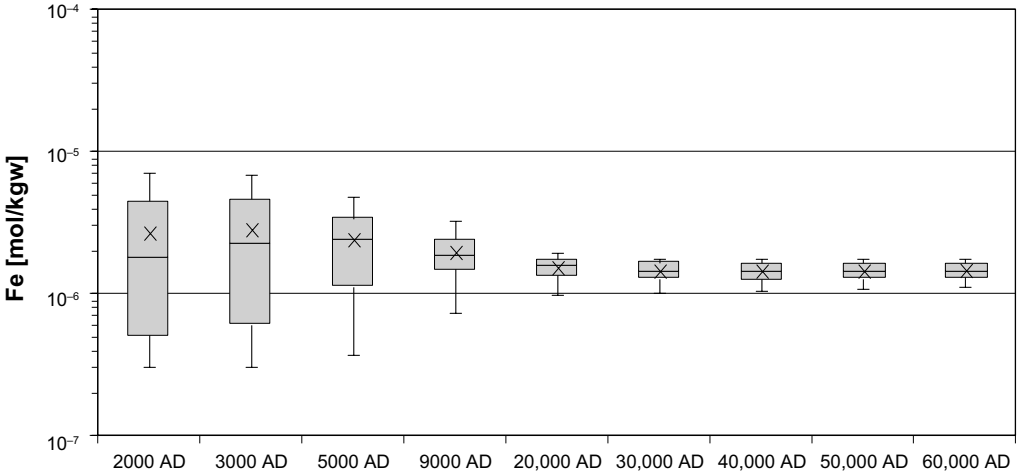


***Figure 4-15.*** *Box and whisker plot showing the statistical distribution of total iron molalities for Case 1 on a regular grid of points within the repository volume between elevations –490 m and –450 m. The statistical measures are the median, the 25th and 75th percentiles (box), the mean (cross) and the 5th and 95th percentiles (whiskers).*

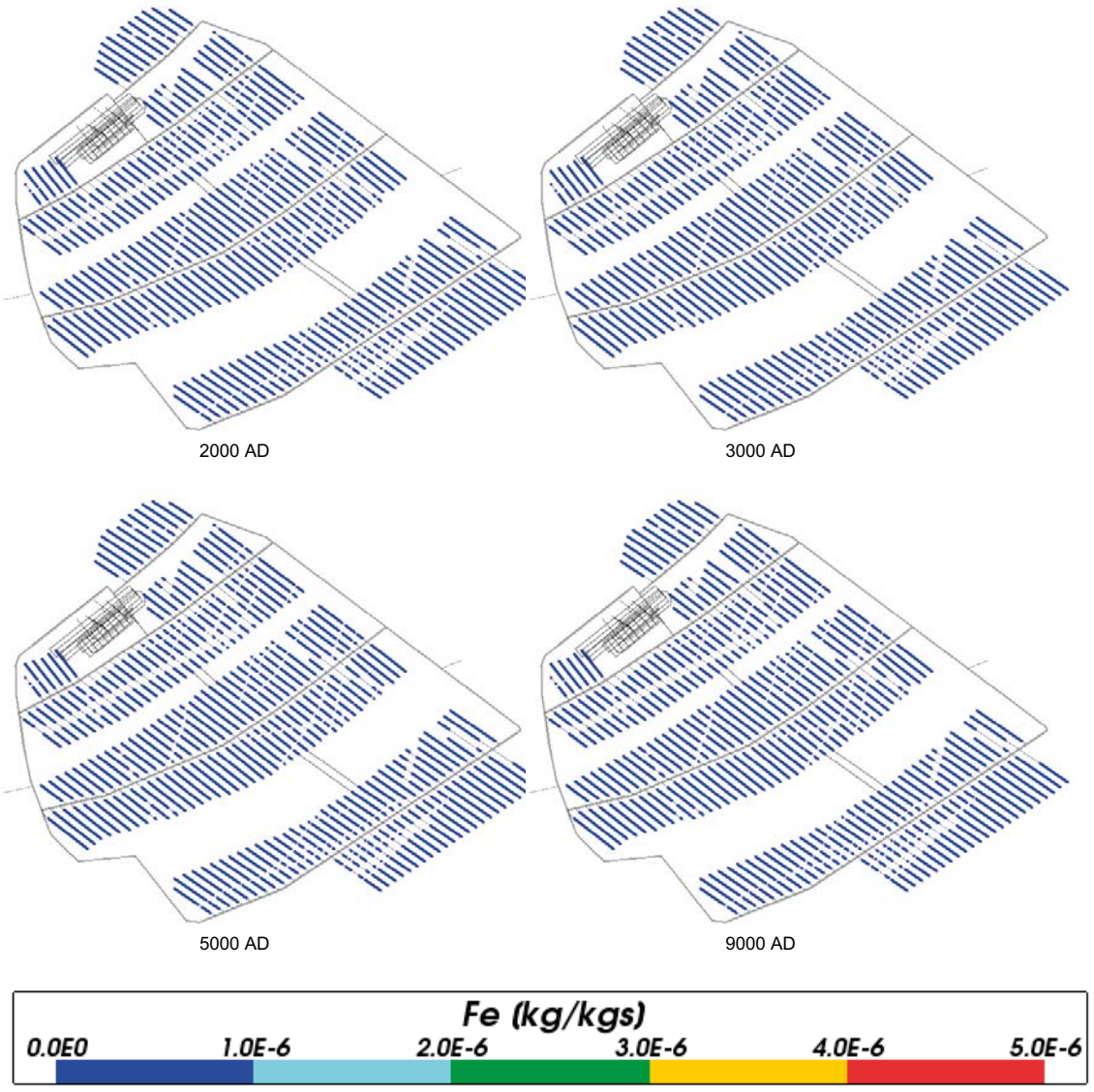


***Figure 4-16.*** *Total iron mass fractions for Case 1 at deposition hole locations for time periods 2000 AD to 9000 AD.*

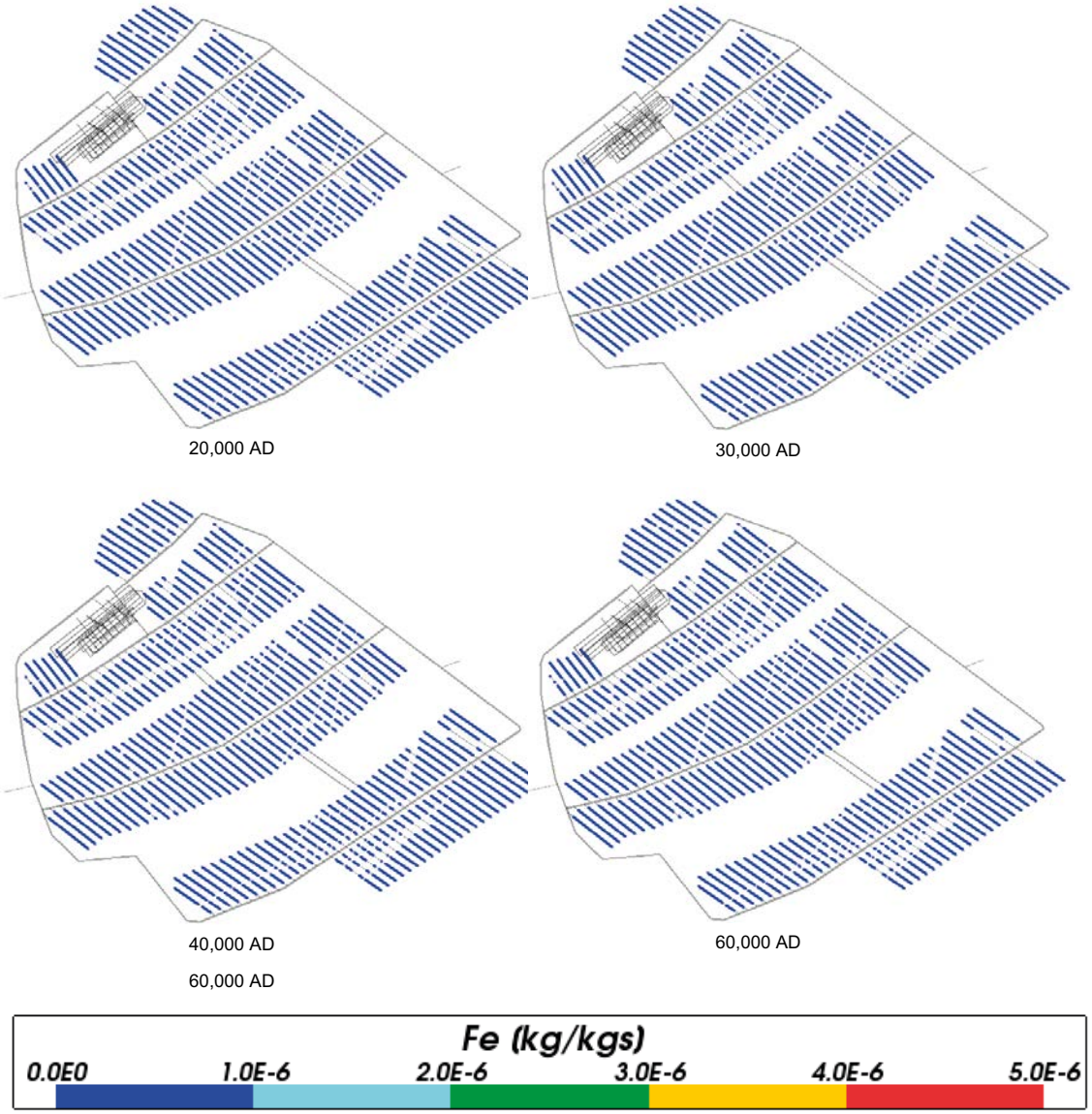


***Figure 4-17.*** *Total iron mass fractions for Case 1 at deposition hole locations for time periods 20,000 AD to 60,000 AD.*

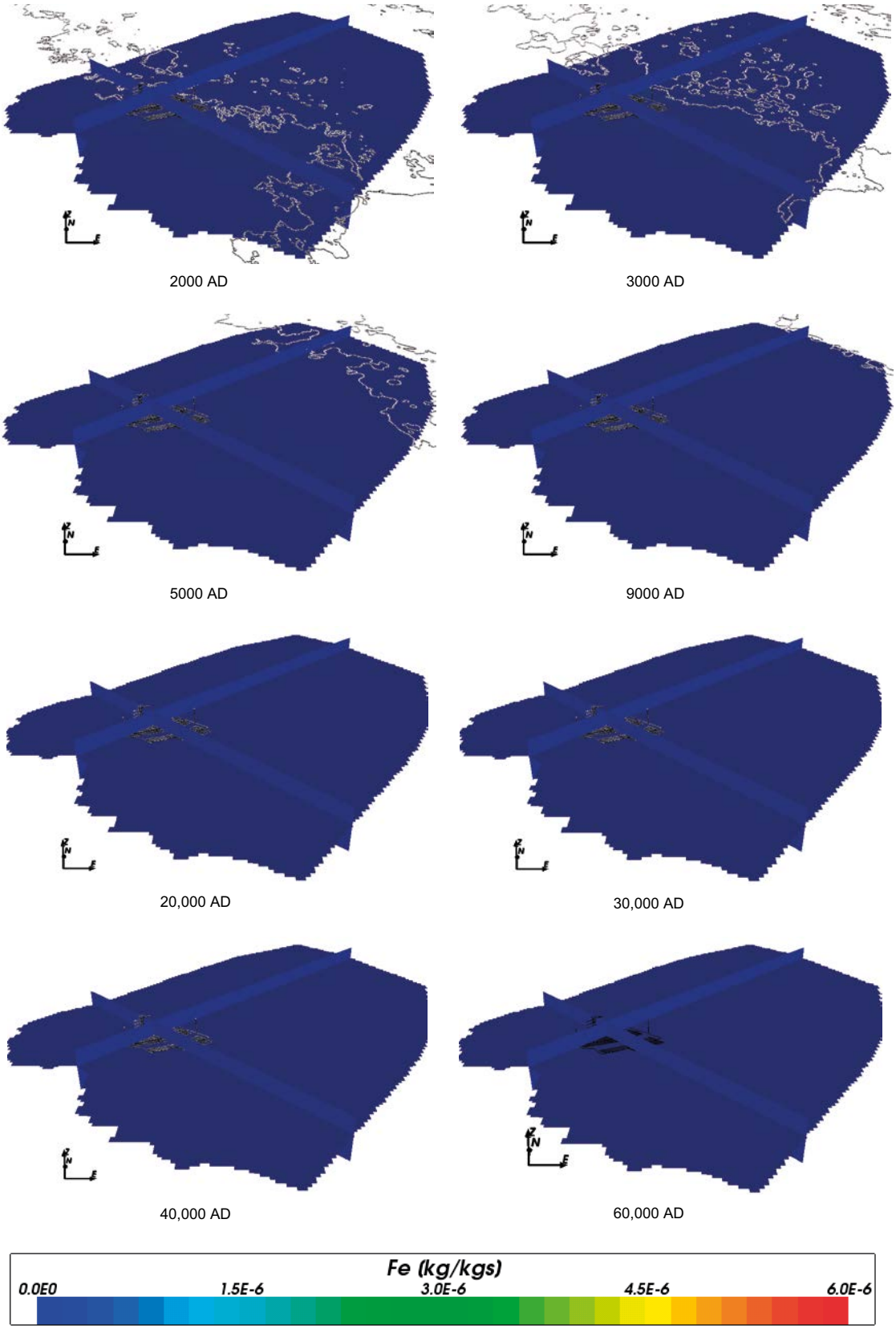


***Figure 4-18.*** *Total iron mass fractions on regional scale slices through the repository volume for Case 1 for time periods 2000 AD to 60,000 AD.*

### 4.2.6 Sodium

The changes in sodium over time are shown in Figure 4-19 to Figure 4-22. The box and whisker plot shows the level of sodium decreasing over time, but levelling off at 20,000 AD with little change following. This trend is also followed in the deposition hole plots in Figure 4-20 and Figure 4-21.

At 2000 AD the concentration of sodium is relatively high across the model (Figure 4-22) due to the presence of Littorina water, but is gradually reduced due to the infiltration of less saline Altered Meteoric water, with the bulk of the area having low sodium concentrations from 20,000 AD onwards.

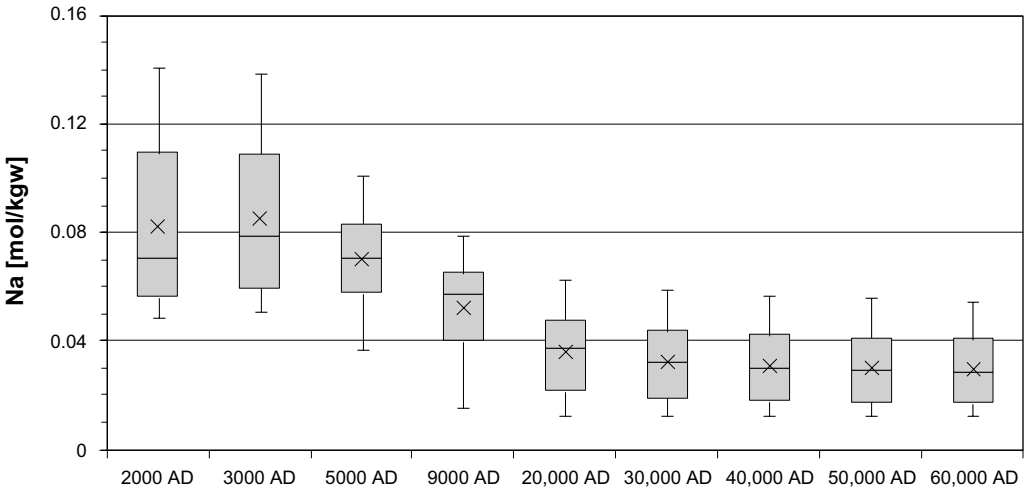


***Figure 4-19.*** *Box and whisker plot showing the statistical distribution of total sodium molalities for Case 1 on a regular grid of points within the repository volume between elevations –490 m and –450 m. The statistical measures are the median, the 25$^{th}$ and 75$^{th}$ percentiles (box), the mean (cross) and the 5$^{th}$ and 95$^{th}$ percentiles (whiskers).*

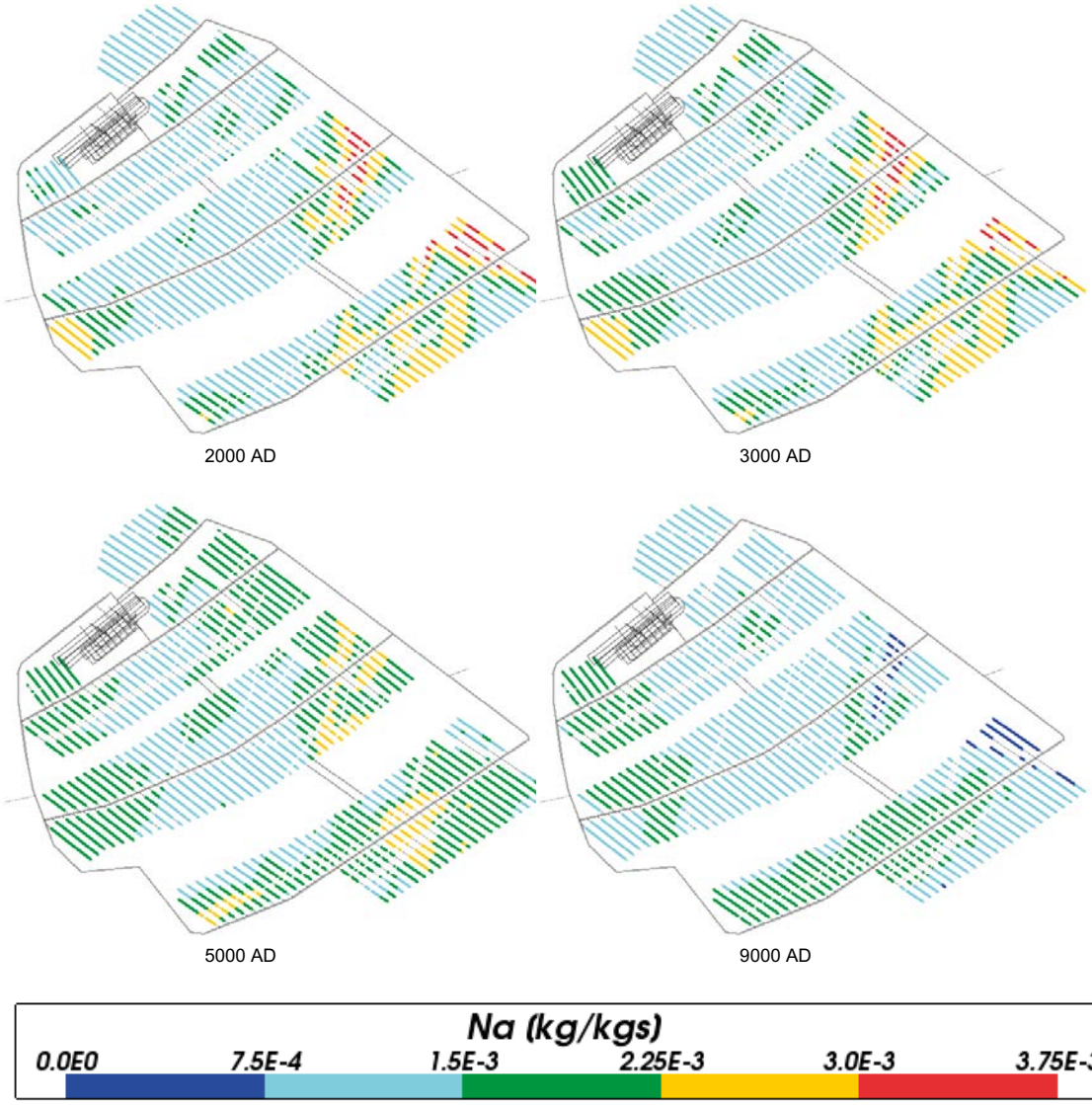


***Figure 4-20.*** *Total sodium mass fractions for Case 1 at deposition hole locations for time periods 2000 AD to 9000 AD.*

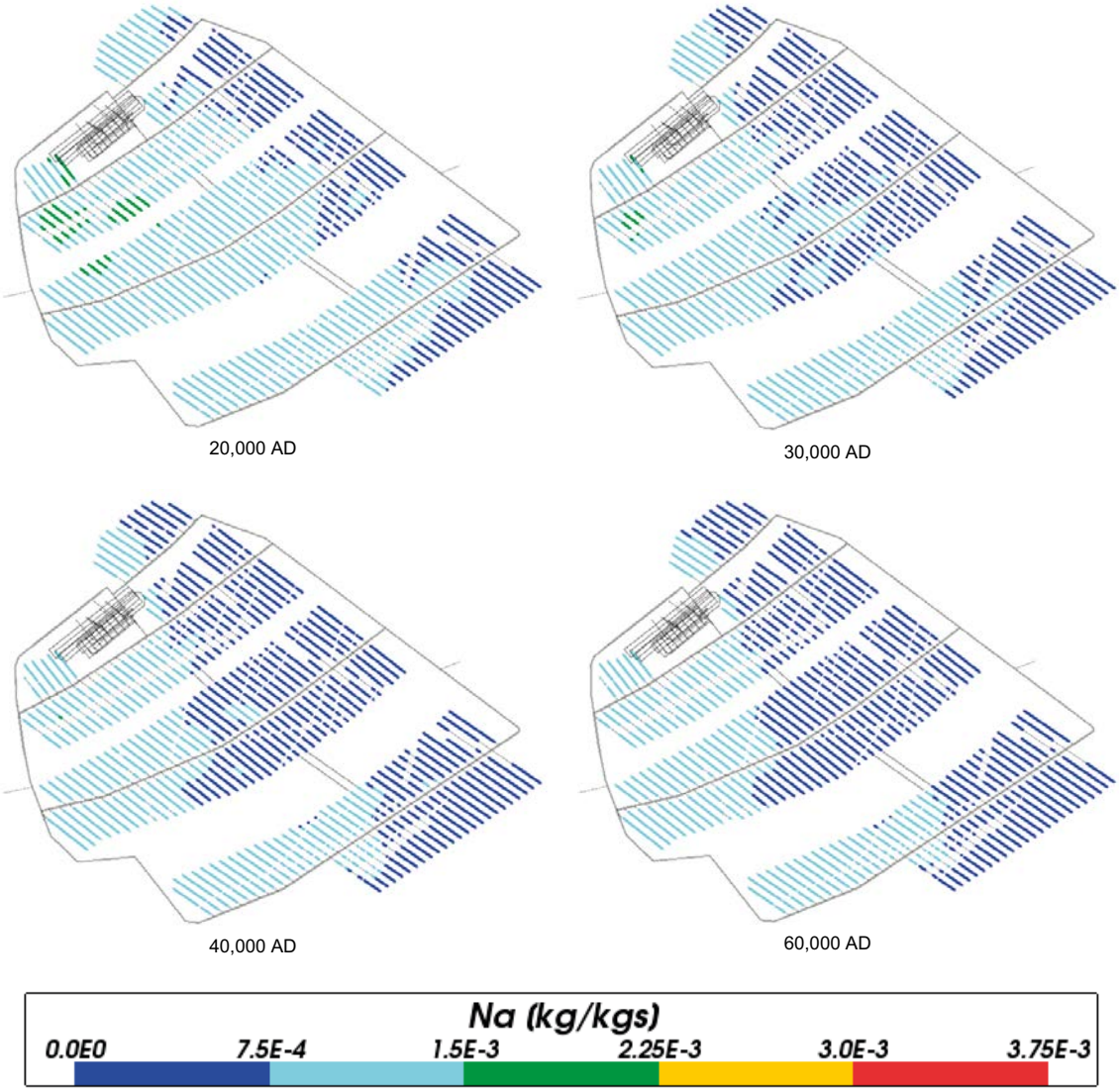


***Figure 4-21.*** *Total sodium mass fractions for Case 1 at deposition hole locations for time periods 20,000 AD to 60,000 AD.*

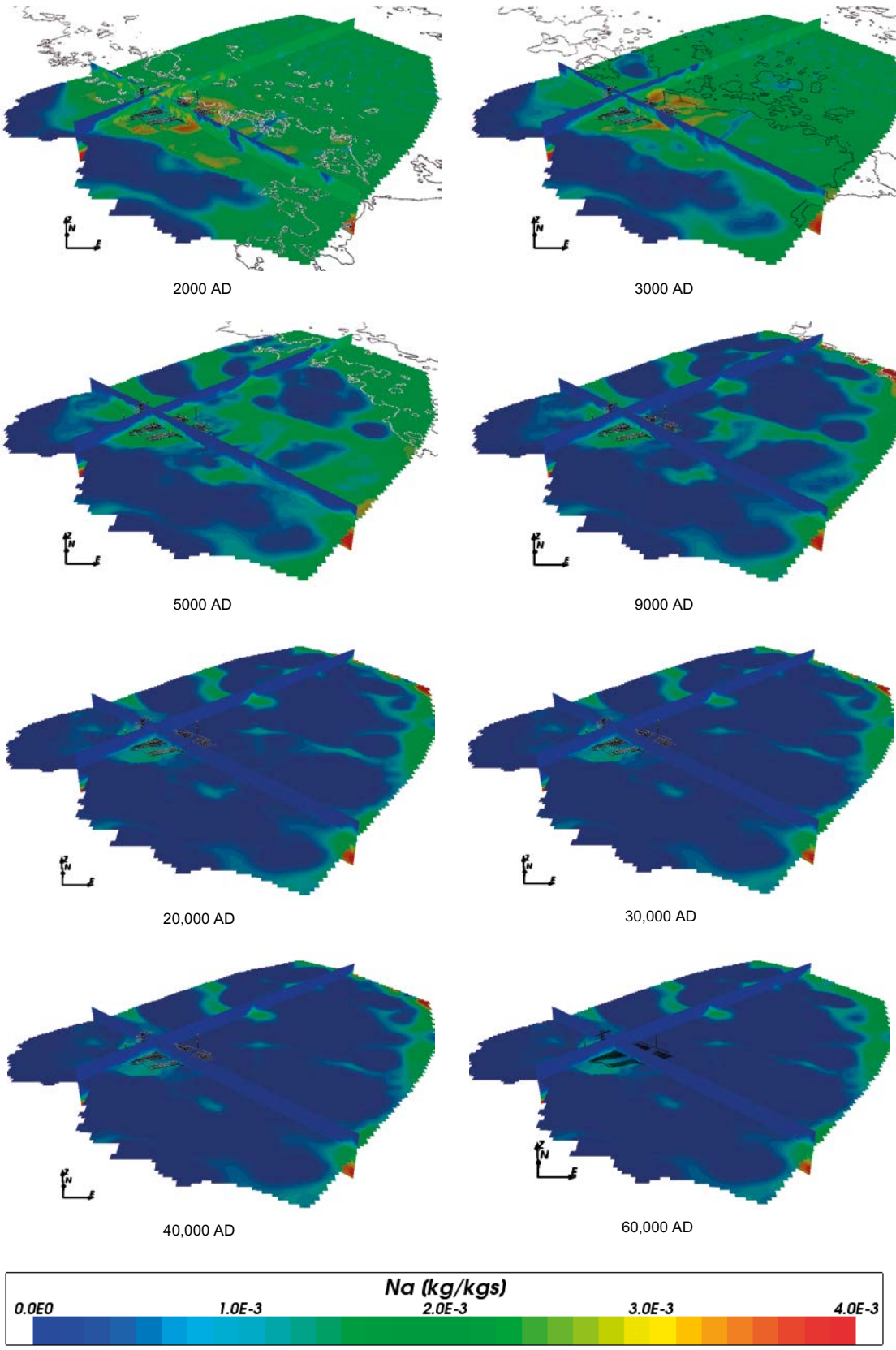


***Figure 4-22.*** *Total sodium mass fractions on regional scale slices through the repository volume for Case 1 for time periods 2000 AD to 60,000 AD.*

### 4.2.7 Potassium

The changes in total potassium concentrations over time are shown in Figure 4-23 to Figure 4-26. The box and whisker plot (Figure 4-23) shows the level of potassium decreasing over time (as expected due to dilution with meteoric water), but levelling off at 20,000 AD with little subsequent change. This trend is also followed in the deposition hole plots in Figure 4-24 and Figure 4-25.

At 2000 AD the concentration of potassium is relatively high across the model (Figure 4-26) due to the presence of Littorina water, but is gradually reduced due to the infiltration of less saline Altered Meteoric water, with the bulk of the area having low potassium concentrations from 20,000 AD onwards.

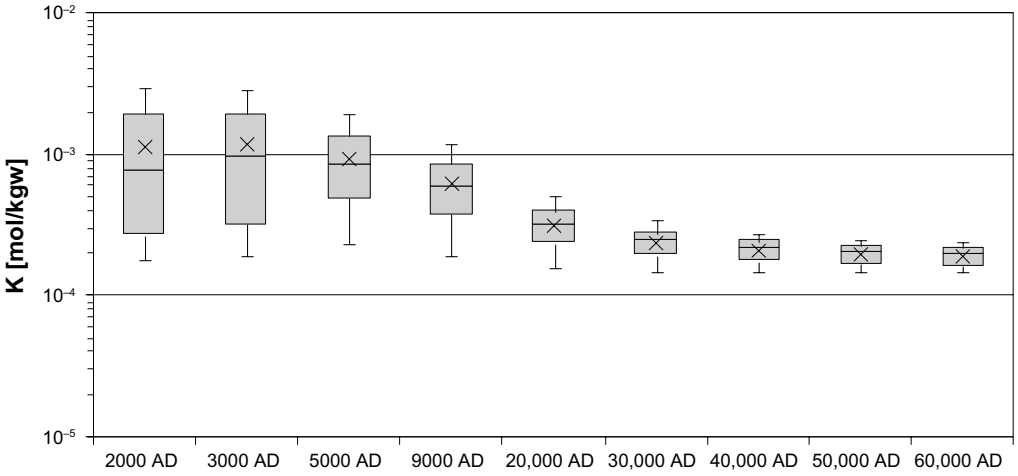


***Figure 4-23.*** *Box and whisker plot showing the statistical distribution of total potassium molalities for Case 1 on a regular grid of points within the repository volume between elevations –490 m and –450 m. The statistical measures are the median, the 25$^{th}$ and 75$^{th}$ percentiles (box), the mean (cross) and the 5$^{th}$ and 95$^{th}$ percentiles (whiskers).*

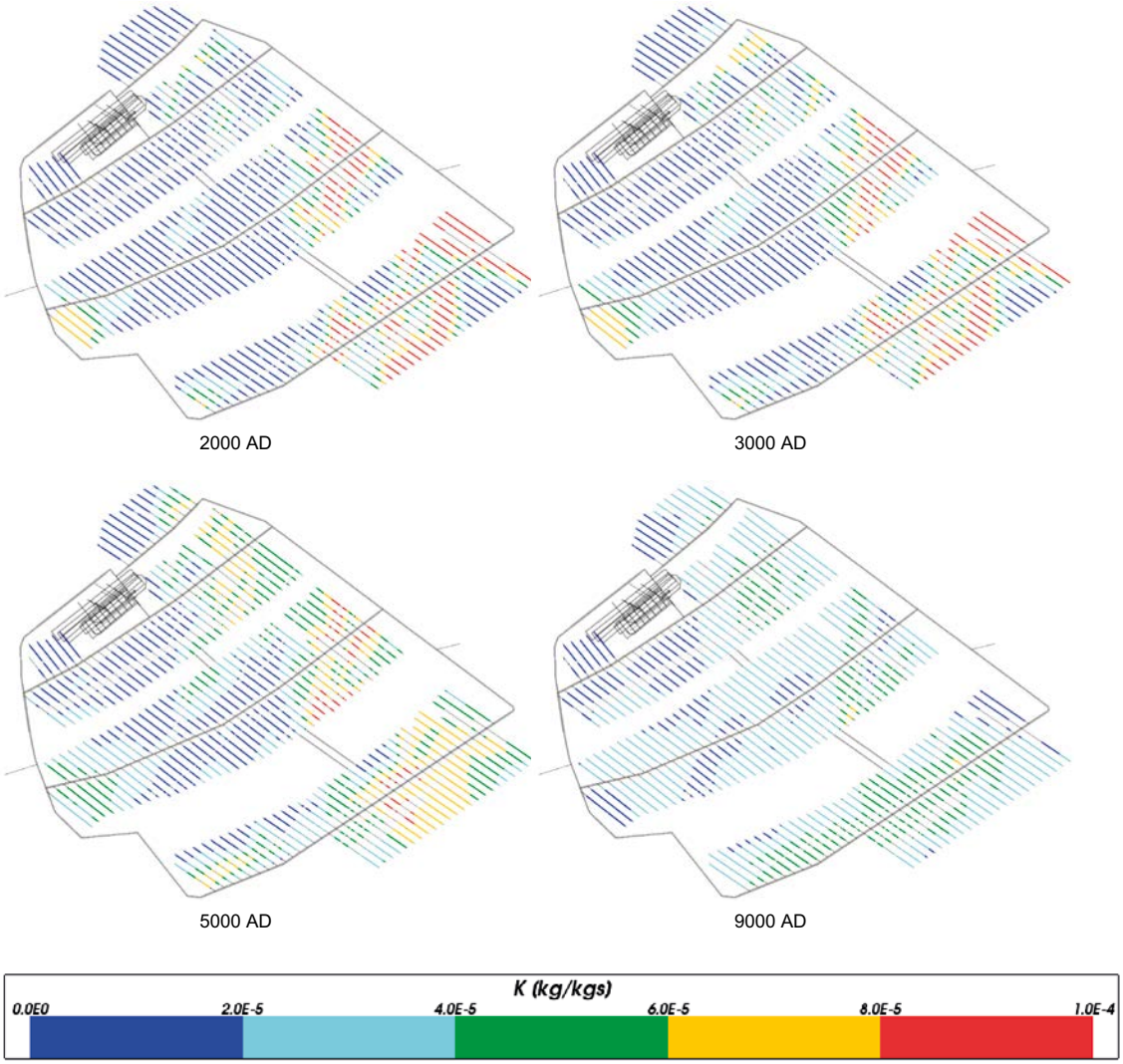


***Figure 4-24.*** *Total potassium mass fractions for Case 1 at deposition hole locations for time periods 2000 AD to 9000 AD.*

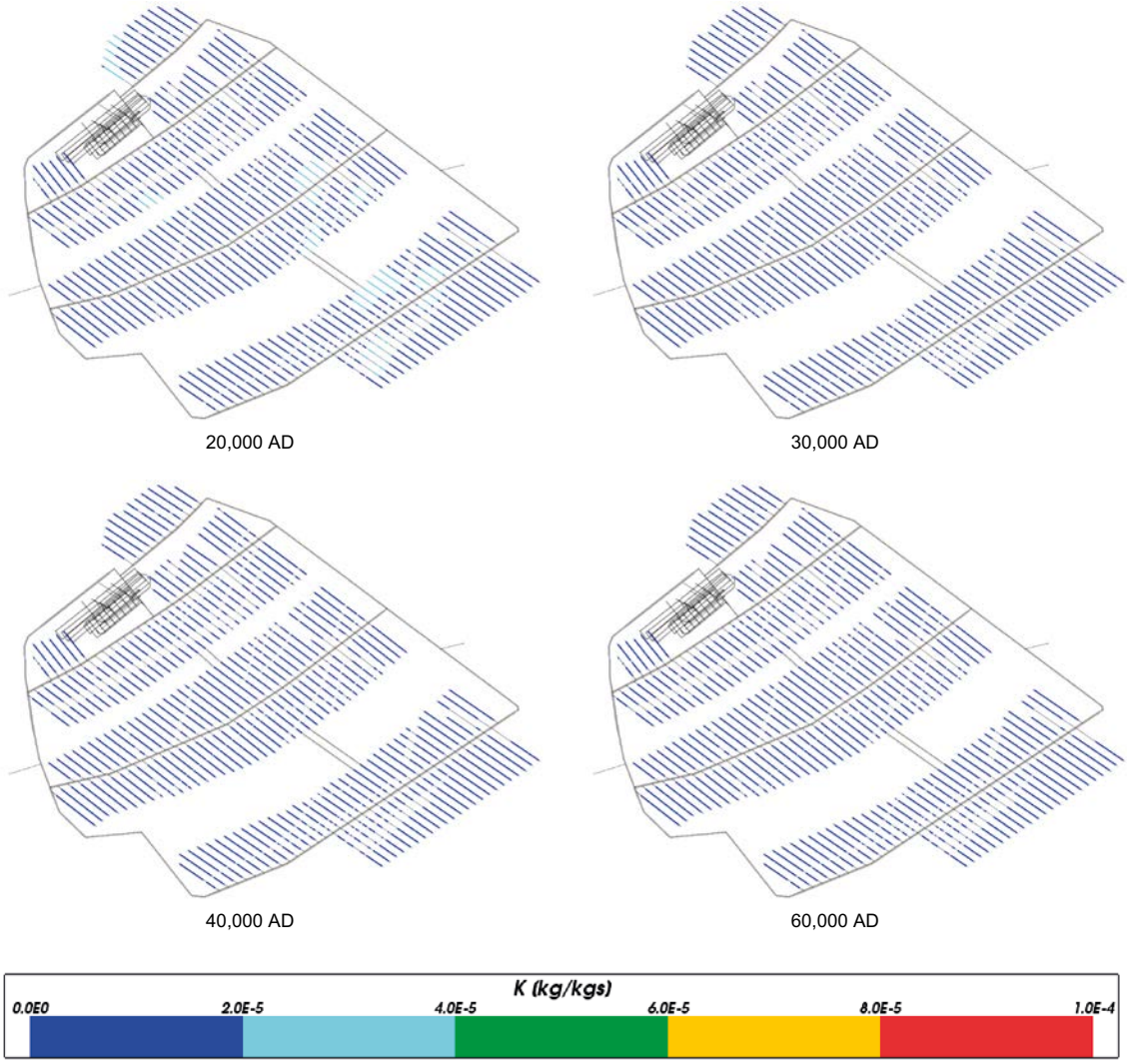


***Figure 4-25.*** *Total potassium mass fractions for Case 1 at deposition hole locations for time periods 20,000 AD to 60,000 AD.*

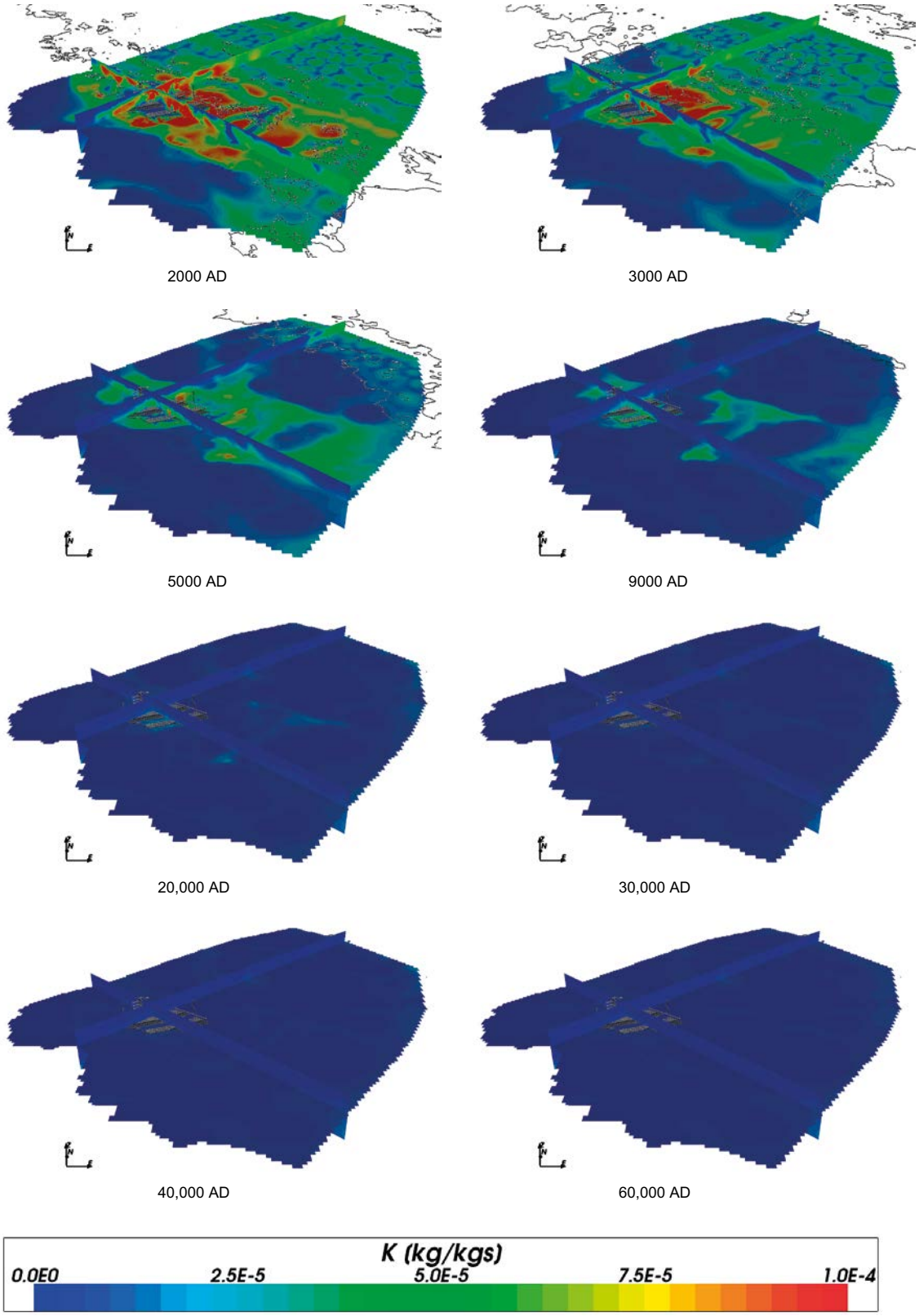


***Figure 4-26.*** *Total potassium mass fractions on regional scale slices through the repository volume for Case 1 for time periods 2000 AD to 60,000 AD.*

### 4.2.8 Sulphur

Cases 2 to 5 show results for sulphate, however Case 1 does not include chemical reactions and so the sulphate concentration is indeterminate. Therefore, results for total sulphur are presented instead for Case 1. The box and whisker plot for total sulphur (Figure 4-27) shows the amount of sulphur decreasing over time, with the spread of values also decreasing, as seen by the decreasing size of the whiskers. Figure 4-28 and Figure 4-29 show that the main changes in concentrations around the deposition holes are between 2000 AD and 9000 AD, with the concentration of total sulphur being low and unchanging for later times.

Figure 4-30 shows that the sulphur concentration behaves in a similar way to sodium, starting reasonably high across the model and dropping to a low value at later times. For sulphur however, the north easterly flow seen for other chemical species is less evident.

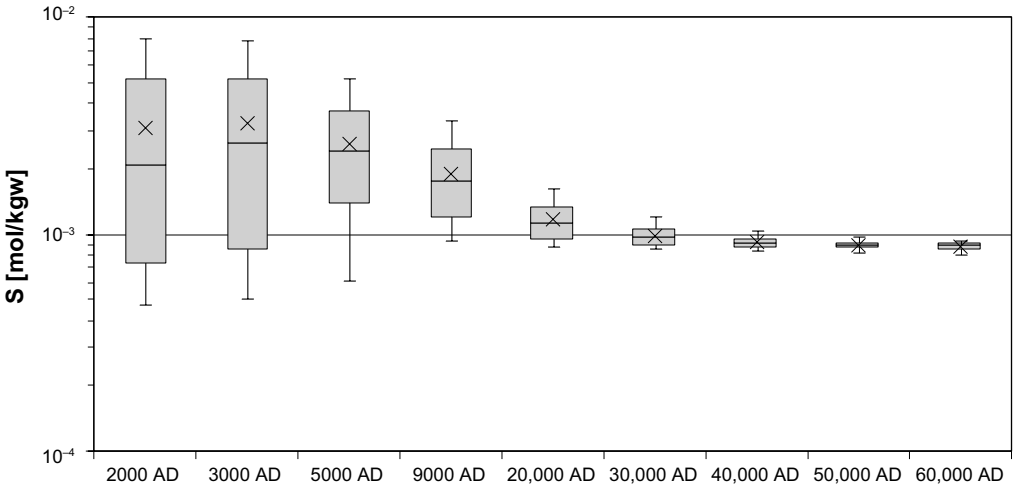


***Figure 4-27.*** *Box and whisker plot showing the statistical distribution of total sulphur molalities for Case 1 on a regular grid of points within the repository volume between elevations –490 m and –450 m. The statistical measures are the median, the 25th and 75th percentiles (box), the mean (cross) and the 5th and 95th percentiles (whiskers).*

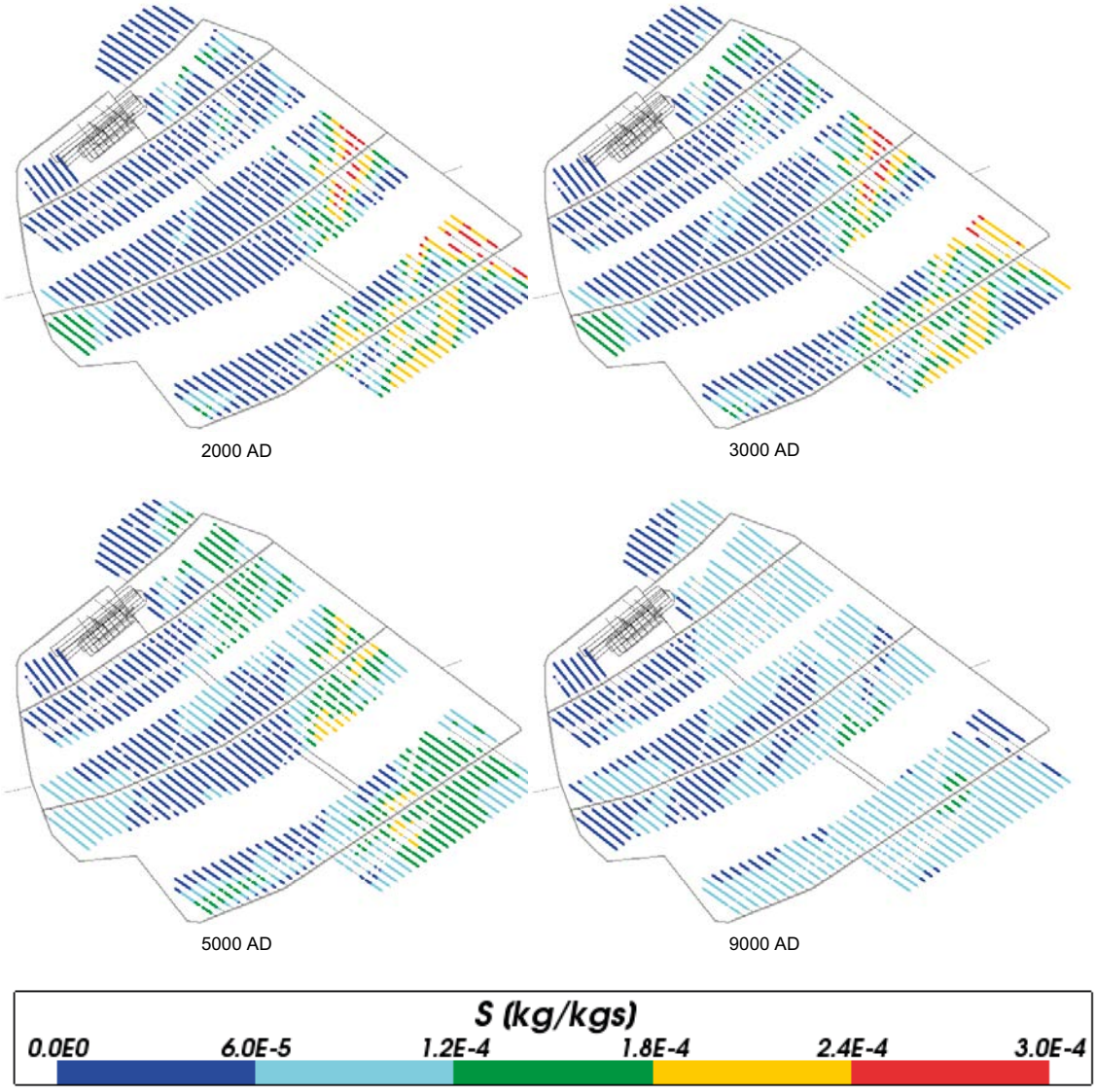


***Figure 4-28.*** *Total sulphur mass fractions for Case 1 at deposition hole locations for time periods 2000 AD to 9000 AD.*

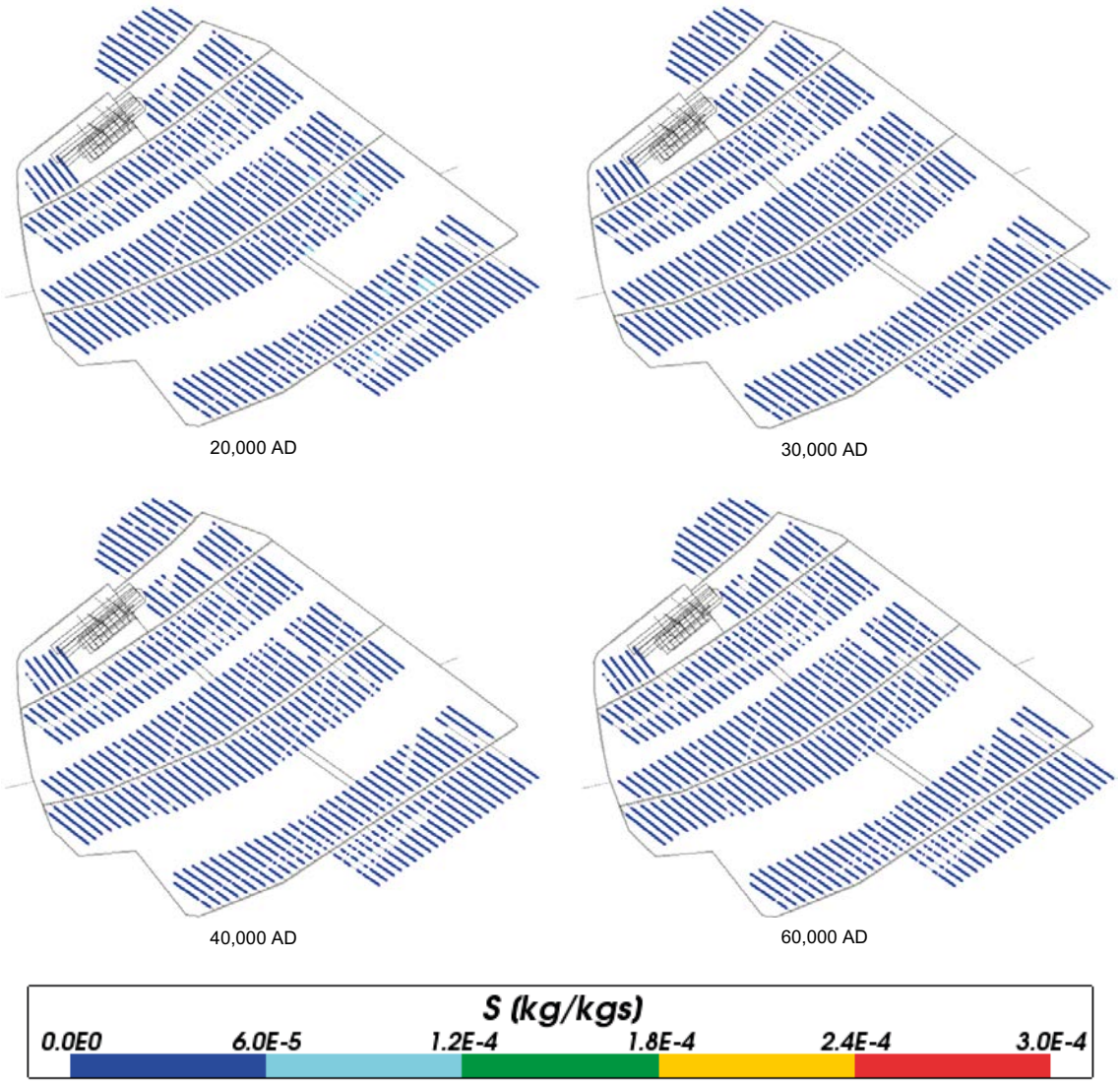


***Figure 4-29.*** *Total sulphur mass fractions for Case 1 at deposition hole locations for time periods 20,000 AD to 60,000 AD.*

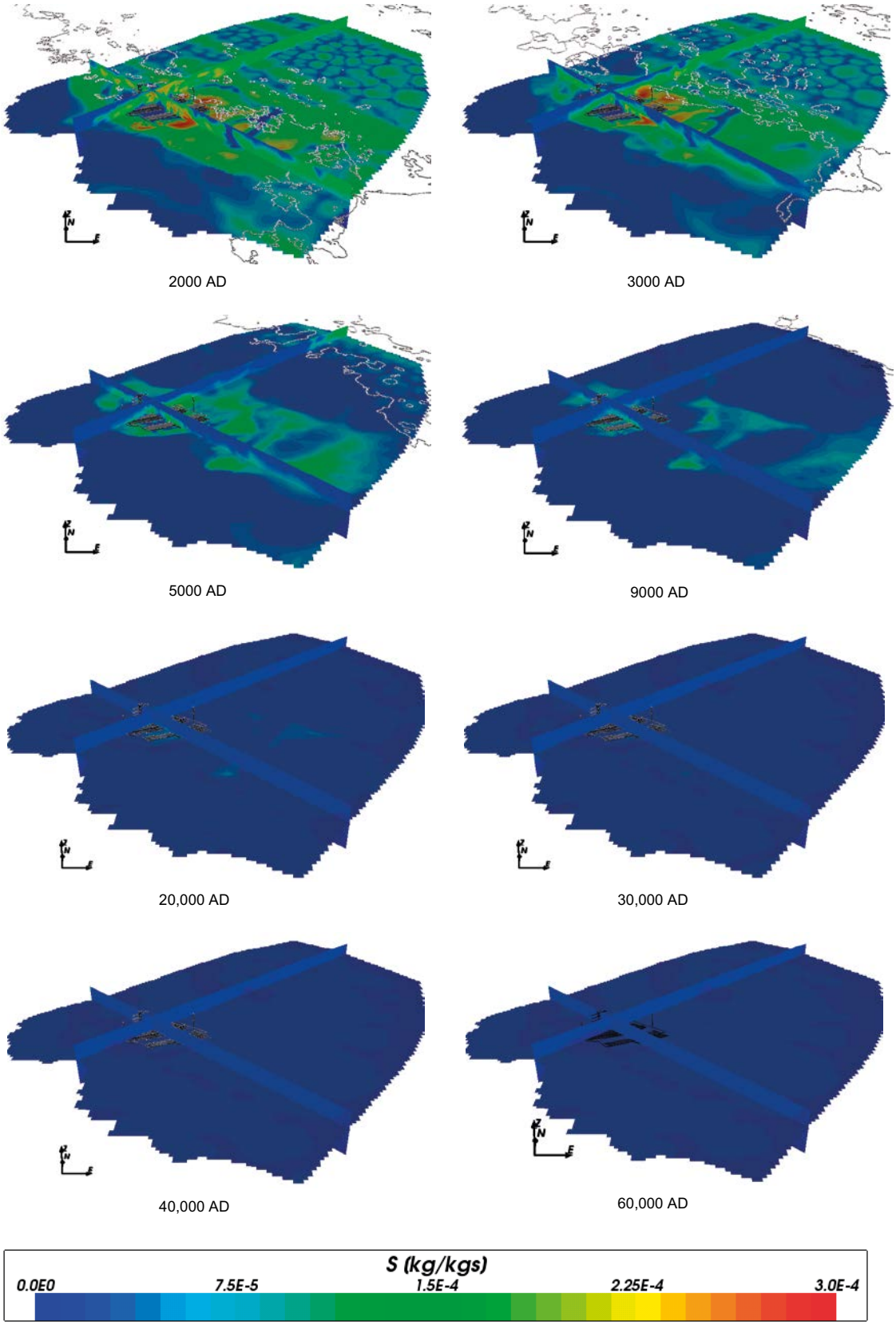


***Figure 4-30.*** *Total sulphur mass fractions on regional scale slices through the repository volume for Case 1 for time periods 2000 AD to 60,000 AD.*

### 4.2.9 Summary for Case 1

Case 1 does not include any chemical reactions and so the geochemical composition of the groundwater is only dependent on flow and transport processes. Due to the presence of the shallow bedrock aquifer, the decreasing fracture intensity with depth and the low permeability of the bedrock in the repository volume, the groundwater flow at Forsmark is relatively shallow and slow. This leads to slow penetration of groundwater from the ground surface to depth and it is further retarded by the effects of rock matrix diffusion. So although some meteoric water did penetrate to repository depth in the model, as shown by the reduction in salinity and an increase in the concentration of total inorganic carbon, the dilution effects were largely limited to the upper elevations of the rock volume and were relatively minor at repository depth. Additionally, there was little change in the salinity within the repository volume beyond 20,000 AD. Therefore the salinity remained within the bounds required for the safety assessment at repository depth over the time period considered.

## 4.3 Case 2

The evolution of groundwater composition for this case is due to the transport and mixing of components originating from different reference waters. However, the concentrations of reacting species will be modified by the chemical reactions considered for this case, which include equilibration of groundwater with calcite, quartz and amorphous iron (II) sulphide. It is expected that the reactions will have an effect on pH, Eh, and the concentrations of total inorganic carbon, calcium, sulphur and iron. The concentrations of non-reacting species such as chloride and sodium should be the same as for Case 1, except possibly with very minor differences caused by slight changes in groundwater density, due to dissolution or precipitation of solutes, which might affect the transport of components.

### 4.3.1 pH

Figure 4-31, Figure 4-32 and Figure 4-33 show the values of pH around the repository for Case 2 decreasing with time, due to the infiltration of Altered Meteoric water, from a median pH of around 7.6 at 2000 AD, but levelling off at later times to a median pH of approximately 6.8 at 60,000 AD. These results are quite consistent with those of Salas et al. (2010), which had a median pH of around 7.4 at 2000 AD, falling to around 7.1 at 9000 AD. Figure 4-34 shows values of pH over the regional area. There is a general introduction of lower pH values at some locations over the time period. The spatial variation is due to heterogeneity in the bedrock and the influence of deformation zones, which is also seen over a narrower range of pH in the plots at the deposition hole locations in Figure 4-32 and Figure 4-33. There are some spots of higher pH (in red) in Figure 4-34 for earlier times that probably indicate numerical fluctuations in the finite element solution. Investigations of these have found they are isolated short-lived over-shoots/under-shoots in the numerical solution around the edges of the increased refinement of the repository volume. Hence, it is considered that they are unlikely to affect the overall results. Some also correspond to residual areas of Glacial or Old Meteoric water at earlier times. Numerical fluctuations can be reduced or eliminated by increasing grid resolution, reduced time step size or use of a more accurate iterative solution scheme. For this study, it was felt important to maintain numerical settings consistent with those used in SR-Site. The sensitivity of reactive transport calculations to such numerical issues will remain an area for investigation in future studies.

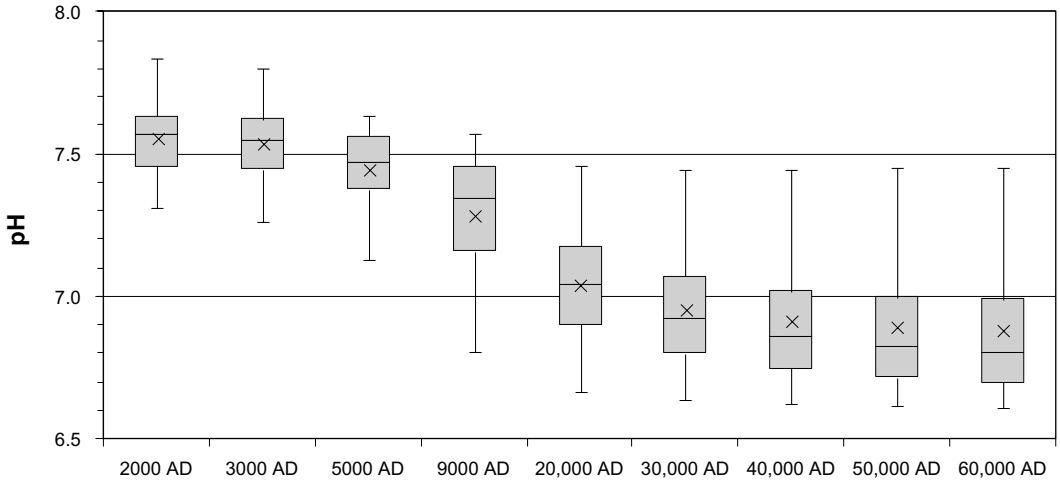


***Figure 4-31.*** *Box and whisker plot showing the statistical distribution of pH for Case 2 on a regular grid of points within the repository volume between elevations –490 m and –450 m. The statistical measures are the median, the 25th and 75th percentiles (box), the mean (cross) and the 5th and 95th percentiles (whiskers).*

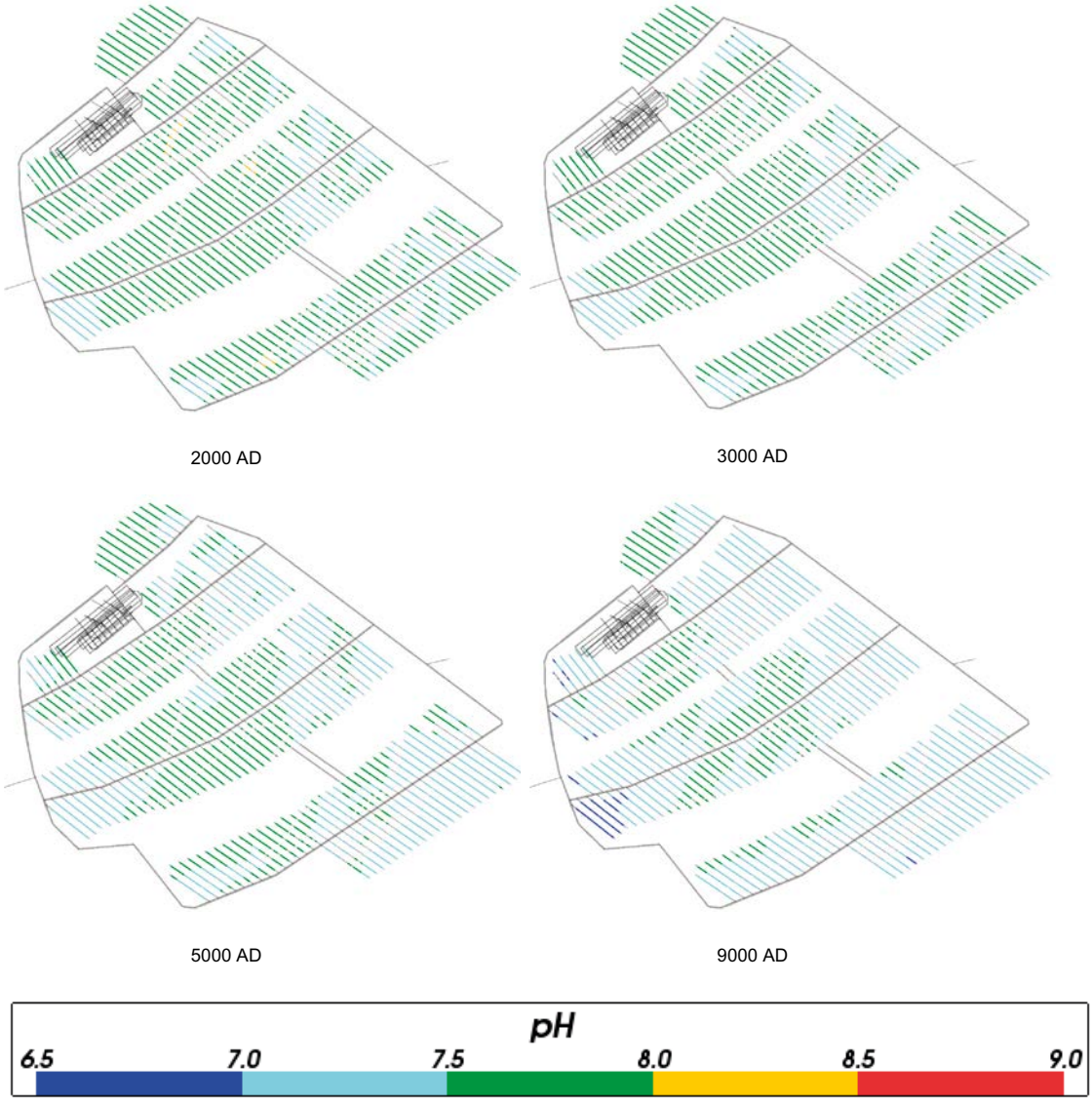


***Figure 4-32.*** *Values of pH for Case 2 at deposition hole locations for time periods 2000 AD to 9000 AD.*

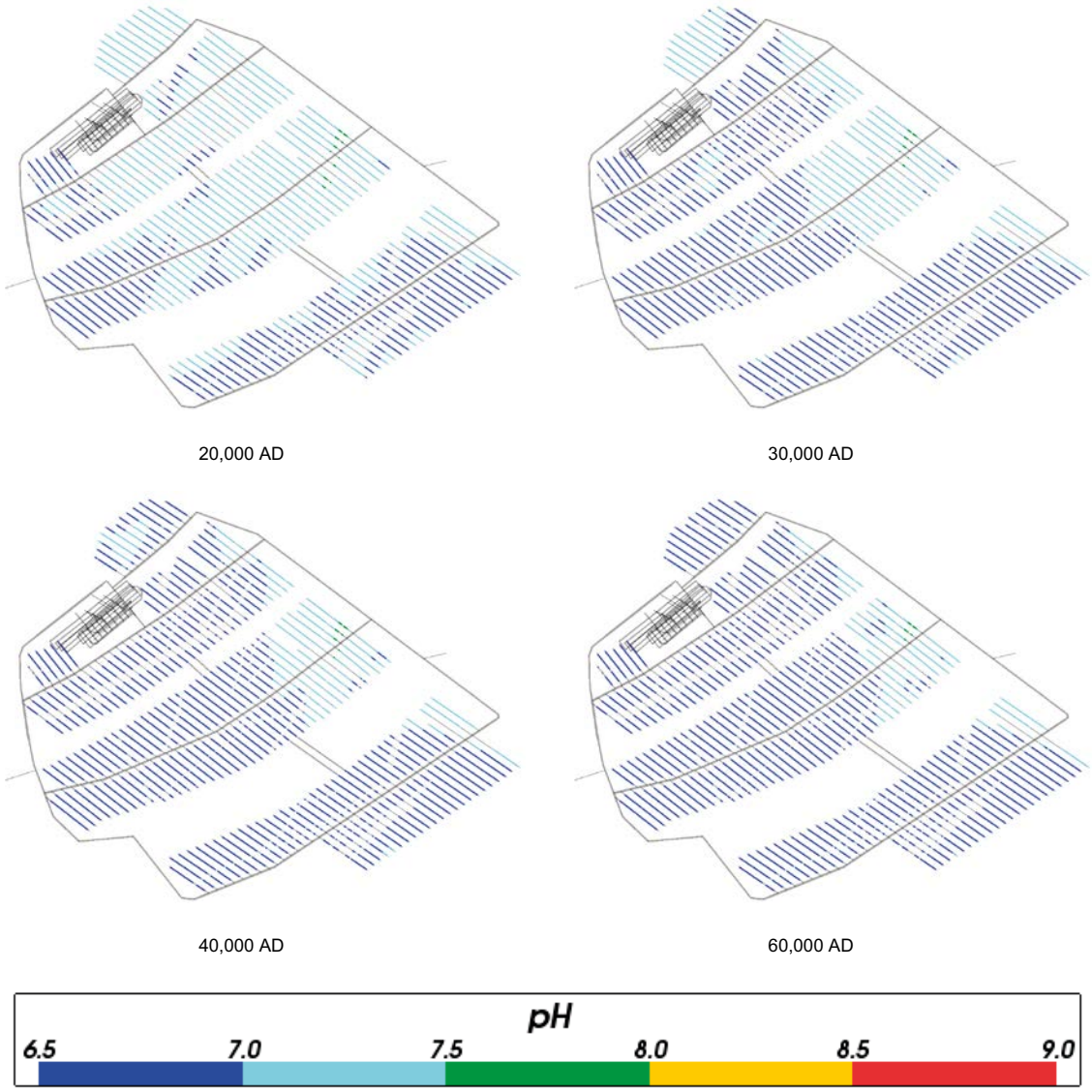


***Figure 4-33.*** *Values of pH for Case 2 at deposition hole locations for time periods 20,000 AD to 60,000 AD.*

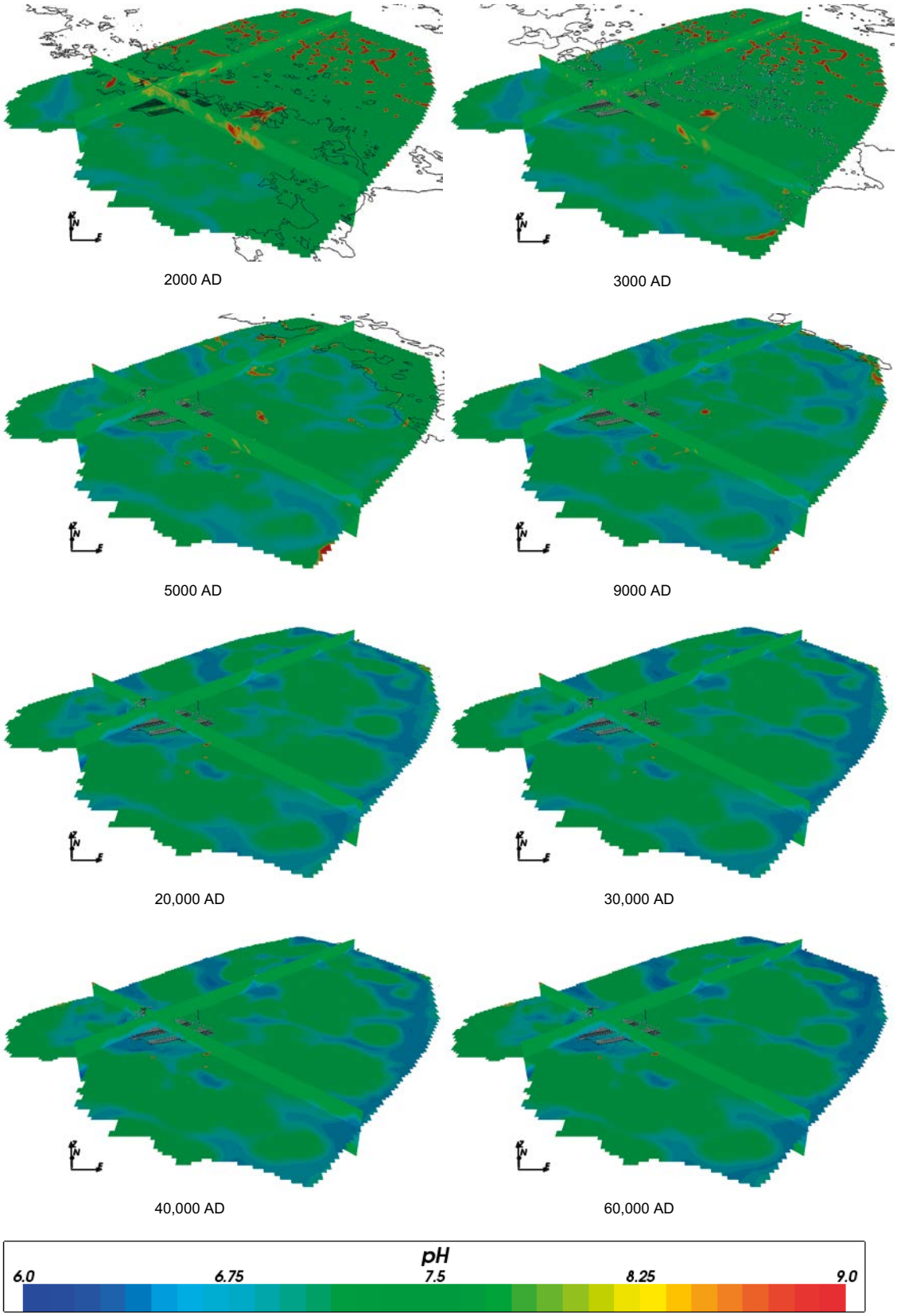


***Figure 4-34.*** *Values of pH on regional scale slices through the repository volume for Case 2 for time periods 2000 AD to 60,000 AD.*

### 4.3.2 Eh (or pe)

Figure 4-35 shows the value of Eh in the repository region for Case 2. Figure 4-35 shows that the value of Eh rises over time, due to infiltration of Altered Meteoric water (which has a less reducing Eh than the other waters) and due to the effect of the pH values in equilibrium with calcite and amorphous iron (II) sulphide, from a medium value of –245 mV at 2000 AD, but flattens off after 30,000 AD to a median of about –190 mV. The values are consistent with those given in Salas et al. (2010) which are in the range between –222 and –199 mV, increasing with time.

Figure 4-36 and Figure 4-37 show the value of pe at the deposition hole locations, showing a similar rise from a pe of around –4.5 (Eh –257 mV) at 2000 AD to around –3.5 mV (Eh –200 mV) at 60,000 AD with some spatial variation due to heterogeneity. This does indicate that different deposition hole locations are likely to experience different redox conditions depending on the distribution of bedrock fractures and deformation zones in their vicinity, although none experience oxidising conditions in the model.

The regional slice plots shown in Figure 4-38 show a similar change in pe over time. In Case 2, pe is increasing at early times, with higher values migrating in a north easterly direction. At later times (20,000 AD onwards) there is little change in pe. There are few spots of low pe (blue spots) in Figure 4-38 at earlier times that may indicate some numerical fluctuation. Since these are isolated, short-lived and distant from the repository, they are unlikely to influence the results (see Section 4.3.1).

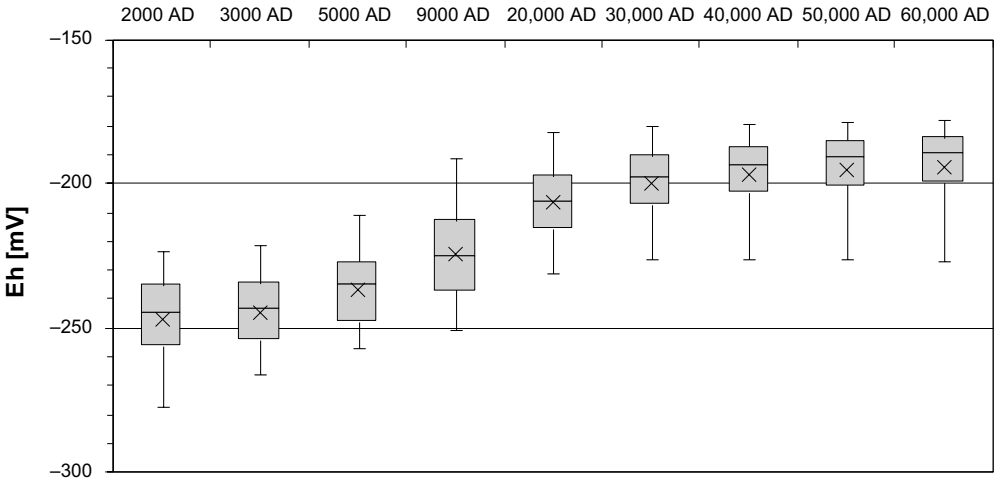


***Figure 4-35.*** *Box and whisker plot showing the statistical distribution of Eh for Case 2 on a regular grid of points within the repository volume between elevations –490 m and –450 m. The statistical measures are the median, the 25th and 75th percentiles (box), the mean (cross) and the 5th and 95th percentiles (whiskers).*

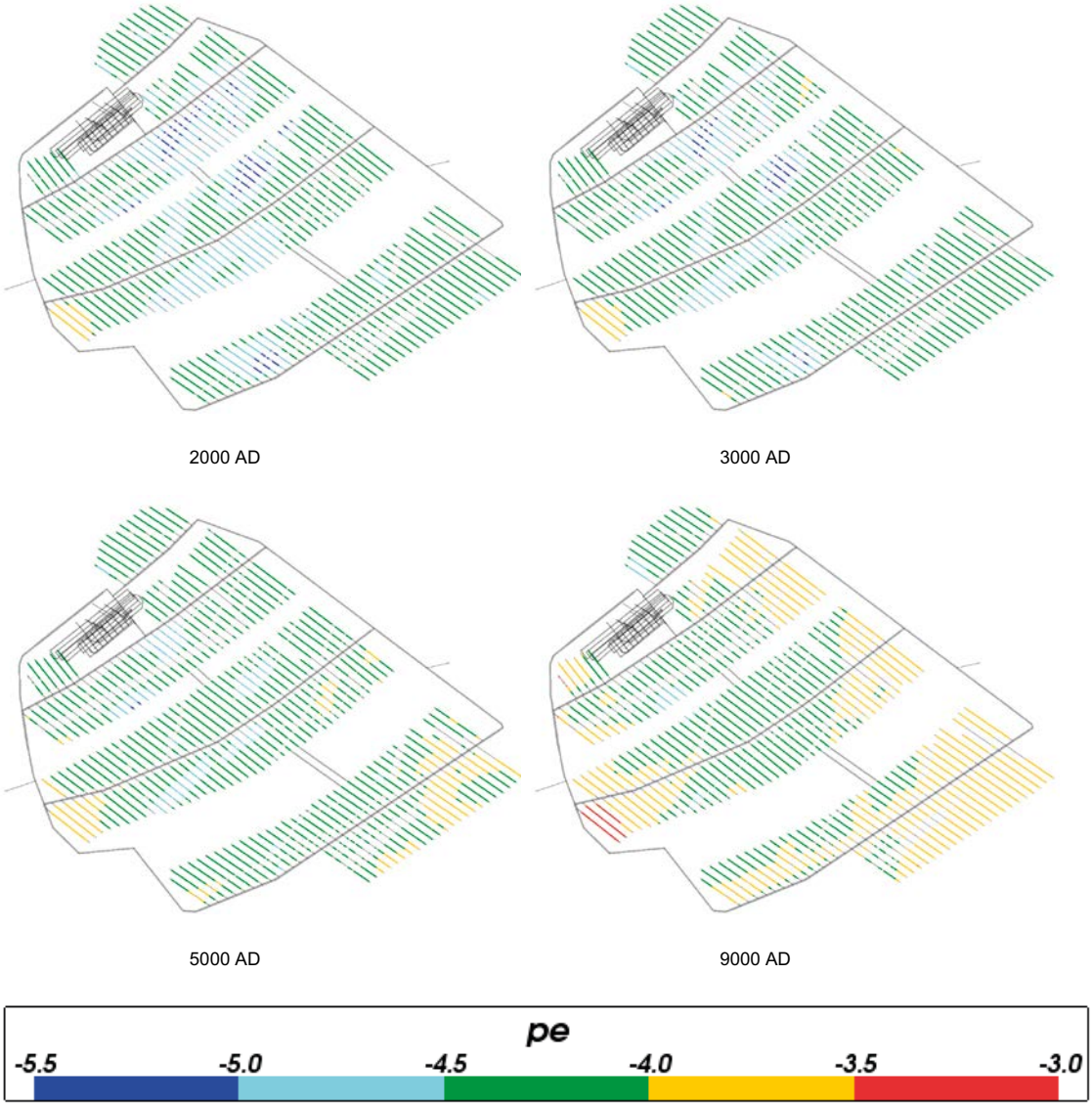


***Figure 4-36.*** *Values of pe for Case 2 at deposition hole locations for time periods 2000 AD to 9000 AD.*

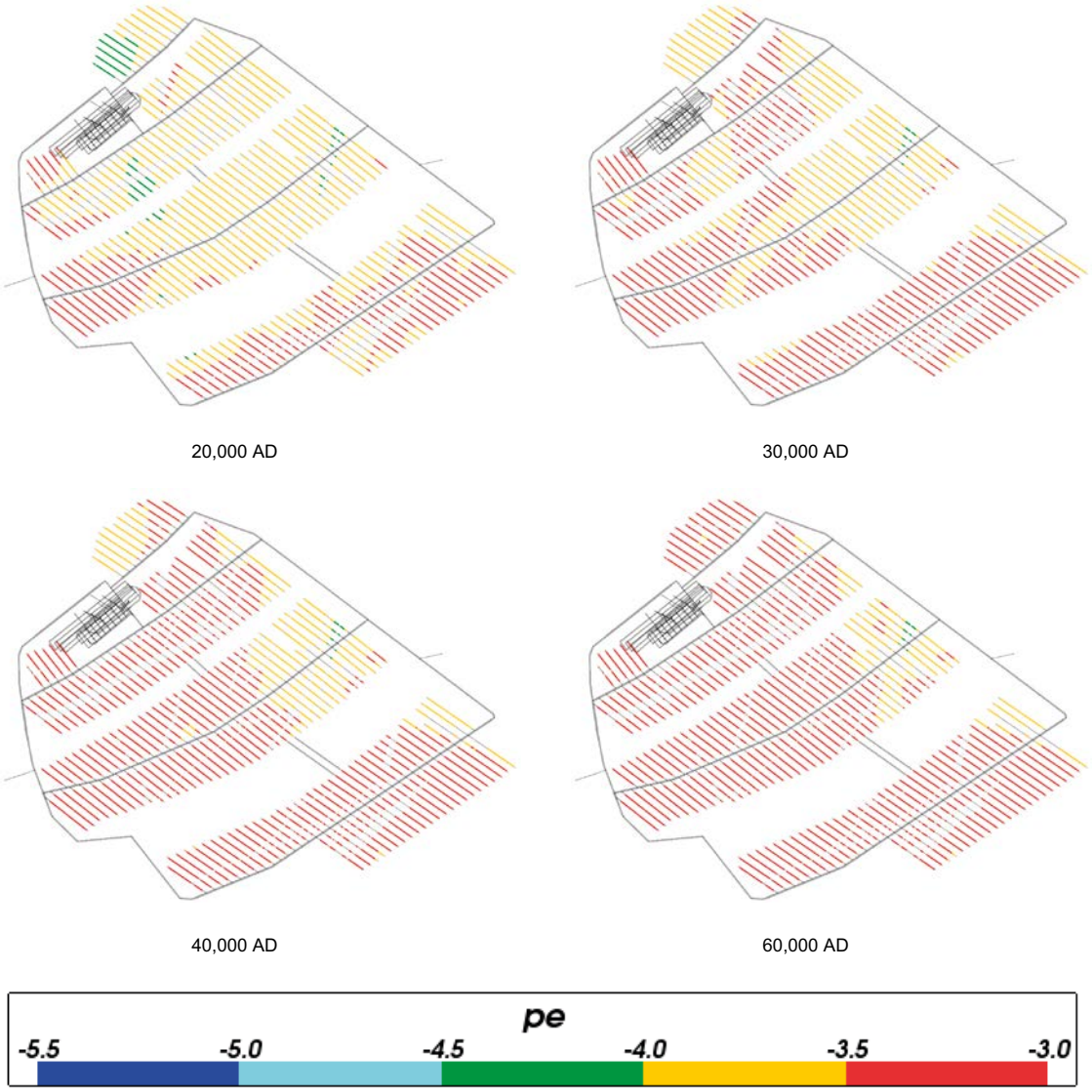


***Figure 4-37.*** *Values of pe for Case 2 at deposition hole locations for time periods 20,000 AD to 60,000 AD.*

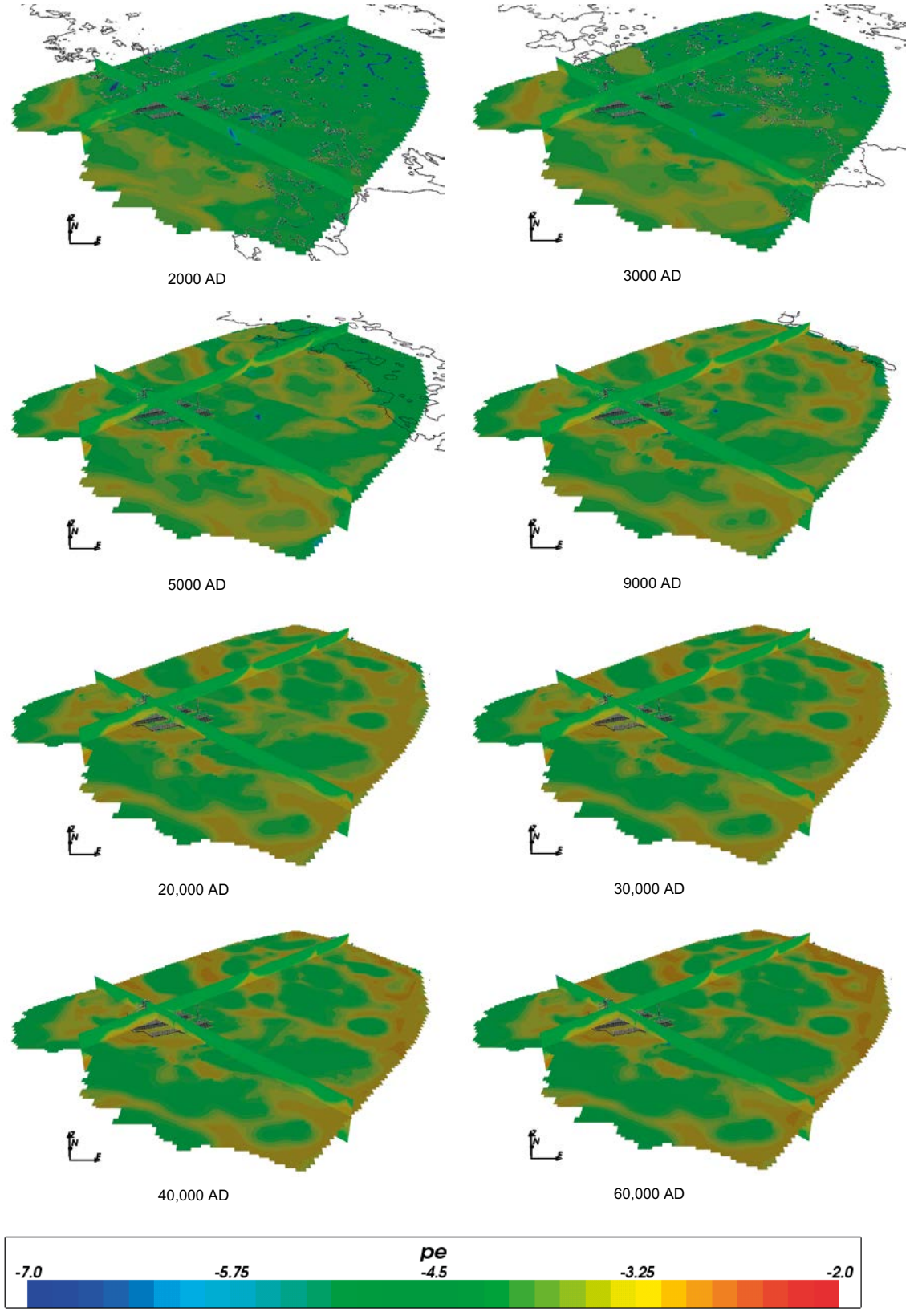


***Figure 4-38.*** *Values of pe on regional scale slices through the repository volume for Case 2 for time periods 2000 AD to 60,000 AD.*

### 4.3.3 TDS and sum of cations

Figure 4-39 and Figure 4-40 show the statistical distribution of total dissolved solids (TDS) and the sum of cation charge molalities for Case 2. As with Case 1, the two plots are closely related, with the sum of cation charges plot showing the same trend as the TDS plot, decreasing gradually over time and levelling out at later times. Both figures are very similar to those for Case 1, with slightly higher concentrations, indicating some overall dissolution of reacting species. The range of TDS values is similar to that reported in Salas et al. (2010) with median values of around 10,000 mg/L at 2000 AD to around 7,000 mg/L at 9000 AD, with the spread of values increasing with time. The range of median cation molalities reported in Salas et al. (2010) of about 183 mM at 2000 AD to about 120 mM at 9000 AD is also consistent with that shown in Figure 4-40 (0.173 mol/$kg_w$ at 2000 AD to 0.140 mol/$kg_w$ at 9000 AD).

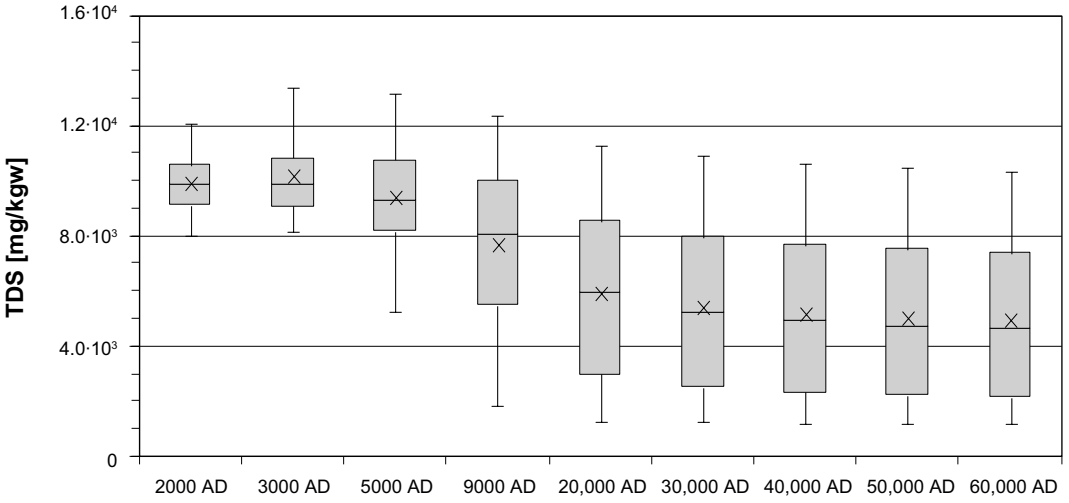


***Figure 4-39.*** *Box and whisker plot showing the statistical distribution of TDS for Case 2 on a regular grid of points within the repository volume between elevations –490 m and –450 m. The statistical measures are the median, the 25th and 75th percentiles (box), the mean (cross) and the 5th and 95th percentiles (whiskers).*

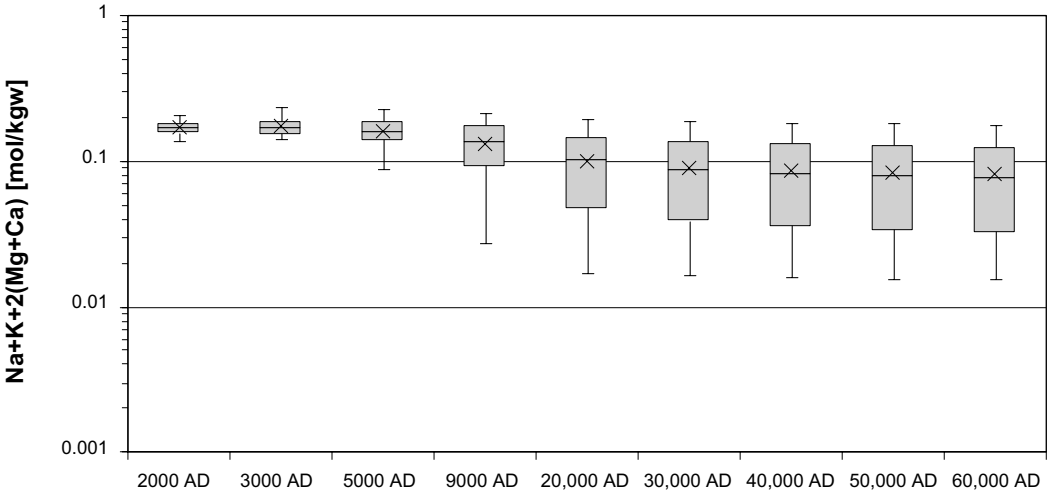


***Figure 4-40.*** *Box and whisker plot showing the statistical distribution of sum of cation charges (Na+K+2(Mg+Ca)) molalities for Case 2 on a regular grid of points within the repository volume between elevations –490 m and –450 m. The statistical measures are the median, the 25th and 75th percentiles (box), the mean (cross) and the 5th and 95th percentiles (whiskers).*

### 4.3.4 Inorganic carbon

Figure 4-41, Figure 4-42, Figure 4-43 and Figure 4-44 show plots of total inorganic carbon for Case 2. The first three figures show very similar trends to those seen for Case 1 (Figure 4-3 to Figure 4-6), but with lower median concentrations of total inorganic carbon and with more spread. The differences are partly due to the effects of chemical reactions, i.e. involving calcite, but the increase in spread at later times is similar to that observed for chloride (a non-reacting species, see Section 4.3.6) and so indicates that minor changes in groundwater flow and transport may be more important. Figure 4-44 shows a similar distribution of total inorganic carbon over the regional scale to Figure 4-6, but again with mass fractions that are a little lower for Case 2. The concentrations of total inorganic carbon for Case 2 are consistent with median values reported in Salas et al. (2010) of around $5.0 \cdot 10^{-4}$ mol/L at 2000 AD to around $3.0 \cdot 10^{-3}$ mol/L at 9000 AD.

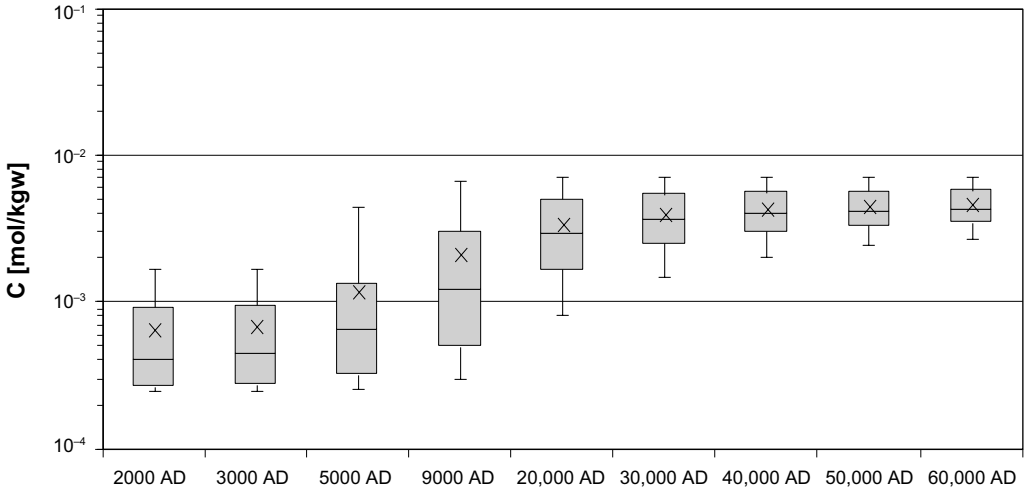


***Figure 4-41.*** *Box and whisker plot showing the statistical distribution of total inorganic carbon molalities for Case 2 on a regular grid of points within the repository volume between elevations –490 m and –450 m. The statistical measures are the median, the 25th and 75th percentiles (box), the mean (cross) and the 5th and 95th percentiles (whiskers).*

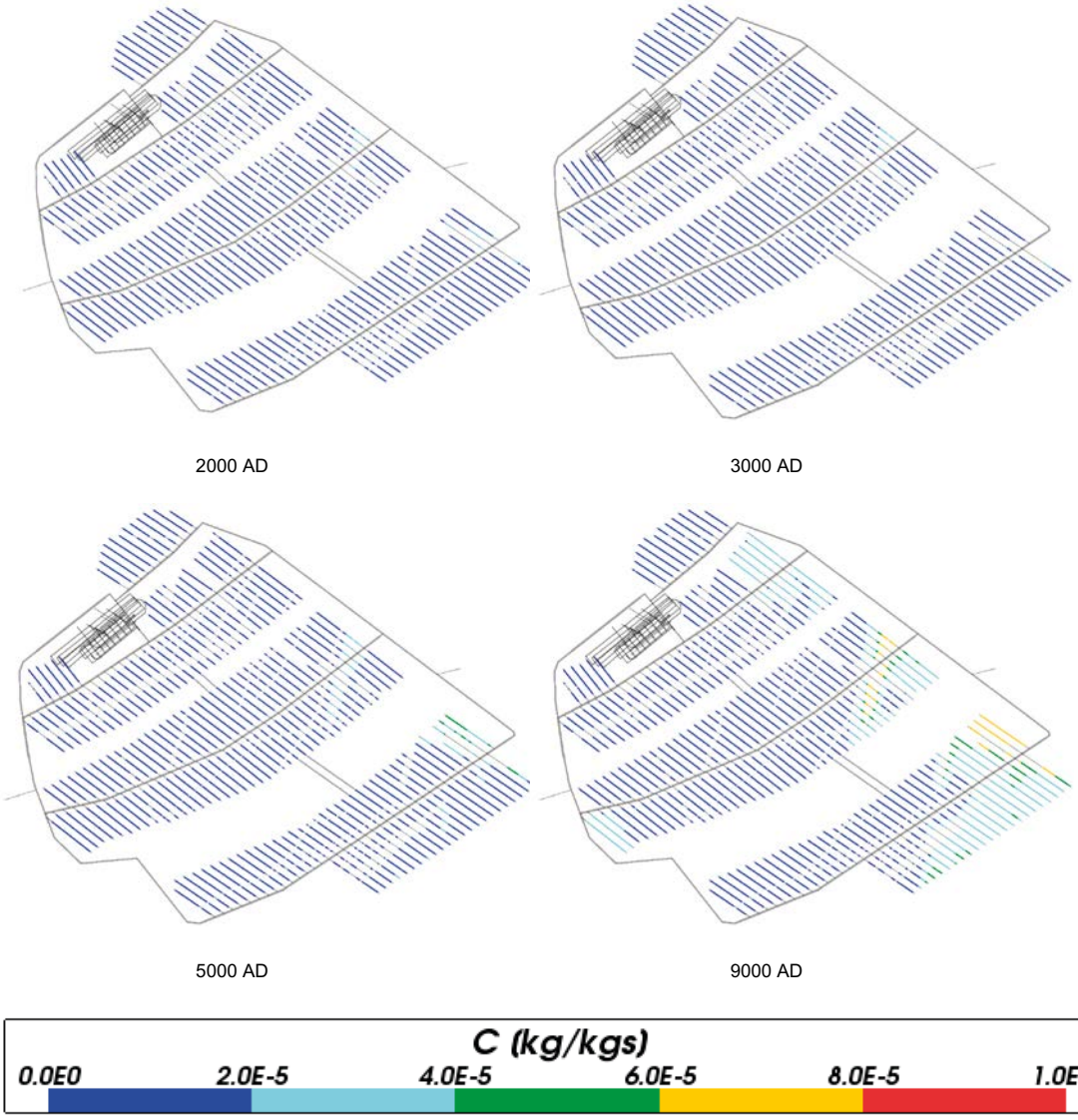


***Figure 4-42.*** *Total inorganic carbon mass fractions for Case 2 at deposition hole locations for time periods 2000 AD to 9000 AD.*

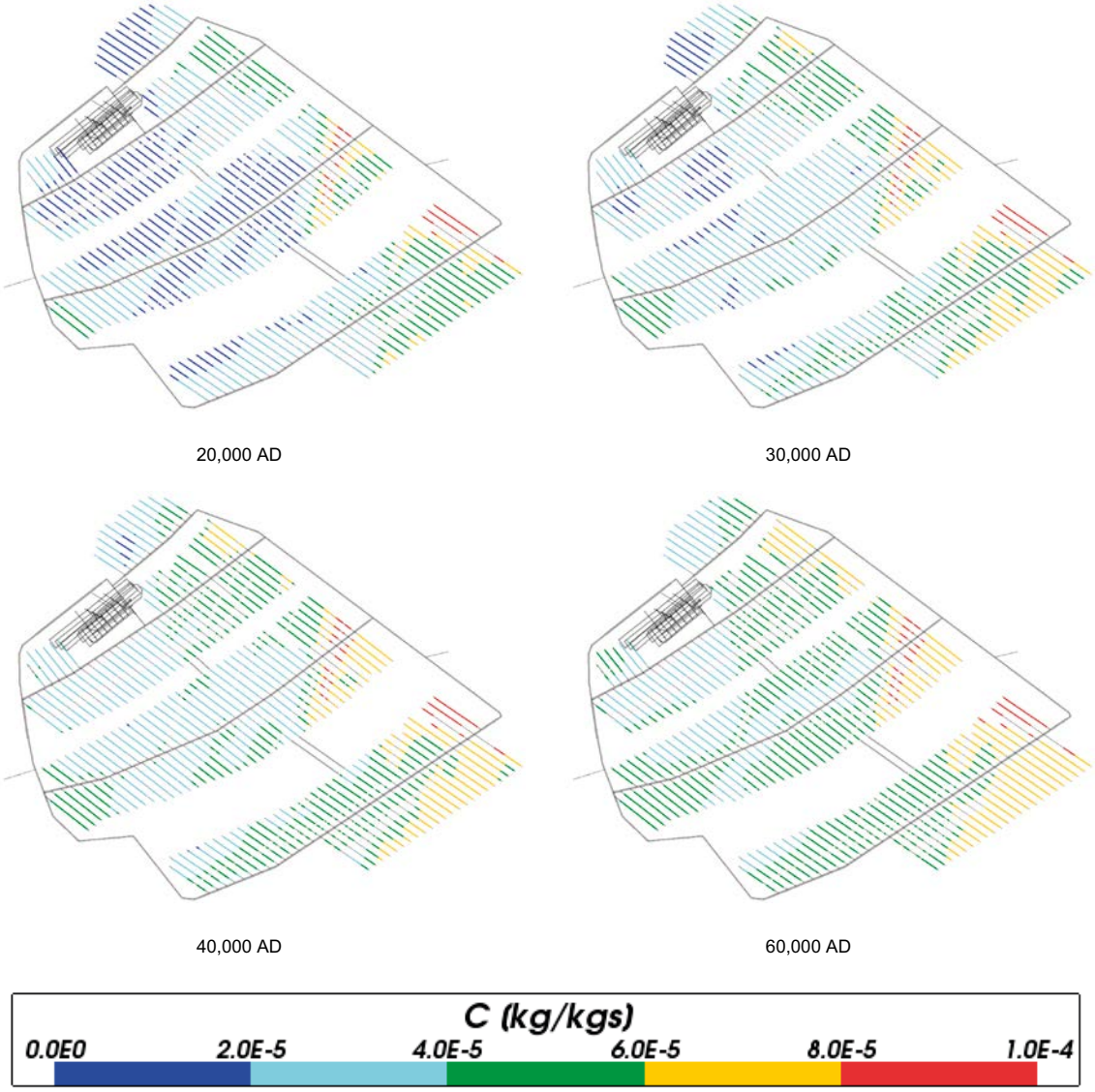


***Figure 4-43.*** *Total inorganic carbon mass fractions for Case 2 at deposition hole locations for time periods 20,000 AD to 60,000 AD.*

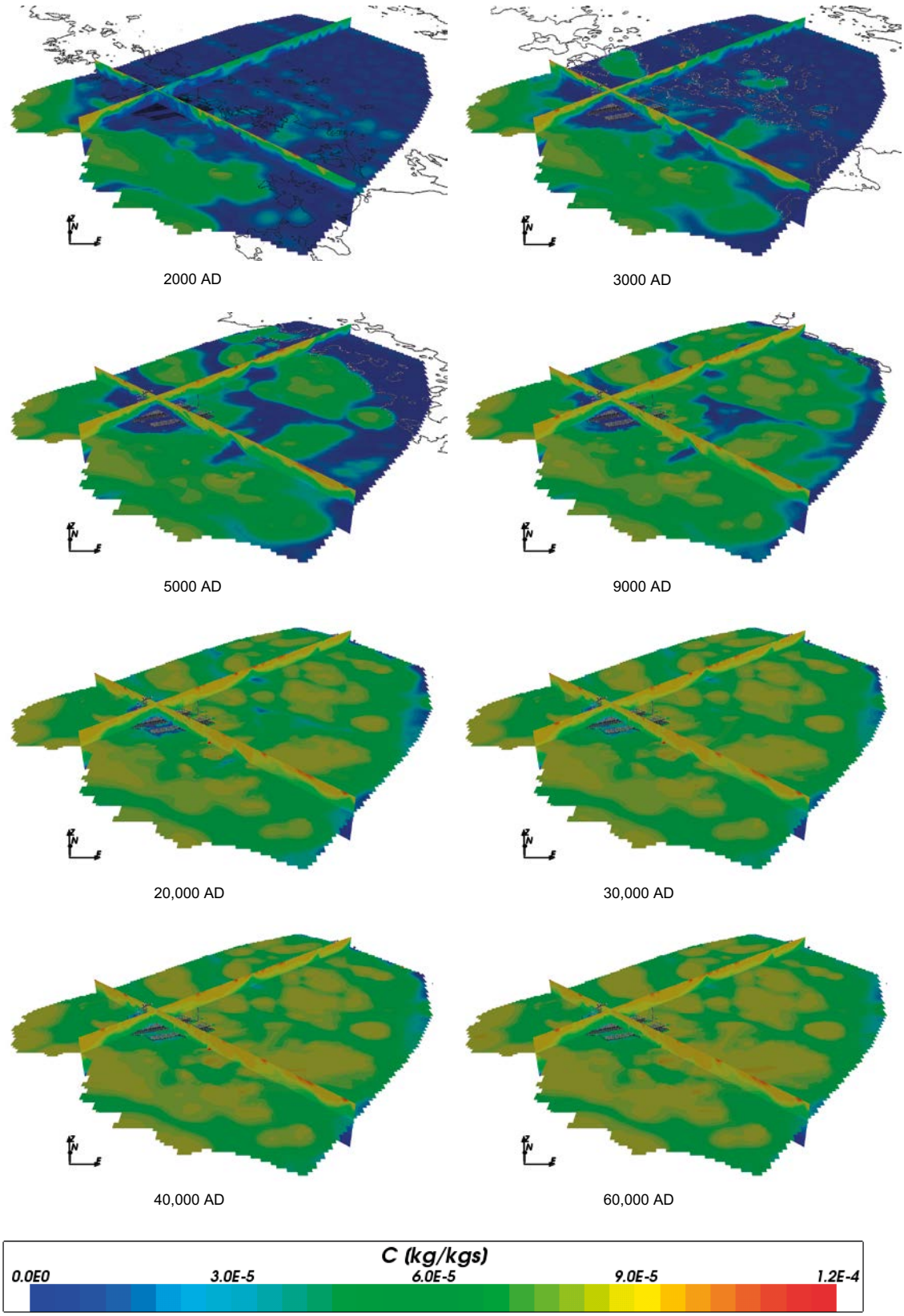


***Figure 4-44.*** *Total inorganic carbon mass fractions on regional scale slices through the repository volume for Case 2 for time periods 2000 AD to 60,000 AD.*

### 4.3.5 Calcium

The concentrations of total calcium both in the repository area and on the regional scale (shown in Figure 4-45 to Figure 4-48) show a similar trend to Case 1, but with median concentrations that are a little higher for Case 2 and with more spread. The differences are partly a result of calcite reactions, but likely to be predominately the result of minor differences in groundwater flow, solute transport and mixing. The increased calcium concentrations and decreased inorganic carbon concentrations in the repository volume relative to Case 1 would be consistent with a greater proportion of Littorina Sea water relative to Altered Meteoric water. The range of median concentrations values is consistent with that reported in Salas et al. (2010) of around 0.05 mol/L at 2000 AD to around 0.02 mol/L at 9000 AD.

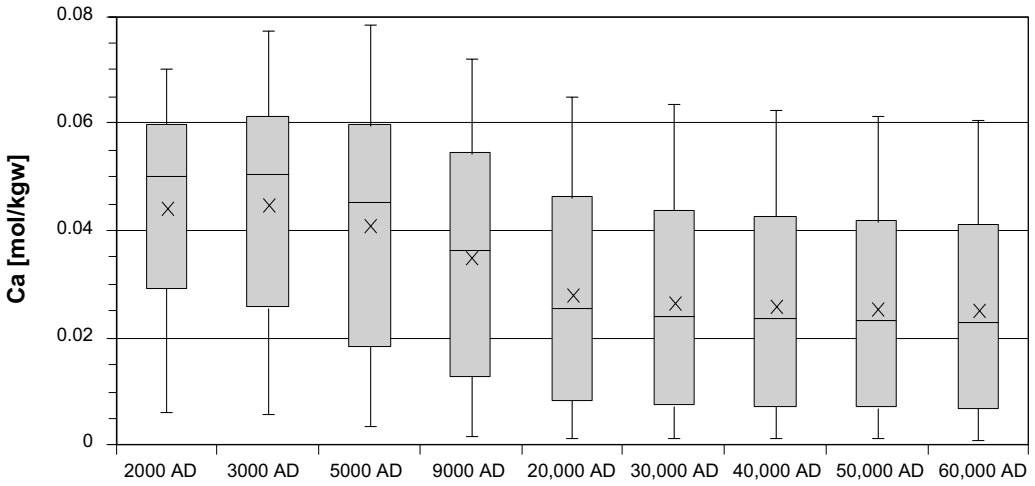


***Figure 4-45.*** *Box and whisker plot showing the statistical distribution of total calcium molalities for Case 2 on a regular grid of points within the repository volume between elevations –490 m and –450 m. The statistical measures are the median, the 25$^{th}$ and 75$^{th}$ percentiles (box), the mean (cross) and the 5$^{th}$ and 95$^{th}$ percentiles (whiskers).*

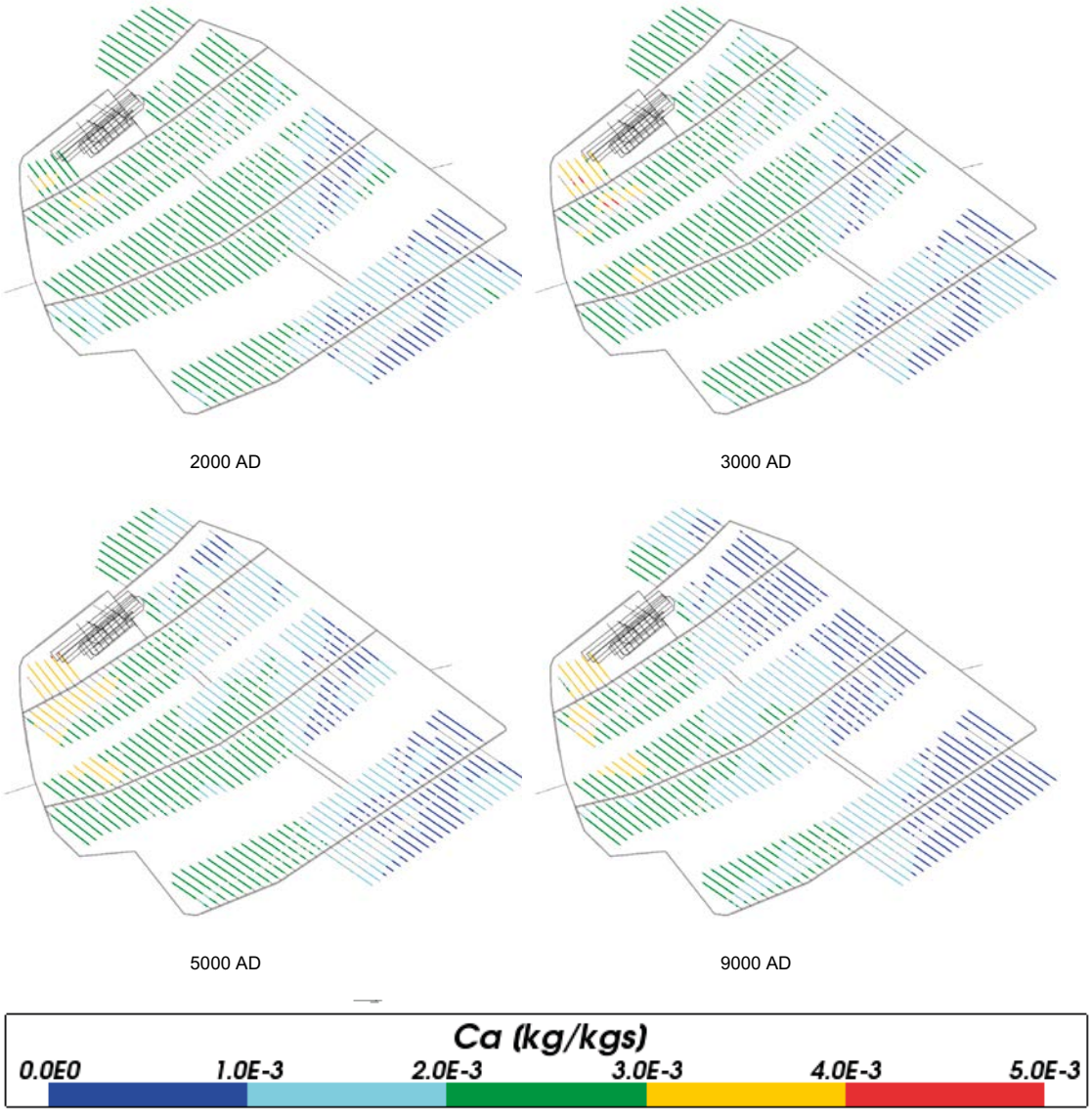


***Figure 4-46.*** *Total calcium mass fractions for Case 2 at deposition hole locations for time periods 2000 AD to 9000 AD.*

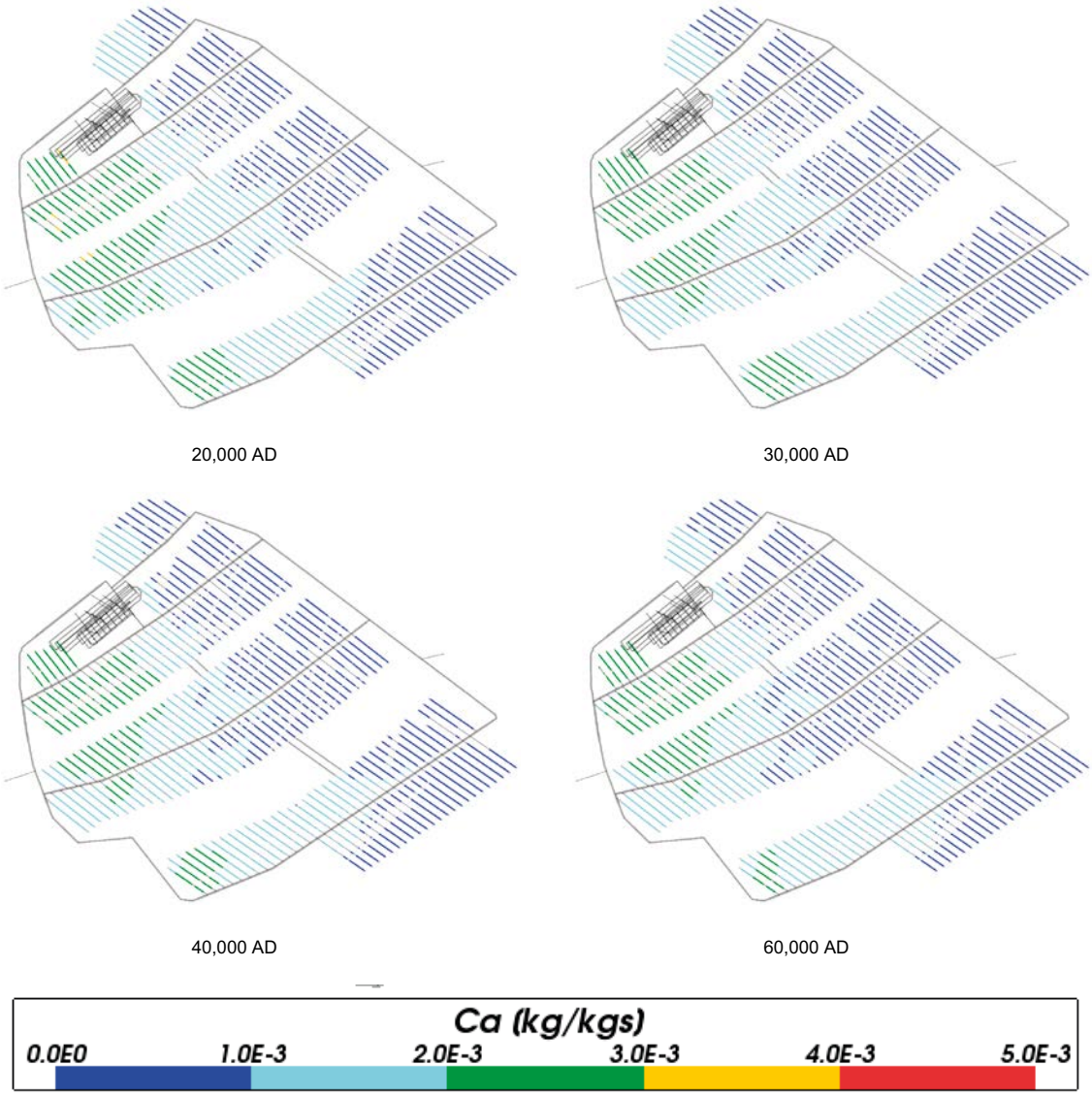


***Figure 4-47.*** *Total calcium mass fractions for Case 2 at deposition hole locations for time periods 20,000 AD to 60,000 AD.*

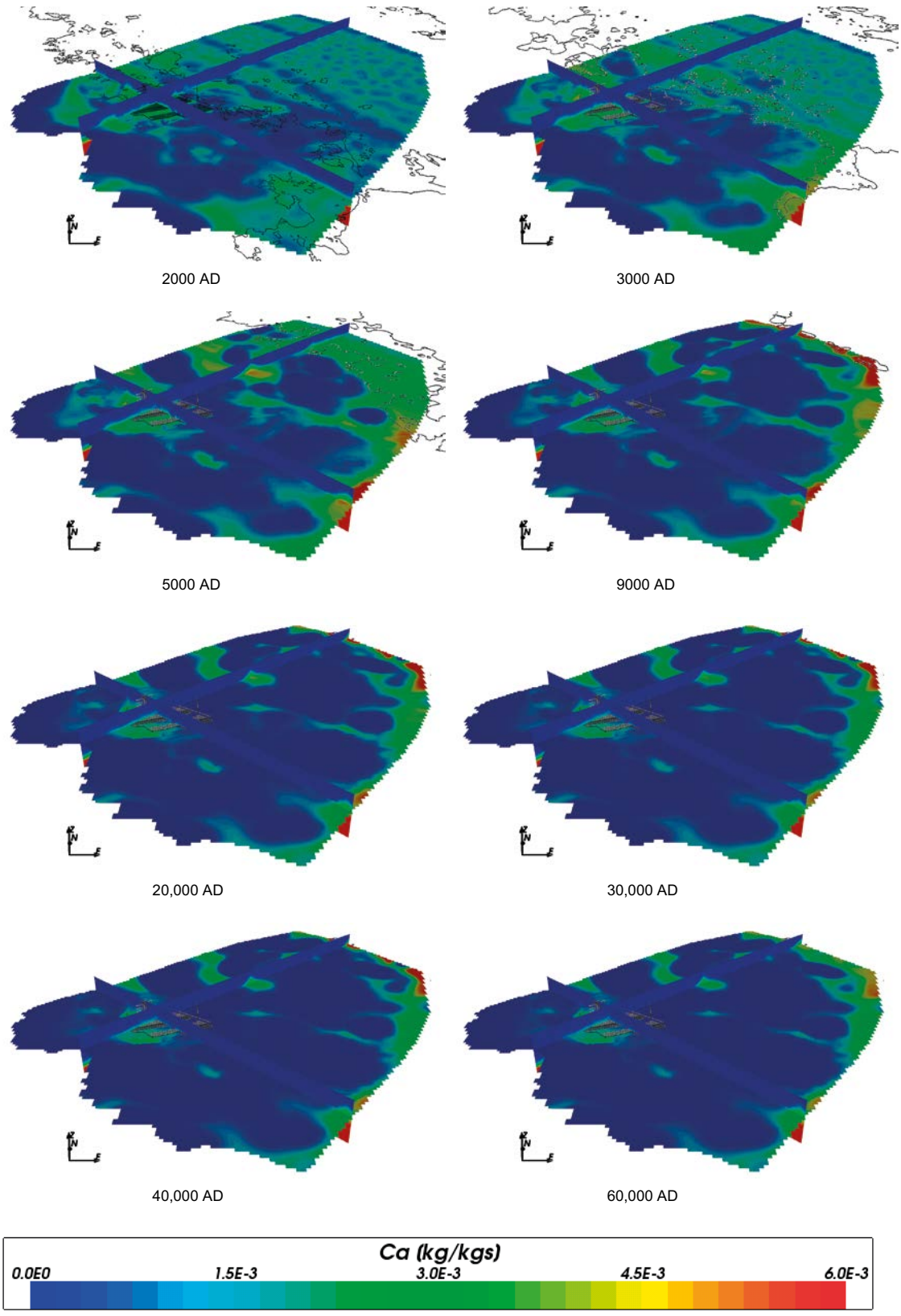


***Figure 4-48.*** *Total calcium mass fractions on regional scale slices through the repository volume for Case 2 for time periods 2000 AD to 60,000 AD.*

### 4.3.6 Chloride

Figure 4-49, Figure 4-50 and Figure 4-51 show the chloride concentrations for Case 2. Since chloride is a non-reacting component, the results are very similar to Case 1 (no chemical reactions), but with some more spread at later times, indicating minor changes to the transport. The concentrations of chloride across the model domain (Figure 4-52) are also very close to Case 1. The concentrations are also similar to those reported in Salas et al. (2010) of around 0.1 mol/L.

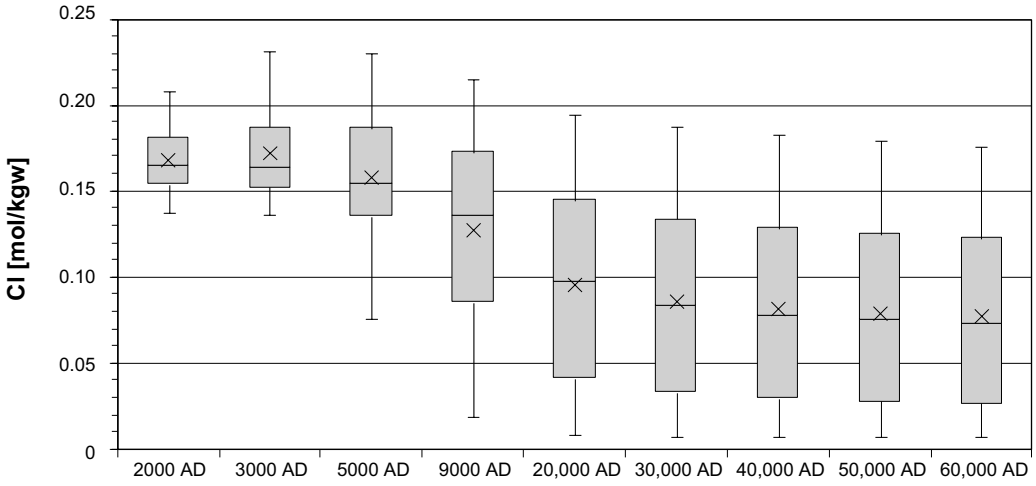


***Figure 4-49.*** *Box and whisker plot showing the statistical distribution of total chloride molalities for Case 2 on a regular grid of points within the repository volume between elevations –490 m and –450 m. The statistical measures are the median, the 25$^{th}$ and 75$^{th}$ percentiles (box), the mean (cross) and the 5$^{th}$ and 95$^{th}$ percentiles (whiskers).*

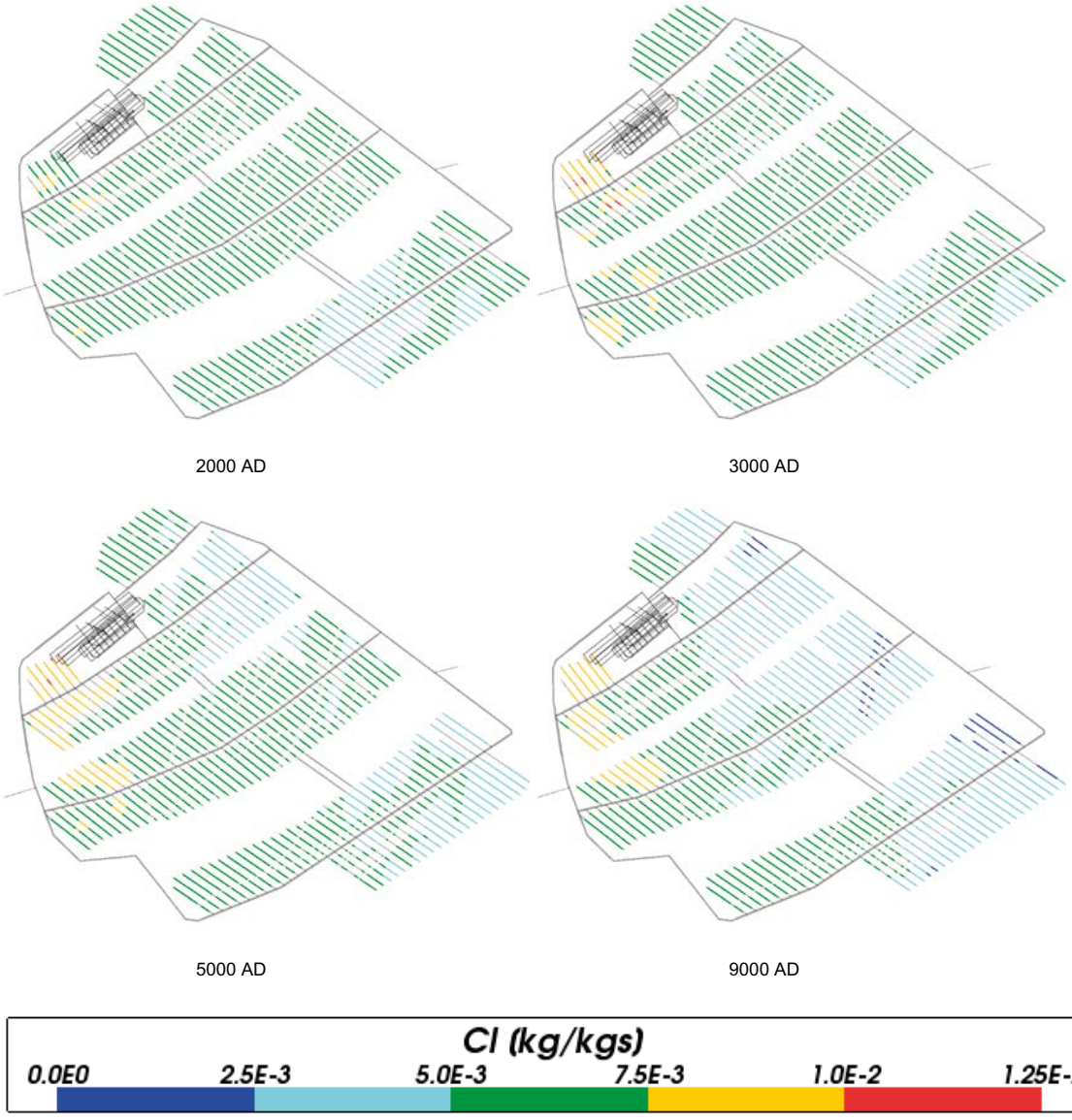


***Figure 4-50.*** *Total chloride mass fractions for Case 2 at deposition hole locations for time periods 2000 AD to 9000 AD.*

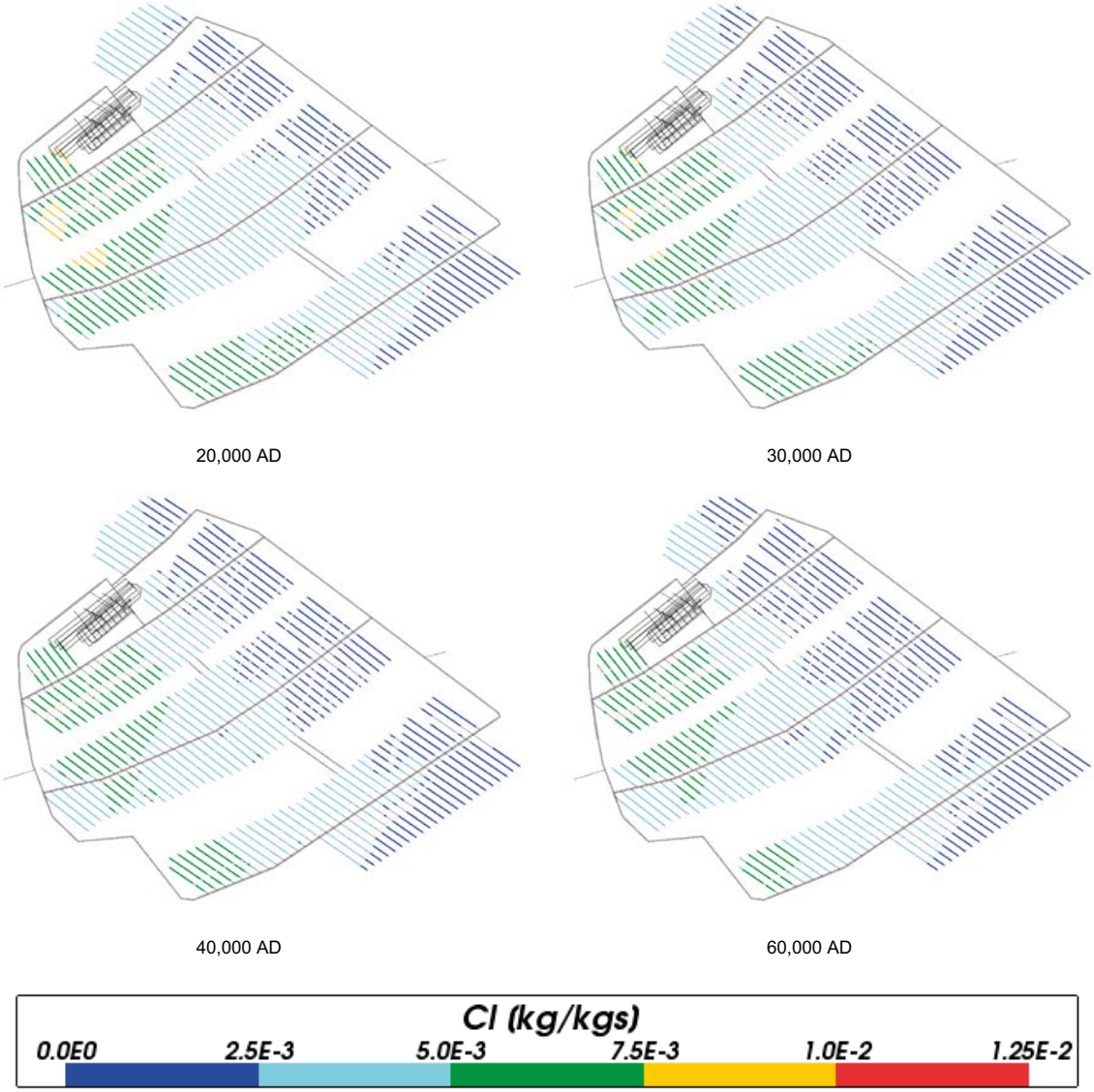


***Figure 4-51.*** *Total chloride mass fractions for Case 2 at deposition hole locations for time periods 20,000 AD to 60,000 AD.*

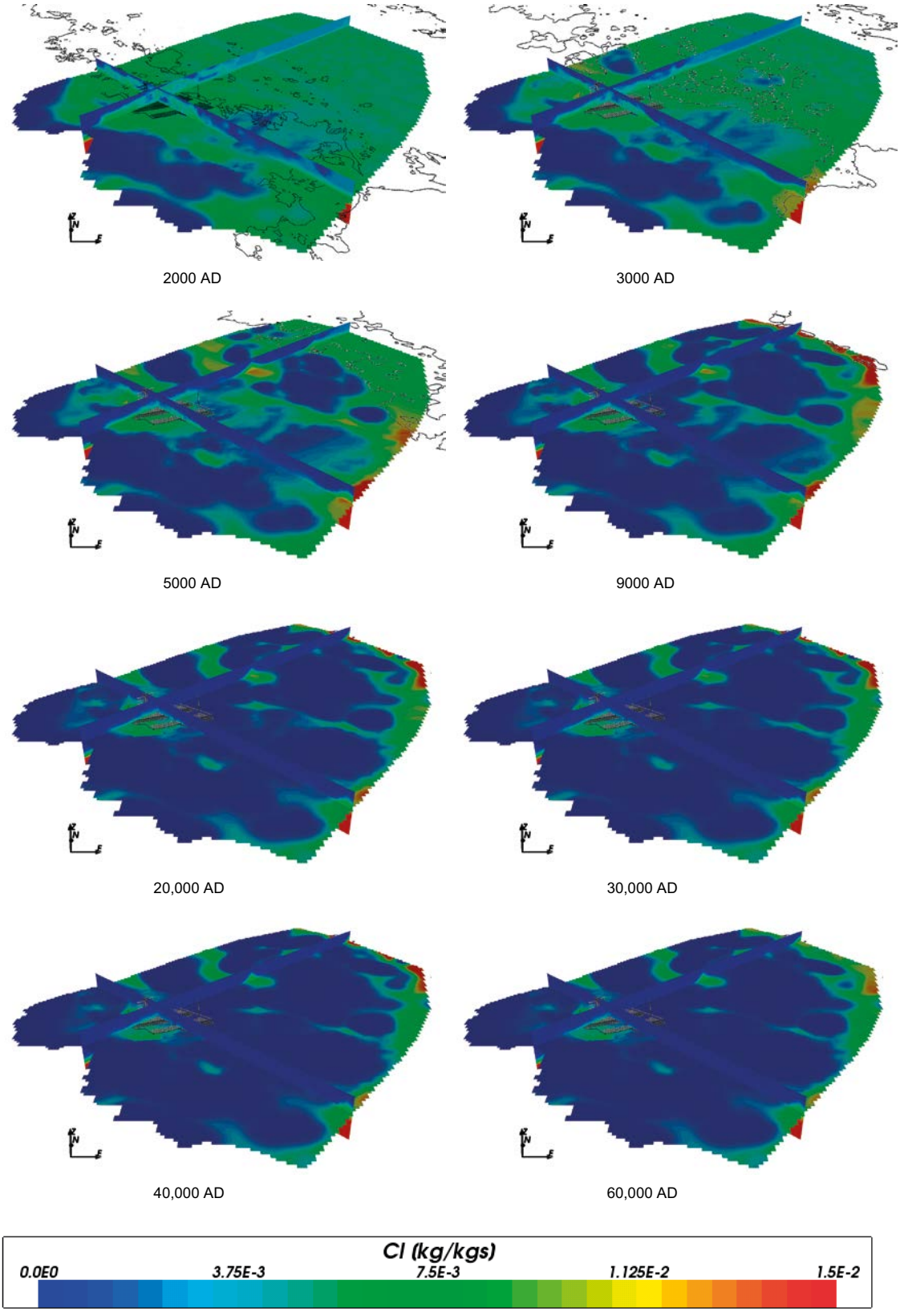


***Figure 4-52.*** *Total chloride mass fractions on regional scale slices through the repository volume for Case 2 for time periods 2000 AD to 60,000 AD.*

### 4.3.7 Iron

The concentrations of total iron around the repository are shown in Figure 4-53, Figure 4-54 and Figure 4-55. In Case 1 the concentration of iron remained low around the repository and little change could be seen over time other than a reduction in the spread of values. For Case 2 however, the concentration of iron increases over time, levelling off after 40,000 AD, and the spread increases a little (Figure 4-53). These results are consistent with those for the corresponding reactions reported in Salas et al. (2010) with median values of around $1.0 \cdot 10^{-5}$ mol/L that increase in magnitude and spread with time.

Figure 4-56 shows the total iron concentration increasing with time over the regional scale from the south west to the north east, in contrast to Case 1 (Figure 4-18) which shows little or no change with time. There are a few isolated high values visible (red dots) which are indicative of numerical fluctuations, but they will not affect the overall results for the repository volume.

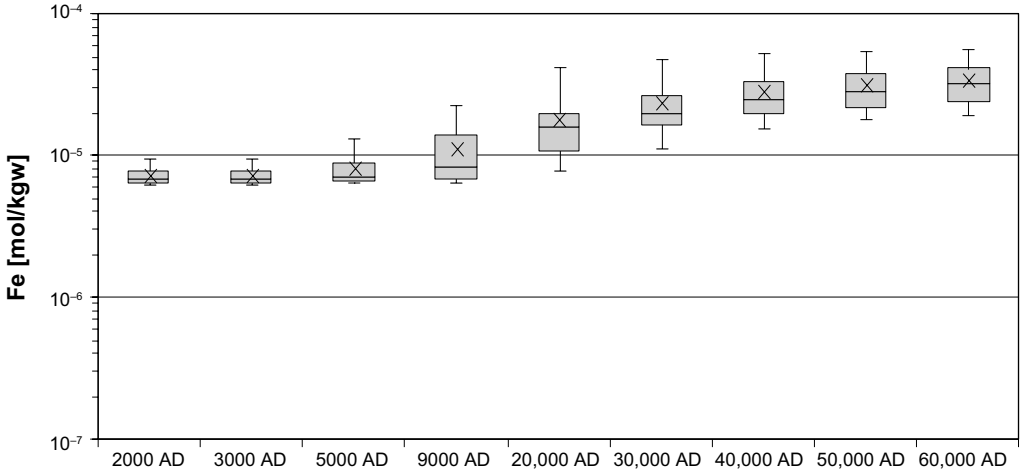


***Figure 4-53.*** *Box and whisker plot showing the statistical distribution of total iron molalities for Case 2 on a regular grid of points within the repository volume between elevations –490 m and –450 m. The statistical measures are the median, the 25th and 75th percentiles (box), the mean (cross) and the 5th and 95th percentiles (whiskers).*

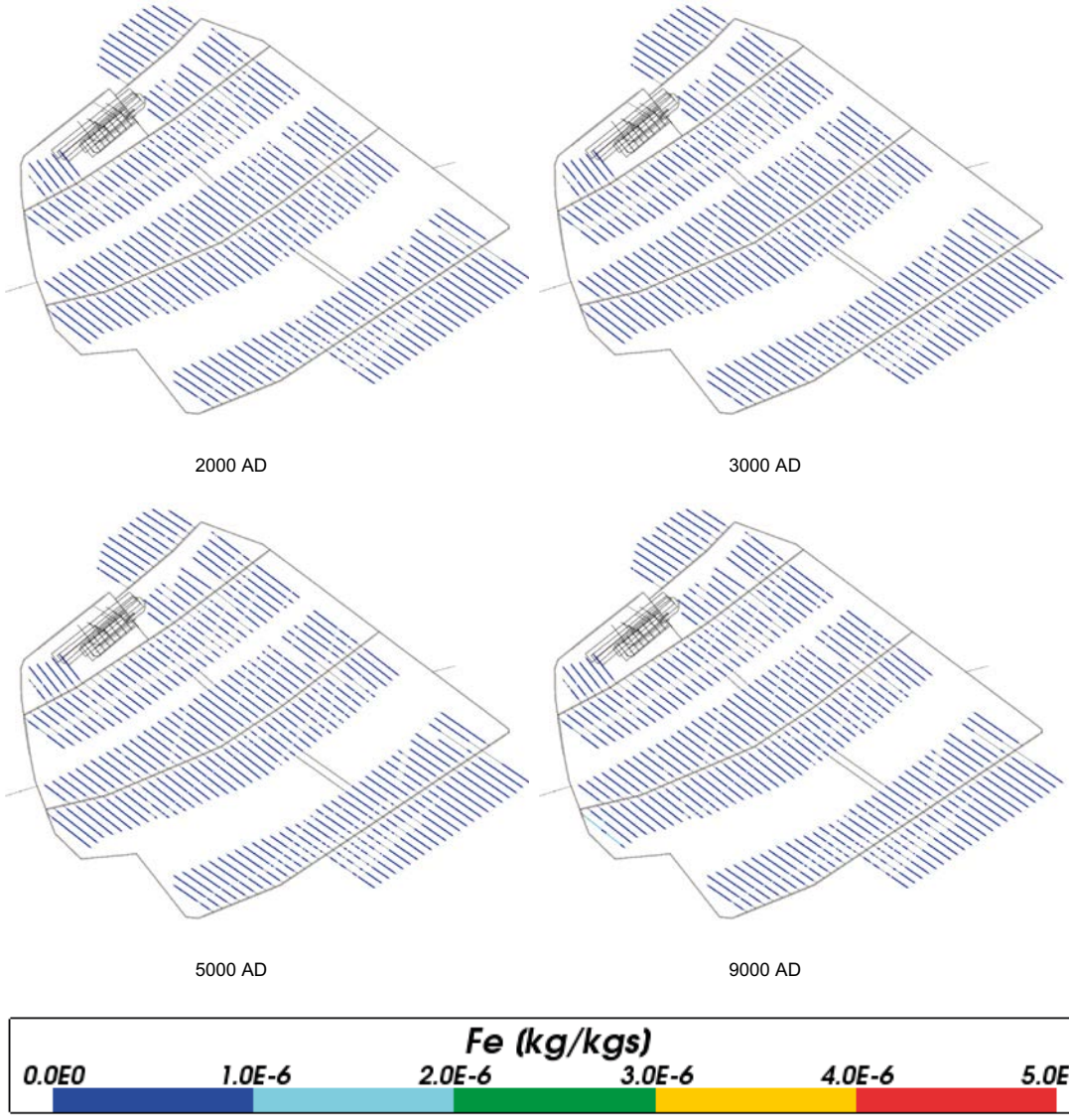


***Figure 4-54.*** *Total iron mass fractions for Case 2 at deposition hole locations for time periods 2000 AD to 9000 AD.*

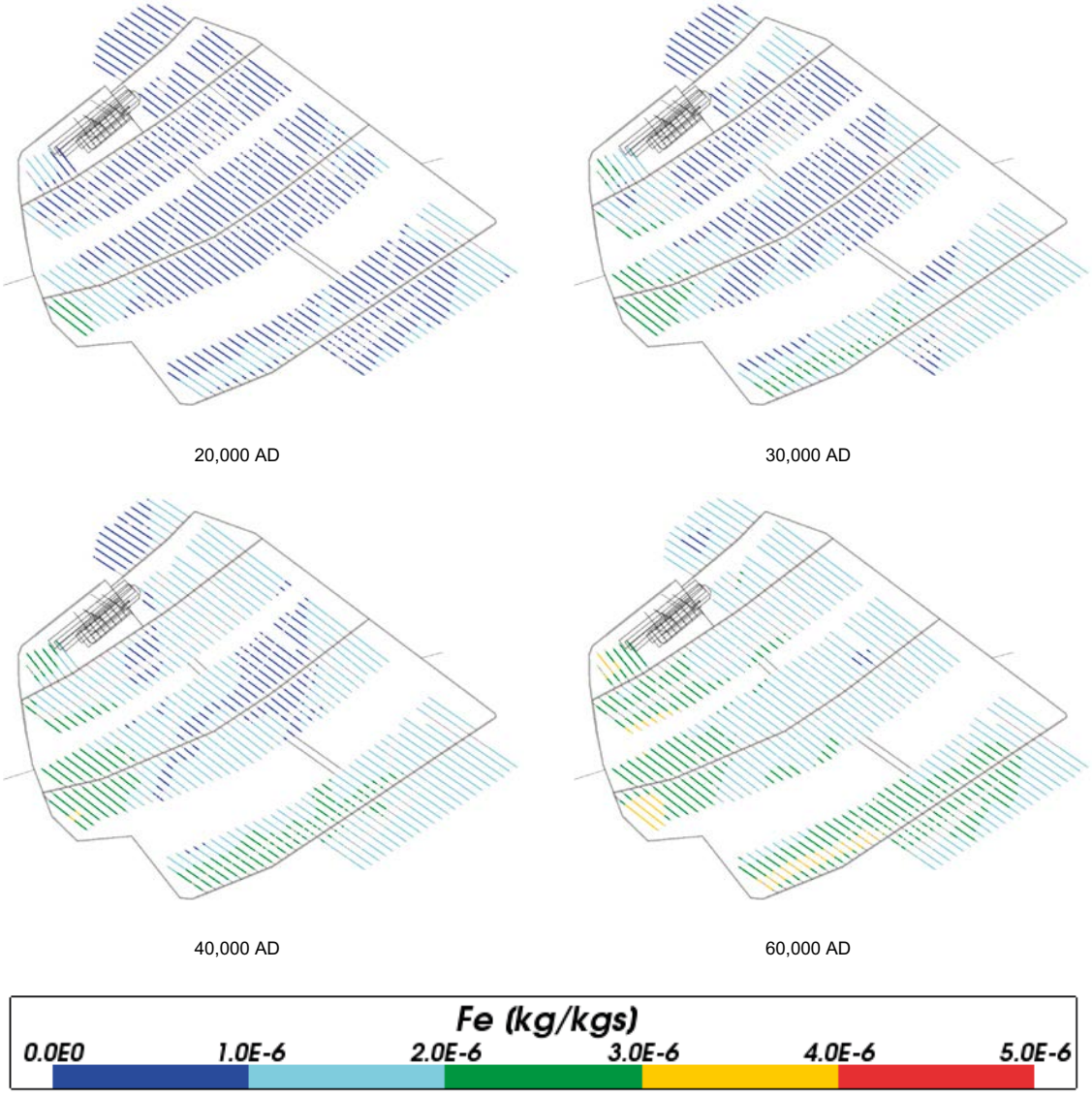


***Figure 4-55.*** *Total iron mass fractions for Case 2 at deposition hole locations for time periods 20,000 AD to 60,000 AD.*

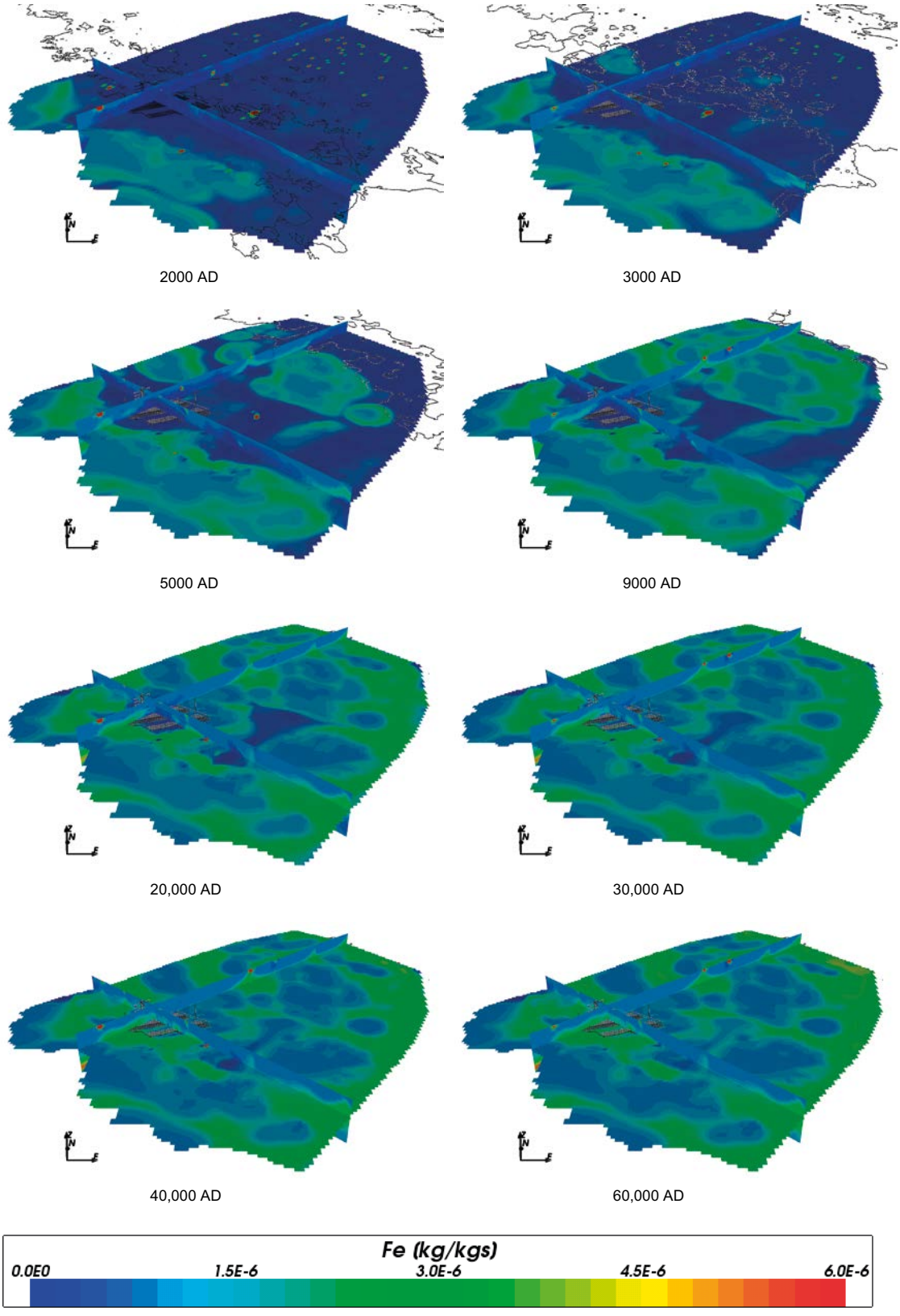


***Figure 4-56.*** *Total iron mass fractions on regional scale slices through the repository volume for Case 2 for time periods 2000 AD to 60,000 AD.*

### 4.3.8 Sodium

The spatial and temporal distribution of sodium concentrations (Figure 4-57, Figure 4-58, Figure 4-59 and Figure 4-60) is very similar to Case 1 as this is a non-reacting species for Case 2. The sodium concentrations are also similar to the median values given in Salas et al. (2010) of between around 0.07 m/L at 2000 AD and 0.06 mol/L at 9000 AD.

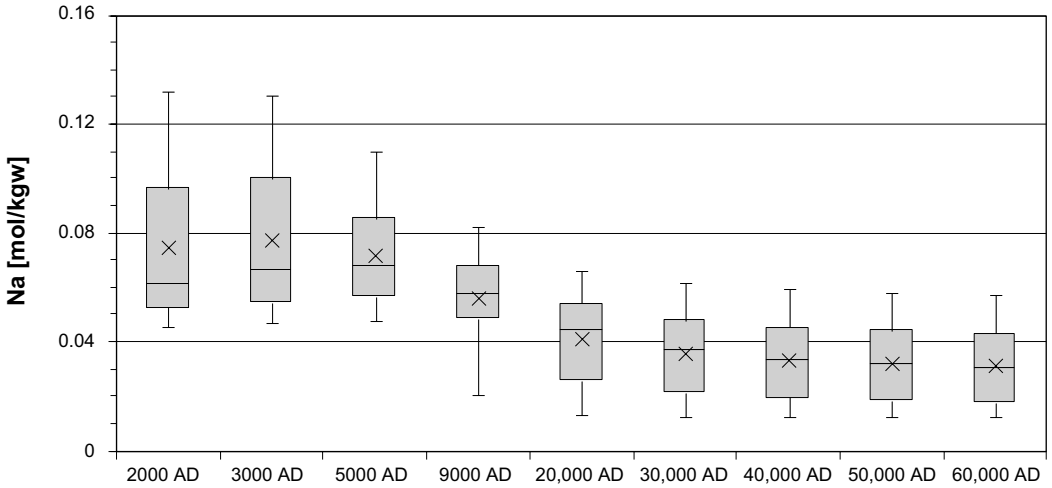


***Figure 4-57.*** *Box and whisker plot showing the statistical distribution of total sodium molalities for Case 2 on a regular grid of points within the repository volume between elevations –490 m and –450 m. The statistical measures are the median, the 25$^{th}$ and 75$^{th}$ percentiles (box), the mean (cross) and the 5$^{th}$ and 95$^{th}$ percentiles (whiskers).*

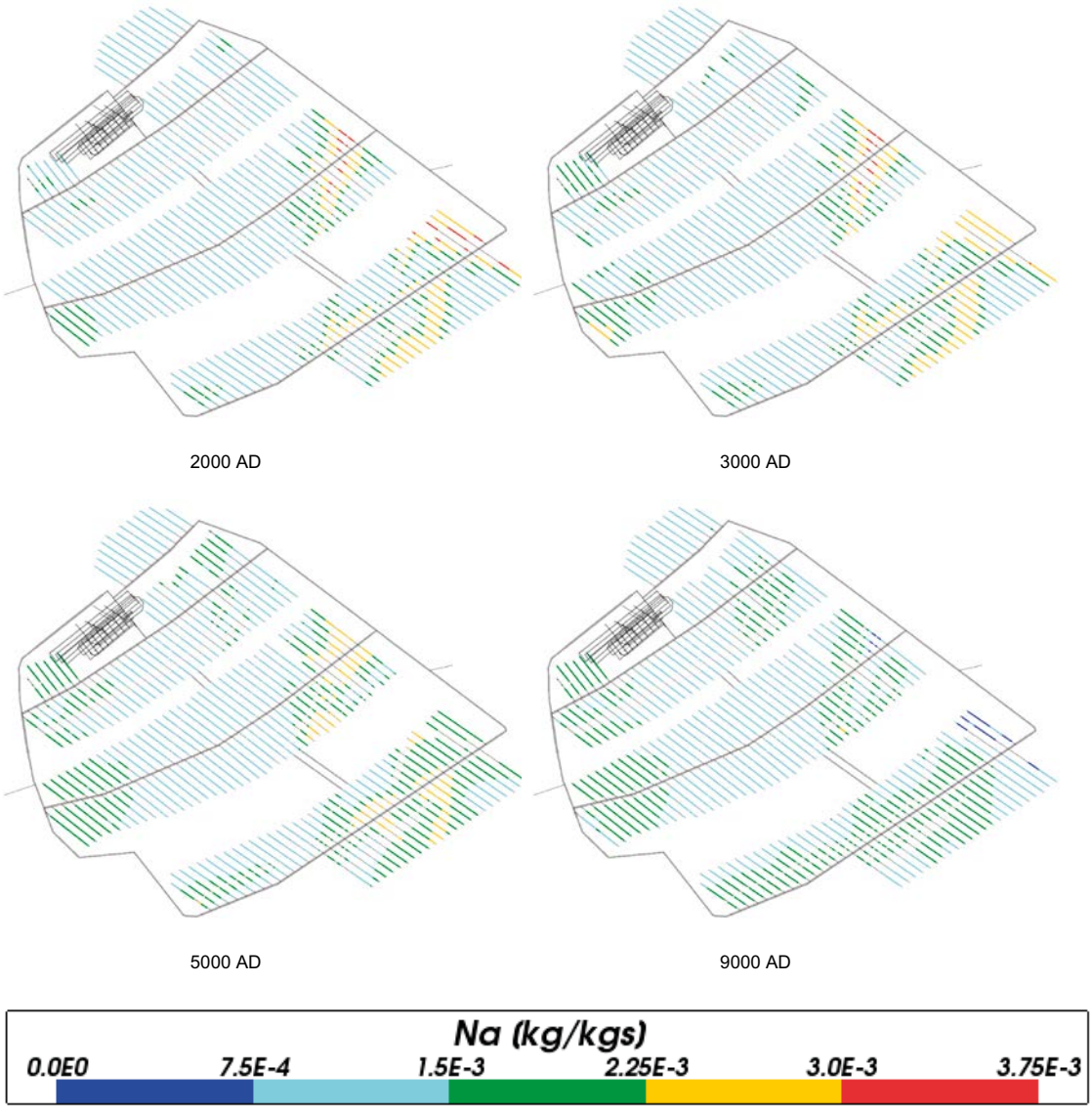


***Figure 4-58.*** *Total sodium mass fractions for Case 2 at deposition hole locations for time periods 2000 AD to 9000 AD.*

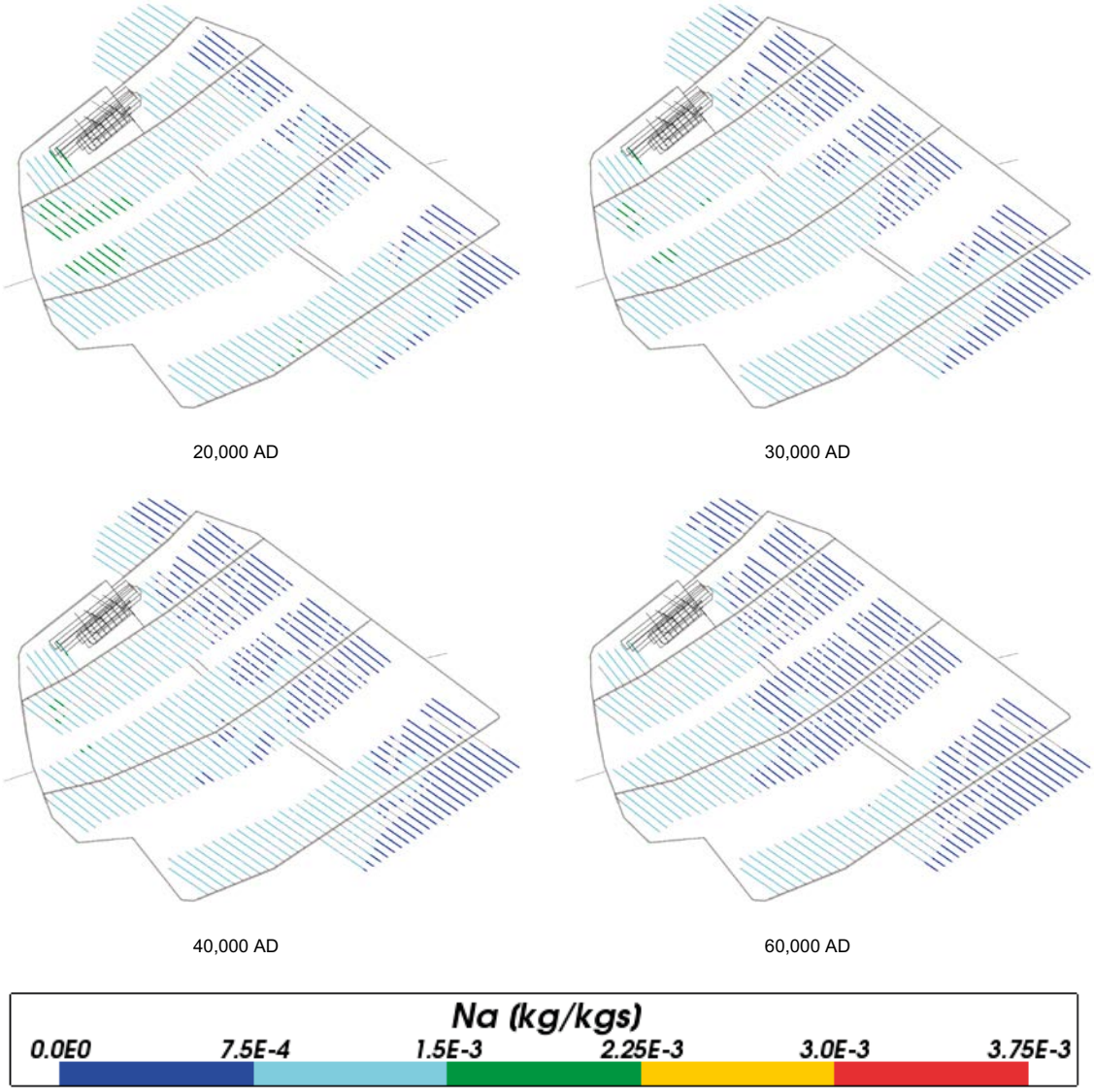


***Figure 4-59.*** *Total sodium mass fractions for Case 2 at deposition hole locations for time periods 20,000 AD to 60,000 AD.*

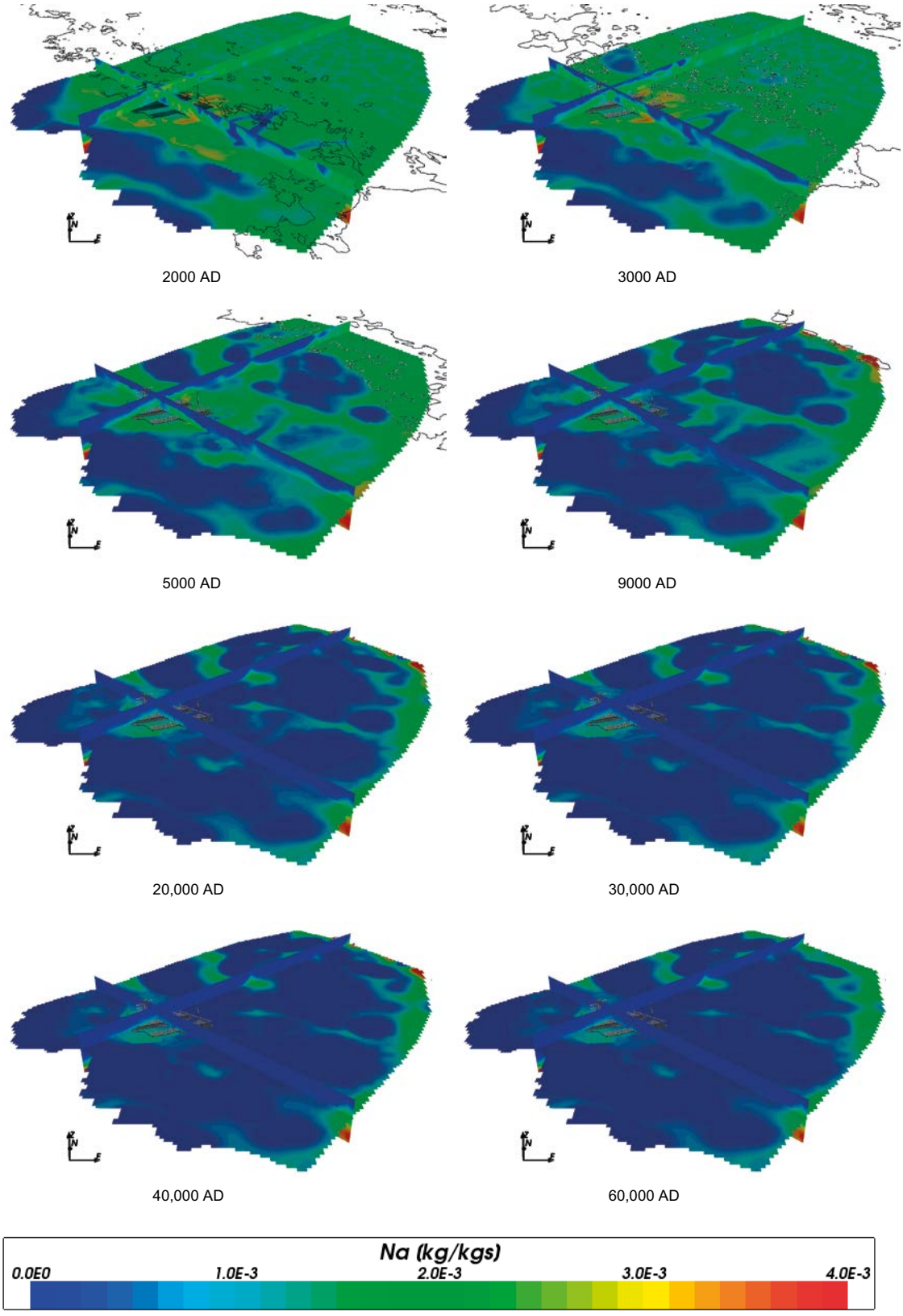


***Figure 4-60.*** *Total sodium mass fractions on regional scale slices through the repository volume for Case 2 for time periods 2000 AD to 60,000 AD.*

### 4.3.9 Potassium

The spatial and temporal distribution of potassium concentrations (Figure 4-61 to Figure 4-64) is very similar to Case 1 as this is a non-reacting species for Case 2. The median concentrations in the repository volume are a little lower at early times for Case 2 (Figure 4 61), although the concentrations are a little higher at the deposition hole locations (Figure 4-62 and Figure 4-63). The median potassium concentrations are similar to the median values given in Salas et al. (2010) of around $8 \cdot 10^{-4}$ m/L between 2000 AD and 9000 AD.

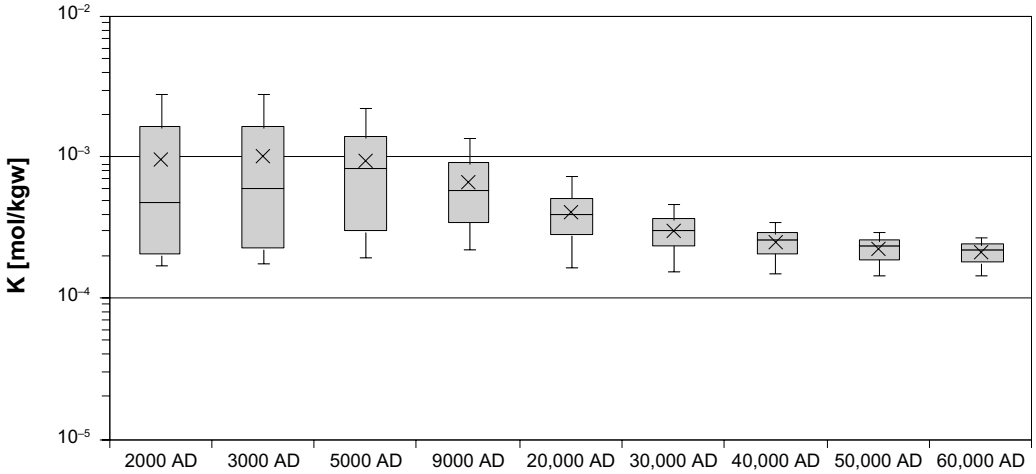


***Figure 4-61.*** *Box and whisker plot showing the statistical distribution of total potassium molalities for Case 2 on a regular grid of points within the repository volume between elevations –490 m and –450 m. The statistical measures are the median, the 25th and 75th percentiles (box), the mean (cross) and the 5th and 95th percentiles (whiskers).*

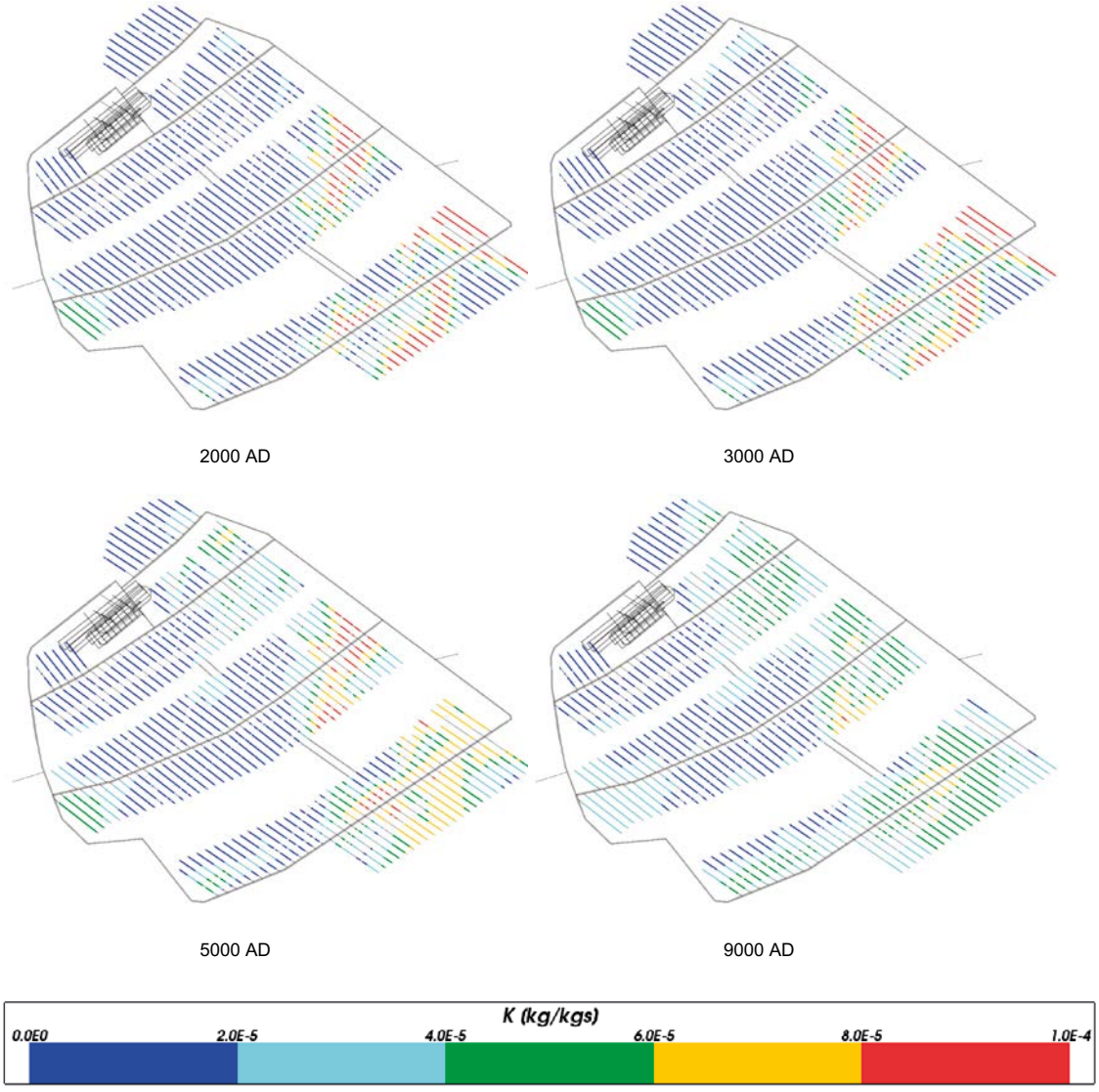


***Figure 4-62.*** *Total potassium mass fractions for Case 2 at deposition hole locations for time periods 2000 AD to 9000 AD.*

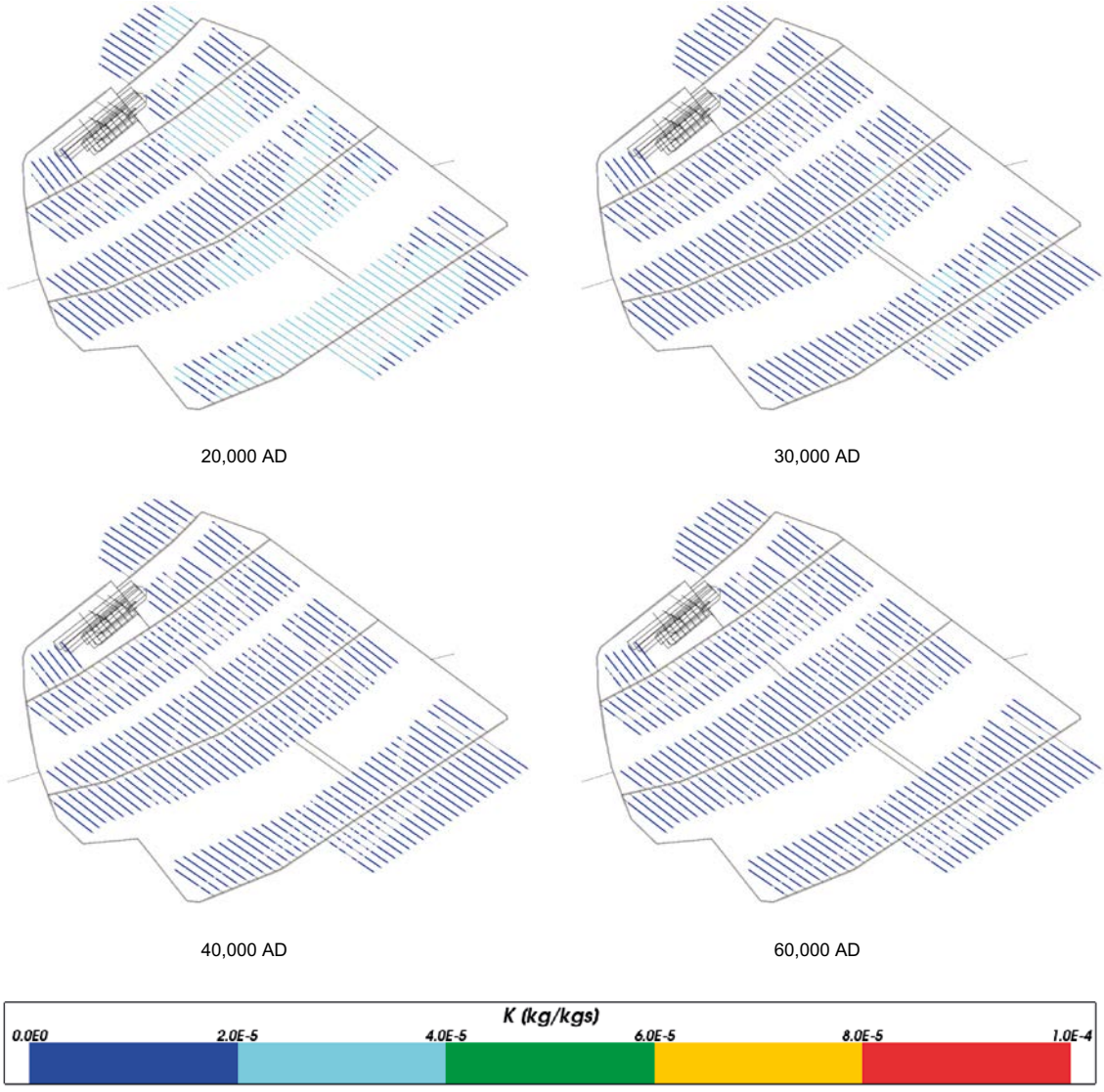


***Figure 4-63.*** *Total potassium mass fractions for Case 2 at deposition hole locations for time periods 20,000 AD to 60,000 AD.*

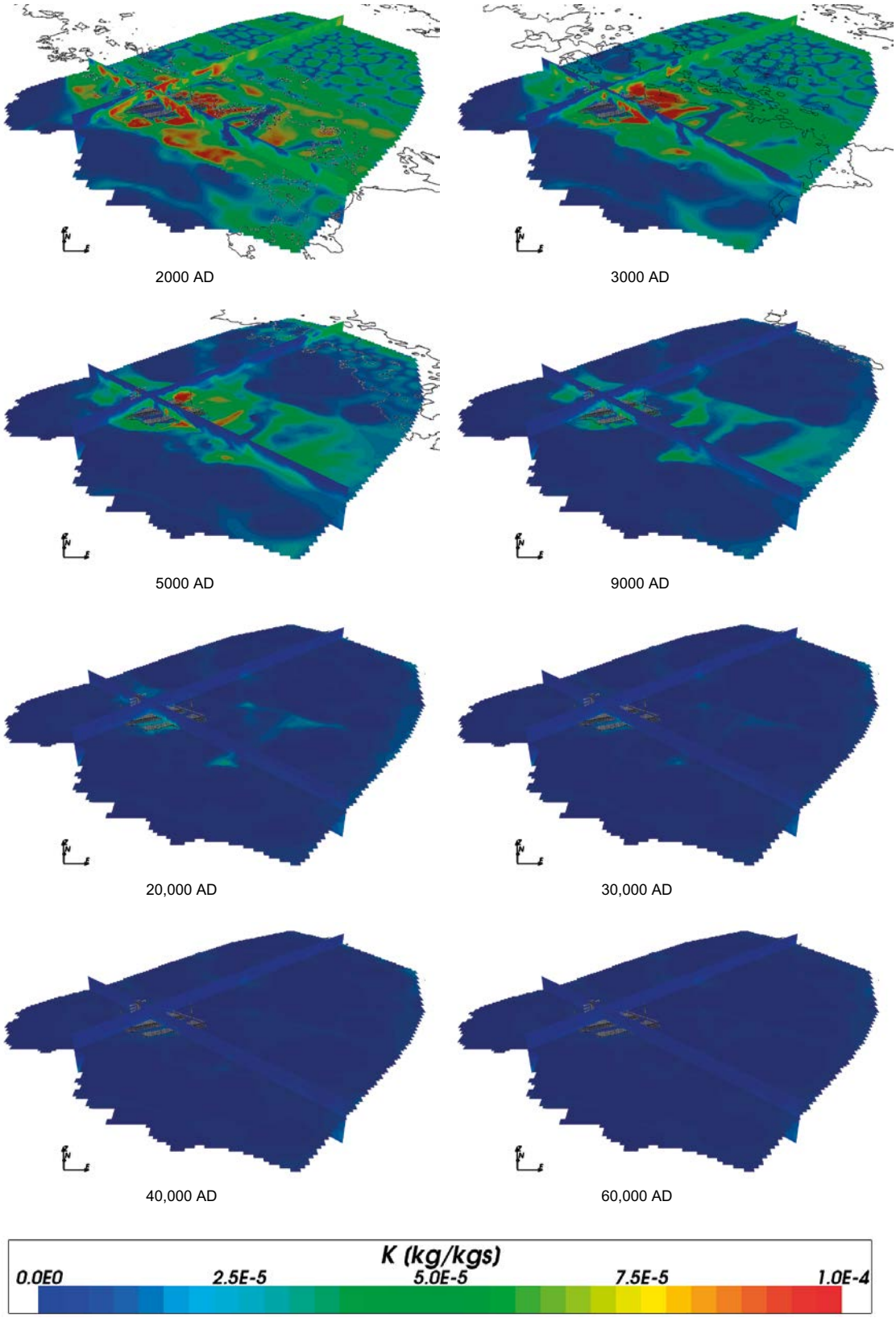


***Figure 4-64.*** *Total potassium mass fractions on regional scale slices through the repository volume for Case 2 for time periods 2000 AD to 60,000 AD.*

### 4.3.10 Sulphate

Figure 4-65, Figure 4-66 and Figure 4-67 show the sulphate concentrations around the repository for Case 2. The median concentrations remain fairly constant at around $1.0 \cdot 10^{-3}$ mol/kg$_w$ but the spread of values (i.e. the spatial variation) reduces over time. Similar results are given in Salas et al. (2010) up to 9000 AD.

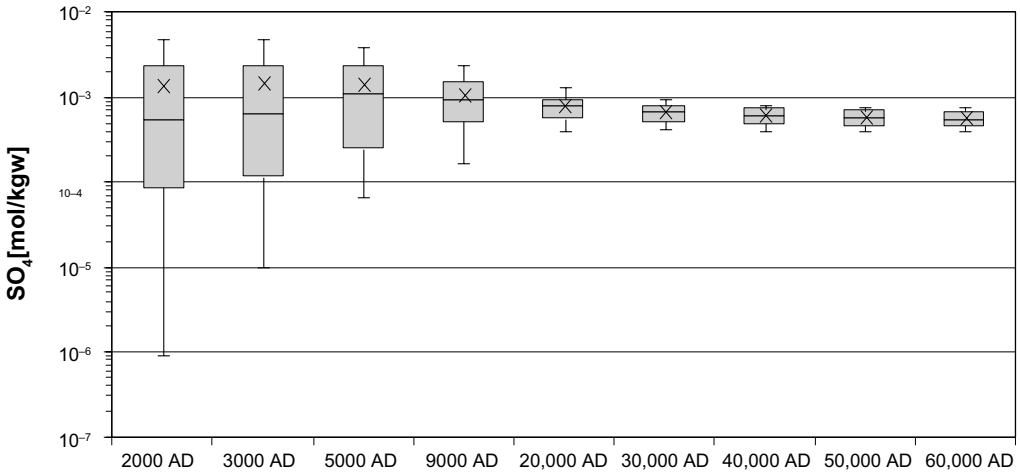


***Figure 4-65.*** *Box and whisker plot showing the statistical distribution of sulphate molalities for Case 2 on a regular grid of points within the repository volume between elevations –490 m and –450 m. The statistical measures are the median, the 25$^{th}$ and 75$^{th}$ percentiles (box), the mean (cross) and the 5$^{th}$ and 95$^{th}$ percentiles (whiskers).*

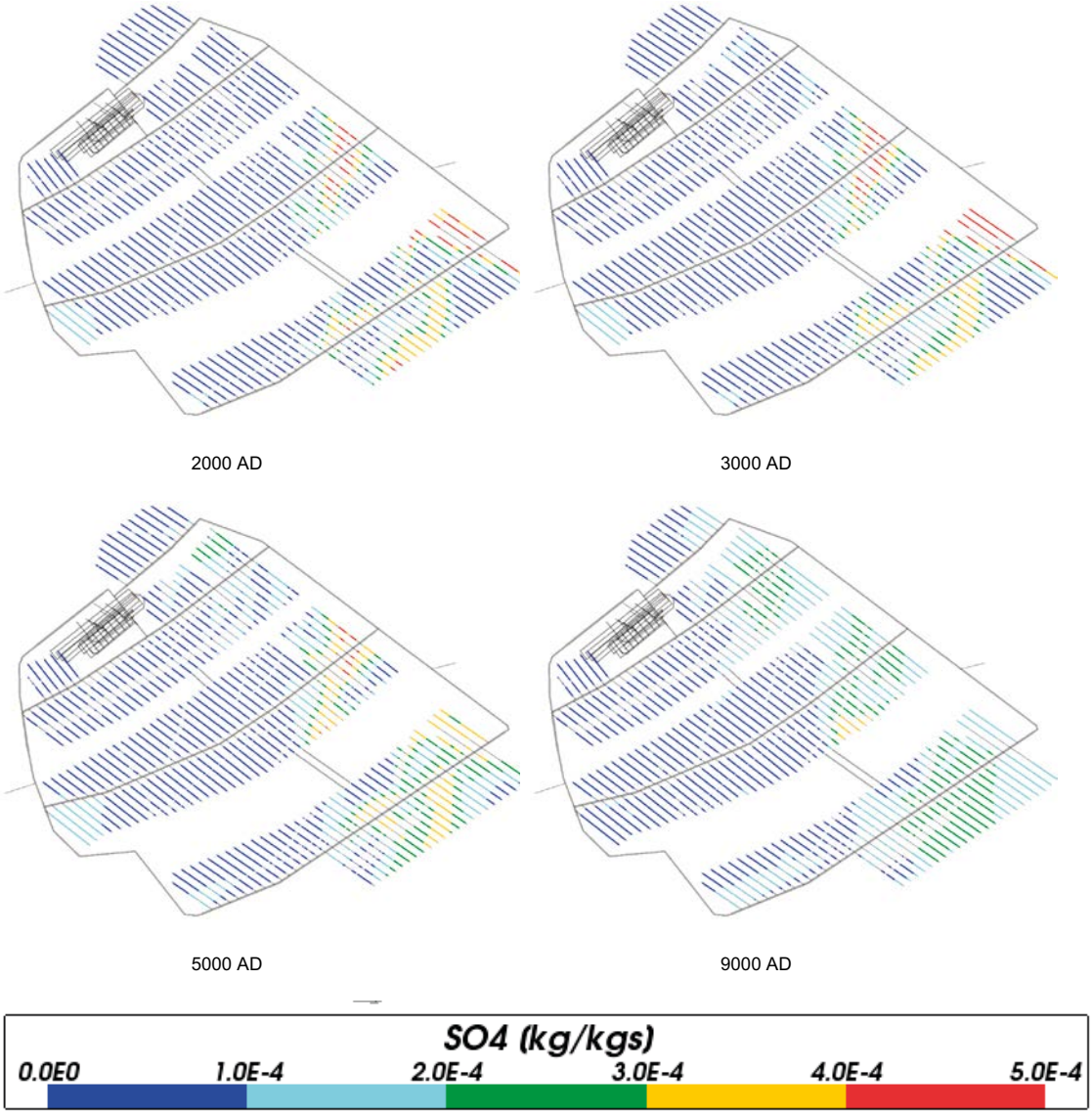


***Figure 4-66.*** *Total sulphate mass fractions for Case 2 at deposition hole locations for time periods 2000 AD to 9000 AD.*

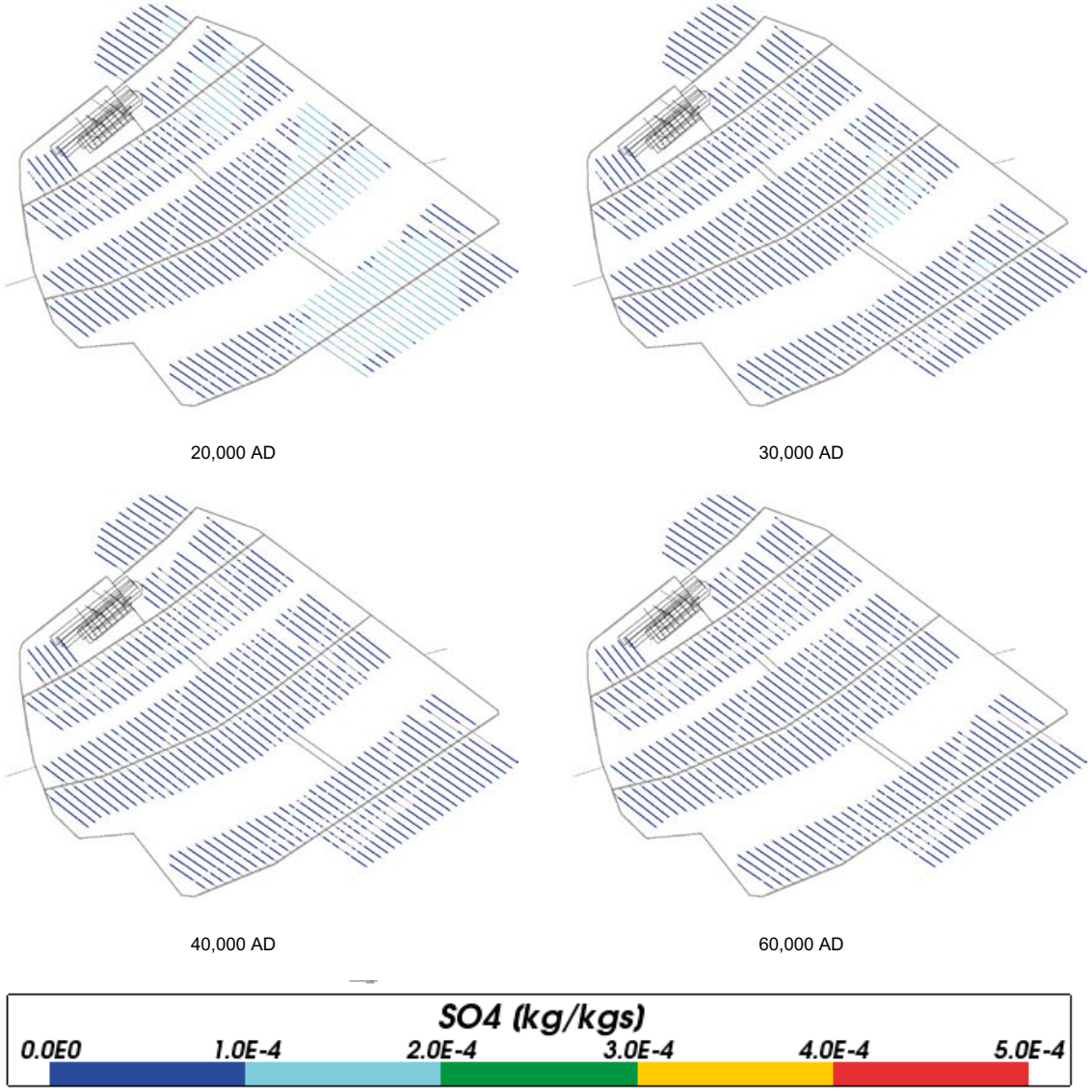


***Figure 4-67.*** *Total sulphate mass fractions for Case 2 at deposition hole locations for time periods 20,000 AD to 60,000 AD.*

### 4.3.11 Summary for Case 2

In addition to the groundwater flow and transport processes considered in Case 1, Case 2 includes equilibration of groundwater with calcite, quartz and amorphous iron (II) sulphide. As expected, the salinity, total cation concentrations and the concentrations of non-reacting species, such as chloride, sodium and potassium, were very similar to those calculated for Case 1, although with higher concentrations at repository depth. This indicates that the concentrations of the major species are determined primarily by groundwater flow and transport. There was also some effect on the concentrations of calcium and total inorganic carbon, partly as a result of the calcite reactions, but also due to changes in transport as a consequence of the reactions (via small changes in groundwater density). There was also a significant effect on the total iron concentrations due to the amorphous iron (II) sulphide reactions. The reactions also determine the pH, which fell from a median of around 7.6 at 2000 AD to around 6.8 at 60,000 AD within the repository volume, whilst the median Eh rose from –245 mV to –190 mV. Thus the geochemical conditions within the repository volume for this case remained within the bounds required by the safety assessment throughout the simulation period.

## 4.4 Case 3

The evolution of groundwater composition for this case will also be due to the transport and mixing of components originating from different reference waters. However, a different set of chemical reactions are considered for this case, which includes equilibration of groundwater with calcite, quartz and iron (III) oxyhydroxide. This is the same as Case 2, but iron (III) oxyhydroxide has replaced amorphous iron (II) sulphide. It is expected that the reactions will have an effect on pH, Eh, and the concentrations of total inorganic carbon, calcium and iron. Since only reactions involving iron and sulphur are different between Case 2 and Case 3, it is expected that only the results for Eh and the concentrations of iron and sulphur will differ significantly between these two cases. The concentrations of non-reacting species should be very similar for all cases.

### 4.4.1 pH

Figure 4-68, Figure 4-69 and Figure 4-70 show the values of pH around the repository for Case 3 decreasing with time, but levelling off at later times to a pH of approximately 6.8. Figure 4-71 shows values of pH over the regional area. As expected, the pH values are nearly identical to Case 2.

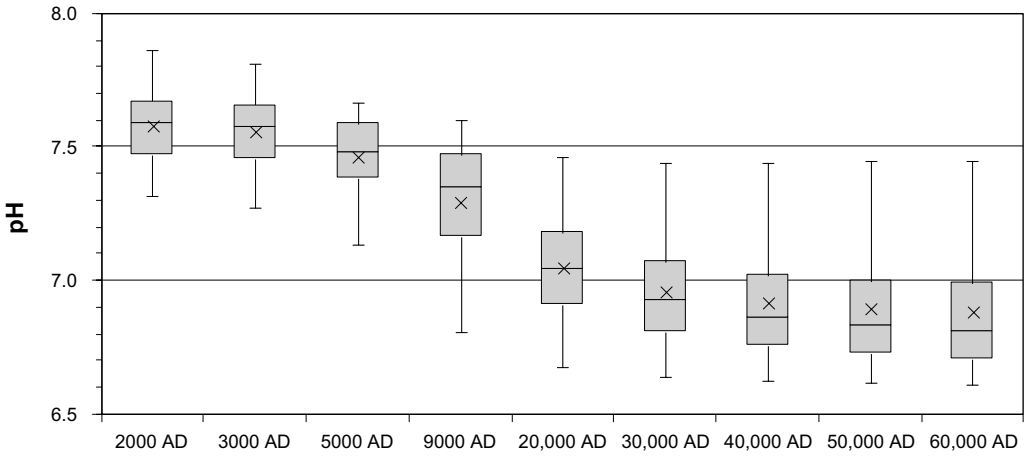


***Figure 4-68.*** *Box and whisker plot showing the statistical distribution of pH for Case 3 on a regular grid of points within the repository volume between elevations –490 m and –450 m. The statistical measures are the median, the 25th and 75th percentiles (box), the mean (cross) and the 5th and 95th percentiles (whiskers).*

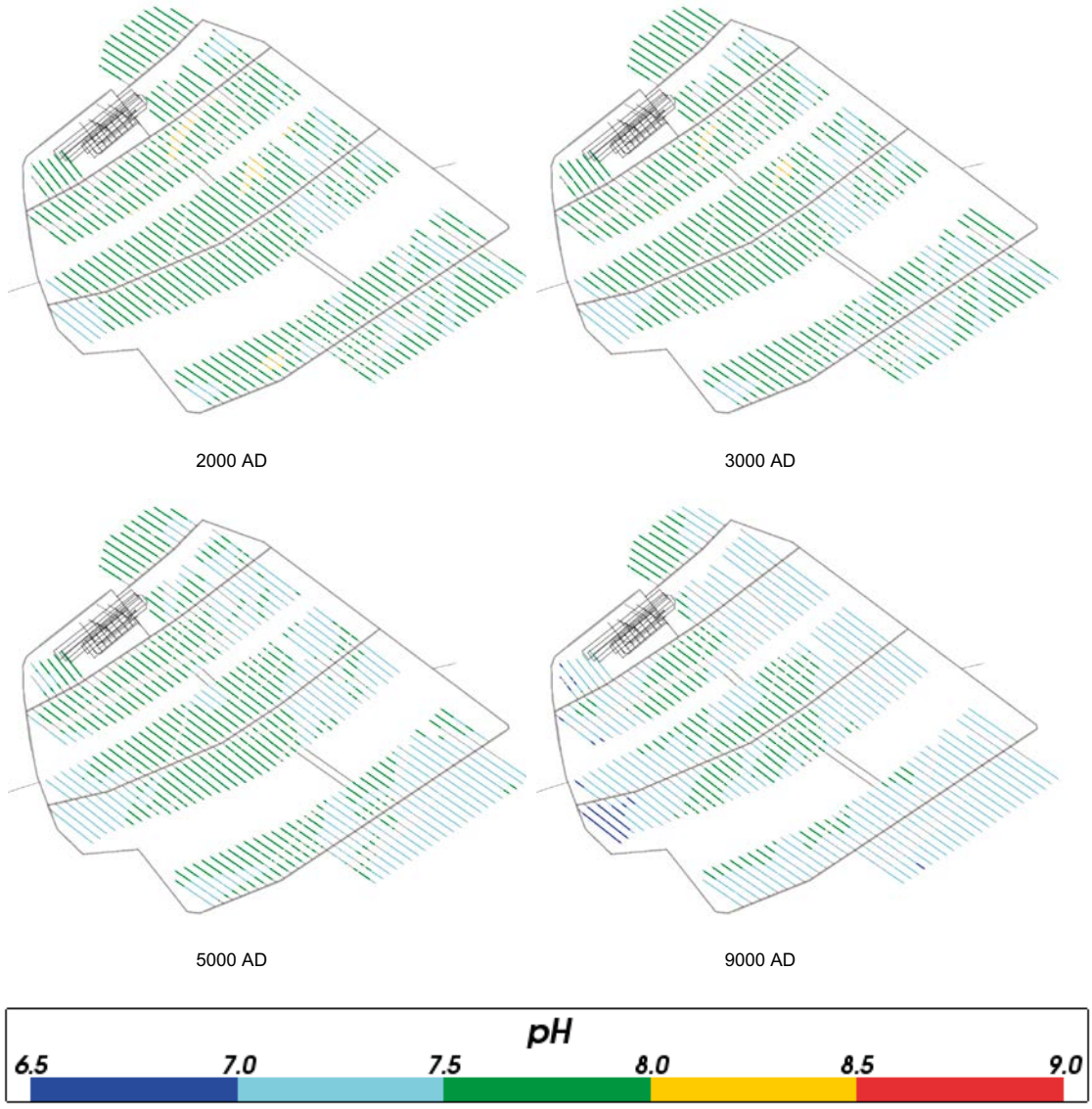


***Figure 4-69.*** *Values of pH for Case 3 at deposition hole locations for time periods 2000 AD to 9000 AD.*

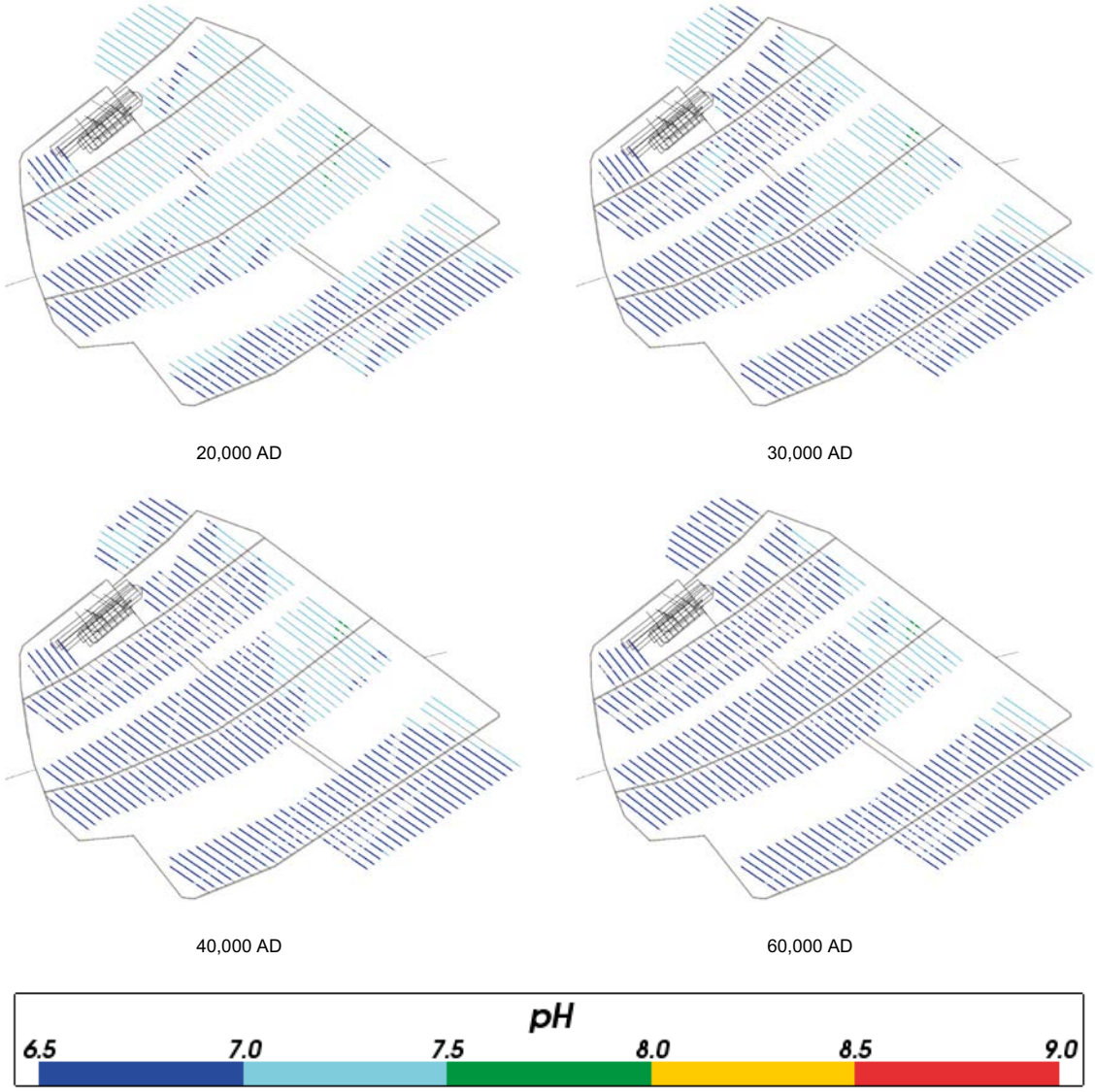


***Figure 4-70.*** *Values of pH for Case 3 at deposition hole locations for time periods 20,000 AD to 60,000 AD.*

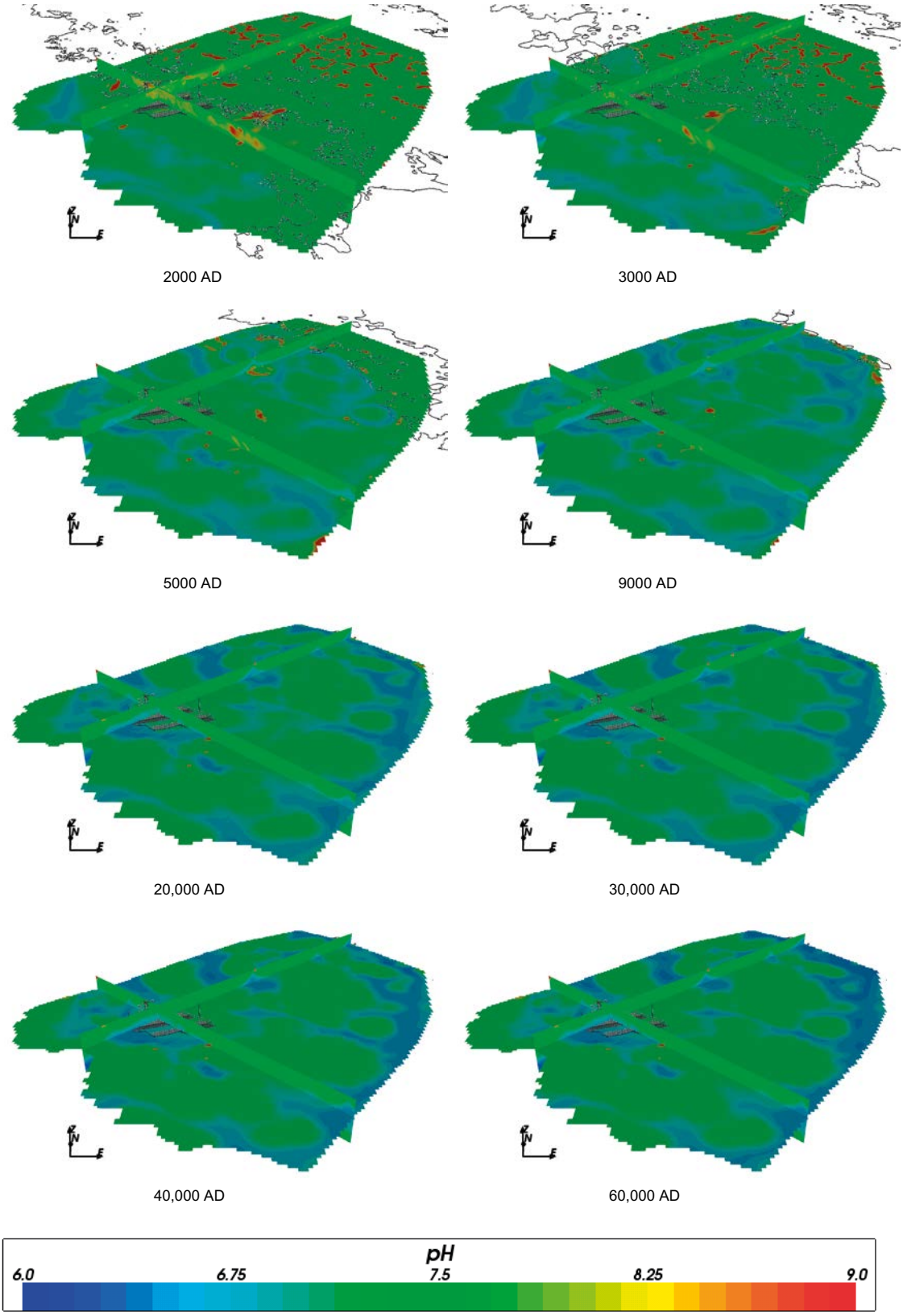


***Figure 4-71.*** *Values of pH on regional scale slices through the repository volume for Case 3 for time periods 2000 AD to 60,000 AD.*

### 4.4.2 Eh (or pe)

Figure 4-72 shows the value of Eh in the repository region and Figure 4-73 and Figure 4-74 show the value of pe at the deposition hole locations for Case 3. Figure 4-72 shows that the value of Eh rises over time due to infiltration of Altered Meteoric water (which has a higher Eh than the other waters), but flattens off after 30,000 AD. A similar pattern is seen for pe at the deposition hole locations in Figure 4-73 and Figure 4-74. These results are very similar to Case 2, although the values are slightly higher for Case 3.

Figure 4-75 shows regional slice plots of pe over time. The pe values are generally similar to Case 2, but with some higher pe values in some regions of the model. Redox reactions are very sensitive to the chemical conditions and so the higher pe values for Case 3 may be the results of numerical artefacts. In Salas et al. (2010) similar Eh values were reported for the different cases, although the case with iron (III) oxyhydroxide did show more spread in Eh values than the amorphous iron (II) sulphide case did, particularly at the high value end and this spread increased with time.

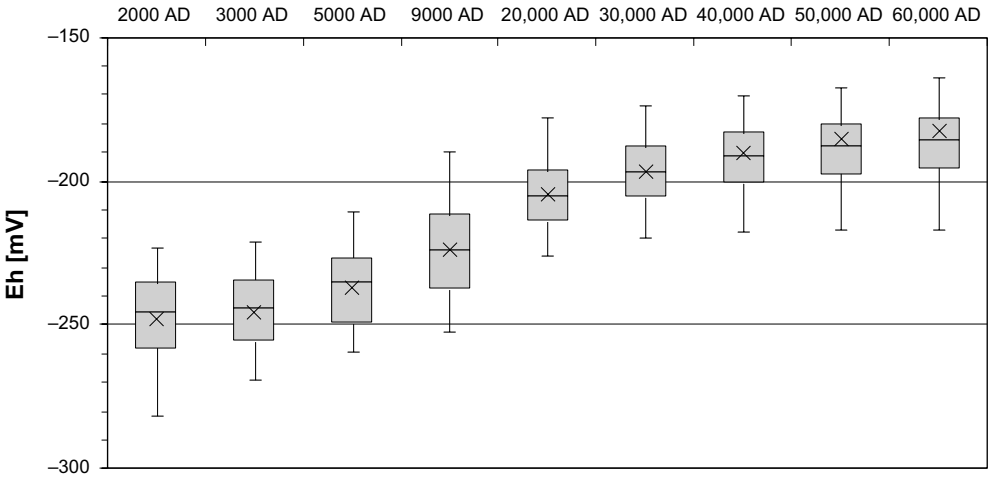


***Figure 4-72.*** *Box and whisker plot showing the statistical distribution of Eh for Case 3 on a regular grid of points within the repository volume between elevations –490 m and –450 m. The statistical measures are the median, the 25th and 75th percentiles (box), the mean (cross) and the 5th and 95th percentiles (whiskers).*

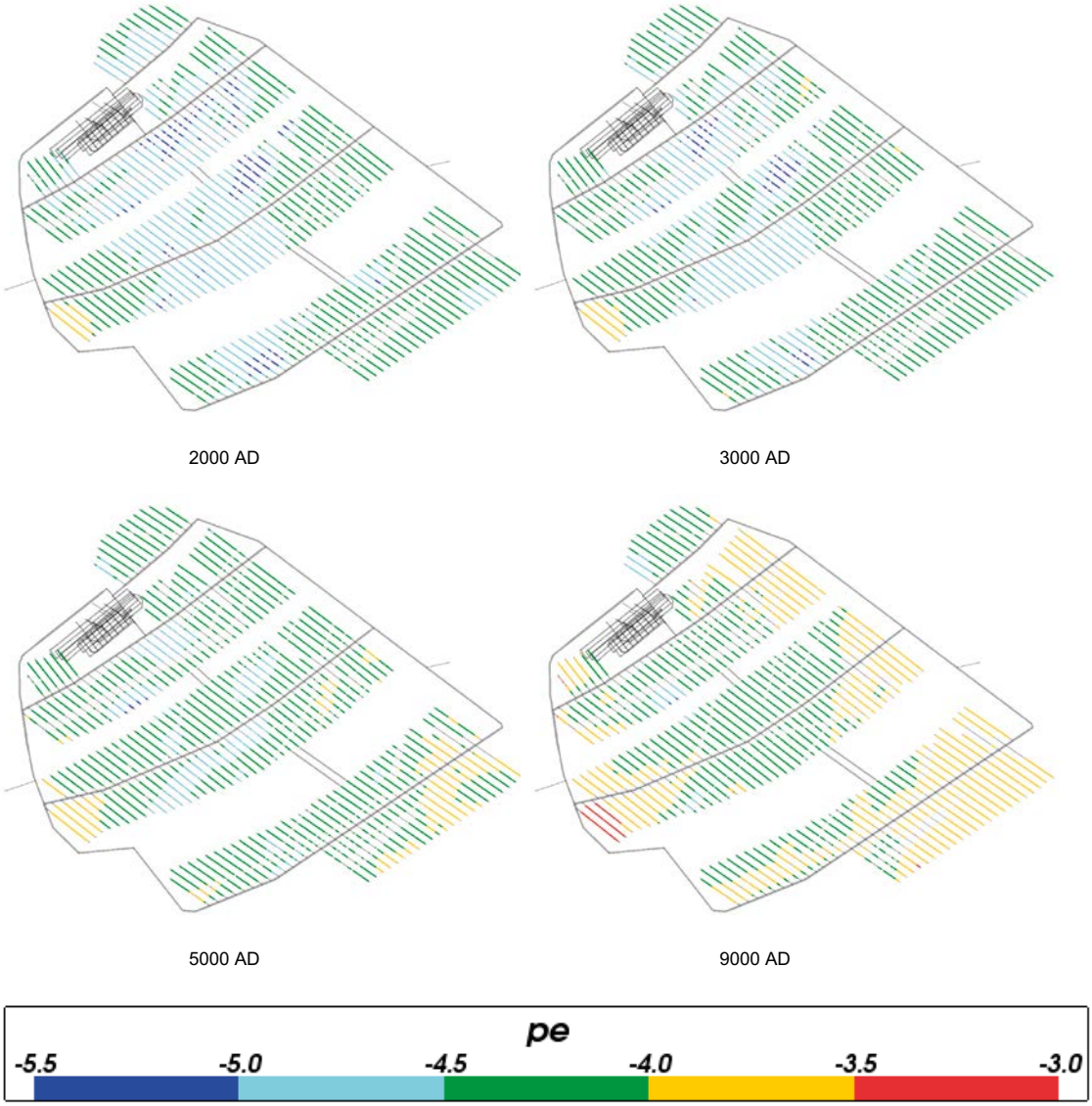


***Figure 4-73.*** *Values of pe for Case 3 at deposition hole locations for time periods 2000 AD to 9000 AD.*

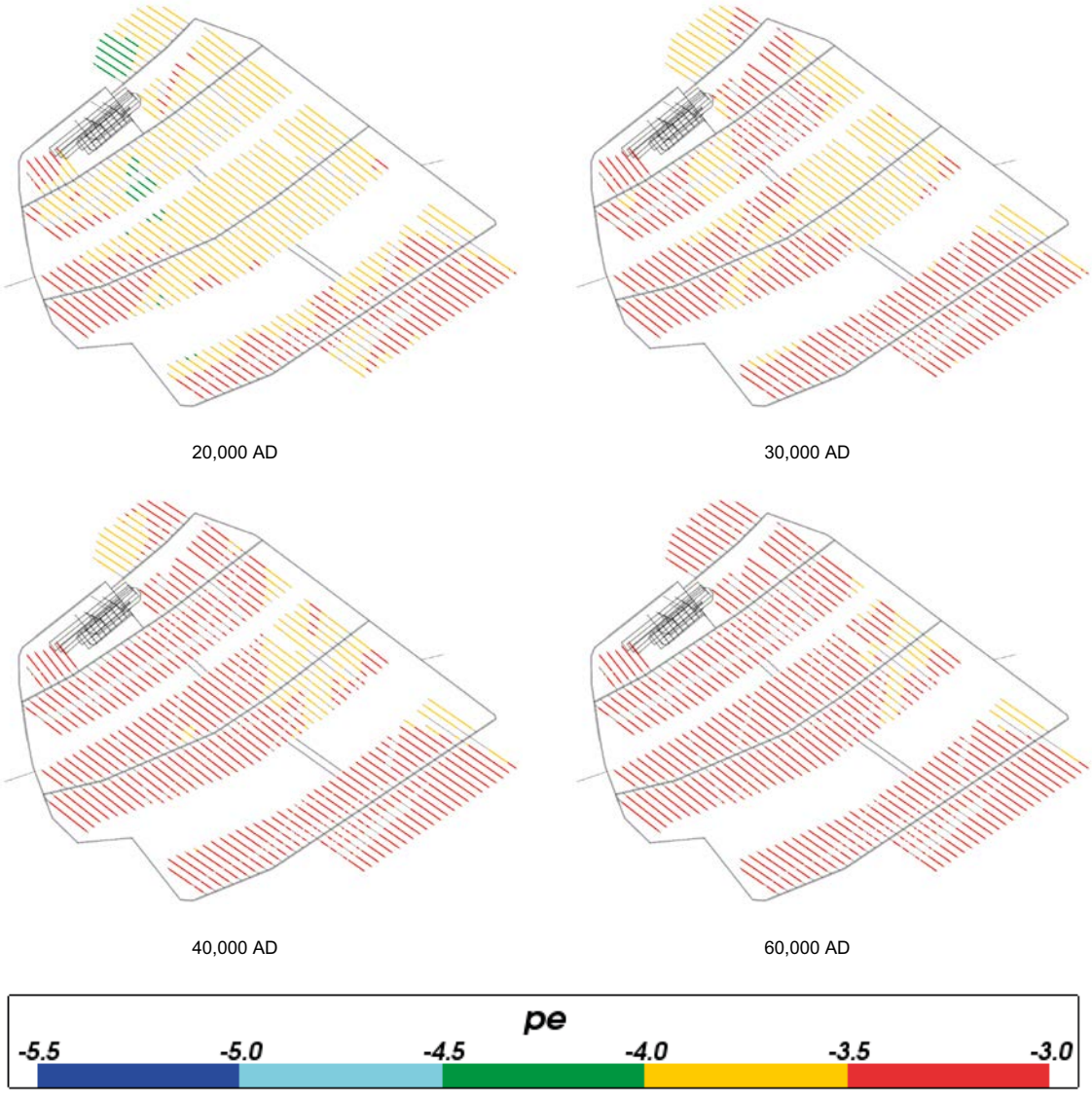


***Figure 4-74.*** *Values of pe for Case 3 at deposition hole locations for time periods 20,000 AD to 60,000 AD.*

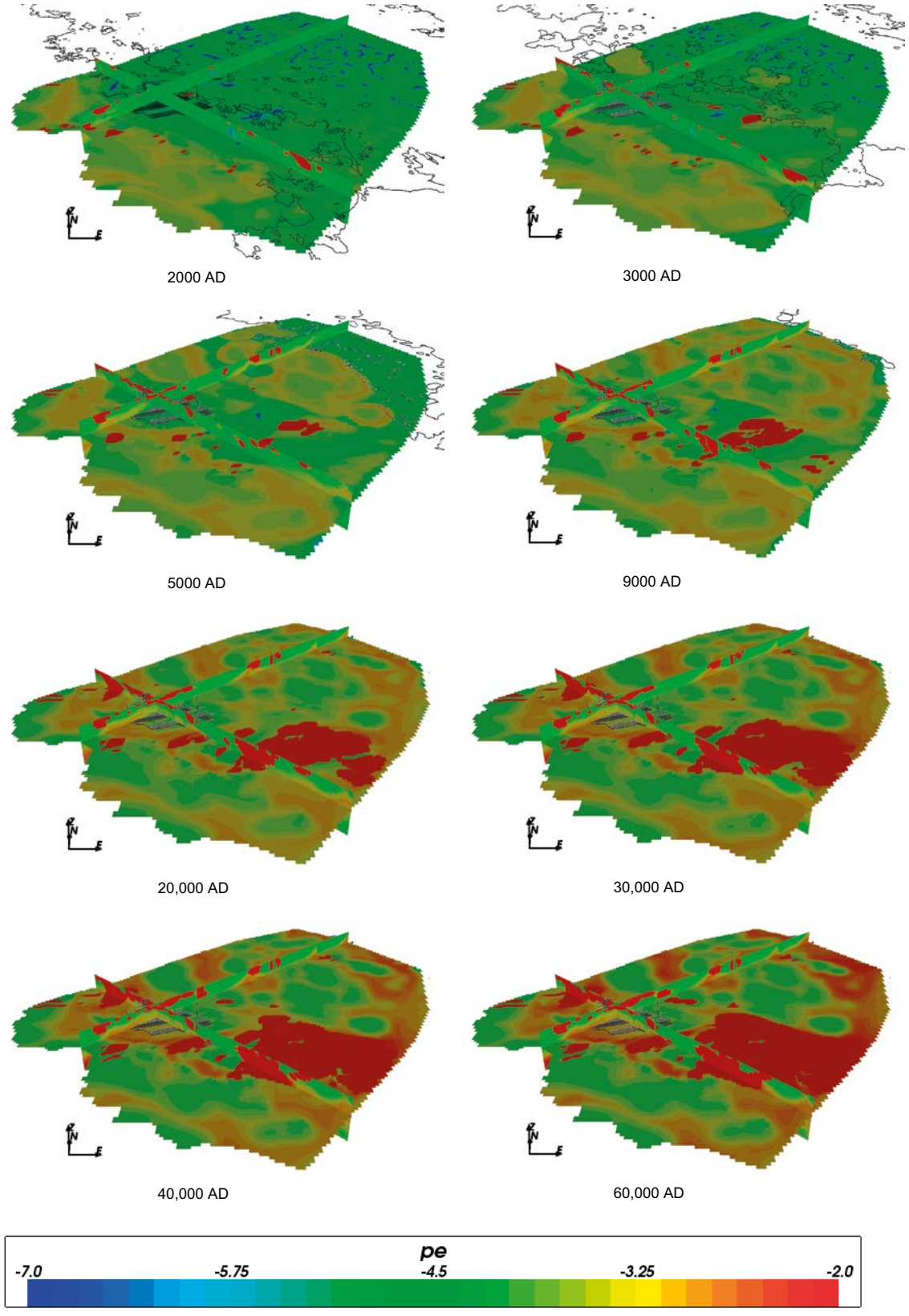


***Figure 4-75.*** *Values of pe on regional scale slices through the repository volume for Case 3 for time periods 2000 AD to 60,000 AD.*

### 4.4.3 TDS and sum of cations

Figure 4-76 and Figure 4-77 show the statistical distribution of TDS and the sum of cation charge molalities for Case 3. Both figures are almost identical to Case 2, decreasing gradually over time (due to the infiltration of dilute Altered Meteoric water) and levelling out at later times.

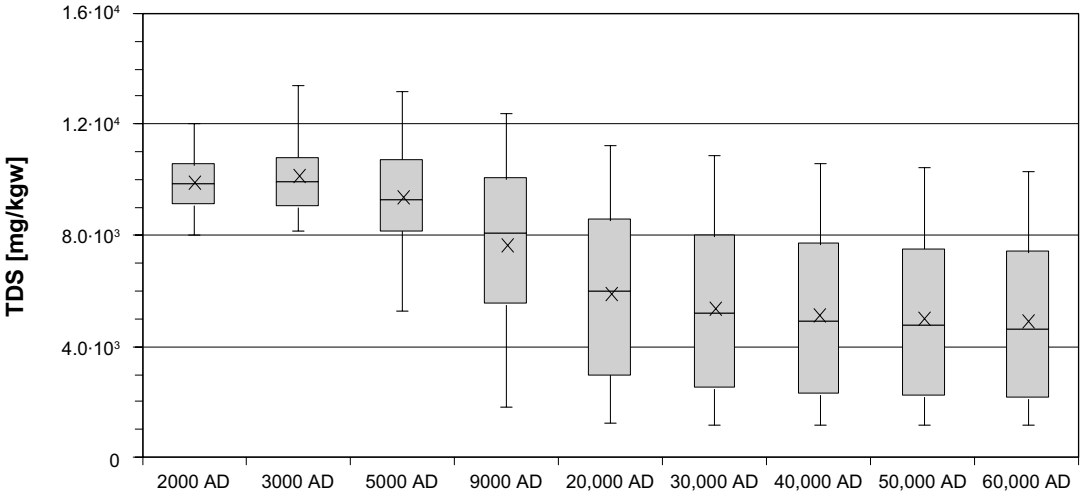


***Figure 4-76.*** *Box and whisker plot showing the statistical distribution of TDS for Case 3 on a regular grid of points within the repository volume between elevations –490 m and –450 m. The statistical measures are the median, the 25th and 75th percentiles (box), the mean (cross) and the 5th and 95th percentiles (whiskers).*

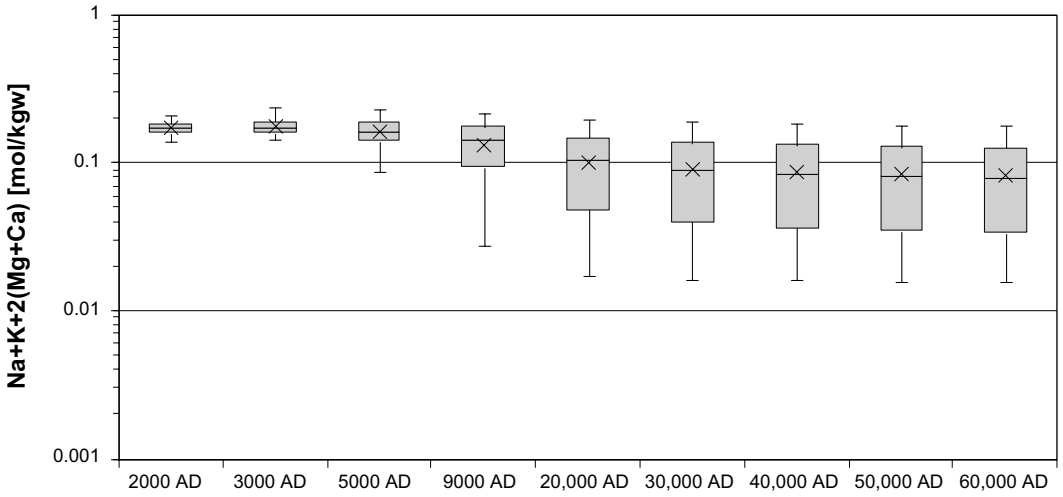


***Figure 4-77.*** *Box and whisker plot showing the statistical distribution of sum of cation charges (Na+K+2(Mg+Ca)) molalities for Case 3 on a regular grid of points within the repository volume between elevations –490 m and –450 m. The statistical measures are the median, the 25th and 75th percentiles (box), the mean (cross) and the 5th and 95th percentiles (whiskers).*

### 4.4.4 Inorganic carbon

Figure 4-78, Figure 4-79, Figure 4-80 and Figure 4-81 show plots of total inorganic carbon for Case 3. Again, the results are very similar to Case 2.

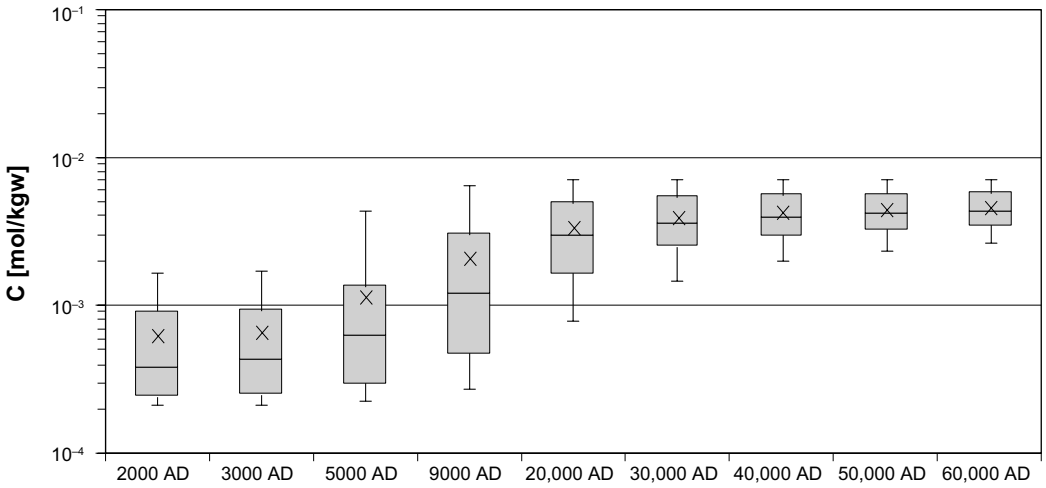


***Figure 4-78.*** *Box and whisker plot showing the statistical distribution of total inorganic carbon molalities for Case 3 on a regular grid of points within the repository volume between elevations –490 m and –450 m. The statistical measures are the median, the 25th and 75th percentiles (box), the mean (cross) and the 5th and 95th percentiles (whiskers).*

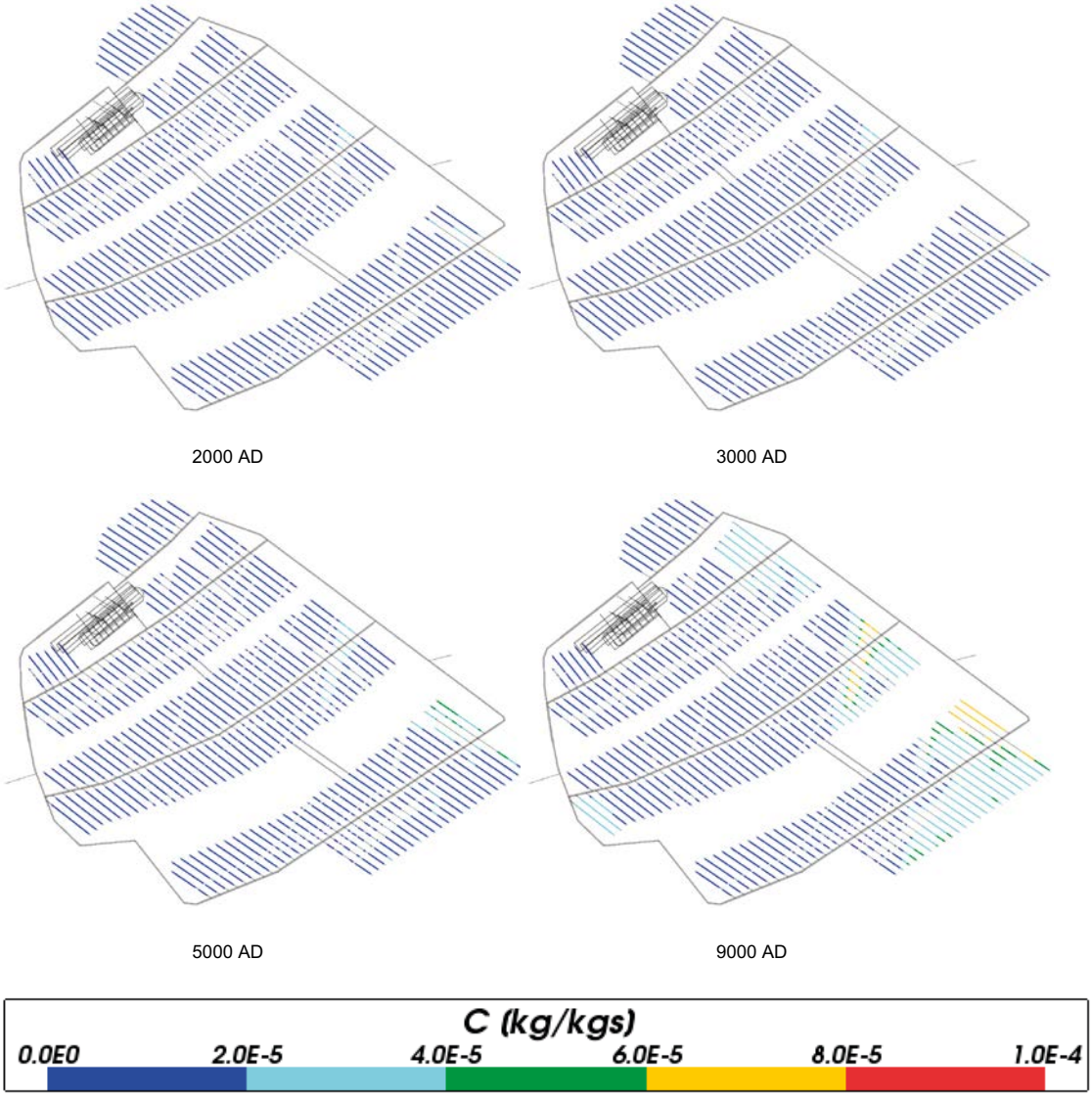


***Figure 4-79.*** *Total inorganic carbon mass fractions for Case 3 at deposition hole locations for time periods 2000 AD to 9000 AD.*

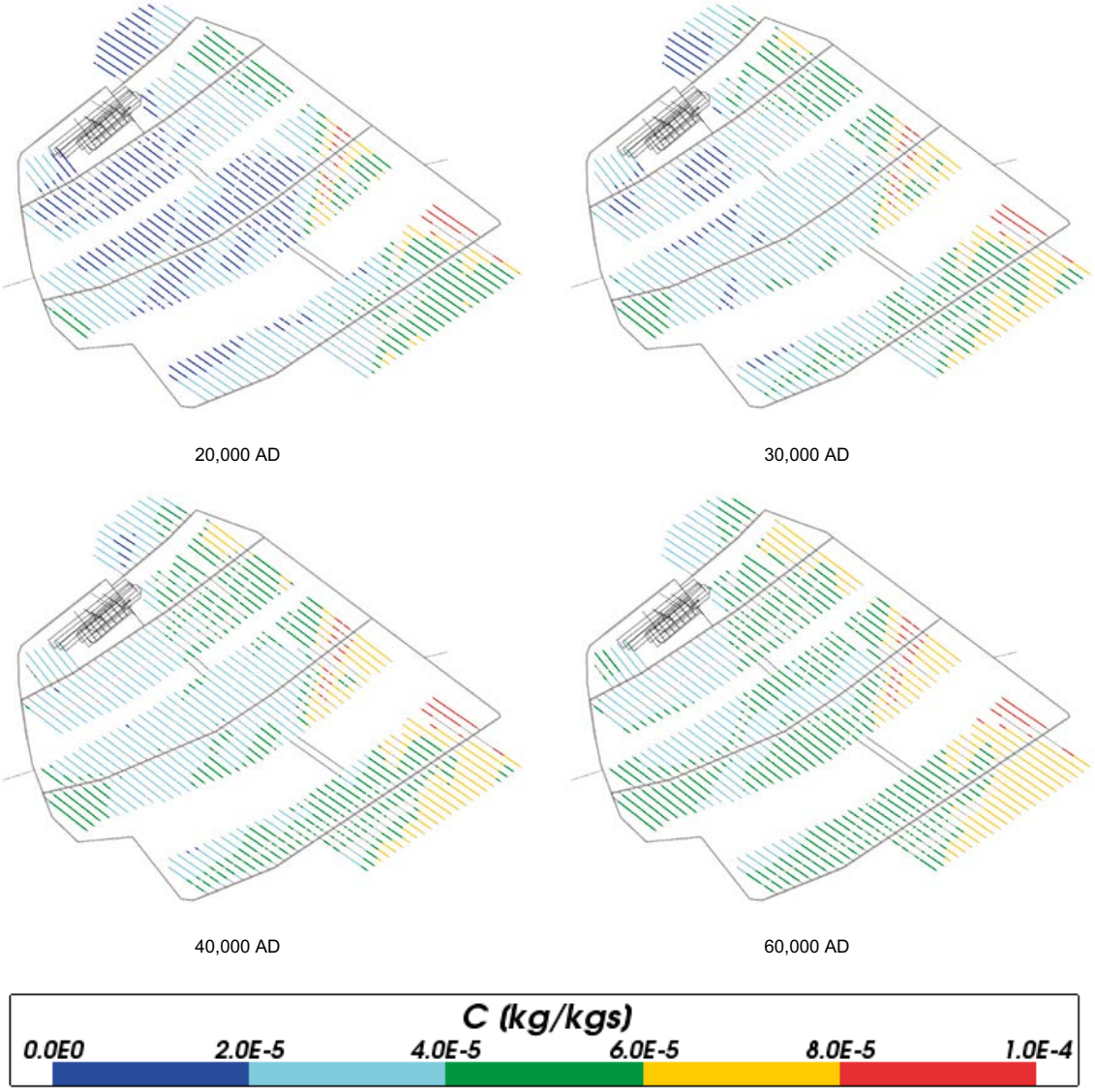


***Figure 4-80.*** *Total inorganic carbon mass fractions for Case 3 at deposition hole locations for time periods 20,000 AD to 60,000 AD.*

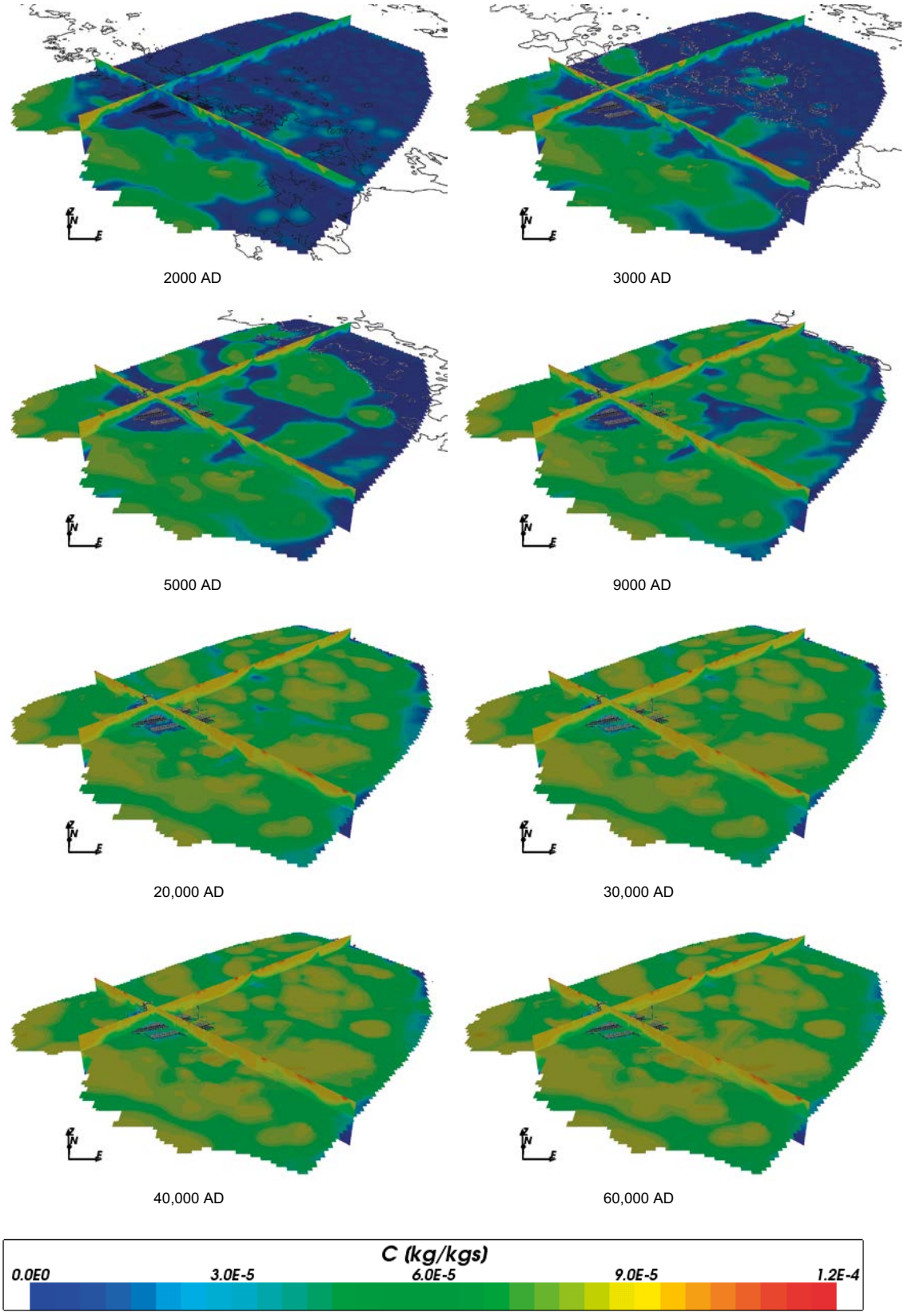


***Figure 4-81.*** *Total inorganic carbon mass fractions on regional scale slices through the repository volume for Case 3 for time periods 2000 AD to 60,000 AD.*

### 4.4.5 Calcium

The concentrations of total calcium both in the repository area and on the regional scale (shown in Figure 4-82 to Figure 4-85) are very similar to those seen in Case 2, which is to be expected given the two cases include the same reactions involving calcium (equilibration with calcite).

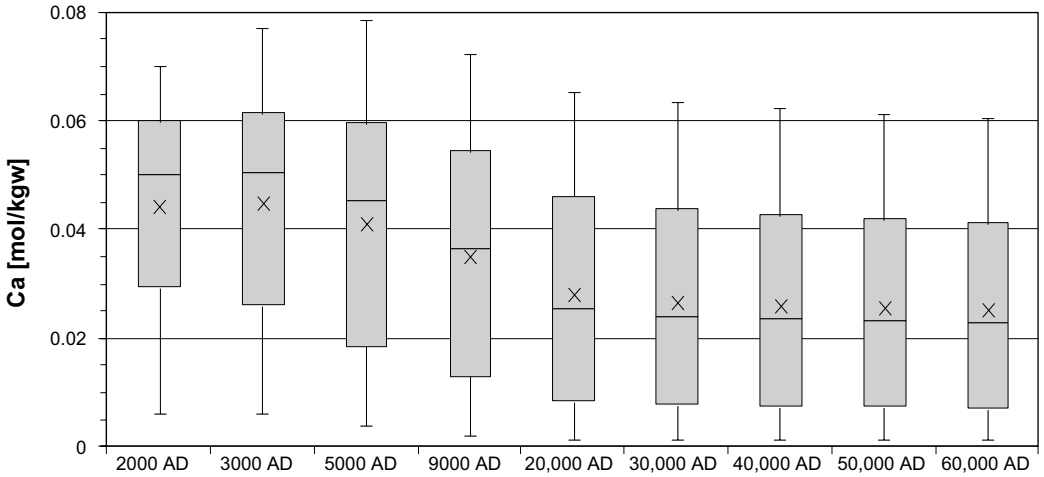


***Figure 4-82.*** *Box and whisker plot showing the statistical distribution of total calcium molalities for Case 3 on a regular grid of points within the repository volume between elevations –490 m and –450 m. The statistical measures are the median, the 25$^{th}$ and 75$^{th}$ percentiles (box), the mean (cross) and the 5$^{th}$ and 95$^{th}$ percentiles (whiskers).*

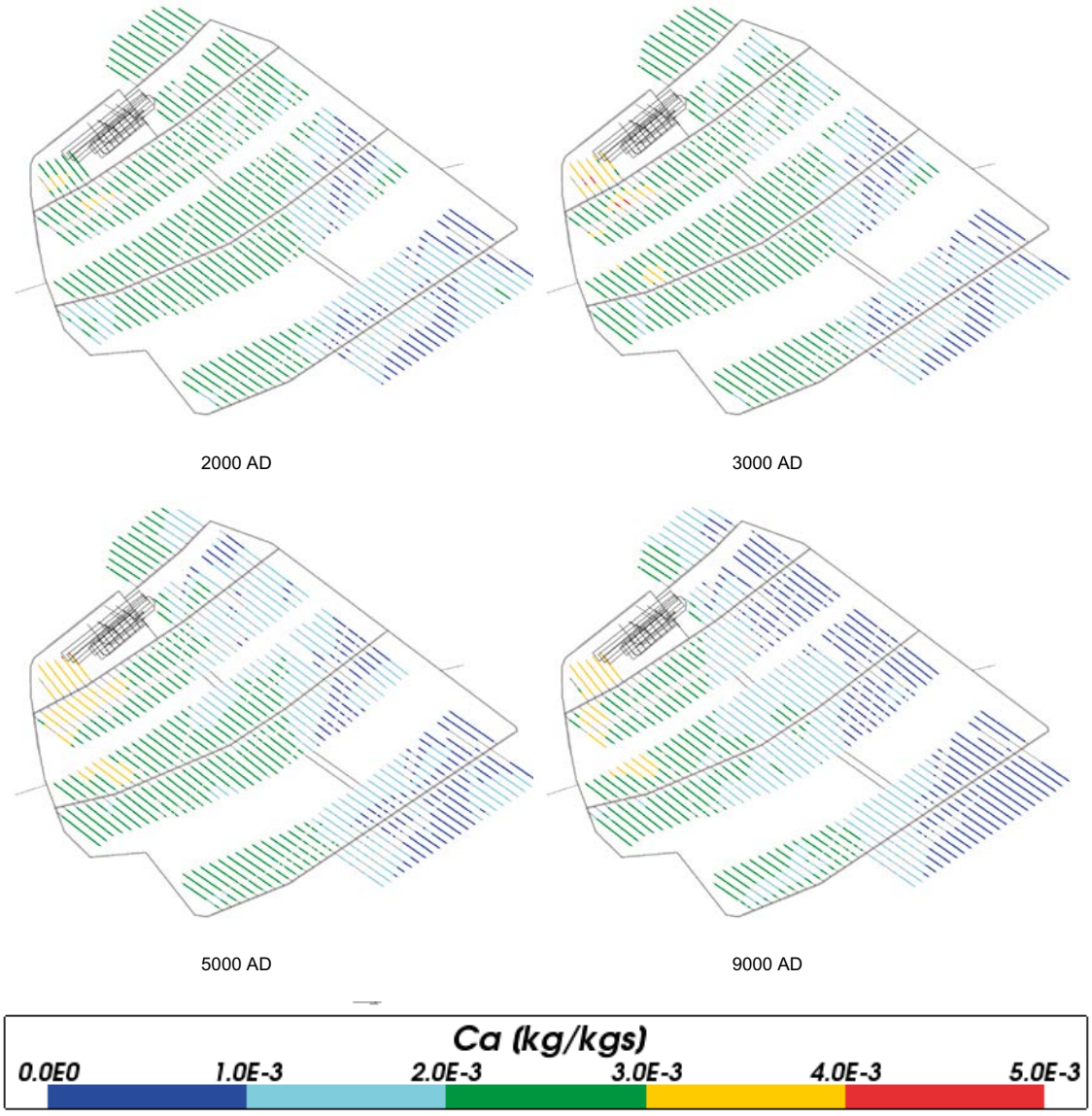


***Figure 4-83.*** *Total calcium mass fractions for Case 3 at deposition hole locations for time periods 2000 AD to 9000 AD.*

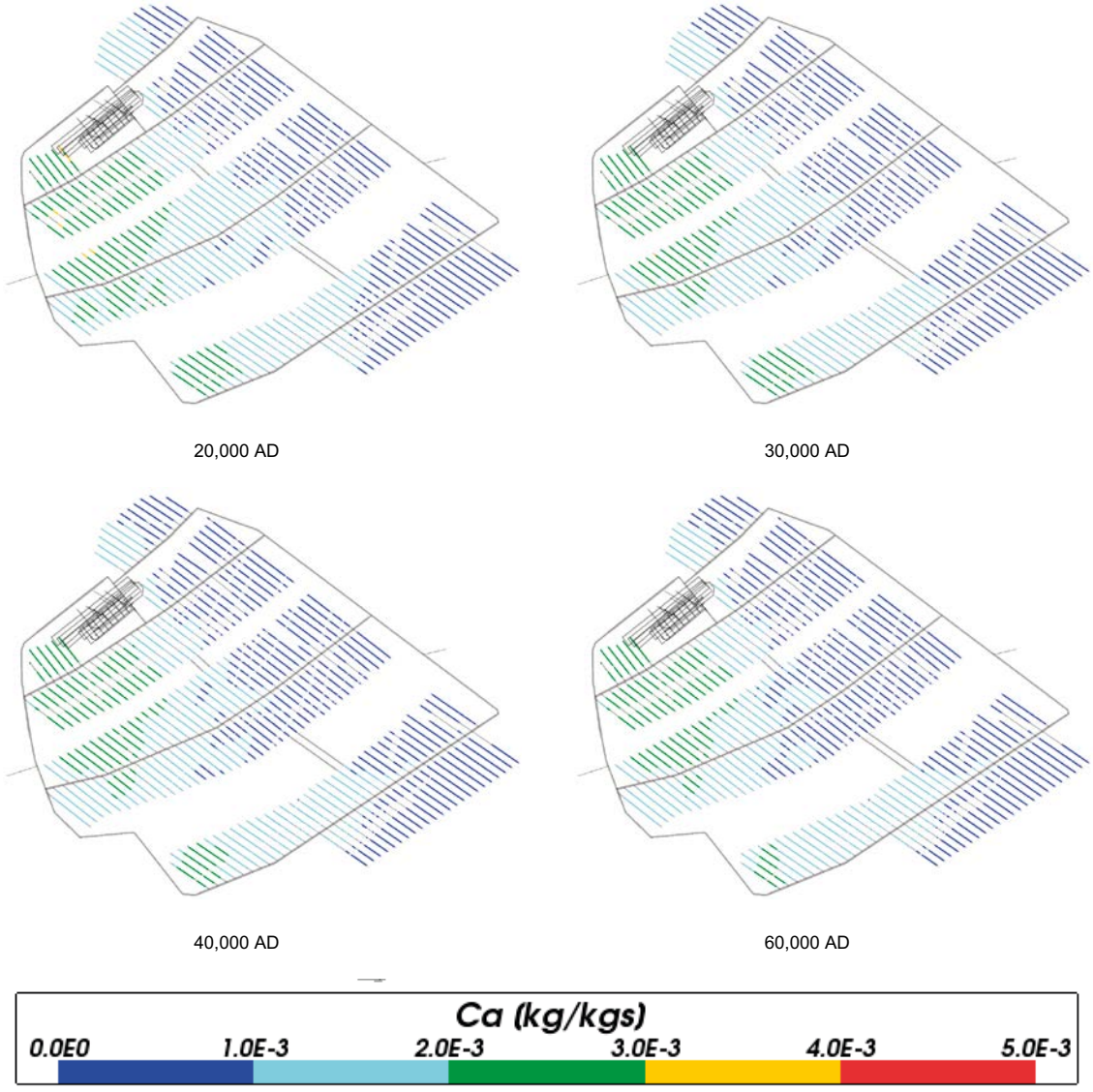


***Figure 4-84.*** *Total calcium mass fractions for Case 3 at deposition hole locations for time periods 20,000 AD to 60,000 AD.*

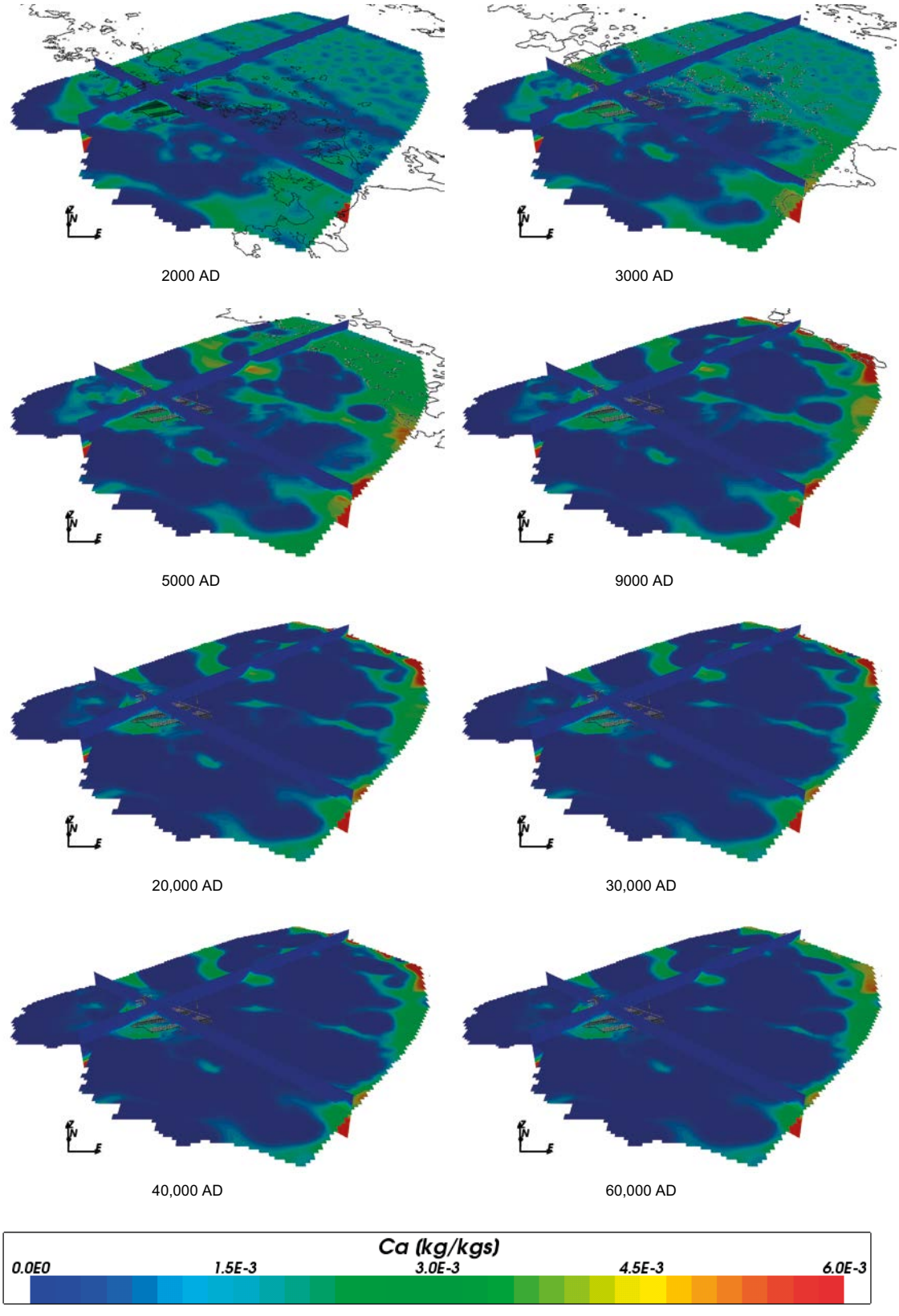


***Figure 4-85.*** *Total calcium mass fractions on regional scale slices through the repository volume for Case 3 for time periods 2000 AD to 60,000 AD.*

### 4.4.6 Chloride

Figure 4-86 to Figure 4-89 show the chloride concentrations around the repository and in the regional area. Since chloride is non-reacting, the results are very similar to Case 1 and Case 2.

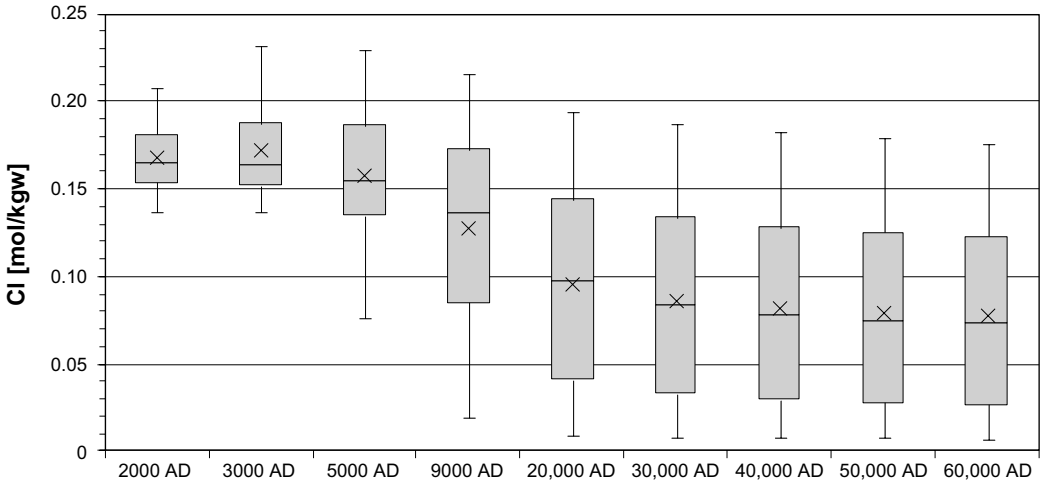


***Figure 4-86.*** *Box and whisker plot showing the statistical distribution of total chloride molalities for Case 3 on a regular grid of points within the repository volume between elevations –490 m and –450 m. The statistical measures are the median, the 25$^{th}$ and 75$^{th}$ percentiles (box), the mean (cross) and the 5$^{th}$ and 95$^{th}$ percentiles (whiskers).*

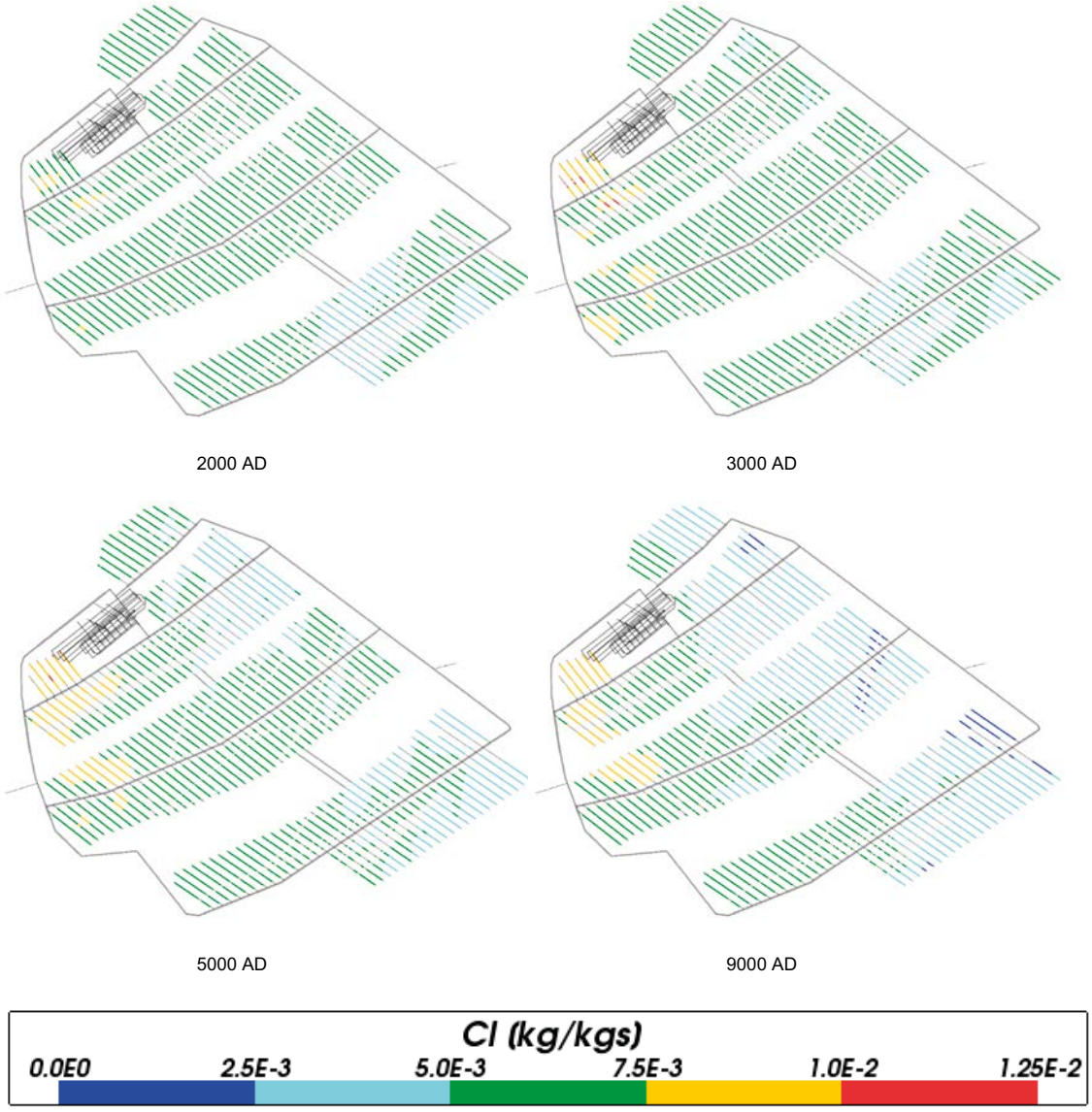


***Figure 4-87.*** *Total chloride mass fractions for Case 3 at deposition hole locations for time periods 2000 AD to 9000 AD.*

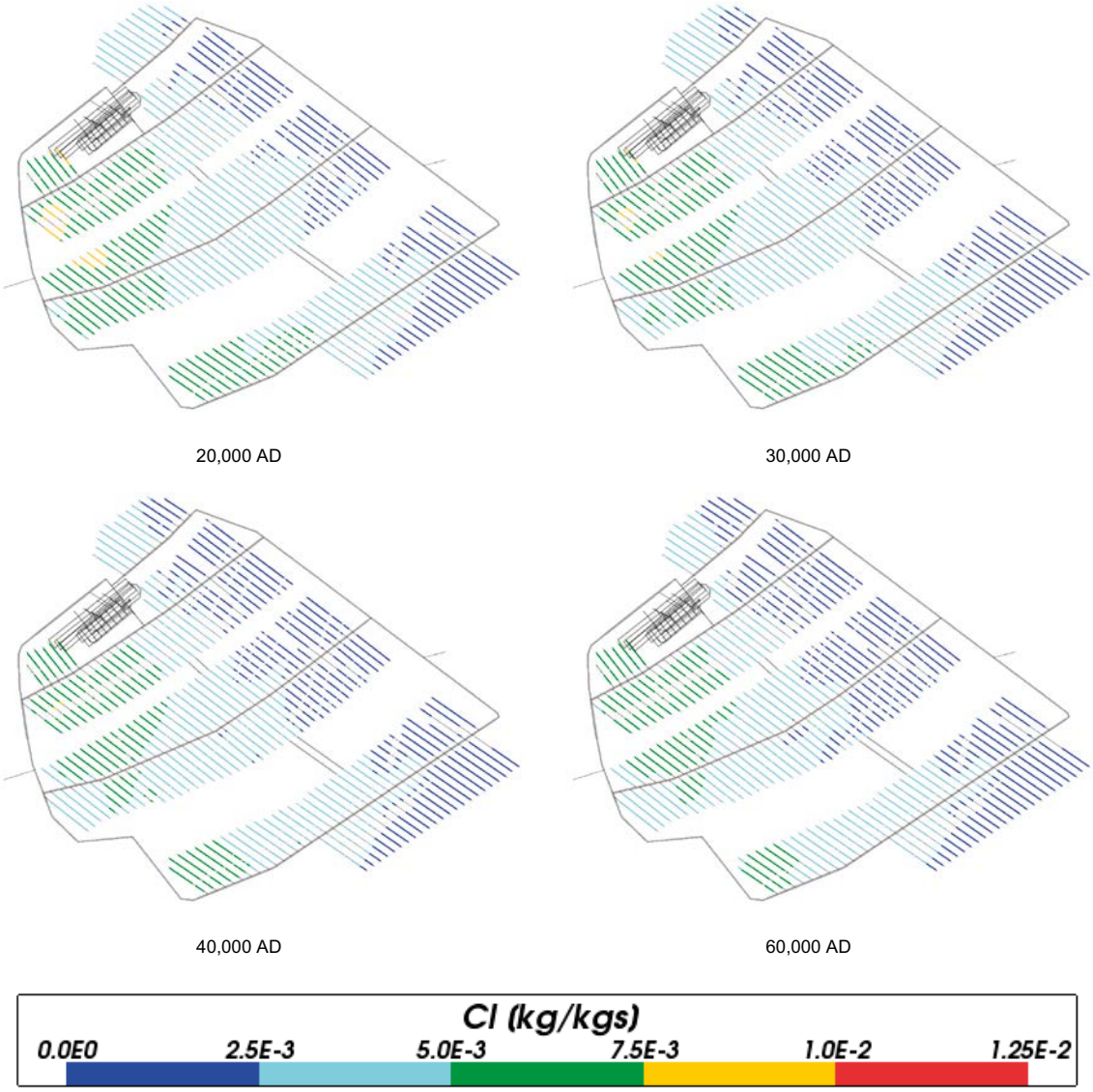


***Figure 4-88.*** *Total chloride mass fractions for Case 3 at deposition hole locations for time periods 20,000 AD to 60,000 AD.*

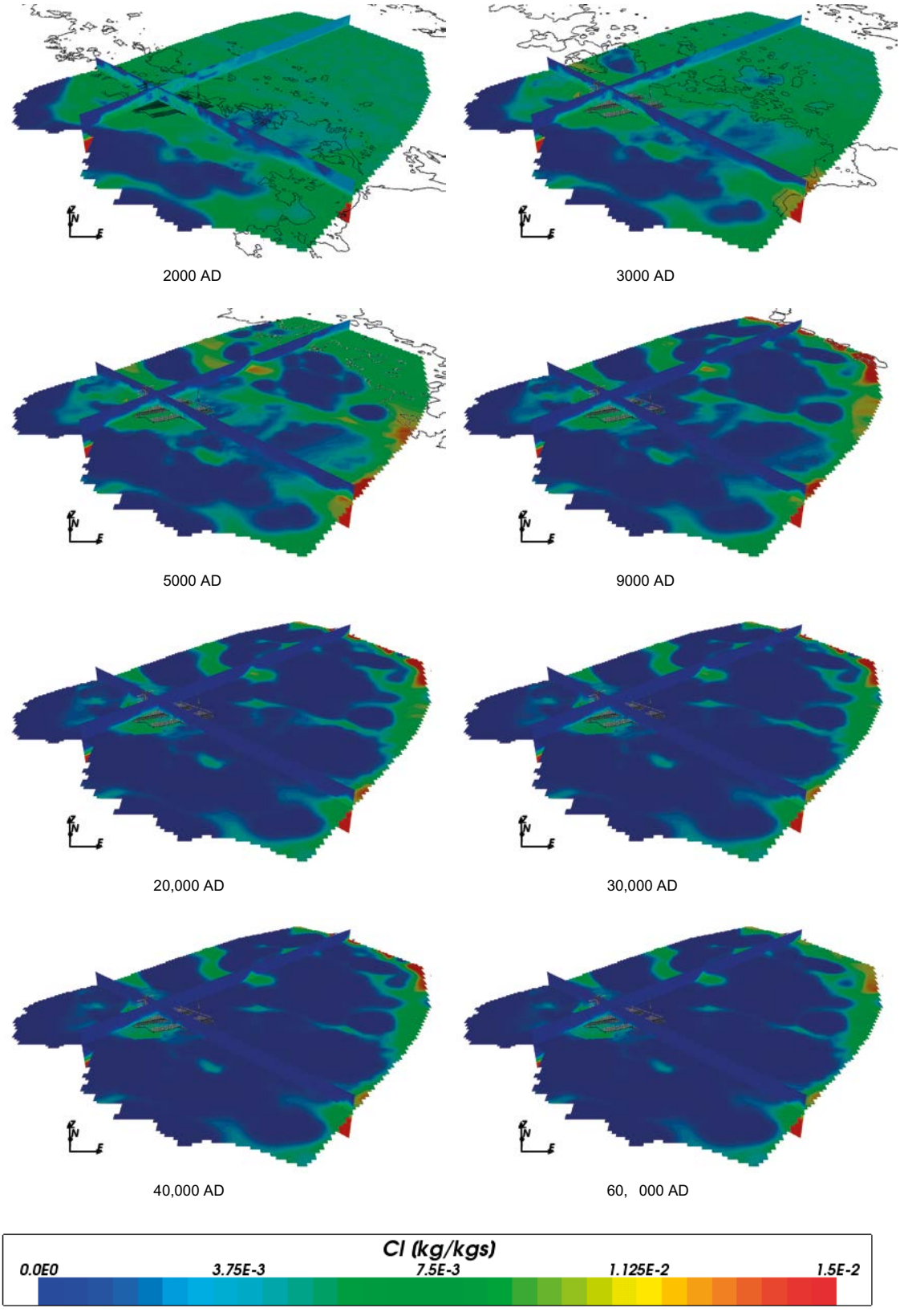


***Figure 4-89.*** *Total chloride mass fractions on regional scale slices through the repository volume for Case 3 for time periods 2000 AD to 60,000 AD.*

### 4.4.7 Iron

The concentrations of total iron around the repository shown in Figure 4-90, Figure 4-91 and Figure 4-92 for Case 3 are more different from the Case 2 results than for other species. This is not unexpected given that the two cases have different reactions involving iron. The Case 3 results have higher iron concentrations at earlier times and they do not vary as much with time, although the spread of values increases with time. This difference is also apparent at the regional scale, as shown in Figure 4-93.

By contrast, Salas et al. (2010) calculate lower iron concentrations for the Case 3 reactions (iron (III) oxyhydroxide) rather than for the Case 2 reactions (amorphous iron (II) sulphide), although the spread of values is higher for iron (III) oxyhydroxide, like the Case 3 results reported here. It should be noted that the iron concentrations are very low and that redox reactions, and hence the iron concentrations, are very sensitive to numerical variation (such as round-off) and to the hydrogeochemical environment so obtaining consistent results between the cases is difficult. Nevertheless, the iron concentrations are all around $1.0 \cdot 10^{-5}$ mol/L for Case 2, Case 3 and the results in Salas et al. (2010). This is in contrast to Case 1 with median values closer to $1.0 \cdot 10^{-6}$ mol/L.

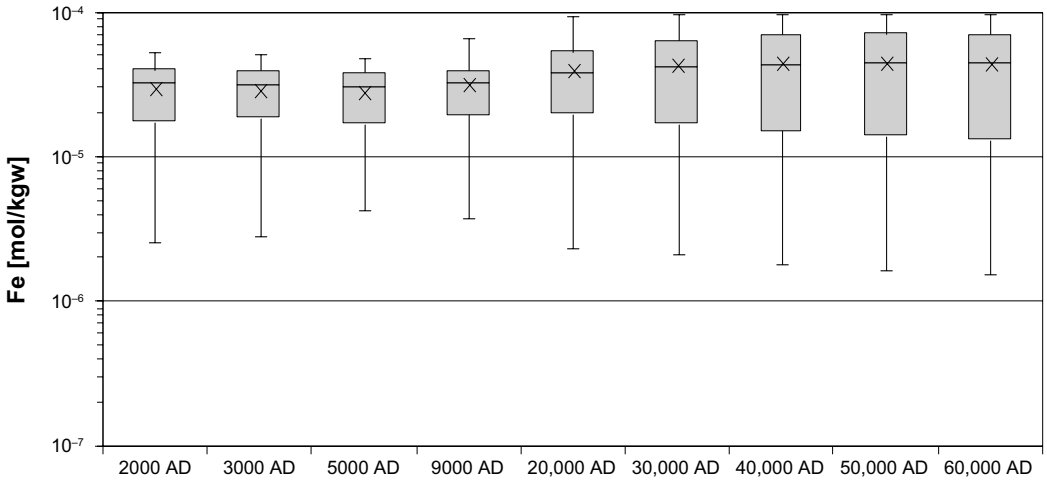


***Figure 4-90.*** *Box and whisker plot showing the statistical distribution of total iron molalities for Case 3 on a regular grid of points within the repository volume between elevations –490 m and –450 m. The statistical measures are the median, the 25th and 75th percentiles (box), the mean (cross) and the 5th and 95th percentiles (whiskers).*

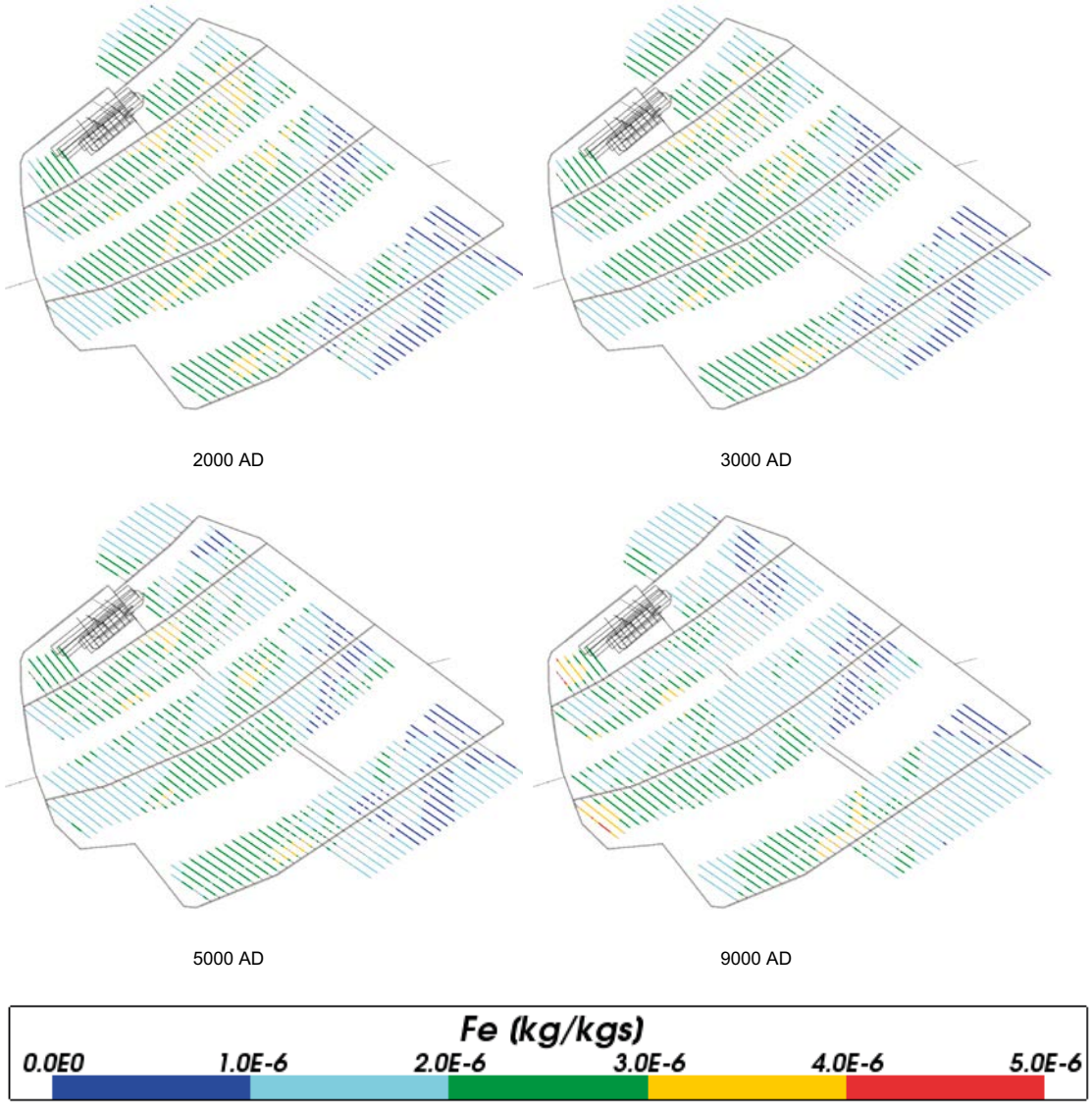


***Figure 4-91.*** *Total iron mass fractions for Case 3 at deposition hole locations for time periods 2000 AD to 9000 AD.*

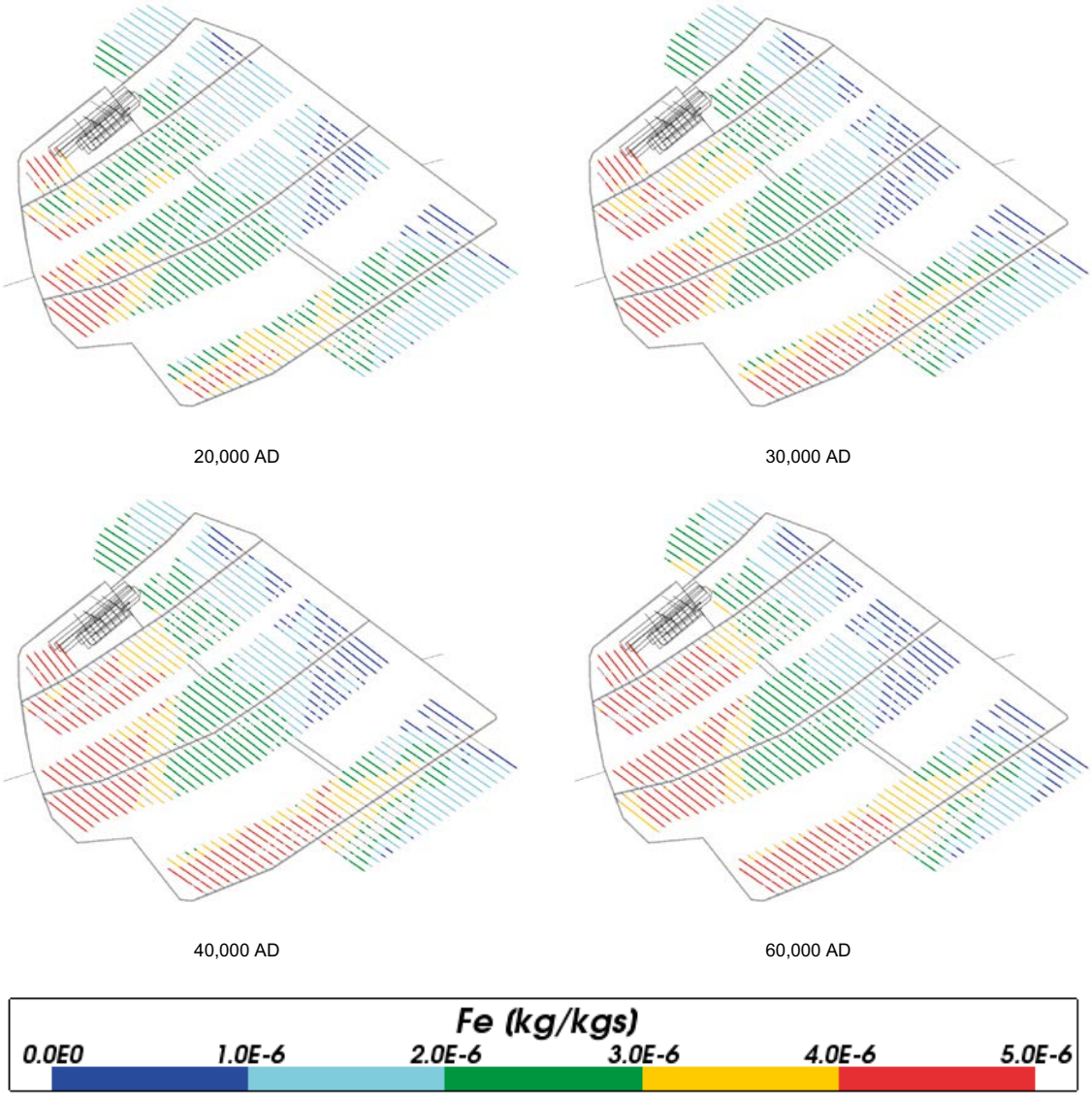


***Figure 4-92.*** *Total iron mass fractions for Case 3 at deposition hole locations for time periods 20,000 AD to 60,000 AD.*

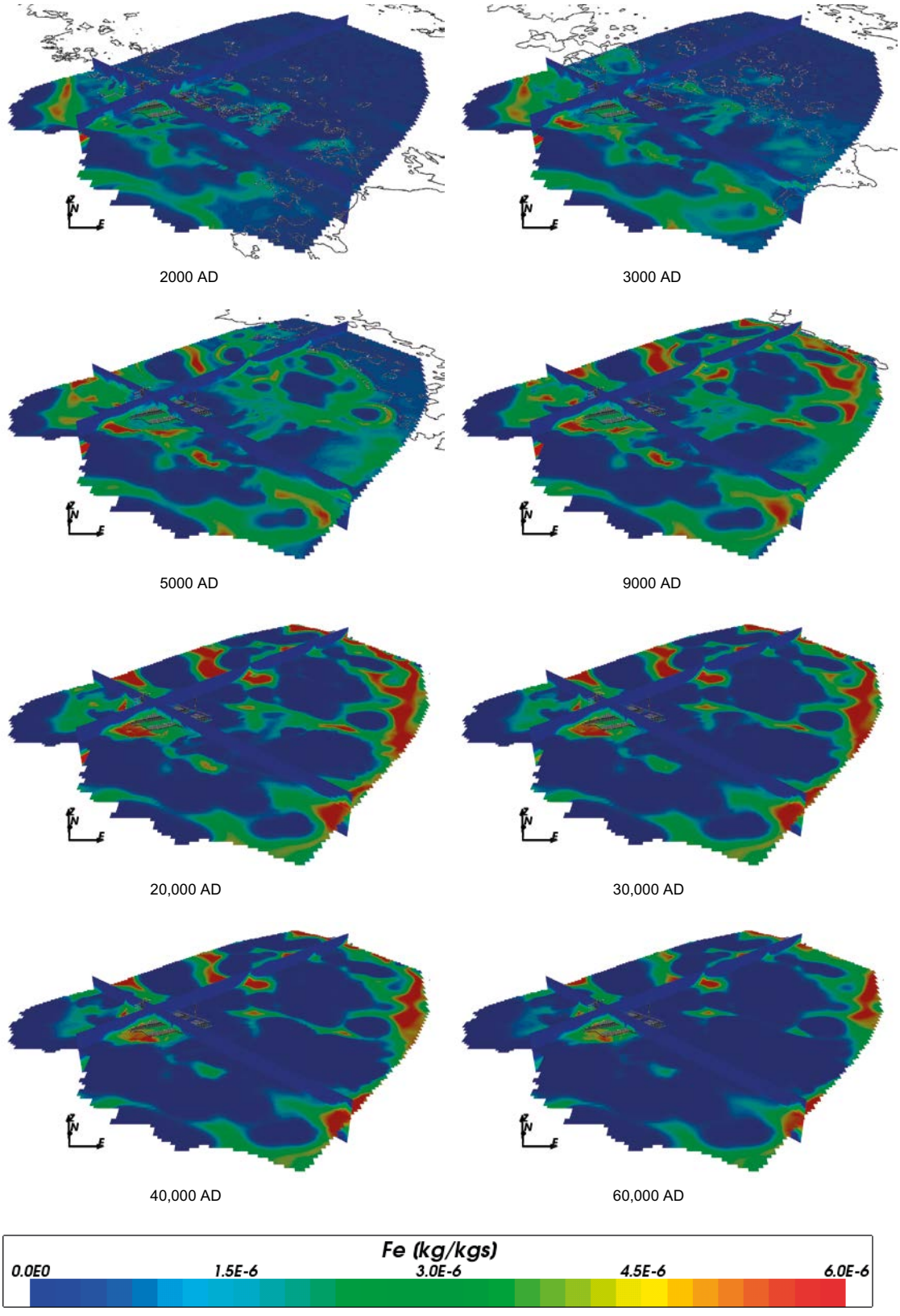


***Figure 4-93.*** *Total iron mass fractions on regional scale slices through the repository volume for Case 3 for time periods 2000 AD to 60,000 AD.*

### 4.4.8 Sodium

The concentration of sodium (Figure 4-94, Figure 4-95, Figure 4-96 and Figure 4-97) is again very similar to Case 1 and Case 2 as this is a non-reacting species for these cases.

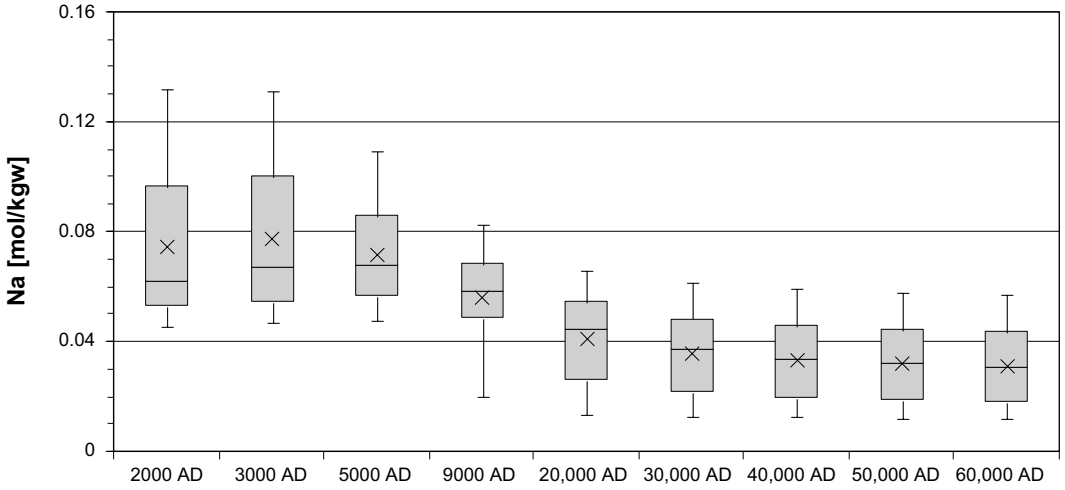


***Figure 4-94.*** *Box and whisker plot showing the statistical distribution of total sodium molalities for Case 3 on a regular grid of points within the repository volume between elevations –490 m and –450 m. The statistical measures are the median, the 25$^{th}$ and 75$^{th}$ percentiles (box), the mean (cross) and the 5$^{th}$ and 95$^{th}$ percentiles (whiskers).*

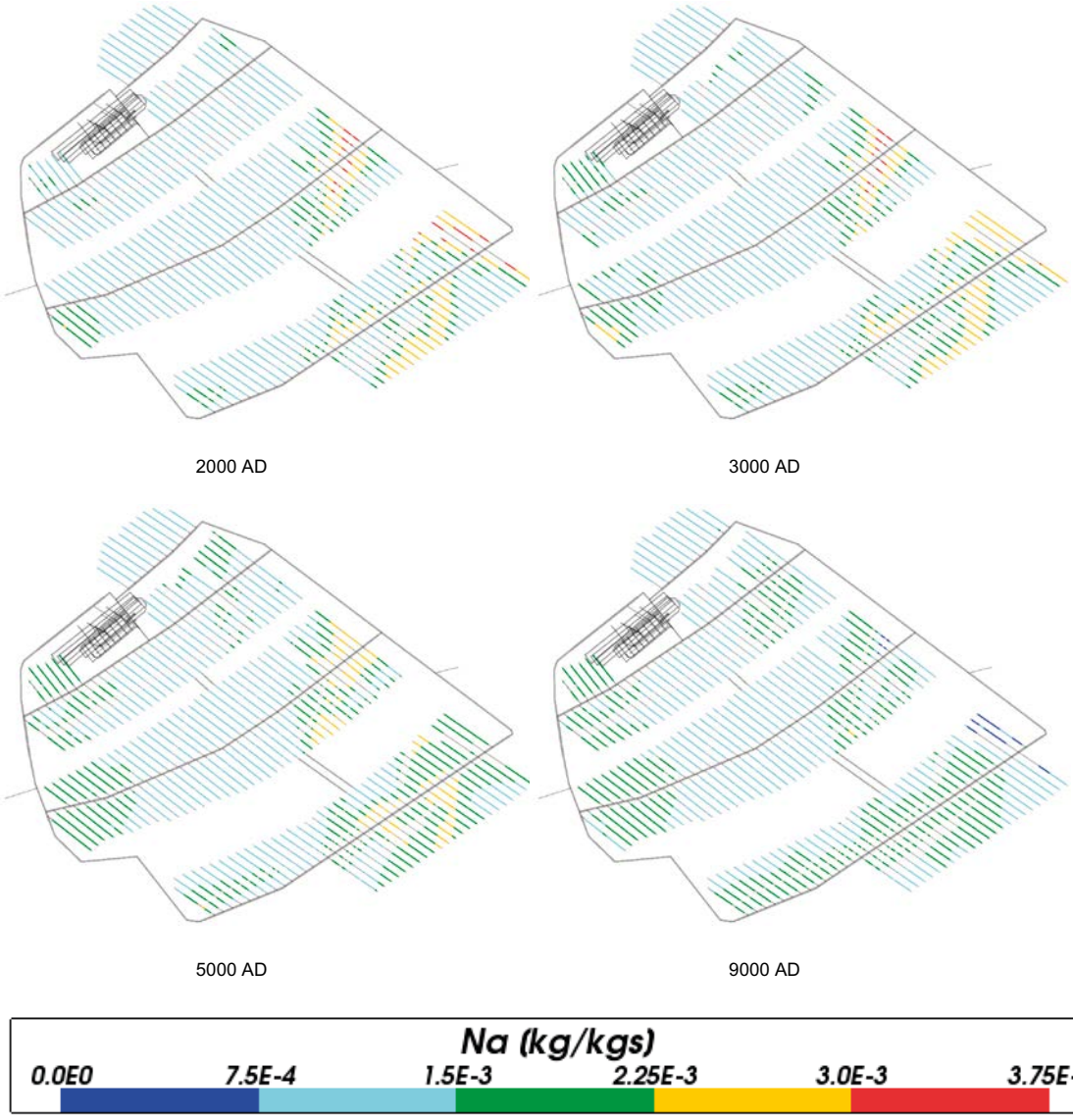


***Figure 4-95.*** *Total sodium mass fractions for Case 3 at deposition hole locations for time periods 2000 AD to 9000 AD.*

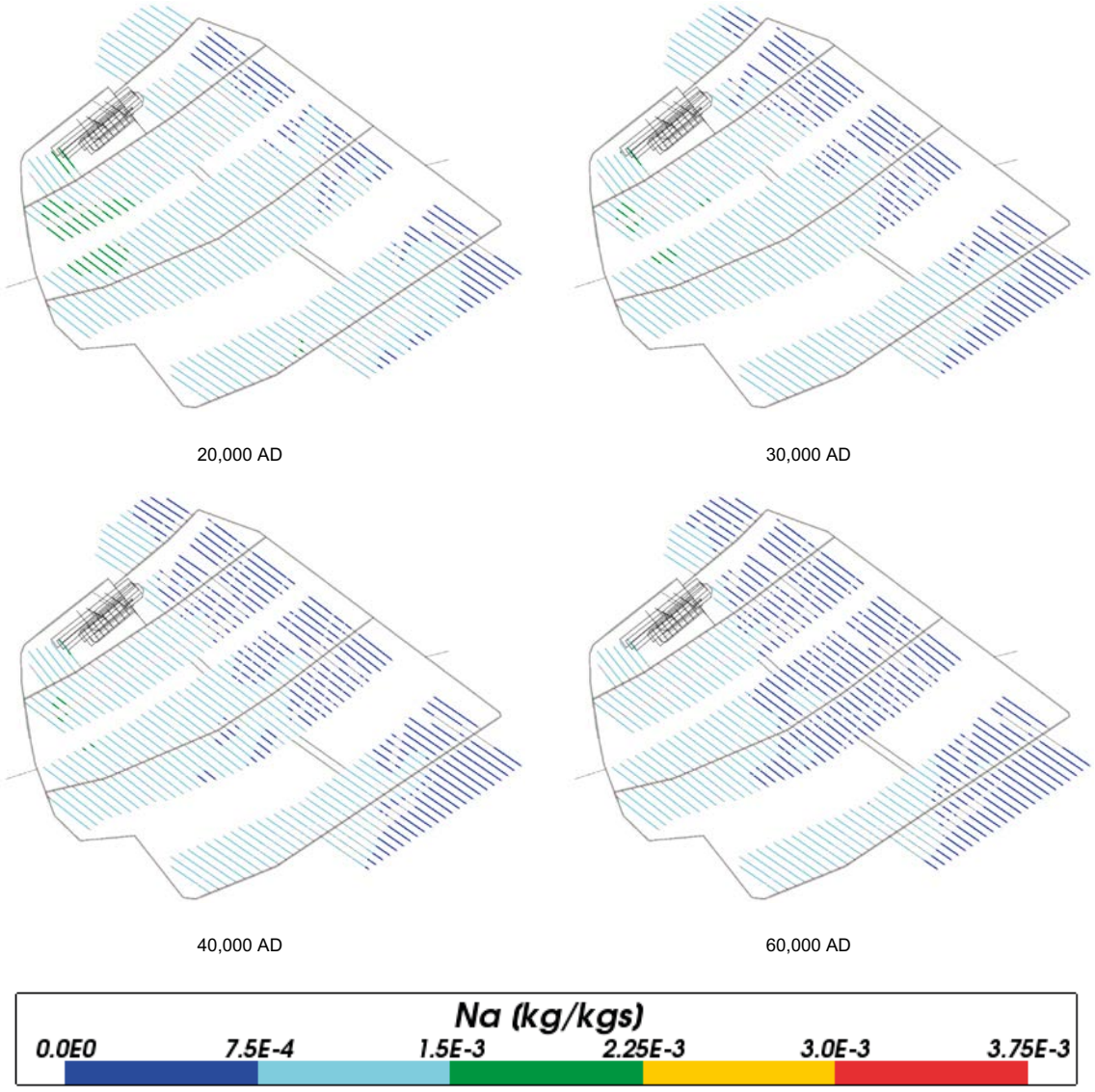


***Figure 4-96.*** *Total sodium mass fractions for Case 3 at deposition hole locations for time periods 20,000 AD to 60,000 AD.*

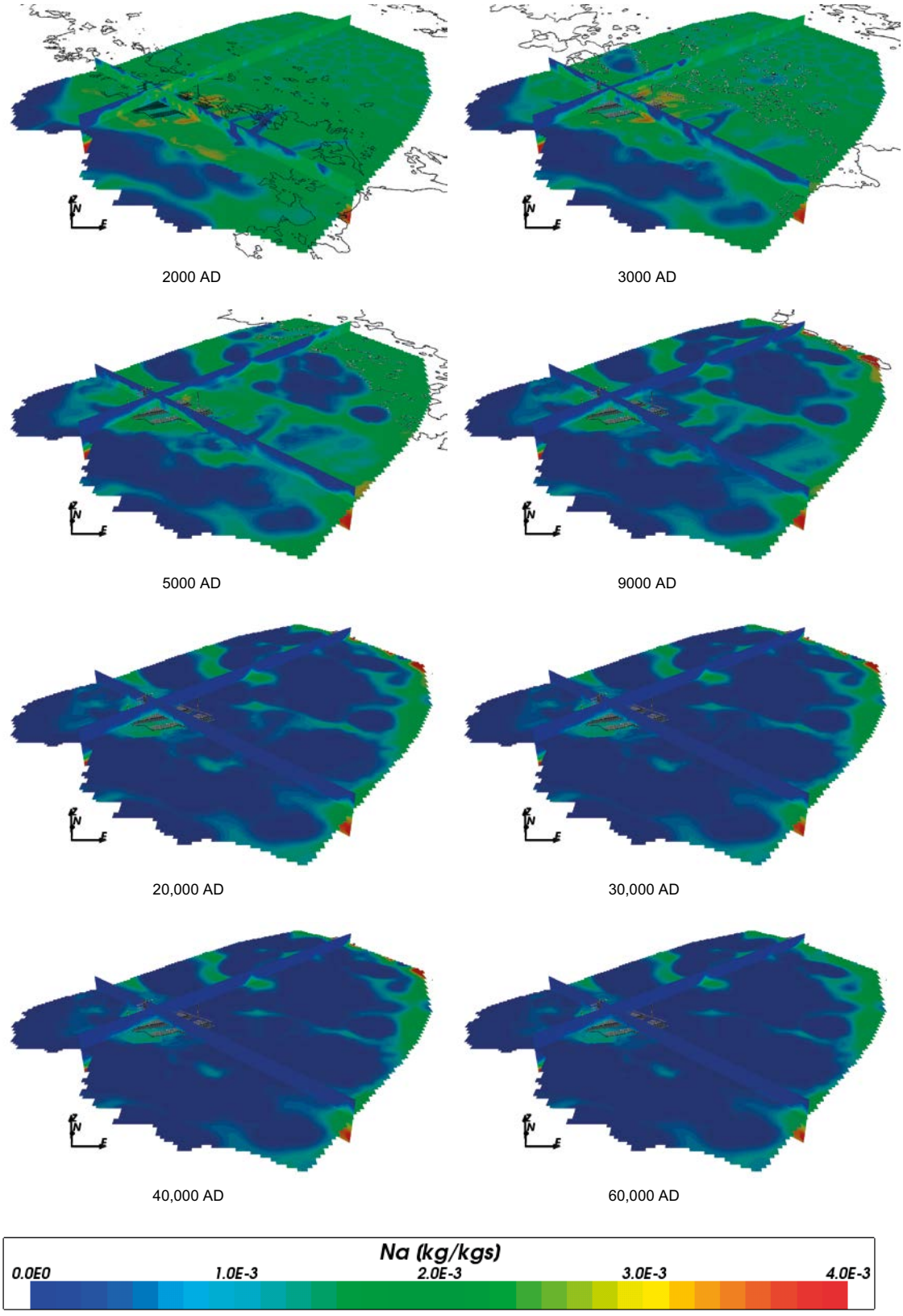


***Figure 4-97.*** *Total sodium mass fractions on regional scale slices through the repository volume for Case 3 for time periods 2000 AD to 60,000 AD.*

### 4.4.9 Potassium

The concentration of potassium (Figure 4-98 to Figure 4-101) is almost identical to Case 2. This is to be expected since potassium is not involved in the chemical reactions for Case 2 and Case 3.

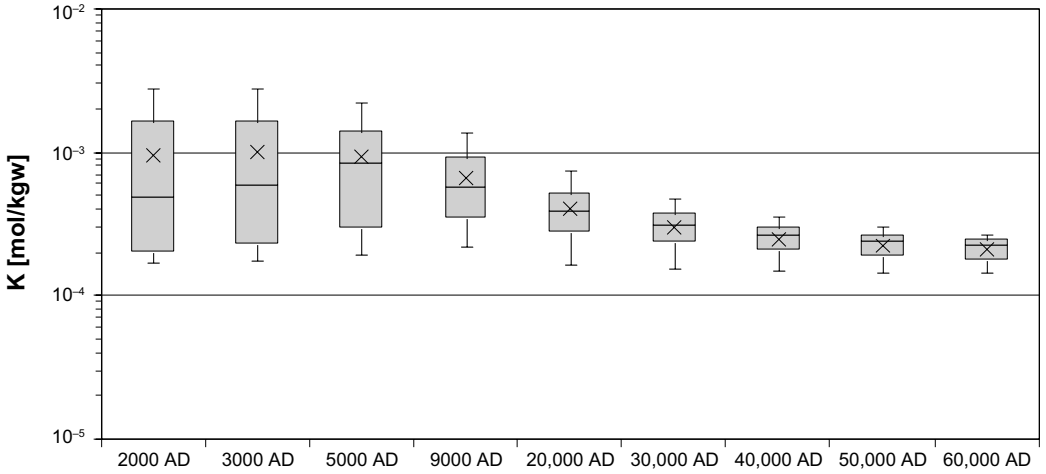


***Figure 4-98.*** *Box and whisker plot showing the statistical distribution of total potassium molalities for Case 3 on a regular grid of points within the repository volume between elevations –490 m and –450 m. The statistical measures are the median, the 25th and 75th percentiles (box), the mean (cross) and the 5th and 95th percentiles (whiskers).*

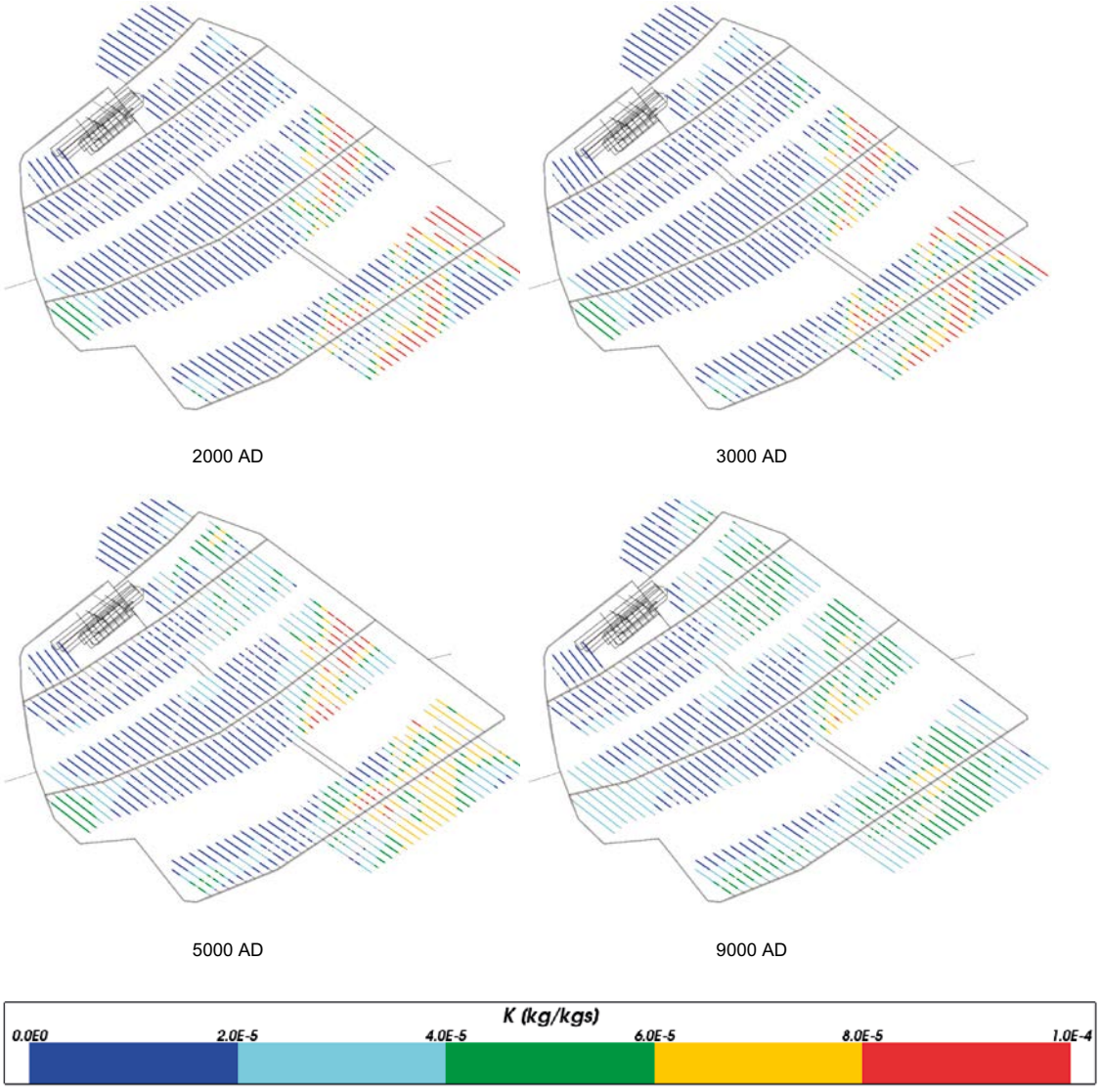


***Figure 4-99.*** *Total potassium mass fractions for Case 3 at deposition hole locations for time periods 2000 AD to 9000 AD.*

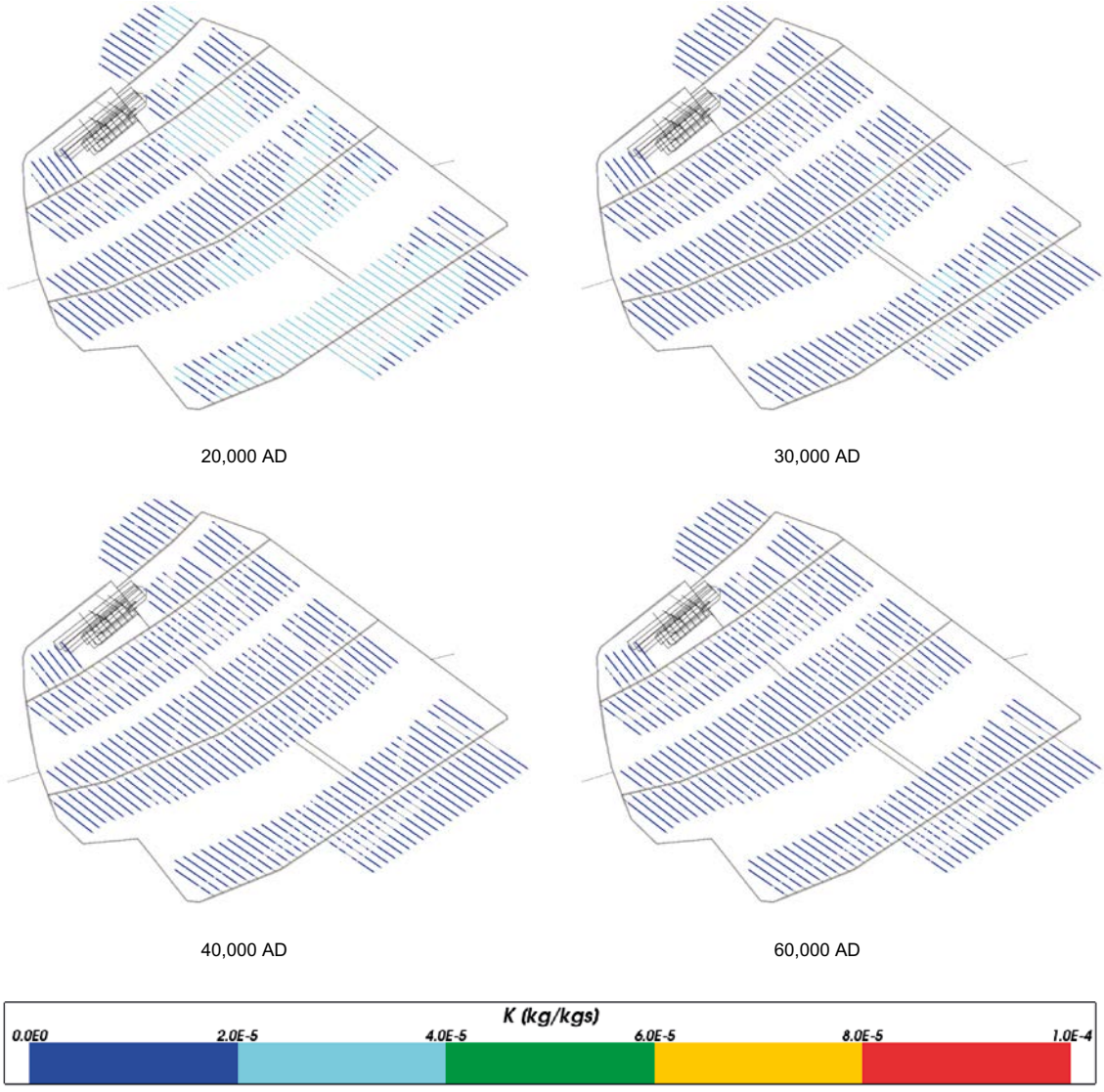


***Figure 4-100.*** *Total potassium mass fractions for Case 3 at deposition hole locations for time periods 20,000 AD to 60,000 AD.*

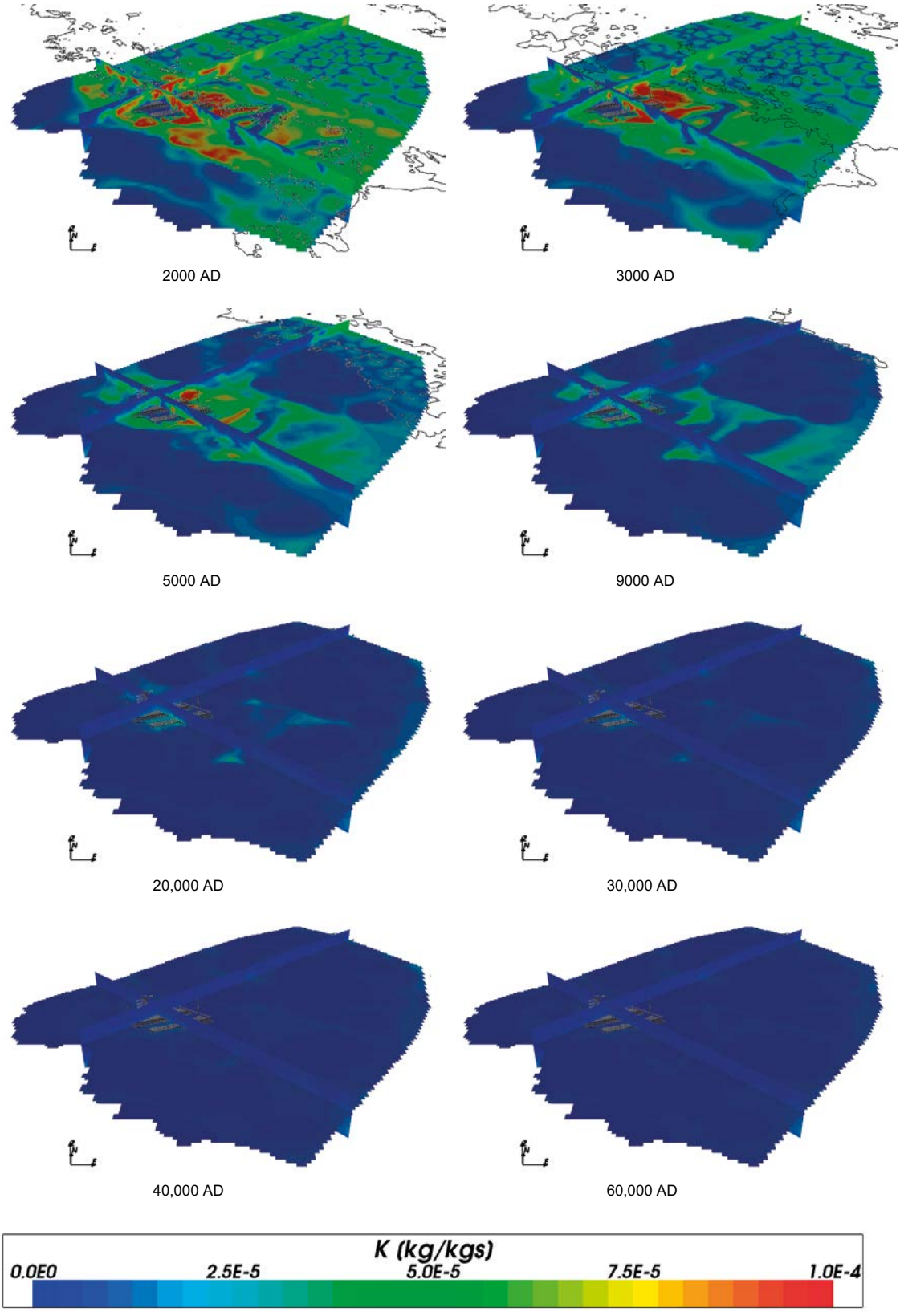


***Figure 4-101.*** *Total potassium mass fractions on regional scale slices through the repository volume for Case 3 for time periods 2000 AD to 60,000 AD.*

### 4.4.10 Sulphate

Figure 4-102, Figure 4-103 and Figure 4-104 show the sulphate concentrations around the repository for Case 3. Although the reactions involving sulphur are different for Case 2 and Case 3, the sulphate concentrations are very similar for the two cases and are consistent with those reported in Salas et al. (2010). The sulphate concentrations are relatively high, compared to iron for example, and are so are more dominated by groundwater flow and transport than by chemical reactions.

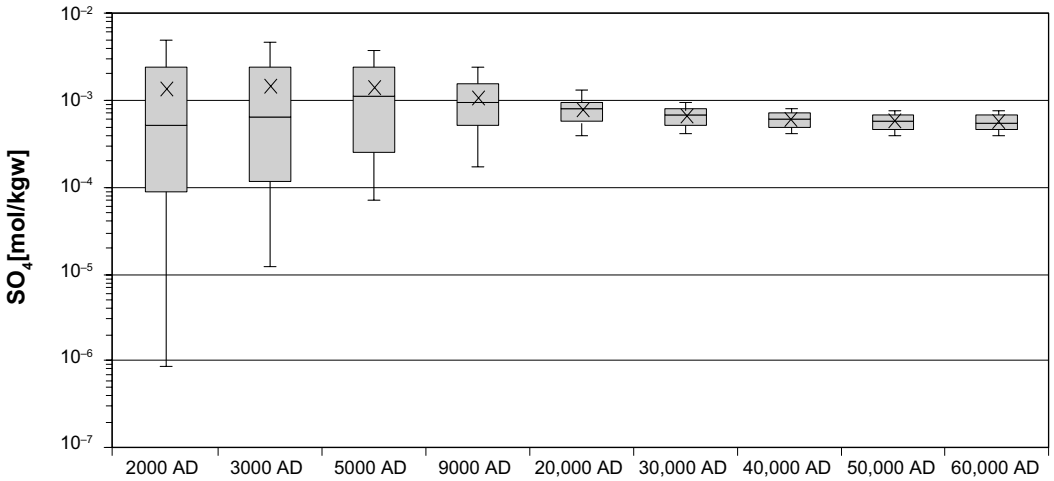


***Figure 4-102.*** *Box and whisker plot showing the statistical distribution of sulphate molalities for Case 3 on a regular grid of points within the repository volume between elevations –490 m and –450 m. The statistical measures are the median, the 25$^{th}$ and 75$^{th}$ percentiles (box), the mean (cross) and the 5$^{th}$ and 95$^{th}$ percentiles (whiskers).*

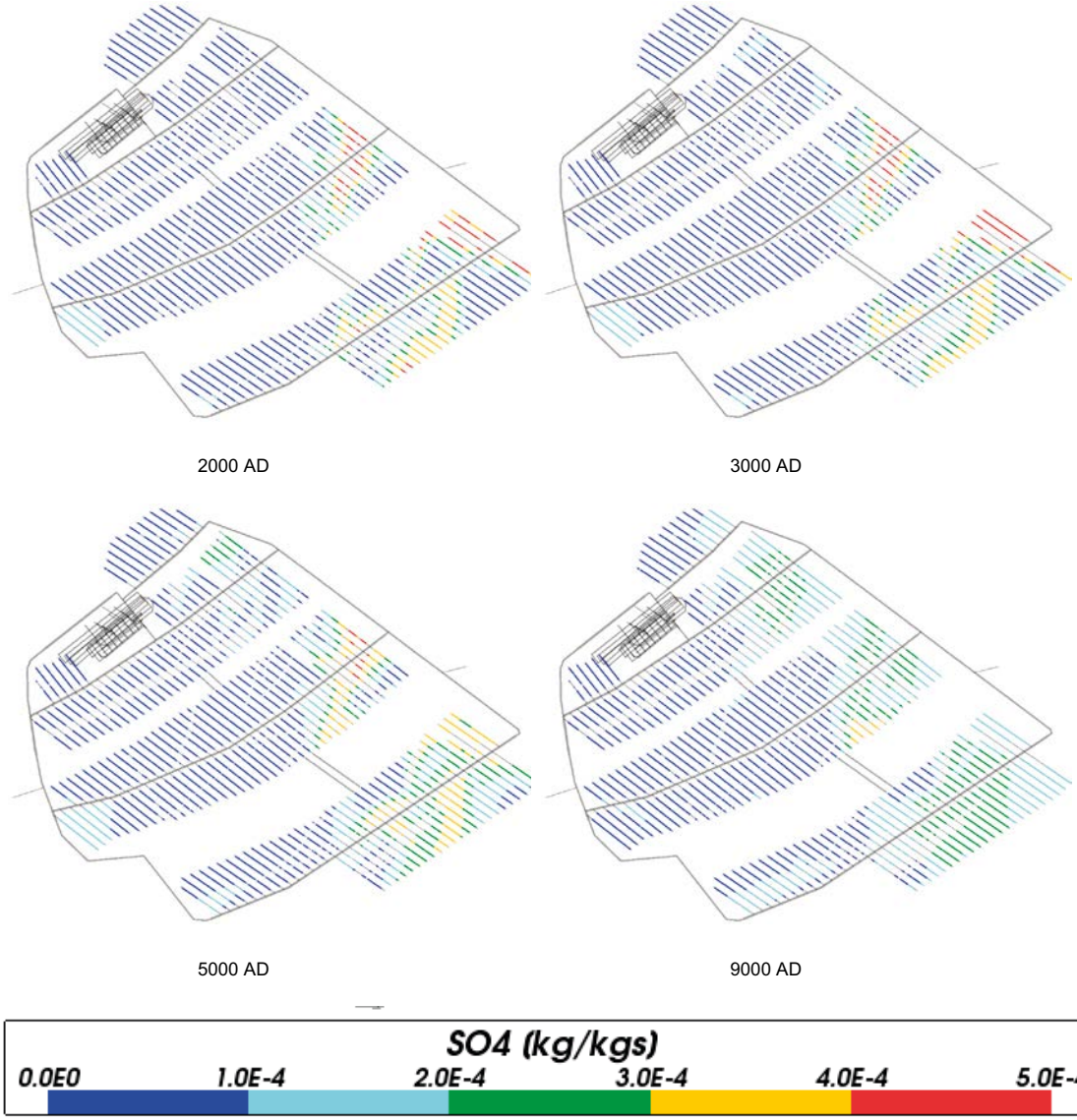


***Figure 4-103.*** *Total sulphate mass fractions for Case 3 at deposition hole locations for time periods 2000 AD to 9000 AD.*

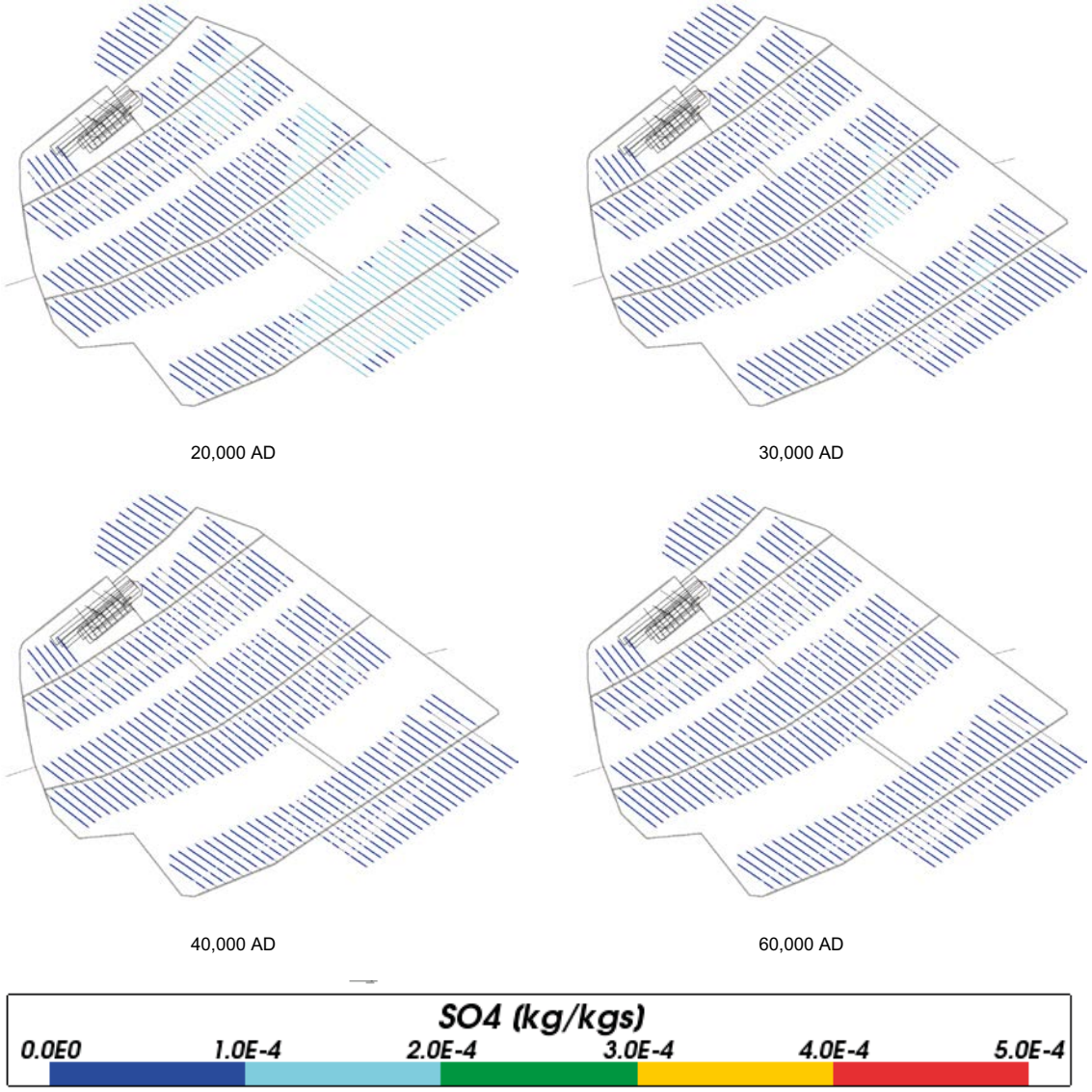


***Figure 4-104.*** *Total sulphate mass fractions for Case 3 at deposition hole locations for time periods 20,000 AD to 60,000 AD.*

### 4.4.11 Summary for Case 3

In addition to the groundwater flow and transport processes considered in Case 1, Case 3 includes equilibration of groundwater with calcite, quartz and iron (III) oxyhydroxide. The results obtained are very similar to Case 2, apart from the total iron concentrations and the Eh values. Both the total iron concentrations and Eh are controlled by the reactions involving iron, which are different for Cases 2 and 3. The median iron concentrations in the repository volume are higher for Case 3 than for Case 2, with more spatial variation but less temporal variation. The median Eh values are a little higher for Case 3, rising from –246 mV at 2000 AD to –186 mV at 60,000 AD. The pH within the repository volume for Case 3 was very similar to Case 2. Thus the geochemical conditions within the repository volume for this case also remained within the bounds required by the safety assessment throughout the simulation period.

## 4.5 Case 4

The evolution of groundwater composition for this case will be due to the transport and mixing of components originating from different reference waters. The concentrations of reactive species will be modified by equilibrium reactions with the mineral phases considered. This case differs from previous cases in the number and types of mineral phases considered (see Section 3.2). Equilibration of groundwater with calcite, quartz, amorphous iron (II) sulphide, kaolinite, albite, and K-feldspar is considered. It is expected that the equilibrium reactions will have an effect on pH, Eh, and the concentrations of total inorganic carbon, sulphur, sodium, potassium, calcium and iron.

### 4.5.1 pH

Figure 4-105, Figure 4-106 and Figure 4-107 show a slight increase in pH over time around the repository for Case 4. This is the opposite trend as compared to previous cases, and is due to the different set of mineral equilibrium reactions considered. Figure 4-108 shows the evolution of pH on a regional scale for Case 4.

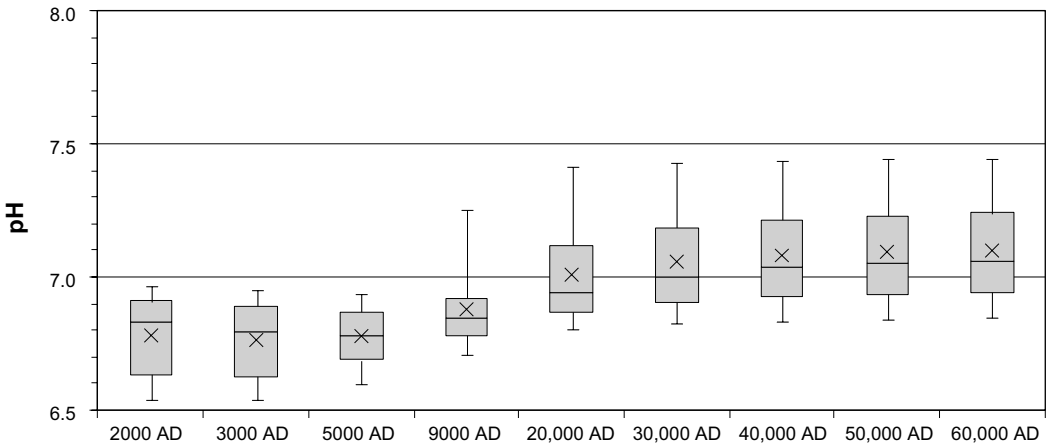


***Figure 4-105.*** *Box and whisker plot showing the statistical distribution of pH for Case 4 on a regular grid of points within the repository volume between elevations –490 m and –450 m. The statistical measures are the median, the 25th and 75th percentiles (box), the mean (cross) and the 5th and 95th percentiles (whiskers).*

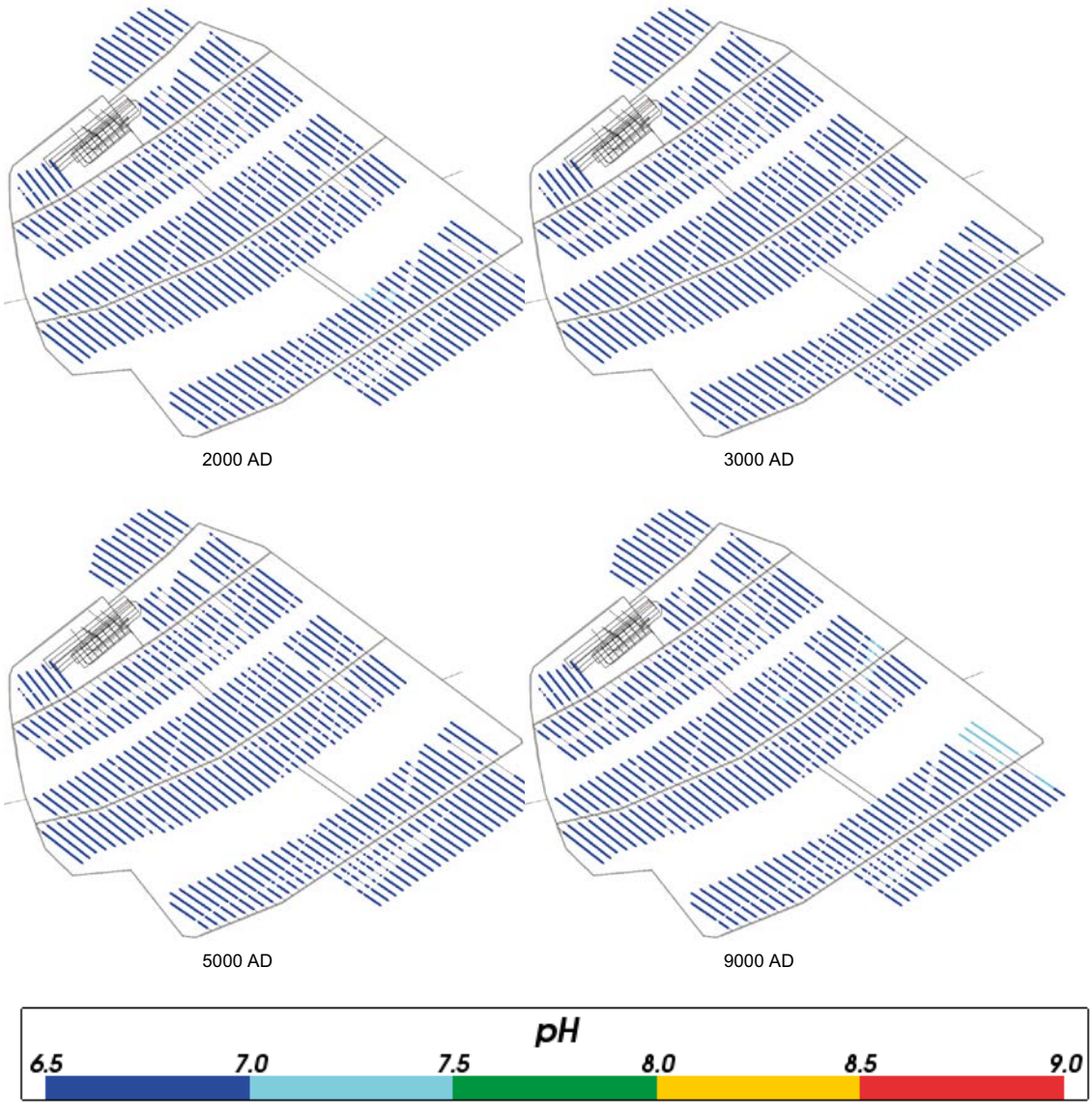


***Figure 4-106.*** *Values of pH for Case 4 at deposition hole locations for time periods 2000 AD to 9000 AD.*

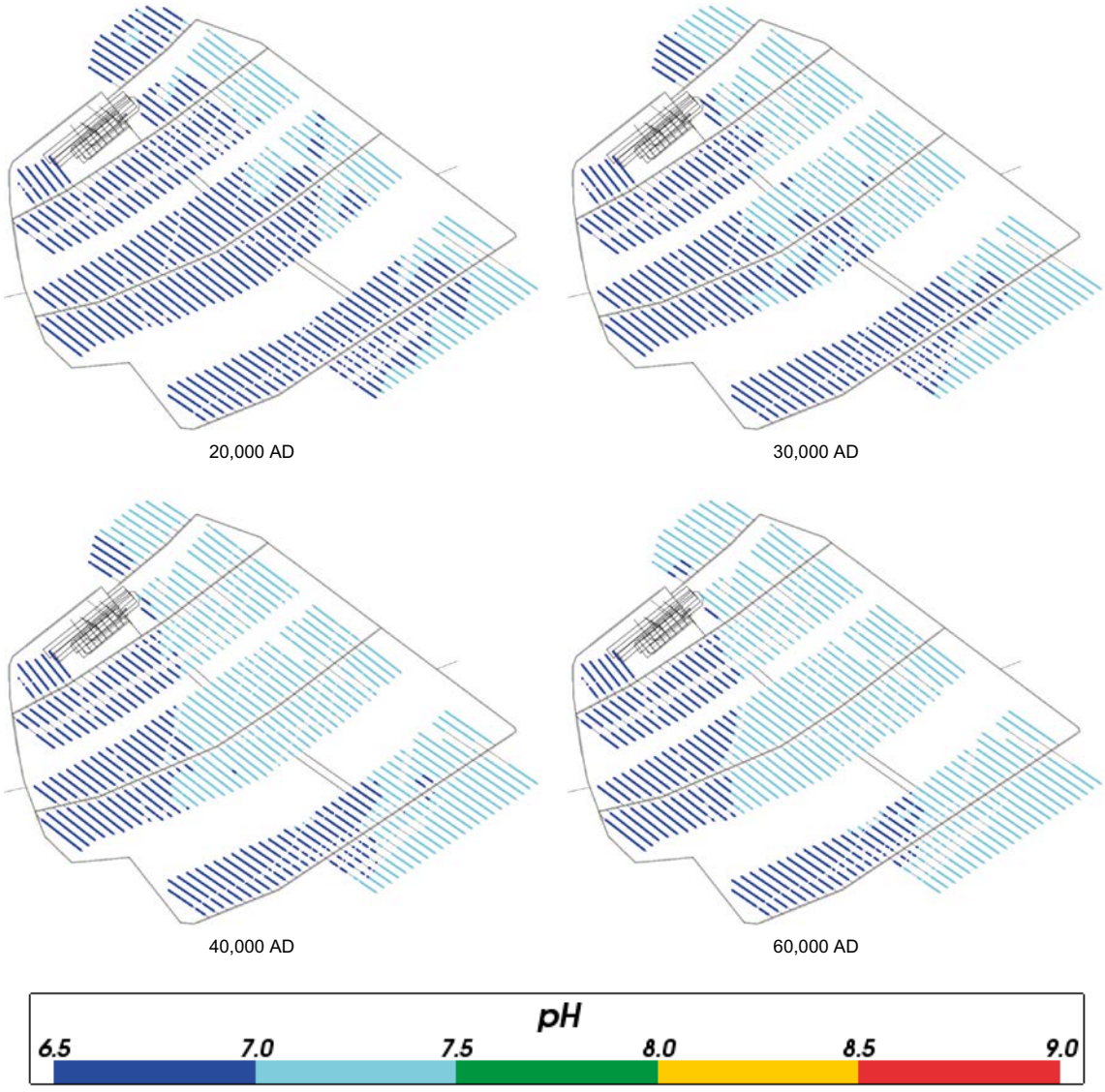


***Figure 4-107.*** *Values of pH for Case 4 at deposition hole locations for time periods 20,000 AD to 60,000 AD.*

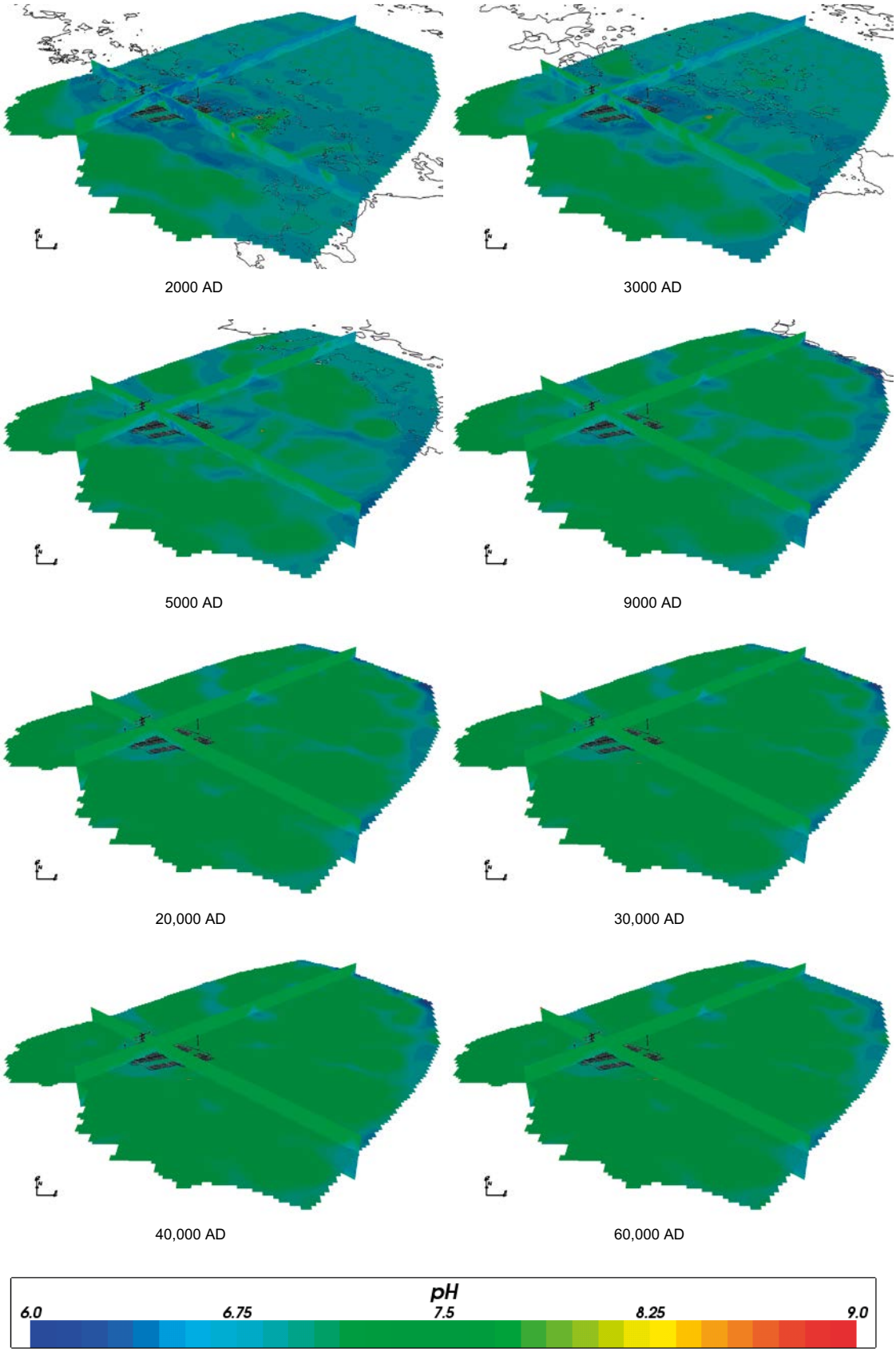


***Figure 4-108.*** *Values of pH on regional scale slices through the repository volume for Case 4 for time periods 2000 AD to 60,000 AD.*

### 4.5.2 Eh (or pe)

Figure 4-109 shows the statistical distribution of Eh around the repository and Figure 4-110 and Figure 4-111 show the value of pe in the deposition hole locations. The Eh is affected to a large extent by the equilibrium constraints with the additional mineral phases in Case 4 as compared with Case 2. A relatively large spatial variability in the repository volume for the earlier times up to 9000 AD is evident from Figure 4-109. At later times the Eh variability decreases significantly. The mean value of pe increases slightly up to 5000 AD after which the spatial variability decreases and the mean value drops slightly over time.

The trend of decreasing spatial variability after 5000 AD is also evident from Figure 4-112 which shows the value of pe on the slices covering the model area.

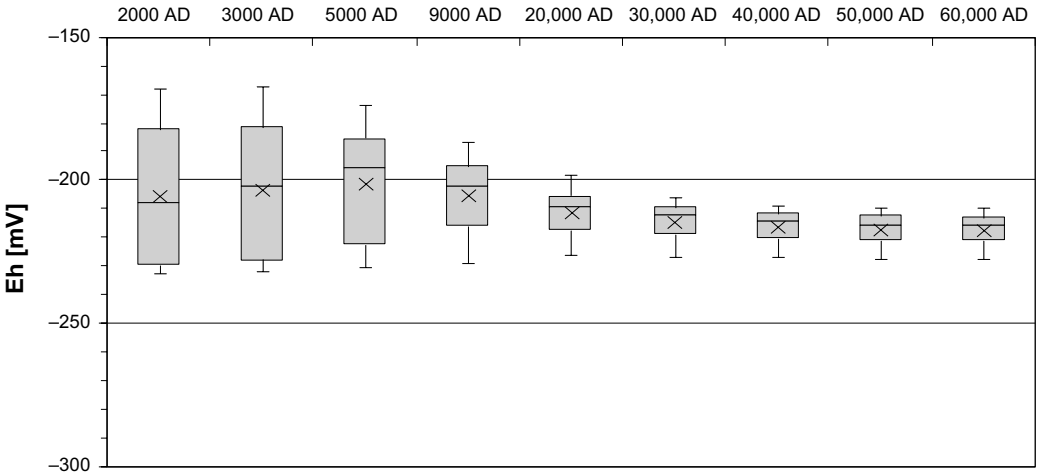


***Figure 4-109.*** *Box and whisker plot showing the statistical distribution of Eh for Case 4 on a regular grid of points within the repository volume between elevations –490 m and –450 m. The statistical measures are the median, the 25$^{th}$ and 75$^{th}$ percentiles (box), the mean (cross) and the 5$^{th}$ and 95$^{th}$ percentiles (whiskers).*

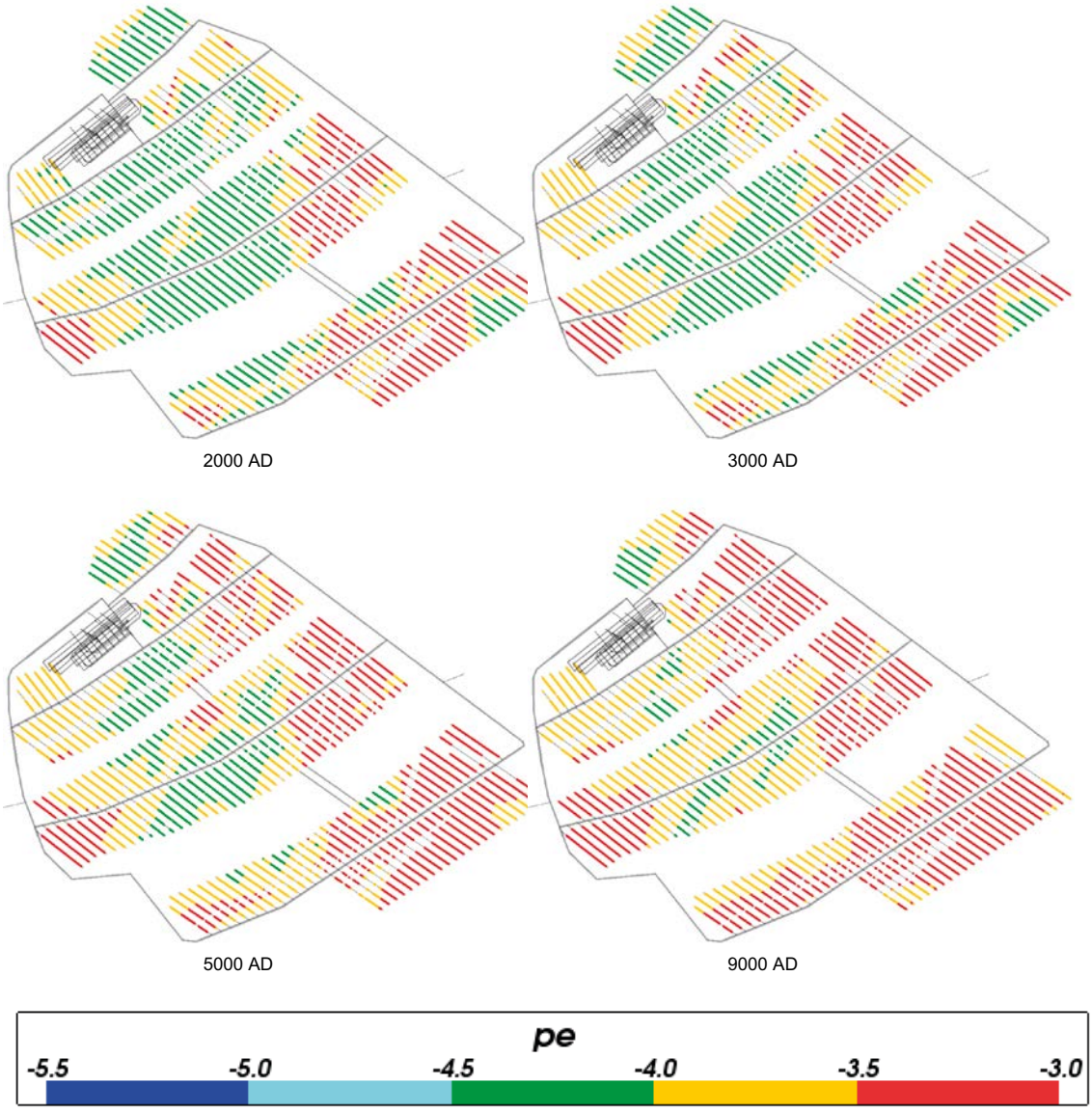


***Figure 4-110.*** *Values of pe for Case 4 at deposition hole locations for time periods 2000 AD to 9000 AD.*

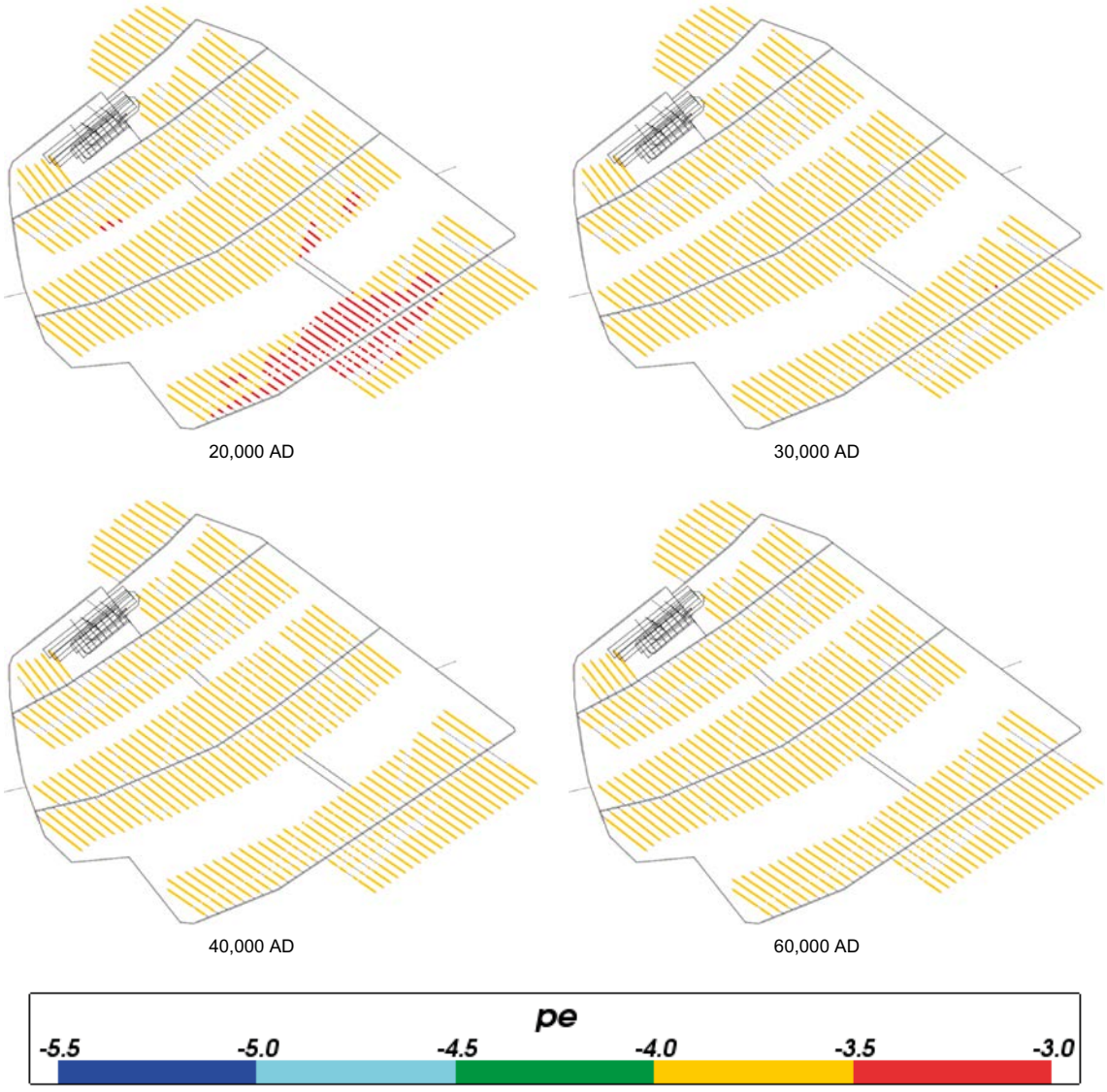


***Figure 4-111.*** *Values of pe for Case 4 at deposition hole locations for time periods 20,000 AD to 60,000 AD.*

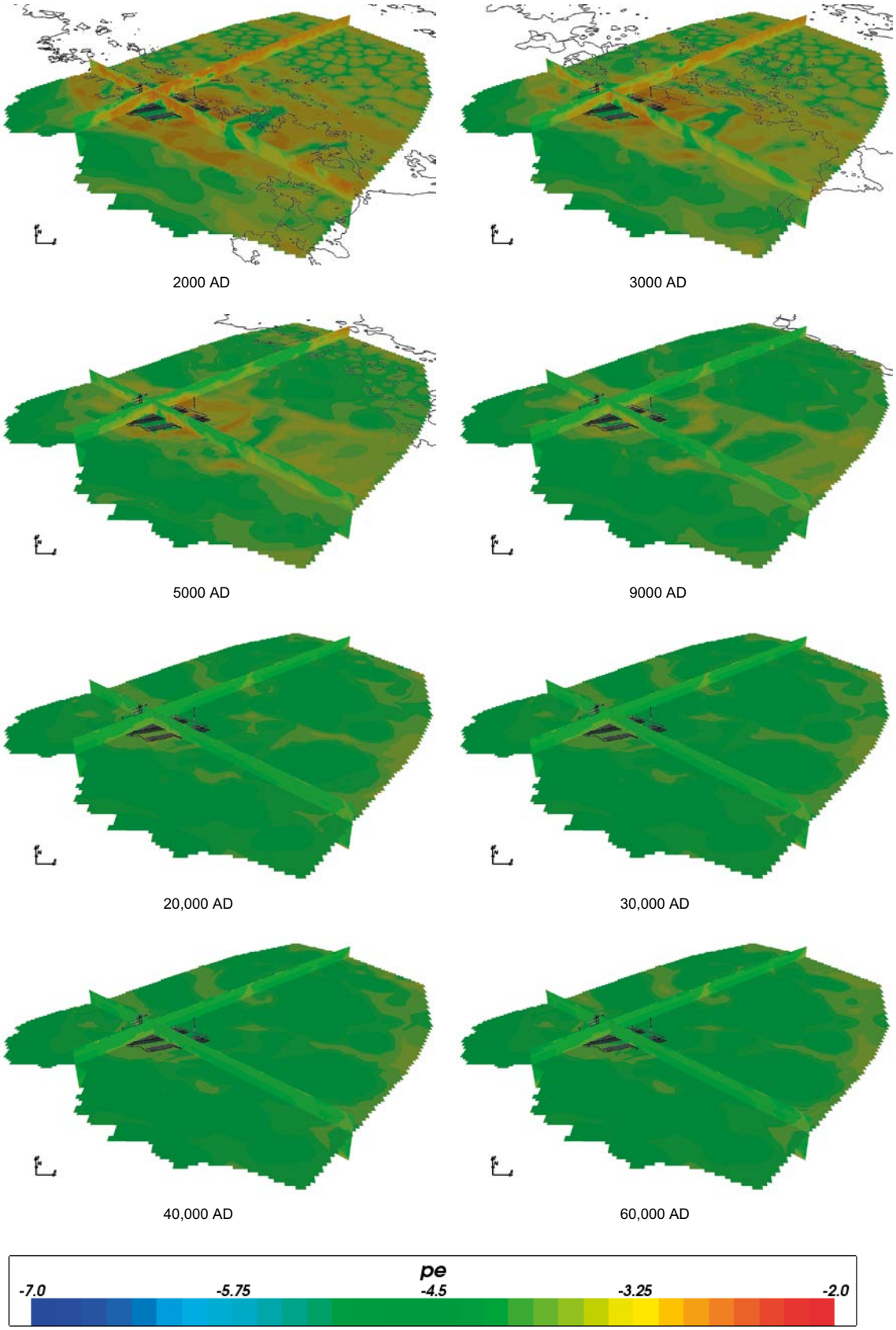


***Figure 4-112.*** *Values of pe on regional scale slices through the repository volume for Case 4 for time periods 2000 AD to 60,000 AD.*

### 4.5.3 TDS and sum of cations

Figure 4-113 and Figure 4-114 show the statistical distribution of TDS and the sum of cation molalities around the repository for Case 4. As for the previous cases, the plots are closely related, with the sum of cations plot showing the same trend as the TDS plot. The TDS and sum of cations do reduce significantly over time as for Cases 1 and 2, and tend to level out after 30,000 AD.

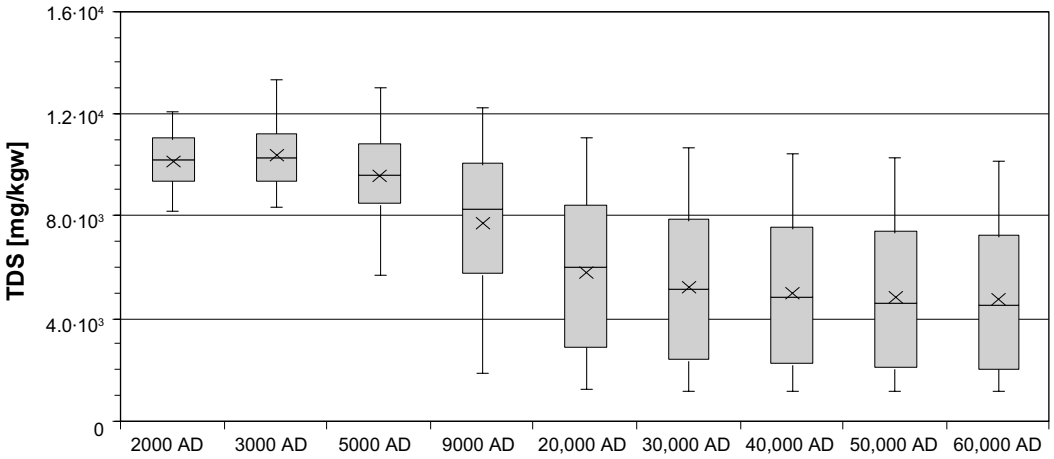


***Figure 4-113.*** *Box and whisker plot showing the statistical distribution of TDS for Case 4 on a regular grid of points within the repository volume between elevations –490 m and –450 m. The statistical measures are the median, the 25th and 75th percentiles (box), the mean (cross) and the 5th and 95th percentiles (whiskers).*

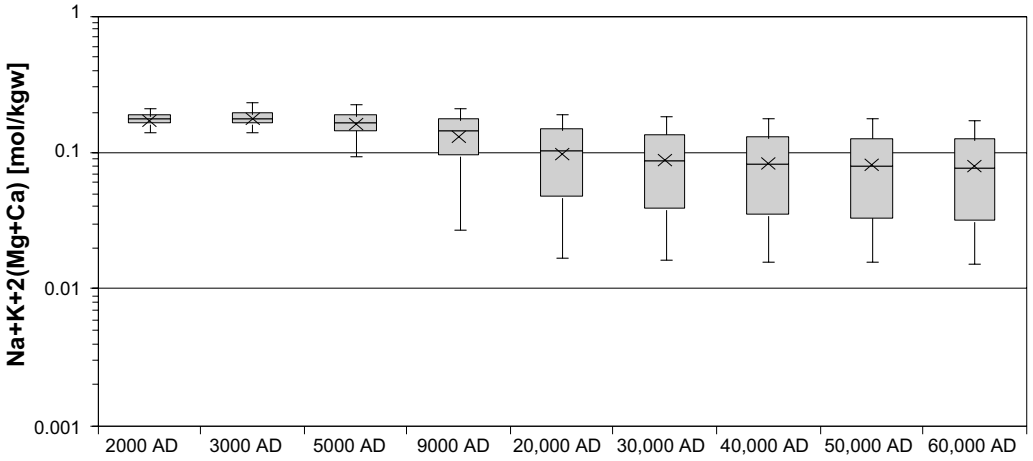


***Figure 4-114.*** *Box and whisker plot showing the statistical distribution of sum of cation charges (Na+K+2(Mg+Ca)) molalities for Case 4 on a regular grid of points within the repository volume between elevations –490 m and –450 m. The statistical measures are the median, the 25th and 75th percentiles (box), the mean (cross) and the 5th and 95th percentiles (whiskers).*

### 4.5.4 Inorganic carbon

Figure 4-115, Figure 4-116 and Figure 4-117 show the concentrations of total inorganic carbon around the repository for Case 4. Unlike the previous cases, the mean value of total inorganic carbon molalities decreases slightly over time, and shows a larger spatial variability at the early times up to 9000 AD. The spatial distribution is similar to previous cases with predominance of higher values at the north to north-east part of the repository, but the concentration span and mean value up to 9000 AD is significantly larger in Case 4. At later times, Case 4 shows lower total inorganic carbon concentrations in the deposition holes than Cases 1 and 2. The differences can be attributed to the additional aluminosilicate reactions and their influence on e.g. the pH.

Figure 4-118 shows the evolution of carbon over time on a regional scale. A much higher spatial variability is evident in total inorganic carbon concentrations at the early times as compared to the previous cases. Strong depth dependence is apparent from the figure, in particular during early times, with high total inorganic carbon concentrations at the surface and decreasing with depth.

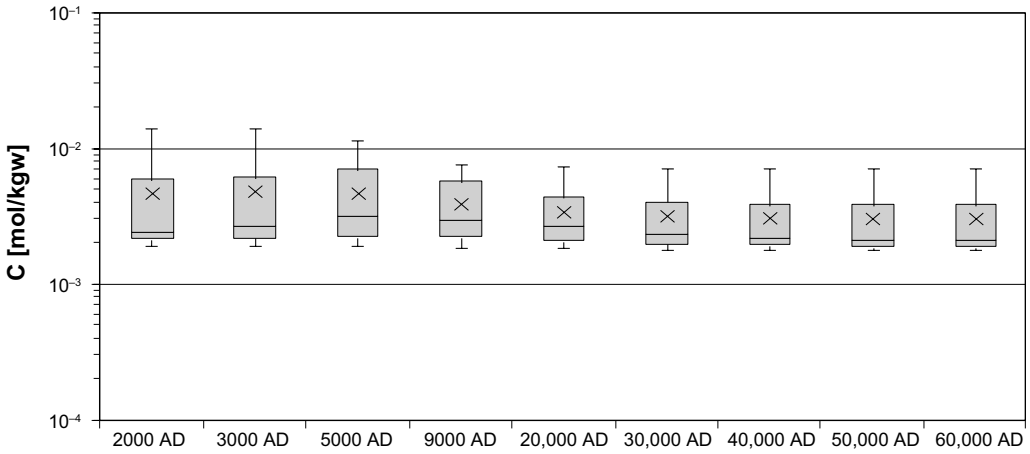


***Figure 4-115.*** *Box and whisker plot showing the statistical distribution of total inorganic carbon molalities for Case 4 on a regular grid of points within the repository volume between elevations –490 m and –450 m. The statistical measures are the median, the 25$^{th}$ and 75$^{th}$ percentiles (box), the mean (cross) and the 5$^{th}$ and 95$^{th}$ percentiles (whiskers).*

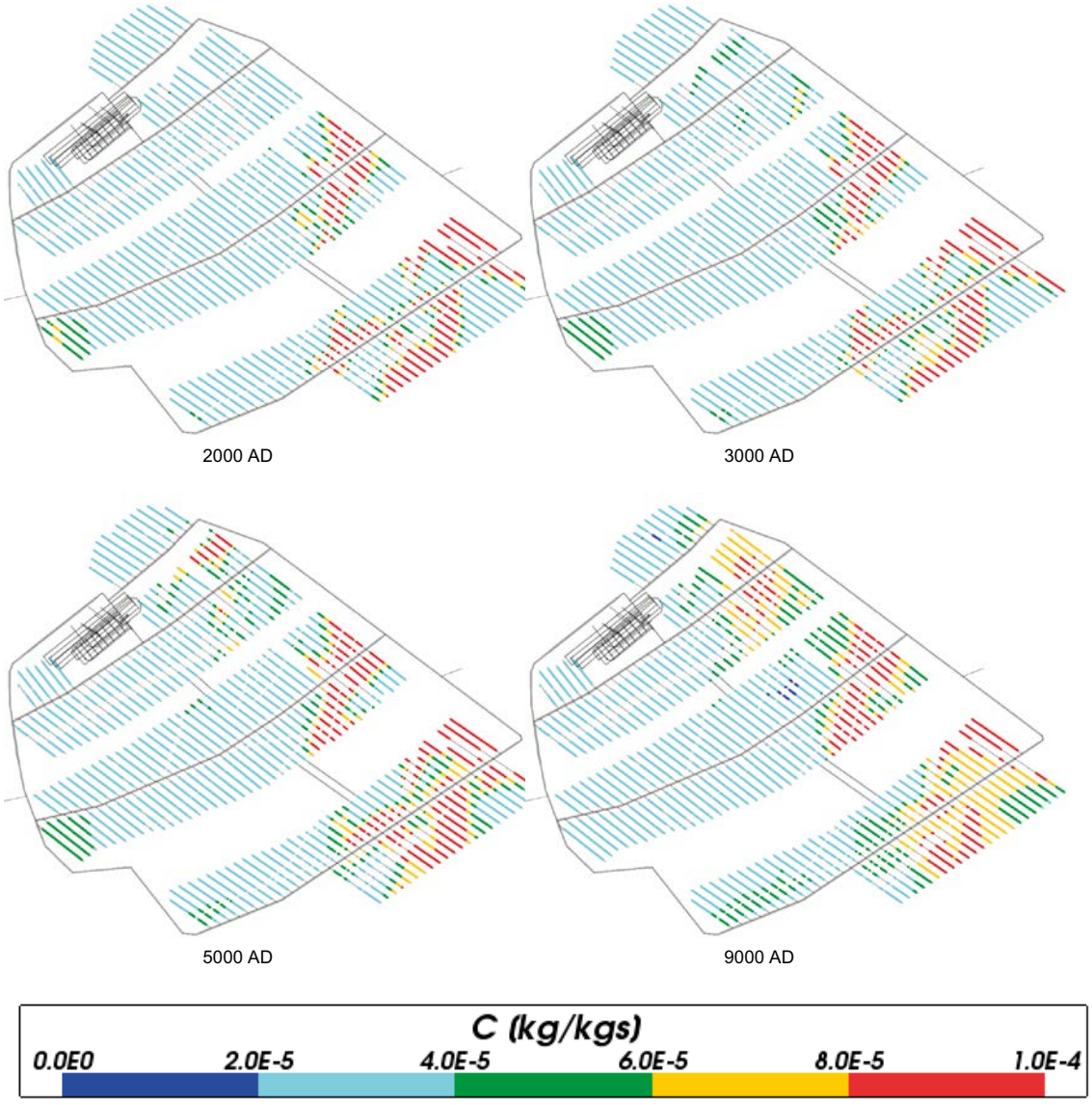


***Figure 4-116.*** *Total inorganic carbon mass fractions for Case 4 at deposition hole locations for time periods 2000 AD to 9000 AD.*

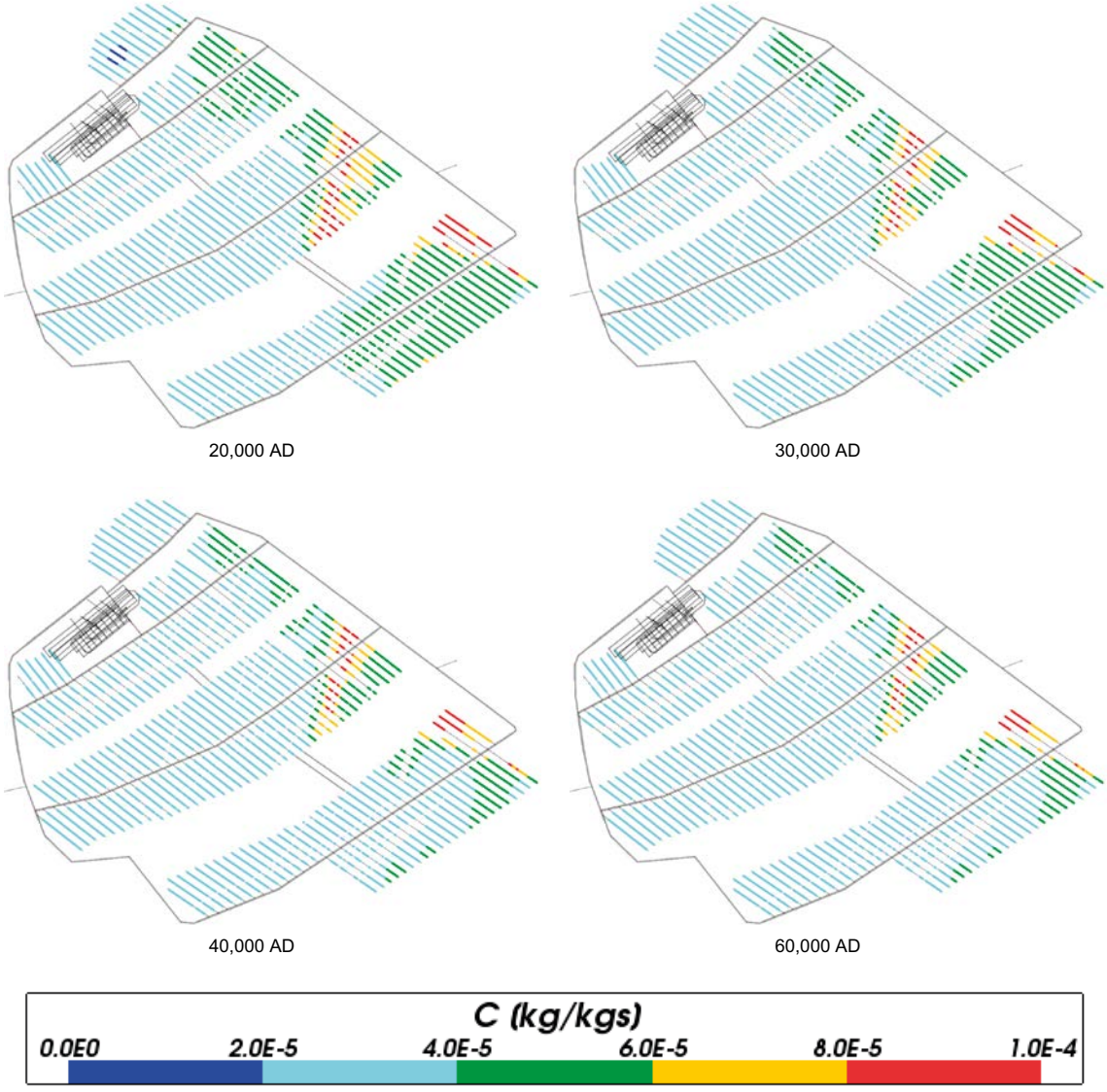


***Figure 4-117.*** *Total inorganic carbon mass fractions for Case 4 at deposition hole locations for time periods 20,000 AD to 60,000 AD.*

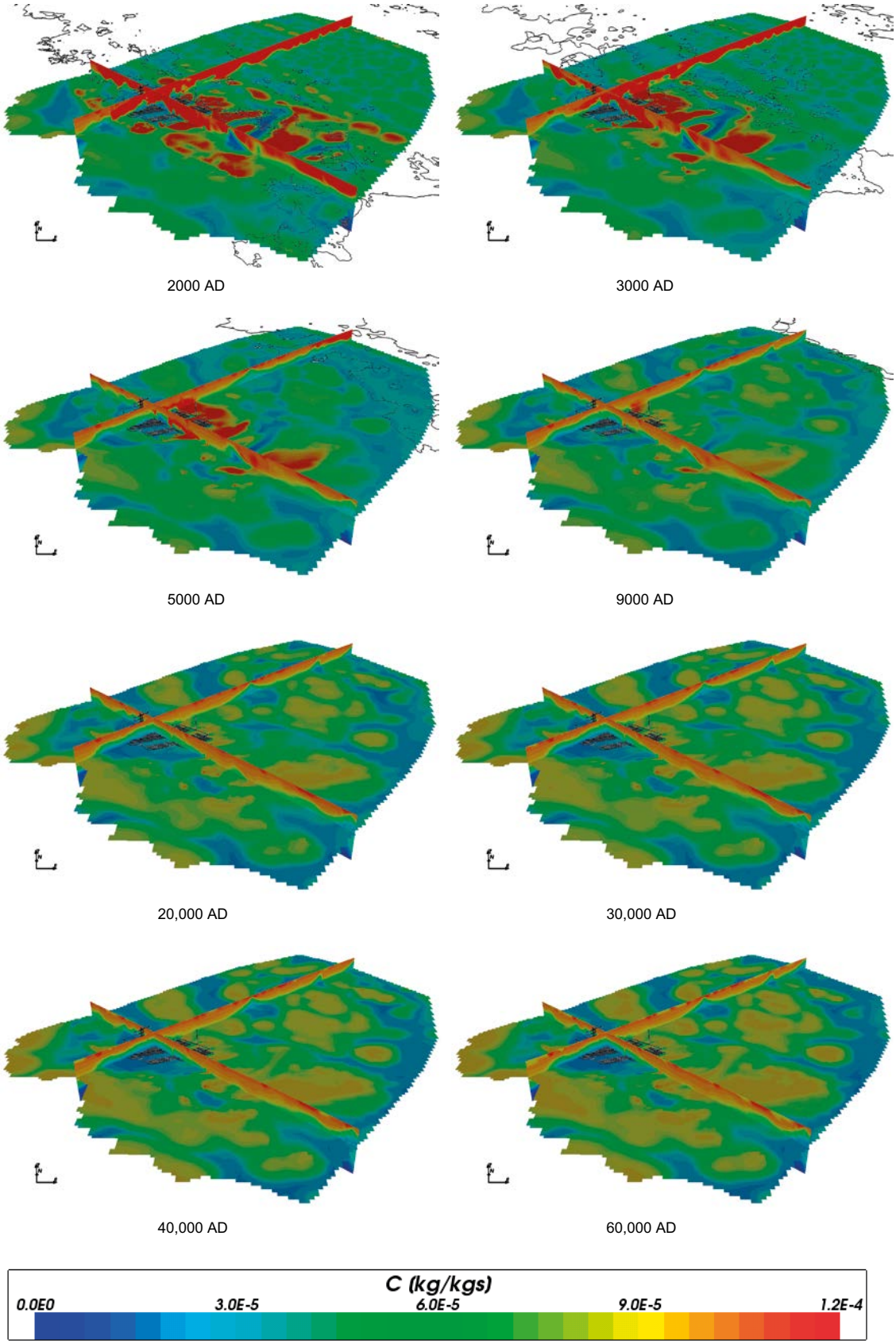


***Figure 4-118.*** *Total inorganic carbon mass fractions on regional scale slices through the repository volume for Case 4 for time periods 2000 AD to 60,000 AD.*

### 4.5.5 Calcium

The values for calcium concentrations around the repository (Figure 4-119, Figure 4-120 and Figure 4-121) for Case 4 are very similar to that of Cases 2 and 3 with a trend of calcium decreasing with time. The ranges of values at each time are also similar to Cases 2 and 3.

Figure 4-122 shows the evolution of calcium over time on the regional scale. These results are also very similar to those of Cases 2 and 3. The close similarity with Case 2 indicates that the additional chemical reactions considered in Case 4 have only minor influence on the calcium concentrations.

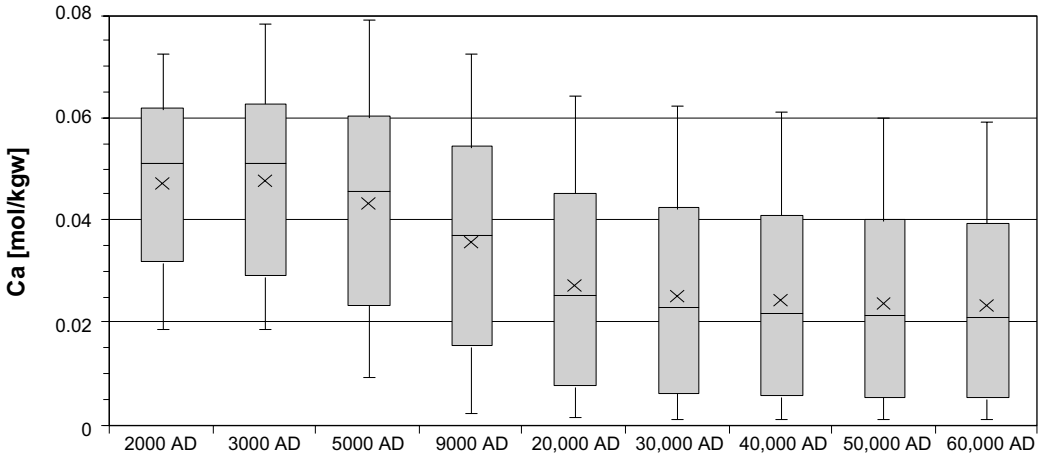


***Figure 4-119.*** *Box and whisker plot showing the statistical distribution of total calcium molalities for Case 4 on a regular grid of points within the repository volume between elevations –490 m and –450 m. The statistical measures are the median, the 25$^{th}$ and 75$^{th}$ percentiles (box), the mean (cross) and the 5$^{th}$ and 95$^{th}$ percentiles (whiskers).*

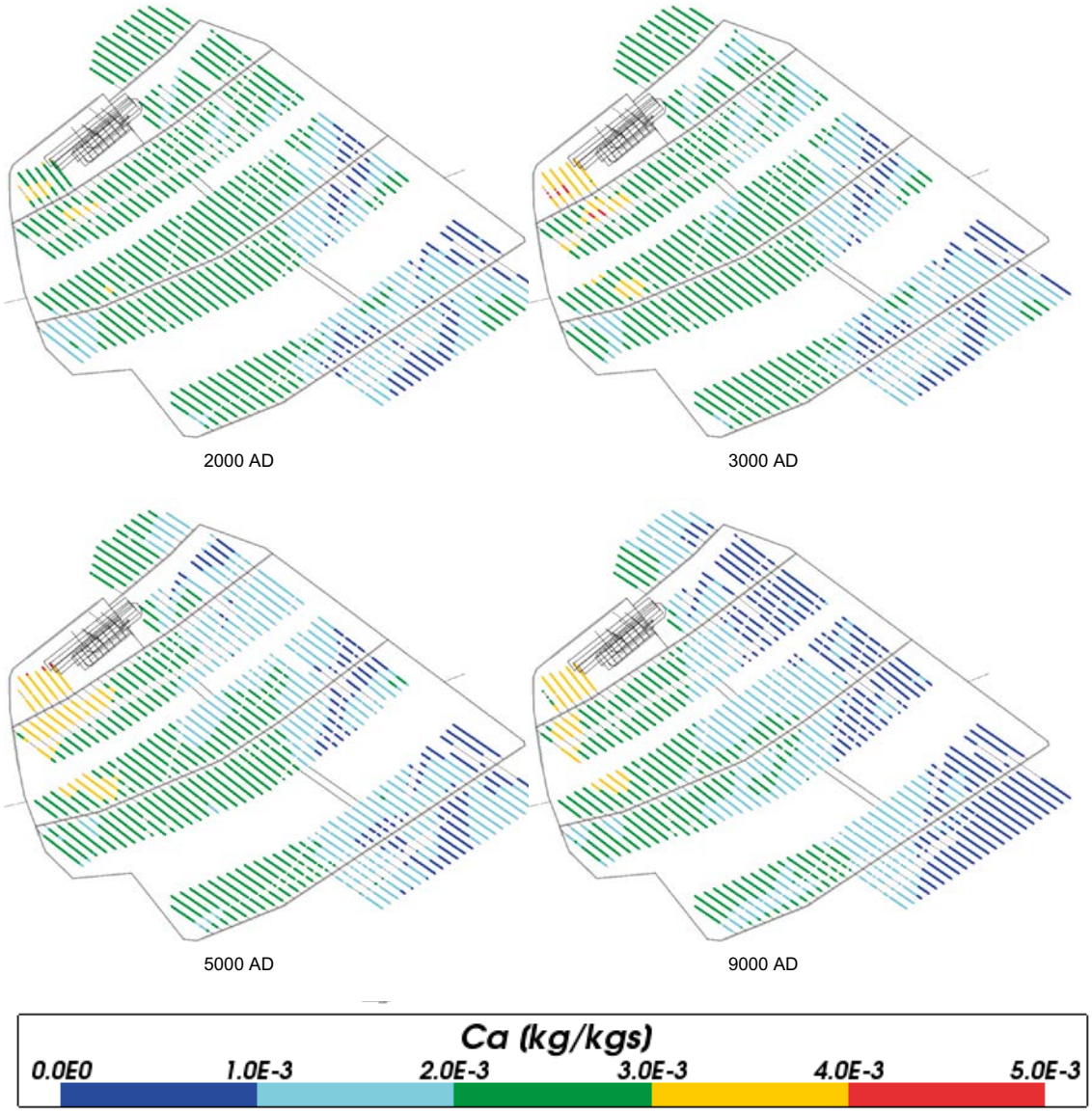


***Figure 4-120.*** *Total calcium mass fractions for Case 4 at deposition hole locations for time periods 2000 AD to 9000 AD.*

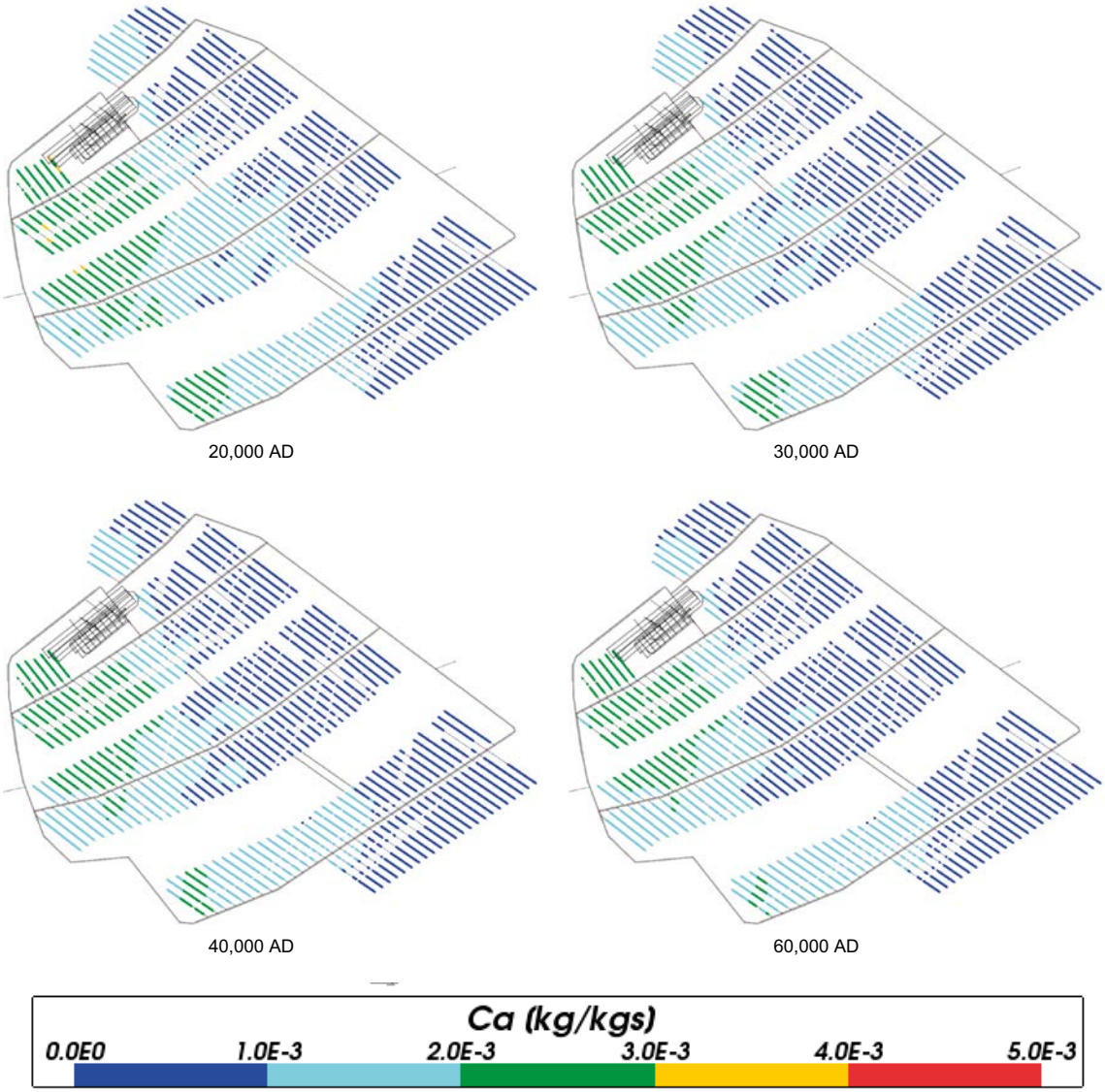


***Figure 4-121.*** *Total calcium mass fractions for Case 4 at deposition hole locations for time periods 20,000 AD to 60,000 AD.*

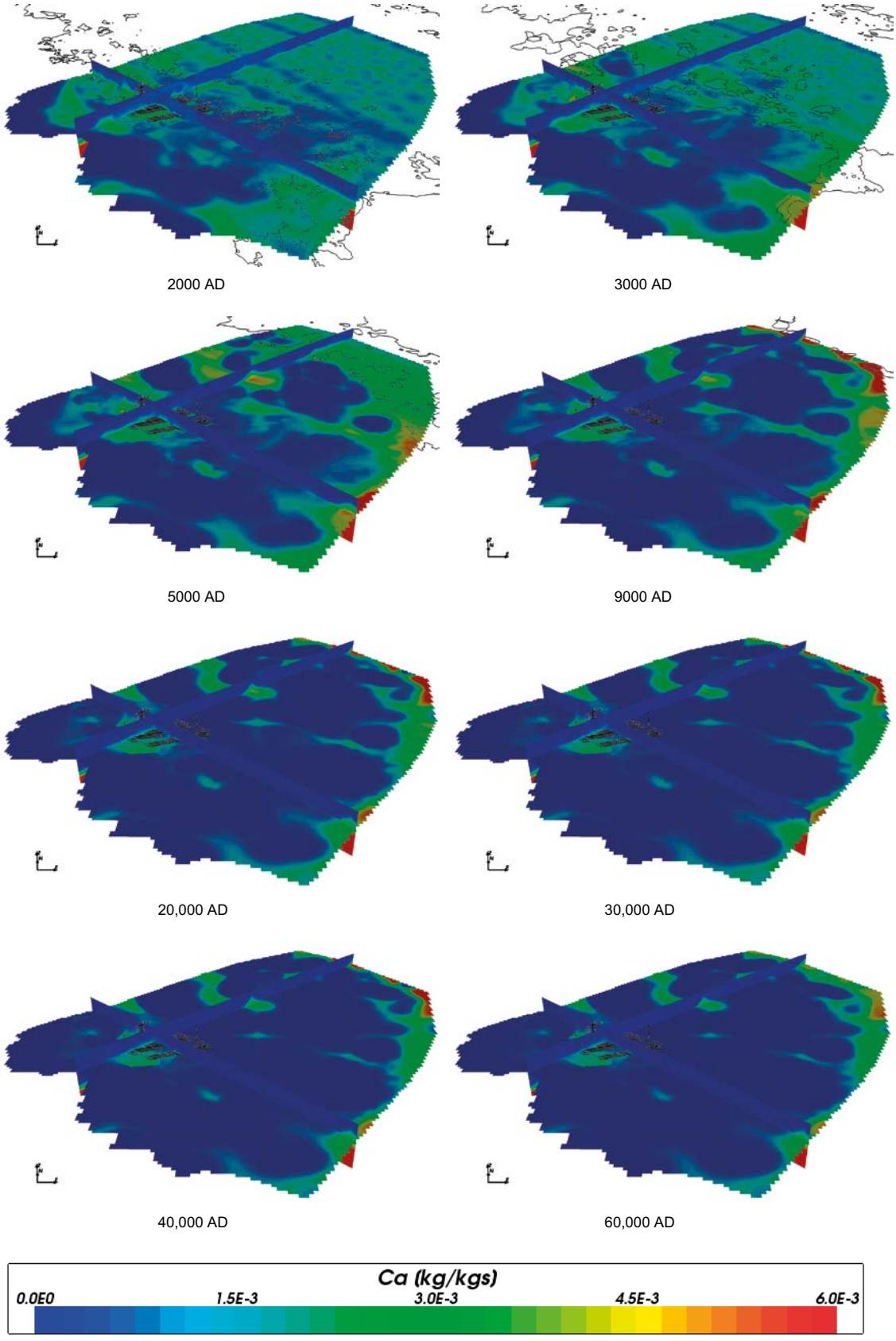


***Figure 4-122.*** *Total calcium mass fractions on regional scale slices through the repository volume for Case 4 for time periods 2000 AD to 60,000 AD.*

### 4.5.6 Chloride

Figure 4-123, Figure 4-124 and Figure 4-125 show the chloride concentrations around the repository. Mean and median values of chloride concentrations decrease over time and the results are very similar to those seen for Cases 1 to 3. Also the spatial variability in the repository volume in Figure 4-124 and Figure 4-125 and in the model volume in Figure 4-126 is very similar to Cases 1 to 3. This similarity indicates that chemical reactions considered in Case 4 have no significant influence on the chloride concentrations, since chloride is non-reacting in this case.

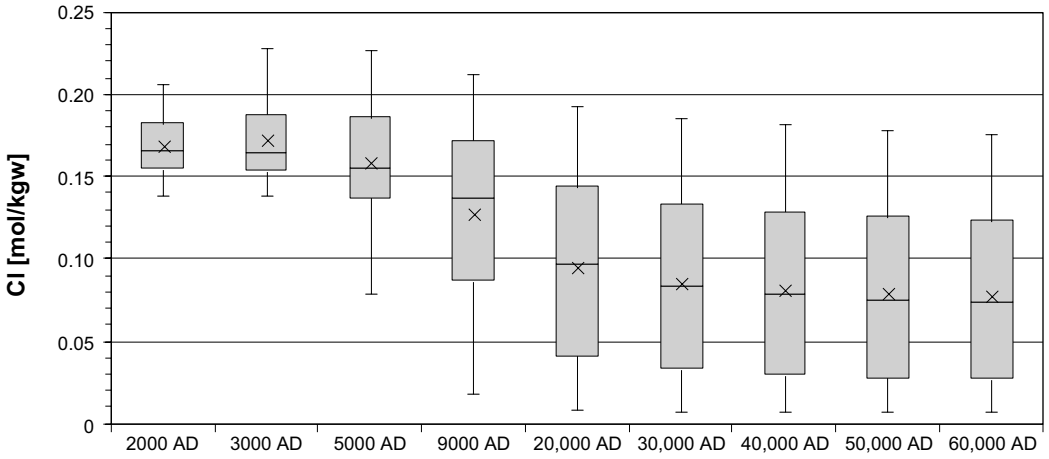


***Figure 4-123.*** *Box and whisker plot showing the statistical distribution of total chloride molalities for Case 4 on a regular grid of points within the repository volume between elevations –490 m and –450 m. The statistical measures are the median, the 25$^{th}$ and 75$^{th}$ percentiles (box), the mean (cross) and the 5$^{th}$ and 95$^{th}$ percentiles (whiskers).*

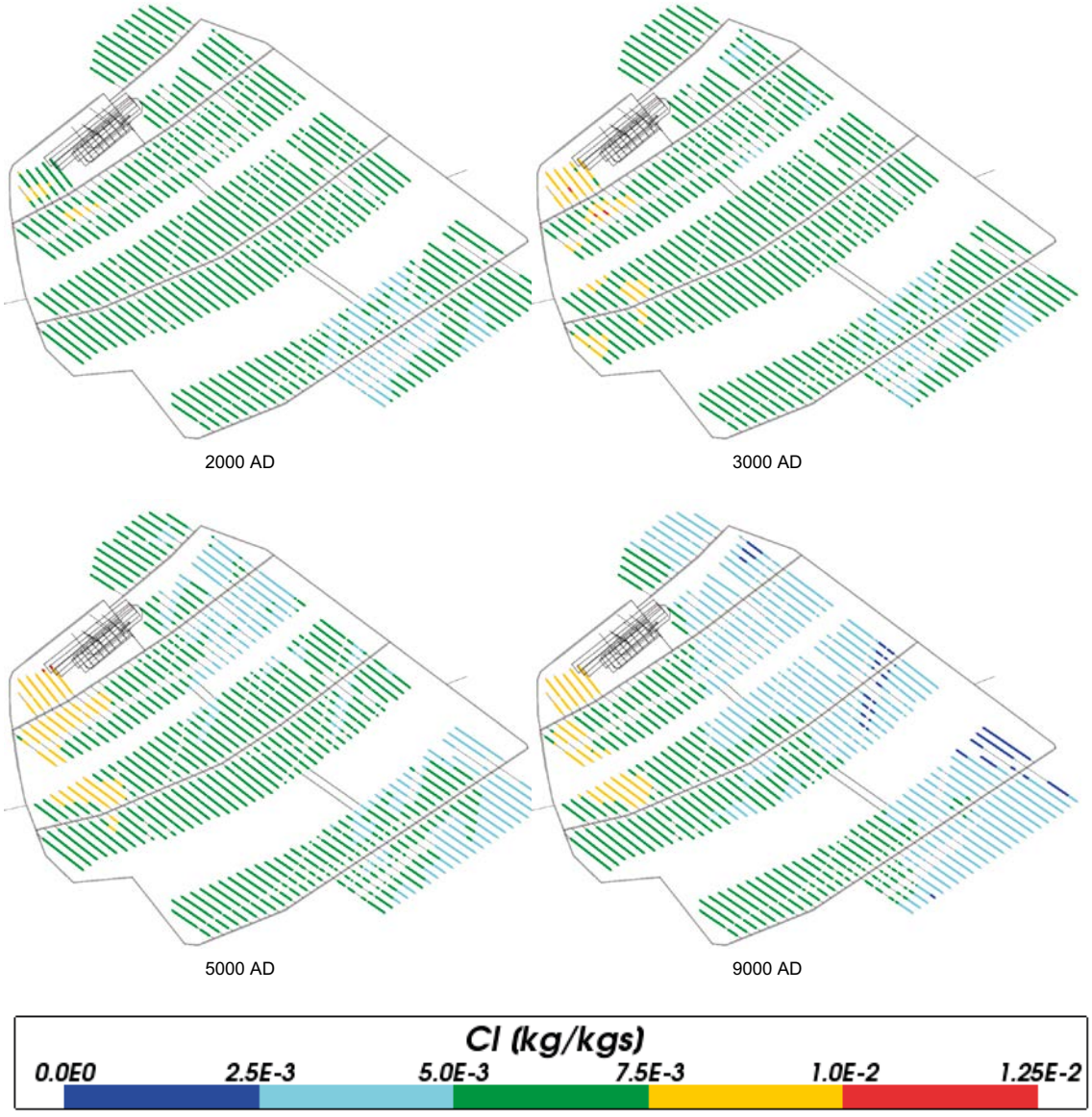


***Figure 4-124.*** *Total chloride mass fractions for Case 4 at deposition hole locations for time periods 2000 AD to 9000 AD.*

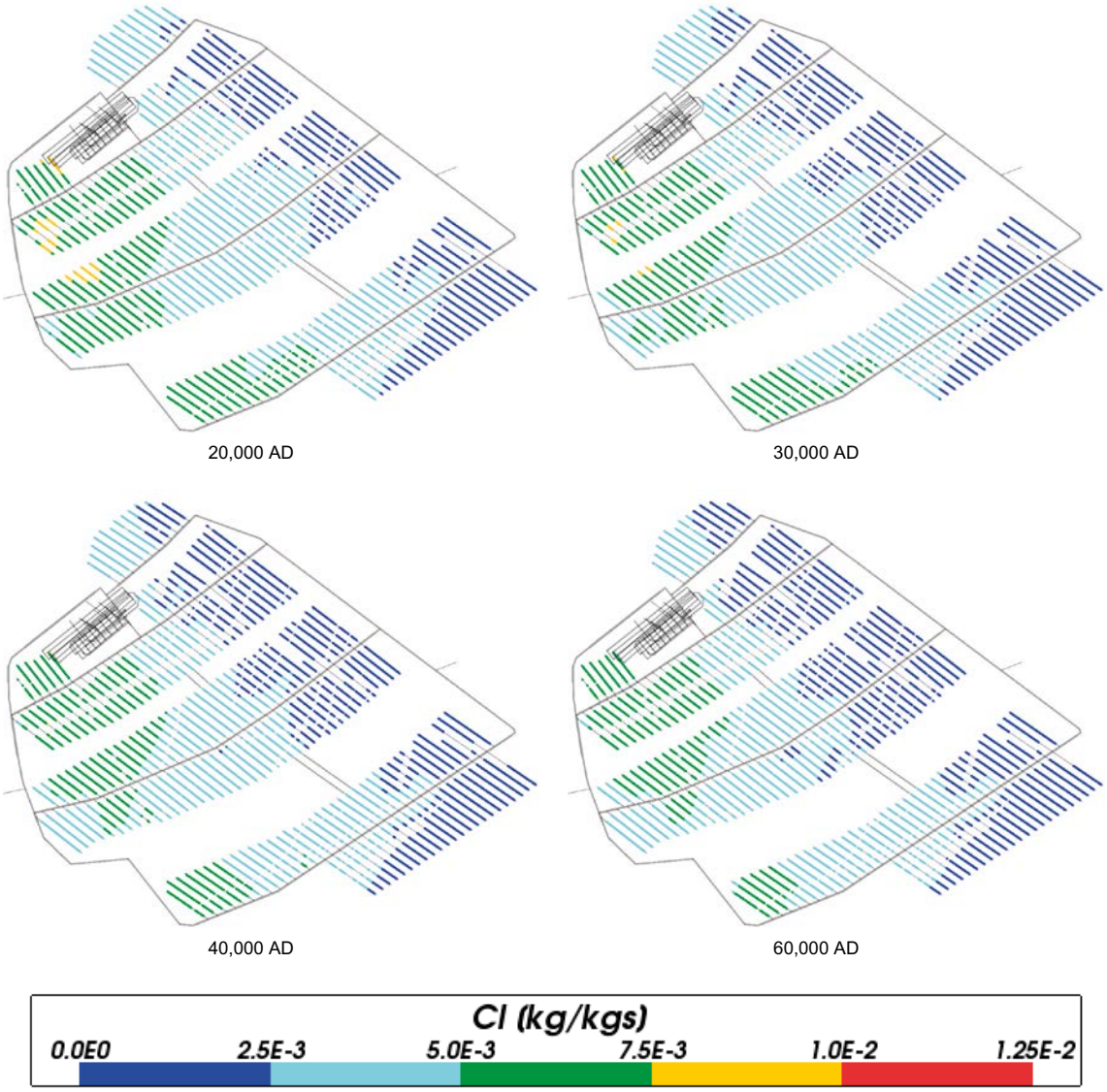


***Figure 4-125.*** *Total chloride mass fractions for Case 4 at deposition hole locations for time periods 20,000 AD to 60,000 AD.*

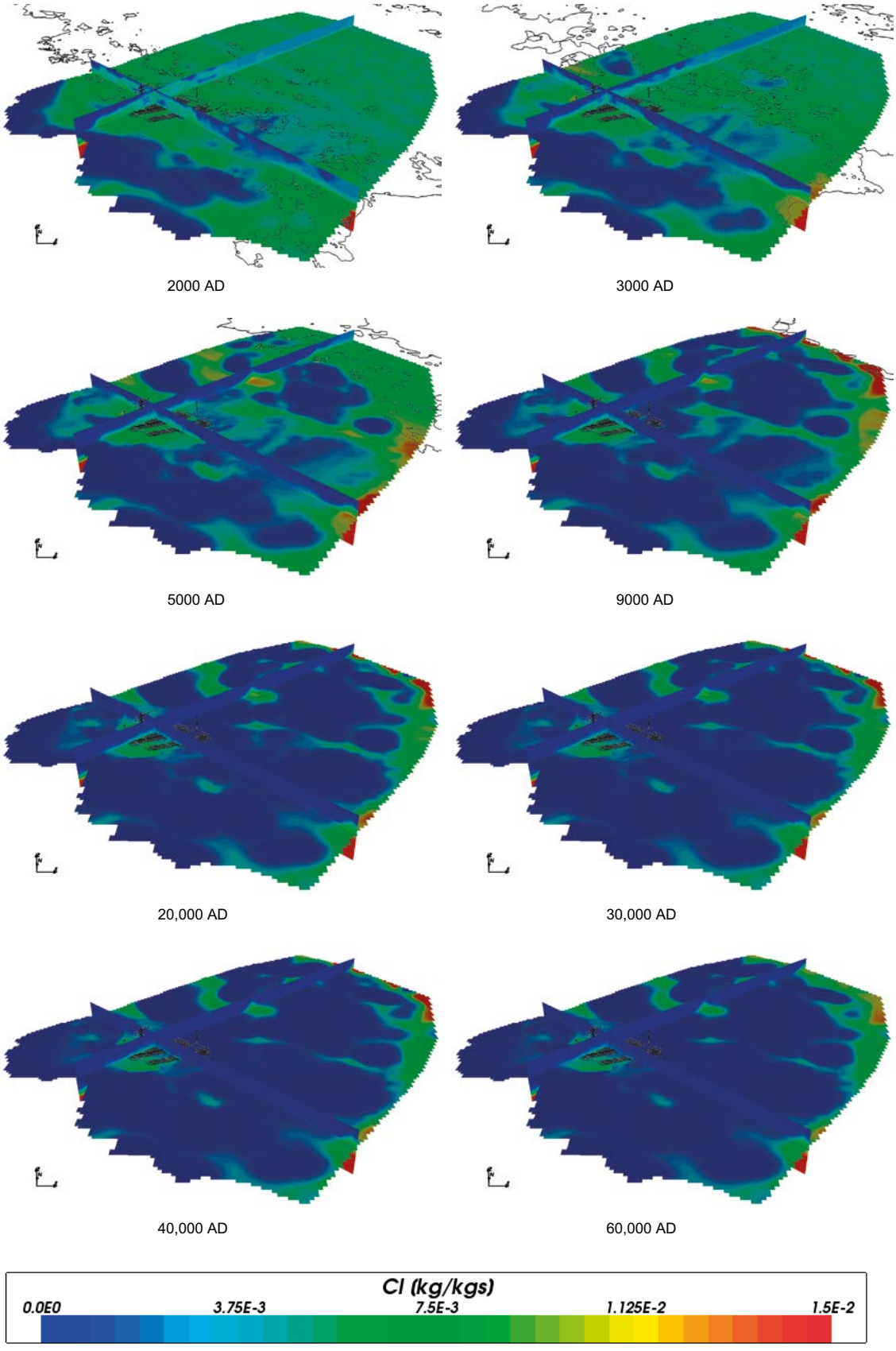


***Figure 4-126.*** *Total chloride mass fractions on regional scale slices through the repository volume for Case 4 for time periods 2000 AD to 60,000 AD.*

### 4.5.7 Iron

The evolution of total iron concentrations in the repository region for Case 4 is shown in Figure 4-127, Figure 4-128 and Figure 4-129 and on the regional scale in Figure 4-130. The change in iron concentration with time in Case 4 is relatively small, with a decreasing spatial variability. The difference in iron concentrations as compared to the other cases is due to the additional mineral reactions affecting e.g. the pH and Eh. On the regional scale a larger spatial variability is evident, particularly at the early times up to 5,000 AD, as compared to Case 1, where no chemical reactions are included.

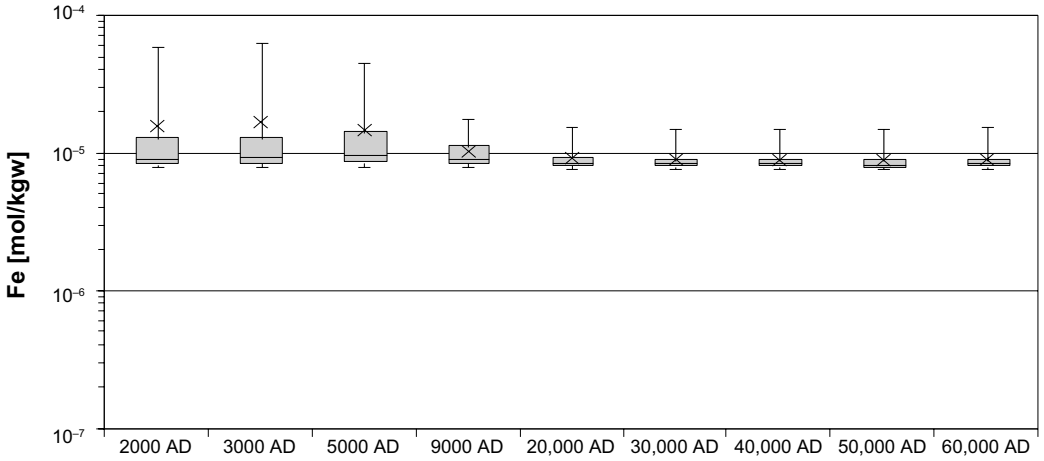


***Figure 4-127.*** *Box and whisker plot showing the statistical distribution of total iron molalities for Case 4 on a regular grid of points within the repository volume between elevations –490 m and –450 m. The statistical measures are the median, the 25$^{th}$ and 75$^{th}$ percentiles (box), the mean (cross) and the 5$^{th}$ and 95$^{th}$ percentiles (whiskers).*

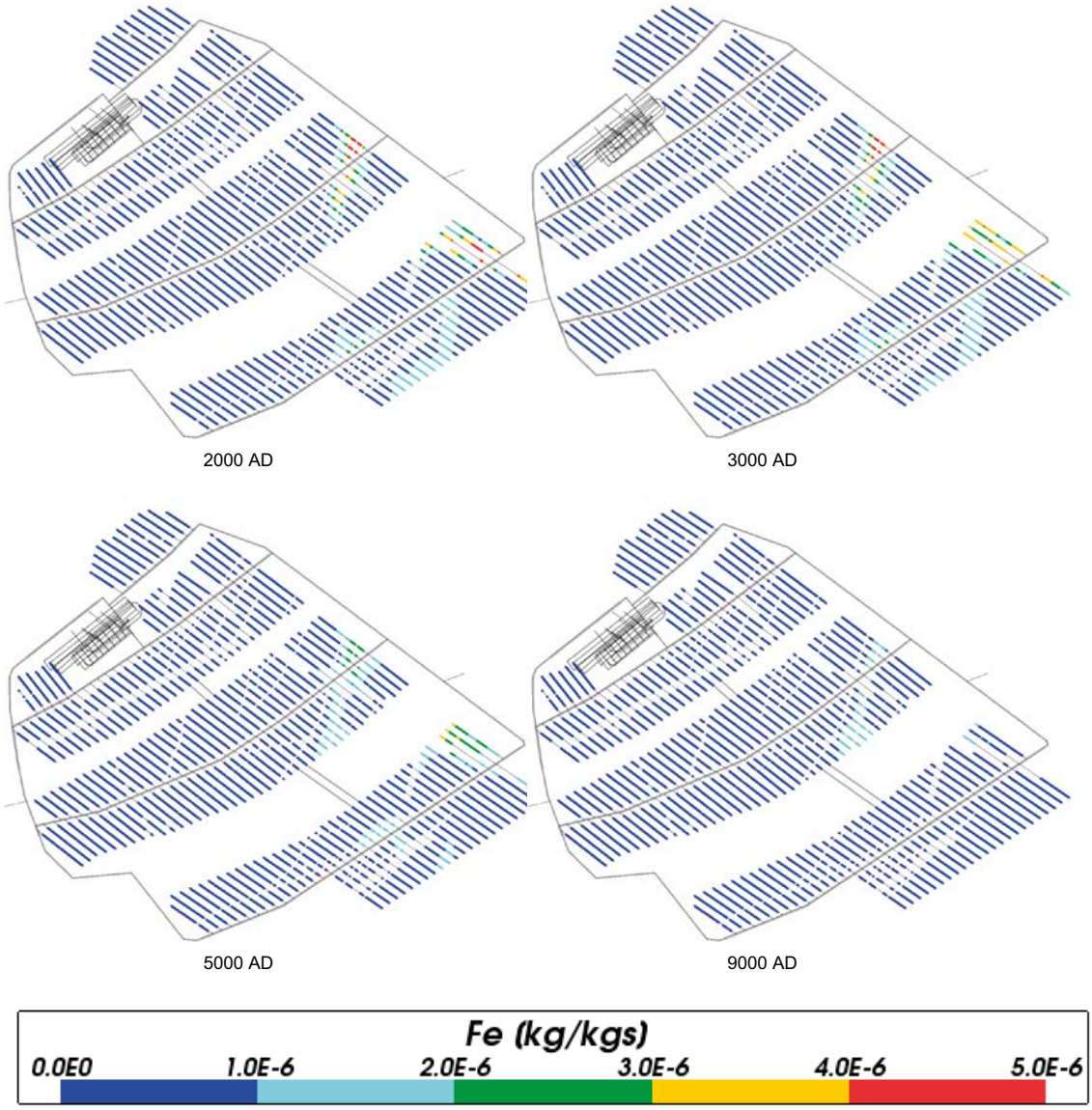


***Figure 4-128.*** *Total iron mass fractions for Case 4 at deposition hole locations for time periods 2000 AD to 9000 AD.*

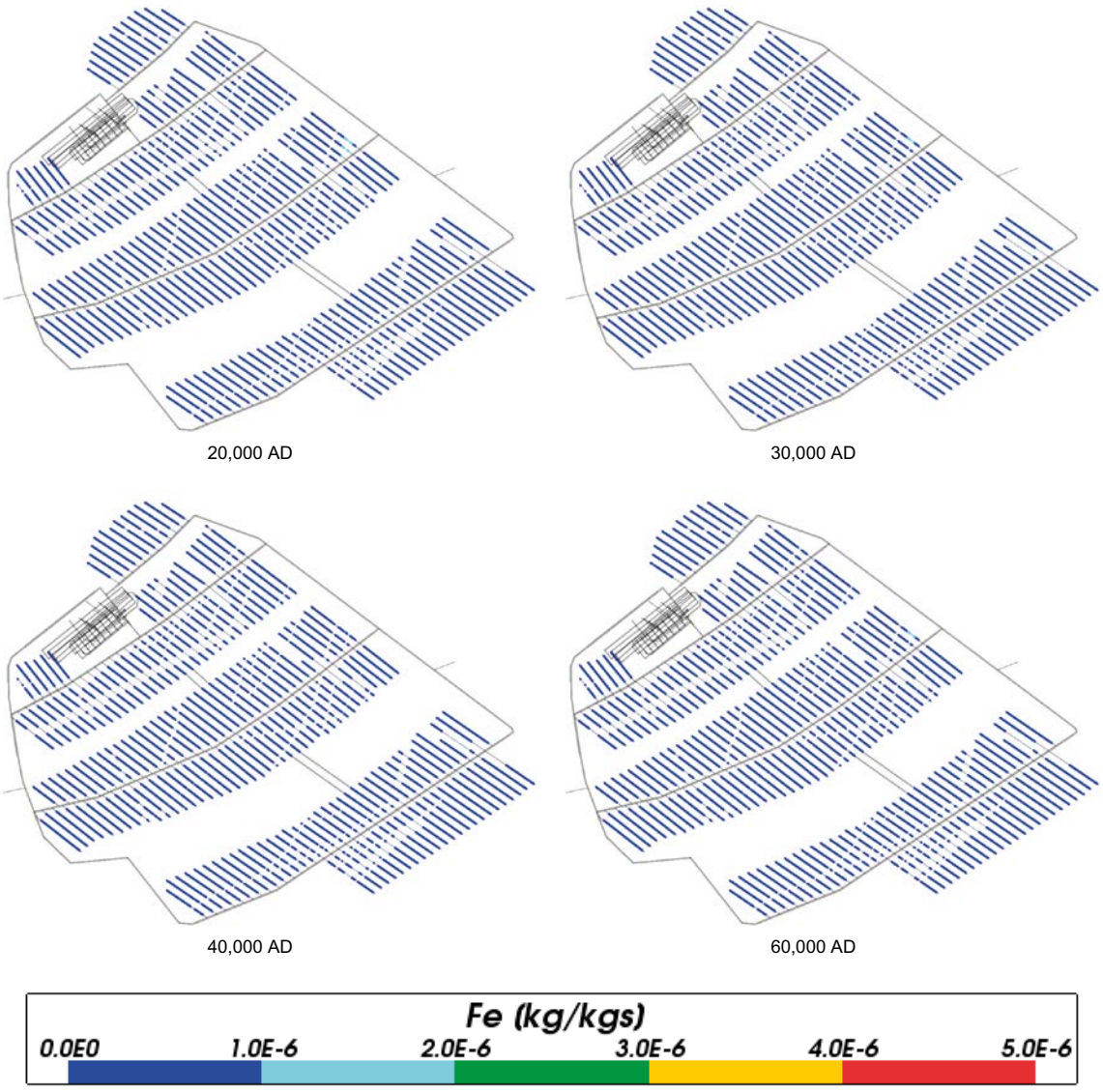


***Figure 4-129.*** *Total iron mass fractions for Case 4 at deposition hole locations for time periods 20,000 AD to 60,000 AD.*

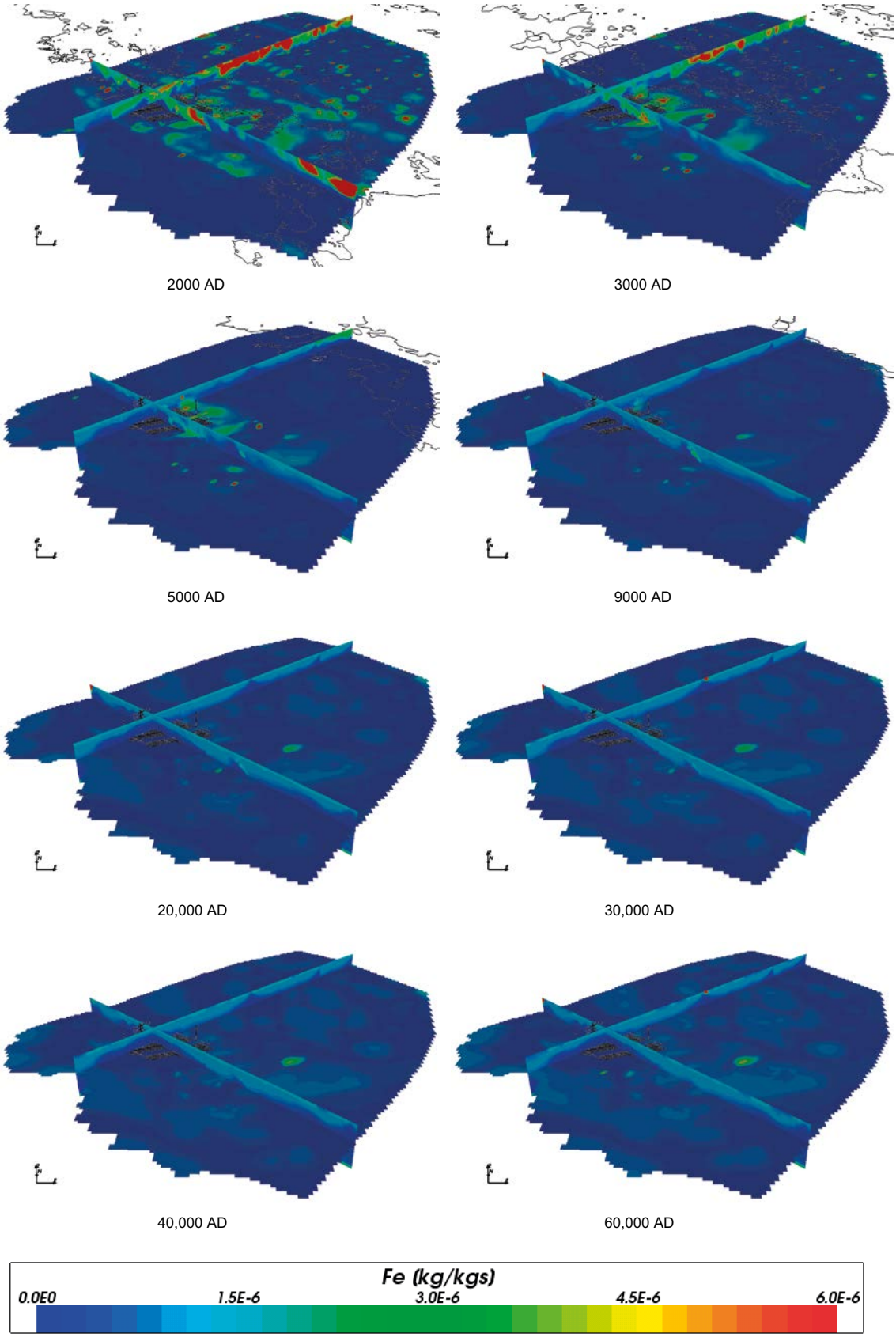


***Figure 4-130.*** *Total iron mass fractions on regional scale slices through the repository volume for Case 4 for time periods 2000 AD to 60,000 AD.*

### 4.5.8 Sodium

The mean value of sodium concentrations around the repository (Figure 4-131, Figure 4-132 and Figure 4-133) decreases with time similarly as for Cases 1 to 3. Also the spatial evolution in sodium concentrations in the repository volume (Figure 4-132 and Figure 4-133) and in the model volume (Figure 4-134) is relatively similar to Cases 1 to 3. This indicates that the chemical equilibrium reactions considered in Case 4 have only minor influence on the sodium concentrations, despite being involved in one of the mineral phases considered.

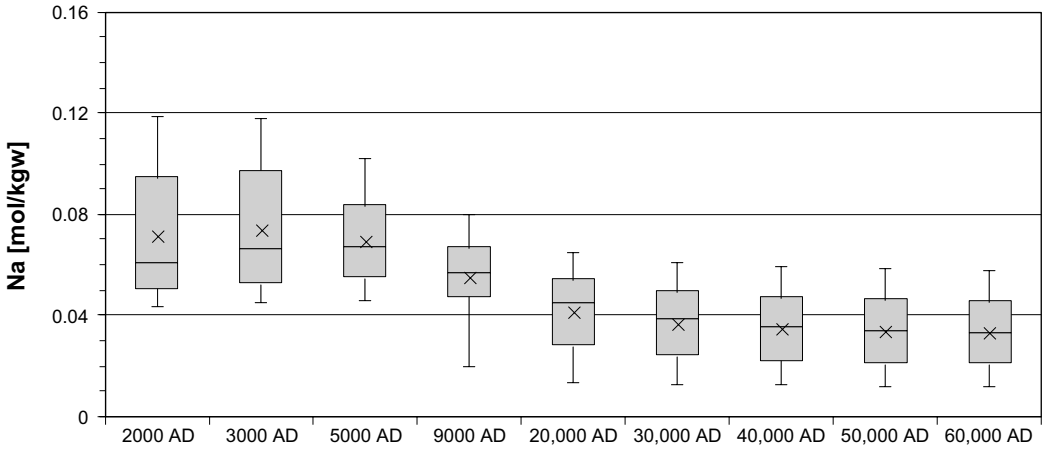


***Figure 4-131.*** *Box and whisker plot showing the statistical distribution of total sodium molalities for Case 4 on a regular grid of points within the repository volume between elevations –490 m and –450 m. The statistical measures are the median, the 25$^{th}$ and 75$^{th}$ percentiles (box), the mean (cross) and the 5$^{th}$ and 95$^{th}$ percentiles (whiskers).*

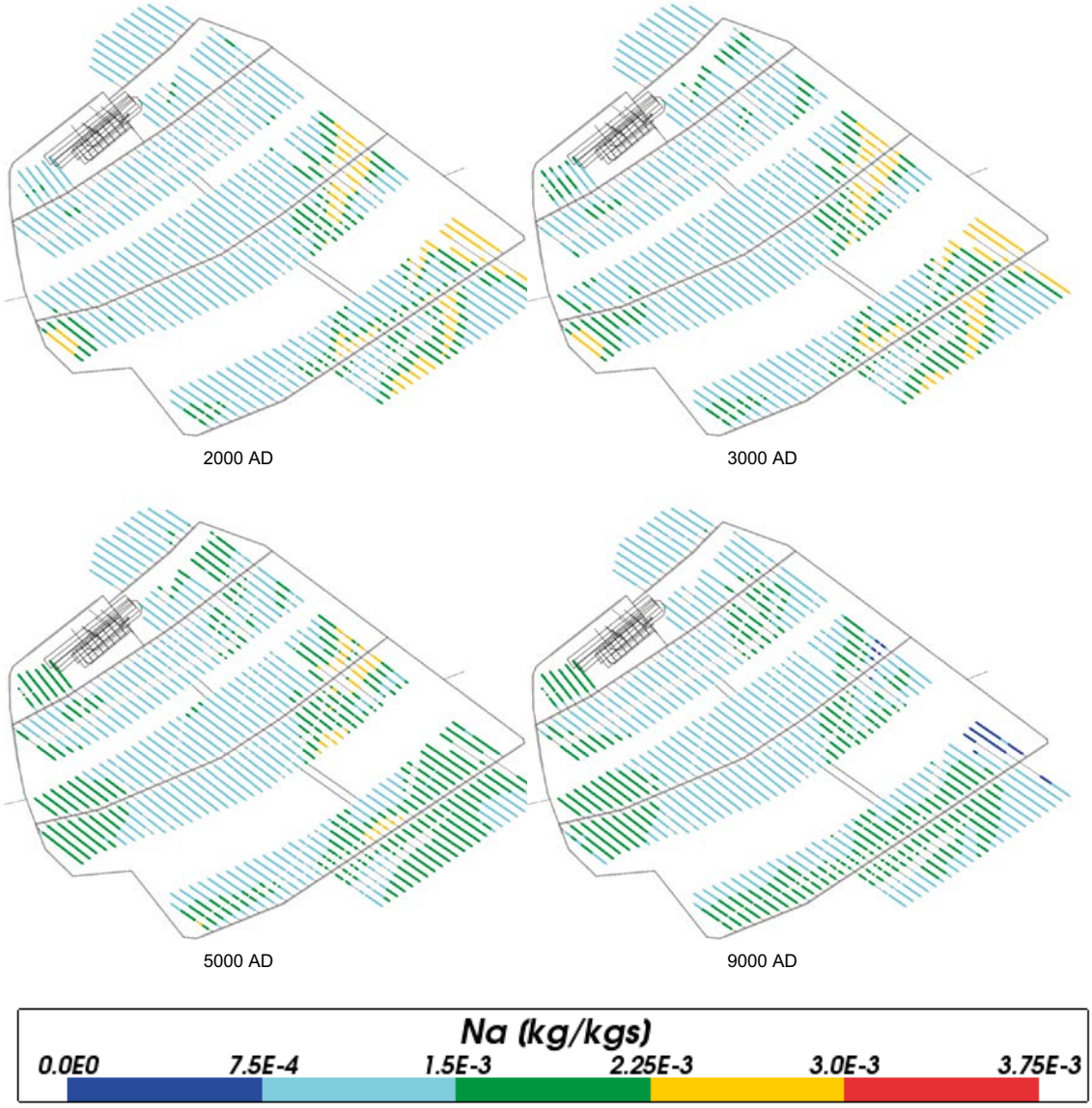


***Figure 4-132.*** *Total sodium mass fractions for Case 4 at deposition hole locations for time periods 2000 AD to 9000 AD.*

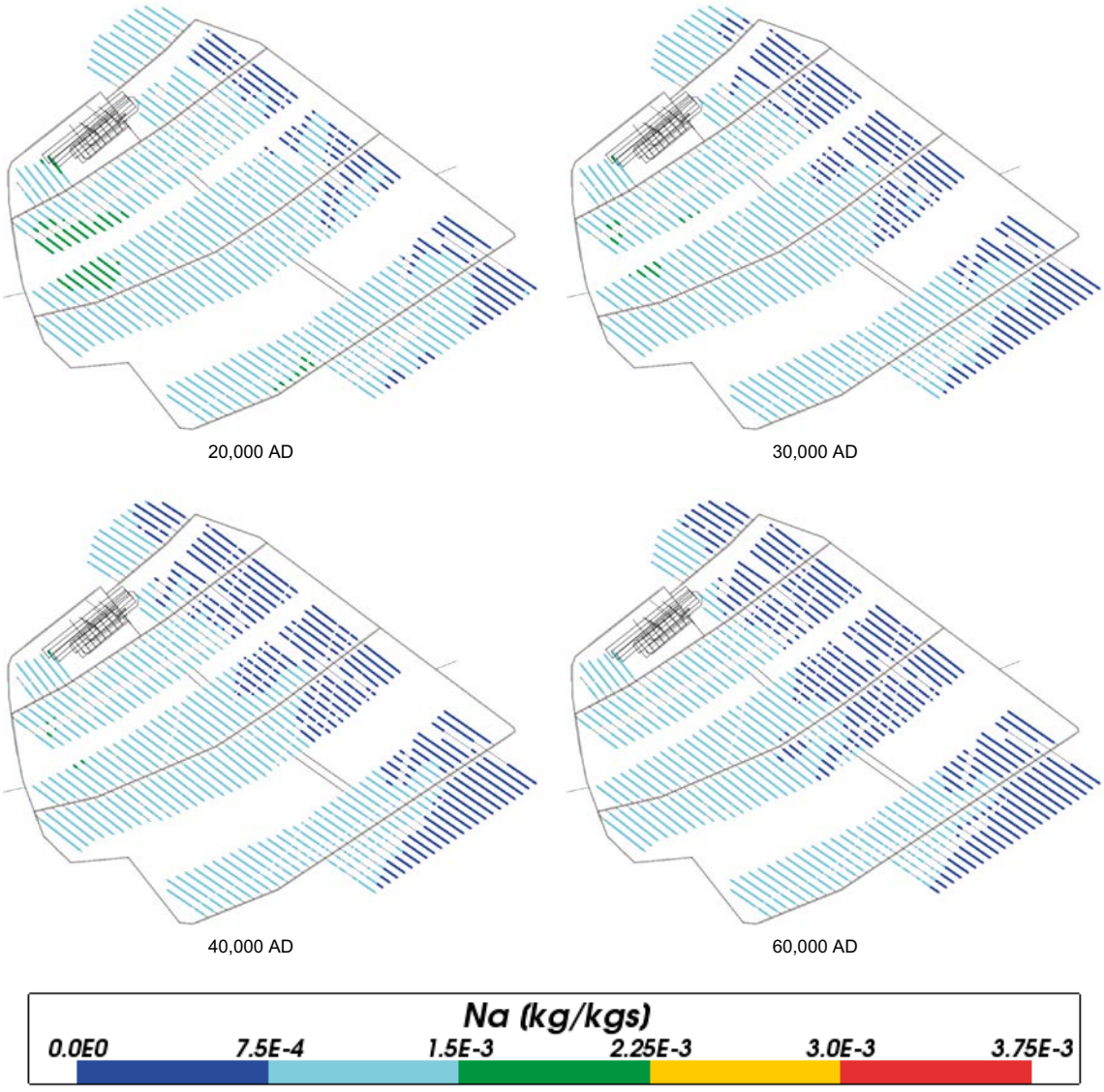


***Figure 4-133.*** *Total sodium mass fractions for Case 4 at deposition hole locations for time periods 20,000 AD to 60,000 AD.*

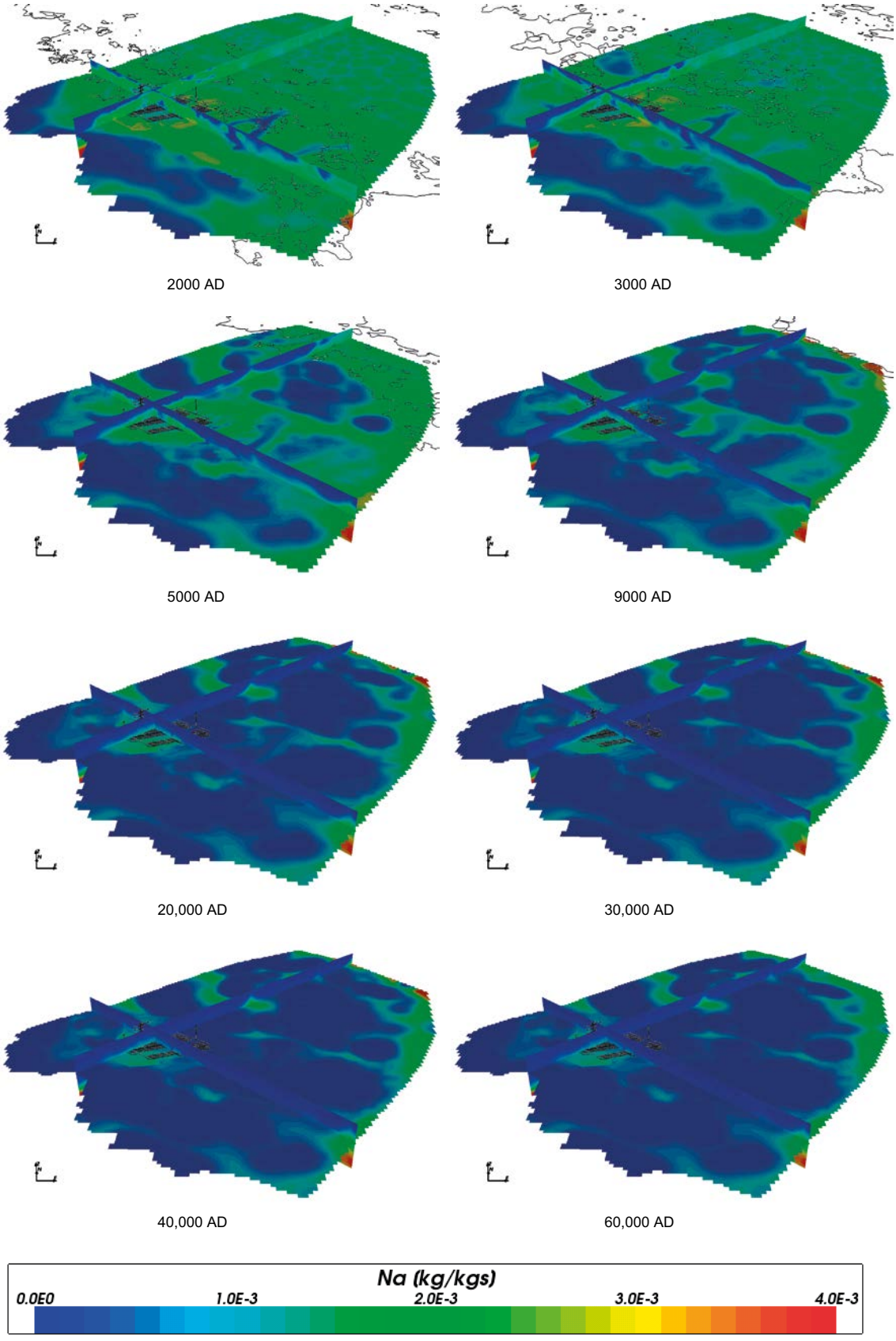


***Figure 4-134.*** *Total sodium mass fractions on regional scale slices through the repository volume for Case 4 for time periods 2000 AD to 60,000 AD.*

### 4.5.9 Potassium

In Case 4, K-feldspar is assumed to be in local equilibrium with the groundwater. This equilibrium constraint is not included in the other cases considered. The combined effect of the additional minerals in Case 4 resulted in a spatial and temporal distribution of potassium that is shifted towards lower concentrations as compared to the other cases considered. This is seen from Figure 4-135 for the repository volume, Figure 4-136 and Figure 4-137 for the canister positions, and Figure 4-138 for the regional model domain. The median potassium concentration in the repository volume is almost one order of magnitude lower as compared to the other cases, approximately $10^{-4}$ mol/kg$_w$ at times up to 9000 AD, after which the concentration declines and stabilises at about half of that value, approximately $5 \cdot 10^{-5}$ mol/kg$_w$.

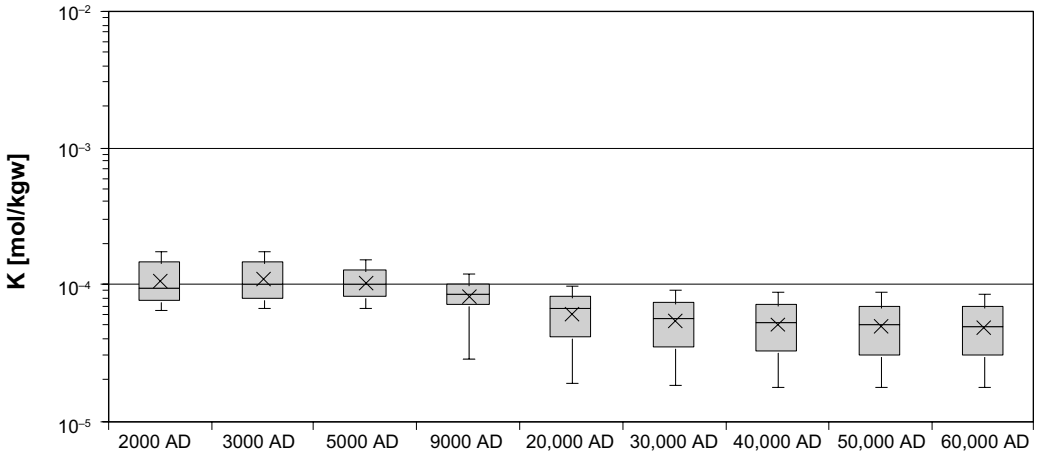


***Figure 4-135.*** *Box and whisker plot showing the statistical distribution of potassium molalities for Case 4 on a regular grid of points within the repository volume between elevations –490 m and –450 m. The statistical measures are the median, the 25$^{th}$ and 75$^{th}$ percentiles (box), the mean (cross) and the 5$^{th}$ and 95$^{th}$ percentiles (whiskers).*

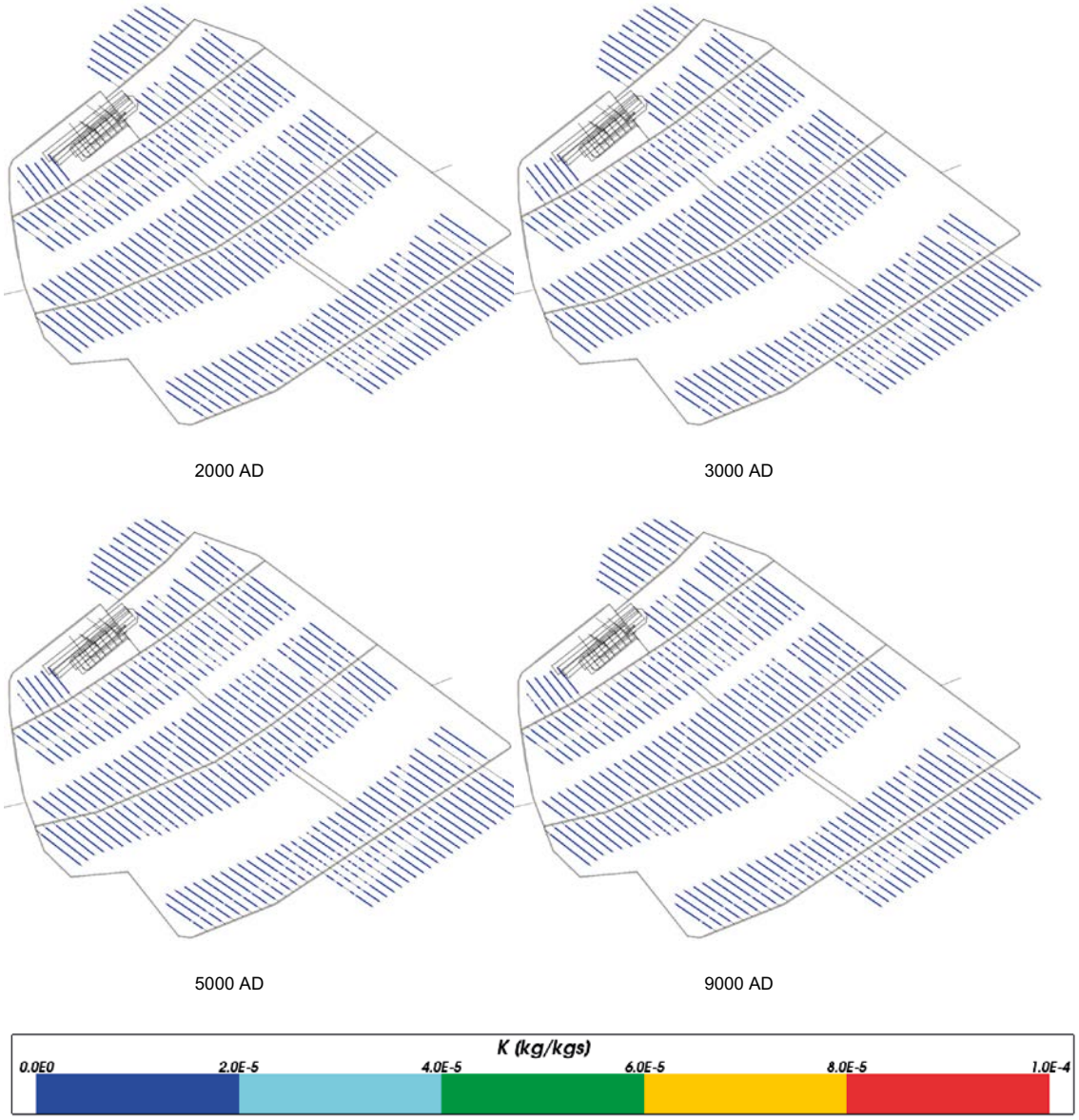


***Figure 4-136.*** *Total potassium mass fractions for Case 4 at deposition hole locations for time periods 2000 AD to 9000 AD.*

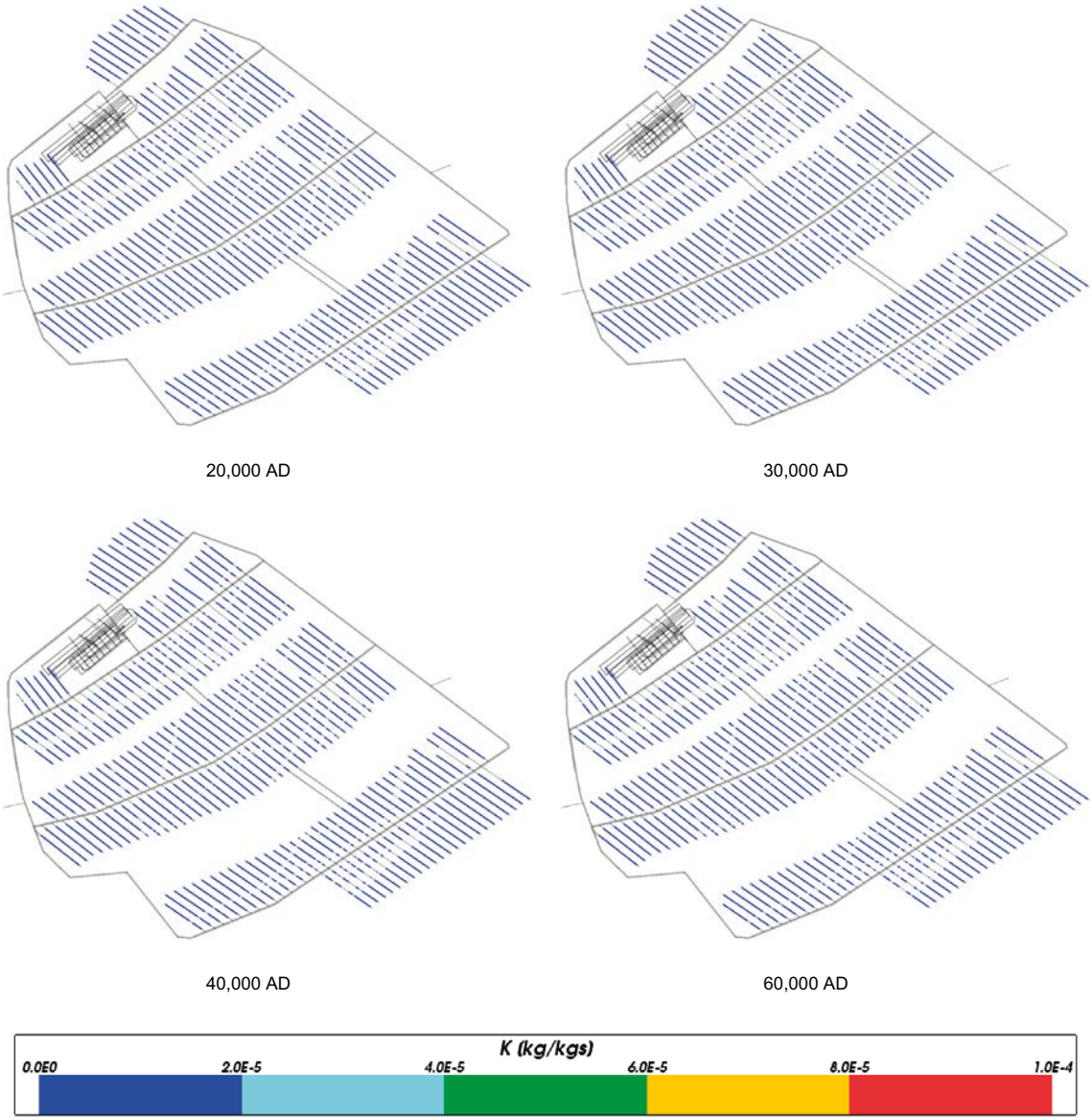


***Figure 4-137.*** *Total potassium mass fractions for Case 4 at deposition hole locations for time periods 20,000 AD to 60,000 AD.*

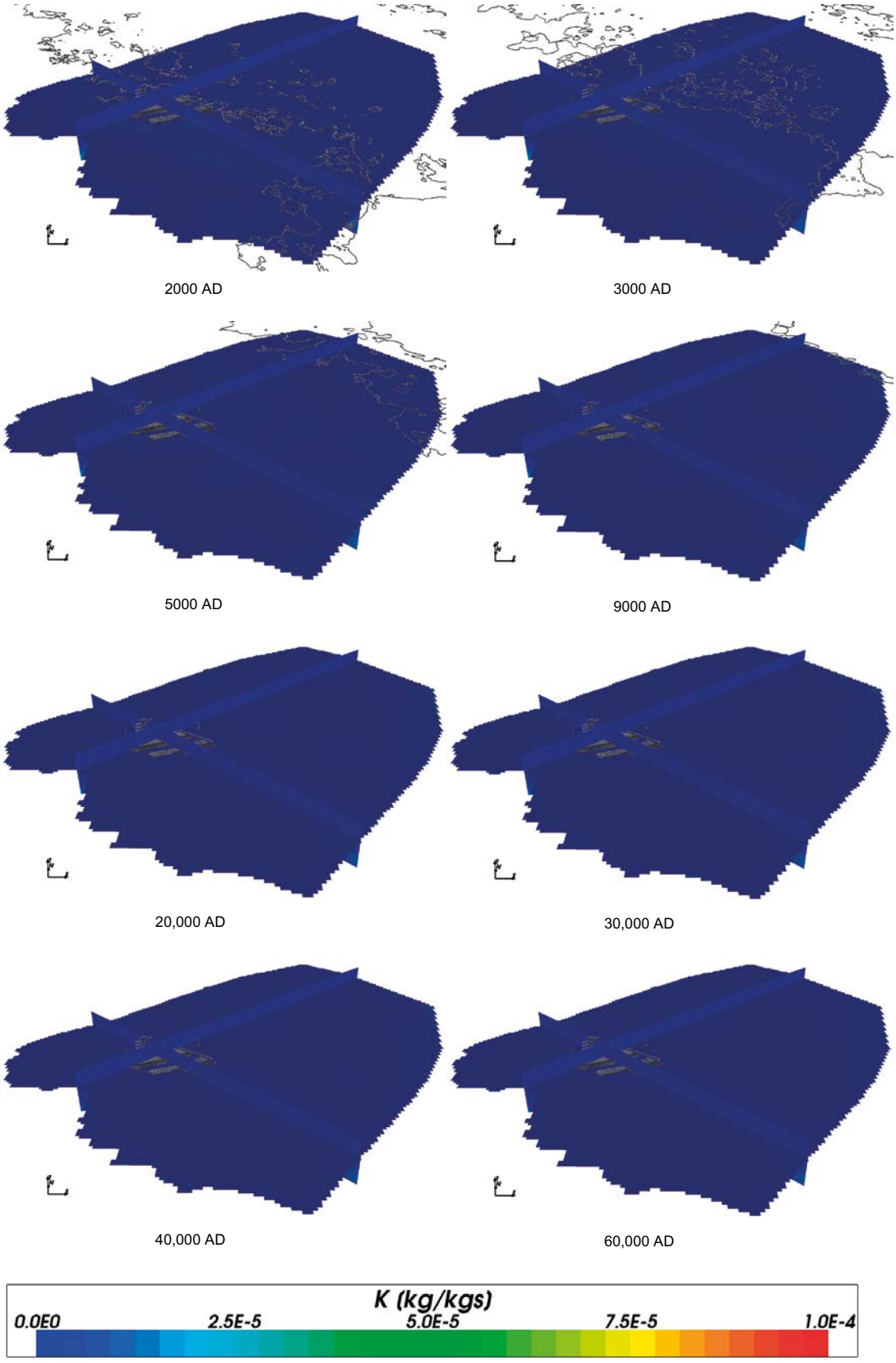


***Figure 4-138.*** *Total potassium mass fractions on regional scale slices through the repository volume for Case 4 for time periods 2000 AD to 60,000 AD.*

### 4.5.10 Sulphate

Figure 4-139 shows the evolution in sulphate concentrations around the repository. The mean values are similar to those in Case 2, but with a greater spatial variability at the early times up to 5,000 AD in Case 4. The increased variability is due to the assumed equilibrium constraints for the additional minerals in Case 4. The total sulphur does not differ significantly between Case 2 and Case 4 (not shown in the figures). This indicates that parts of the volume may contain a larger portion of sulphide. This is also reflected in the larger Eh variability in Case 4 as compared to Case 2. The spatial variability within the repository volume is shown in Figure 4-140 and Figure 4-141.

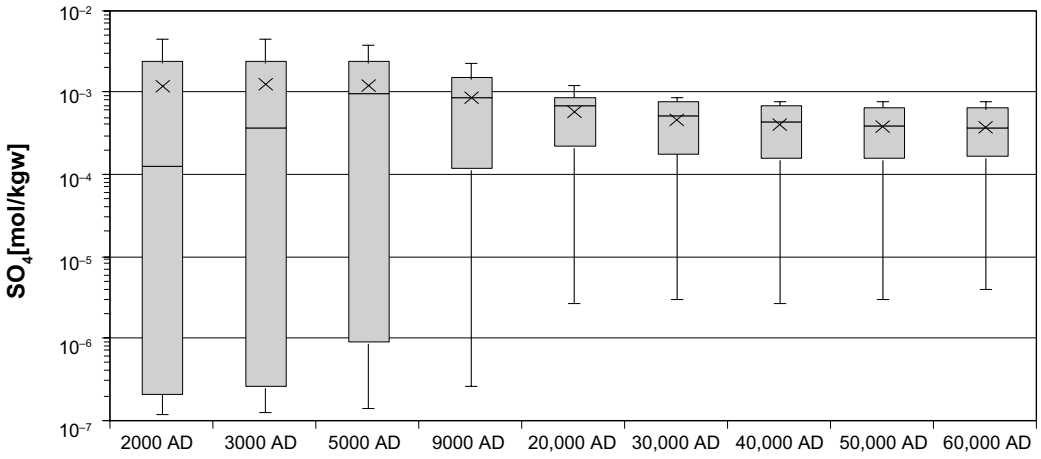


***Figure 4-139.*** *Box and whisker plot showing the statistical distribution of sulphate molalities for Case 4 on a regular grid of points within the repository volume between elevations –490 m and –450 m. The statistical measures are the median, the 25$^{th}$ and 75$^{th}$ percentiles (box), the mean (cross) and the 5$^{th}$ and 95$^{th}$ percentiles (whiskers).*

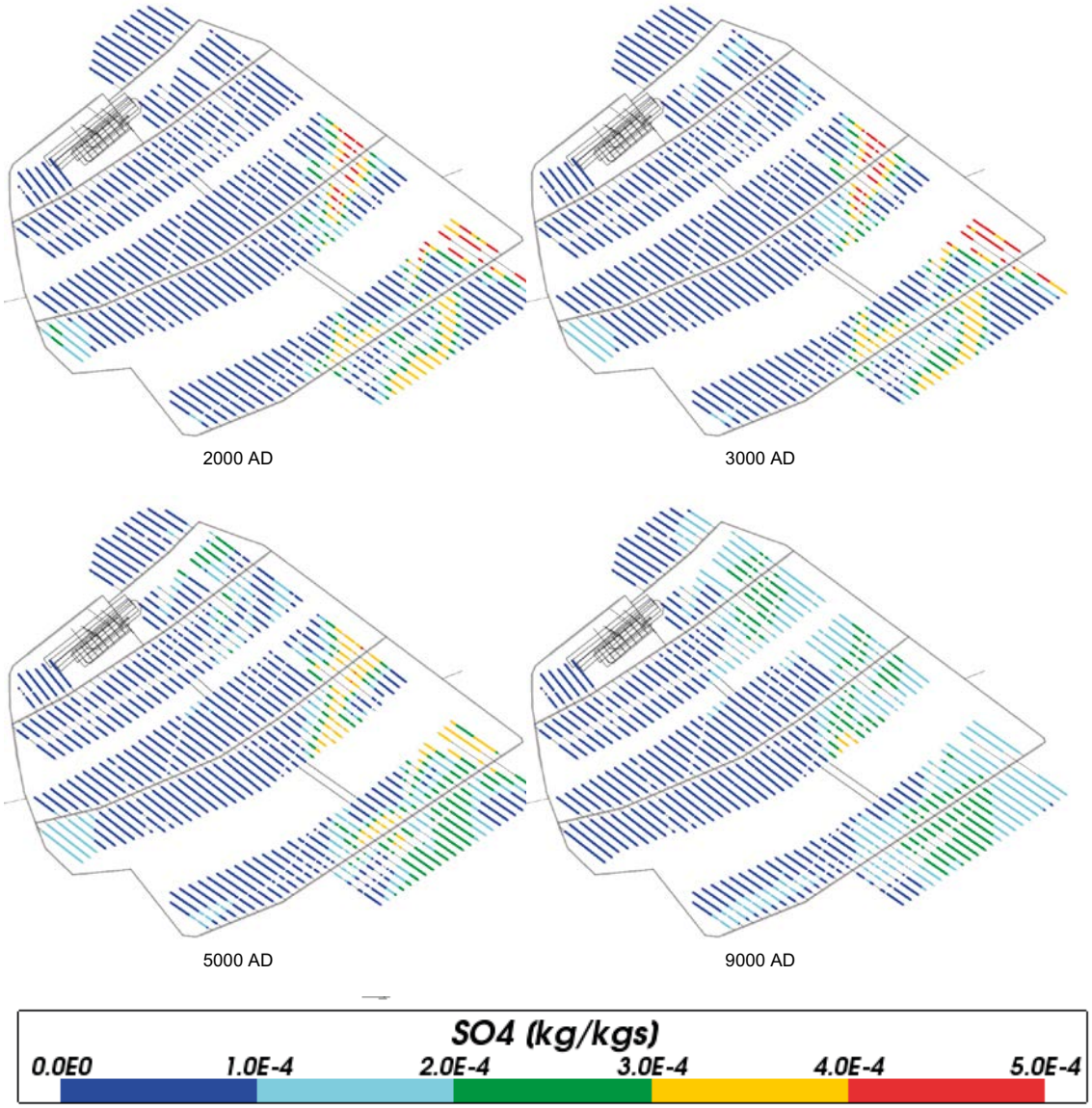


***Figure 4-140.*** *Total sulphate mass fractions for Case 4 at deposition hole locations for time periods 2000 AD to 9000 AD.*

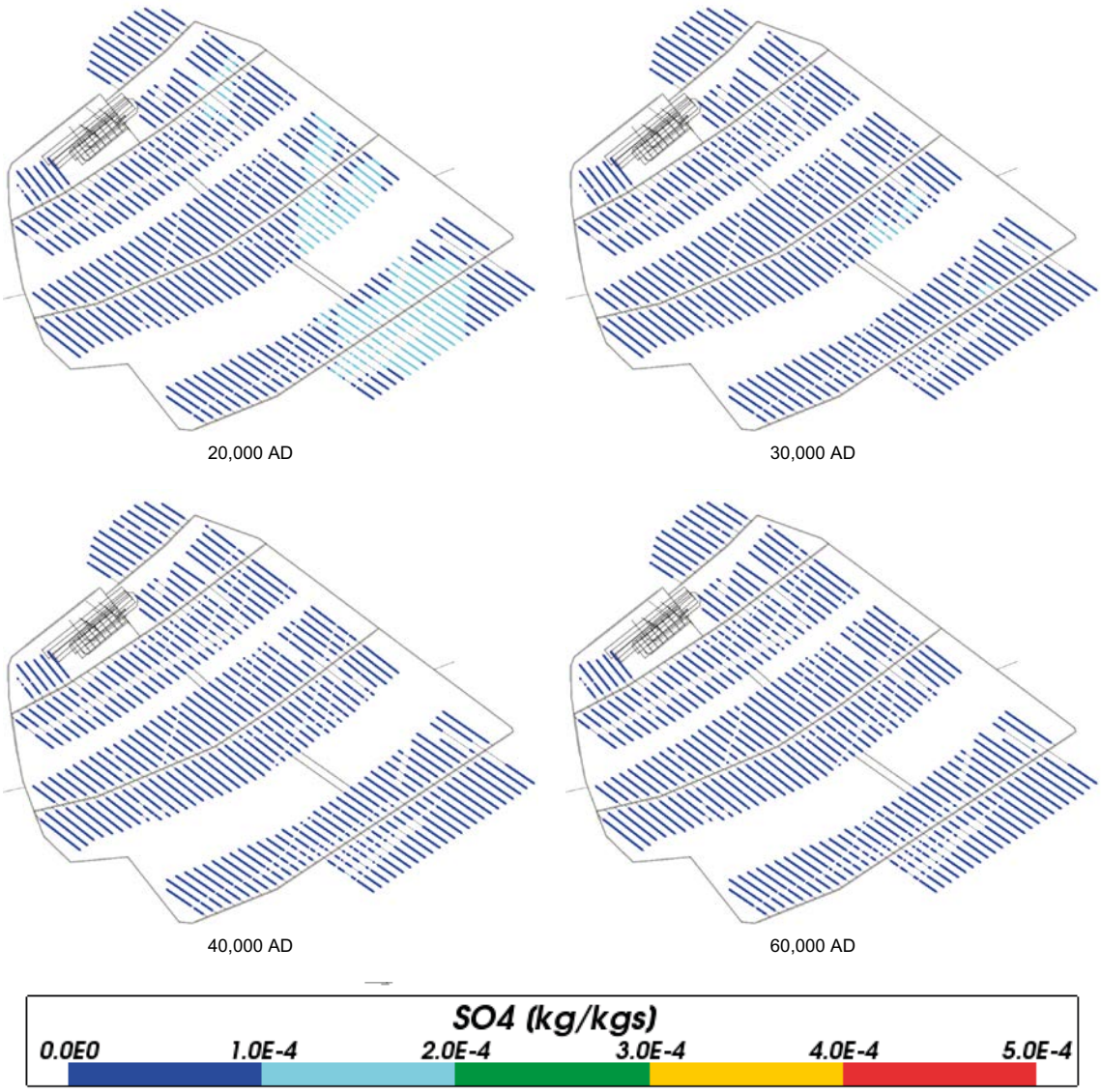


***Figure 4-141.*** *Total sulphate mass fractions for Case 4 at deposition hole locations for time periods 20,000 AD to 60,000 AD.*

### 4.5.11 Summary for Case 4

In addition to the groundwater flow and transport processes considered in Case 1, Case 4 includes equilibration of groundwater with calcite, quartz, amorphous iron (II) sulphide, kaolinite, albite, and K-feldspar. Case 4 differs from Case 2 in that it includes the additional minerals kaolinite, albite and K-feldspar, assumed to be in equilibrium with the groundwater. The effect of the assumed local equilibrium constraints with these additional minerals is primarily seen at the early times up to 9000 AD. The salinity, total cation concentrations, and the concentrations of non-reacting species such as chloride were similar to those calculated for Cases 1 to 3. The results for calcium and sodium were also very similar in Cases 2 and 4. The reactions significantly affected the concentrations of total inorganic carbon, iron, potassium, and sulphate, and also pH and Eh, in particular at the early times up to 9000 AD. The change in Eh was less than in Case 2 with the median slightly falling from approximately –200 mV at 2000 AD to –220 mV at 60,000 AD. The slight decline in median Eh was accompanied by a significantly decreasing spatial variability with time. Also the pH within the repository volume had an opposite evolution as compared with Case 2, and rose from a median of around 6.8 at 2000 AD to around 7.1 at 60,000 AD. The slight decline in median Eh over time is consistent with the rise in pH, which is due to the assumed equilibrium constraints with the additional mineral phases. It should be emphasised that the equilibrium assumption in Case 4 may be considered aggressive, in particular for some of the mineral reactions that are known to be slow under these conditions. The results for this case should therefore be considered with caution and not be regarded as a reliable prediction of a future groundwater evolution. Instead, the results may be taken as a thermodynamically permissible yet probably unrealistic example. Despite the differences in the chemical evolution in Case 4 as compared with the other cases, the geochemical conditions within the repository volume for this case remained within the bounds required by the safety assessment throughout the simulation period.

## 4.6 Case 5

The evolution of groundwater composition for this case will be due to the transport and mixing of components originating from different reference waters. The concentrations of reactive species will be modified by equilibrium reactions with the mineral phases considered. The number and types of mineral phases considered (see Section 3.2) is the same as for Case 2, where equilibration of the groundwater with calcite, quartz and amorphous iron (II) sulphide was included. Case 5 differs in that it includes a more dilute meteoric water (Dilute Meteoric water in Table 3-1) as compared to the other cases, infiltrating at the top boundary for land areas above sea level. It is expected that the equilibrium reactions will have an effect on pH, Eh, and the concentrations of total inorganic carbon, calcium, sulphur, and iron.

### 4.6.1 pH

Figure 4-142, Figure 4-143, Figure 4-144 show a decreasing pH with time for Case 5 around the repository, similar to that in Case 2 but with slightly higher mean pH values and less spatial variability in the repository volume after 30,000 AD. These differences are due to the more dilute meteoric water infiltrating land areas above sea level in Case 5. Figure 4-145 shows values of pH over the regional area.

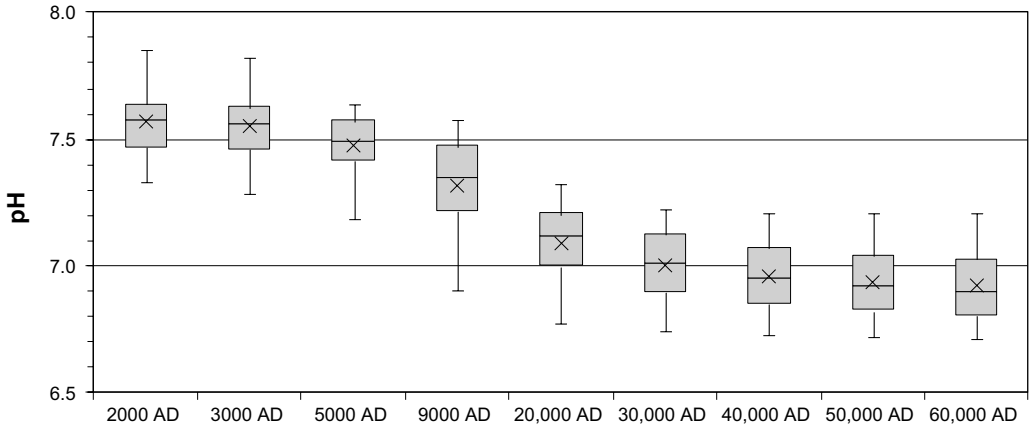


***Figure 4-142.*** *Box and whisker plot showing the statistical distribution of pH for Case 5 on a regular grid of points within the repository volume between elevations –490 m and –450 m. The statistical measures are the median, the 25th and 75th percentiles (box), the mean (cross) and the 5th and 95th percentiles (whiskers).*

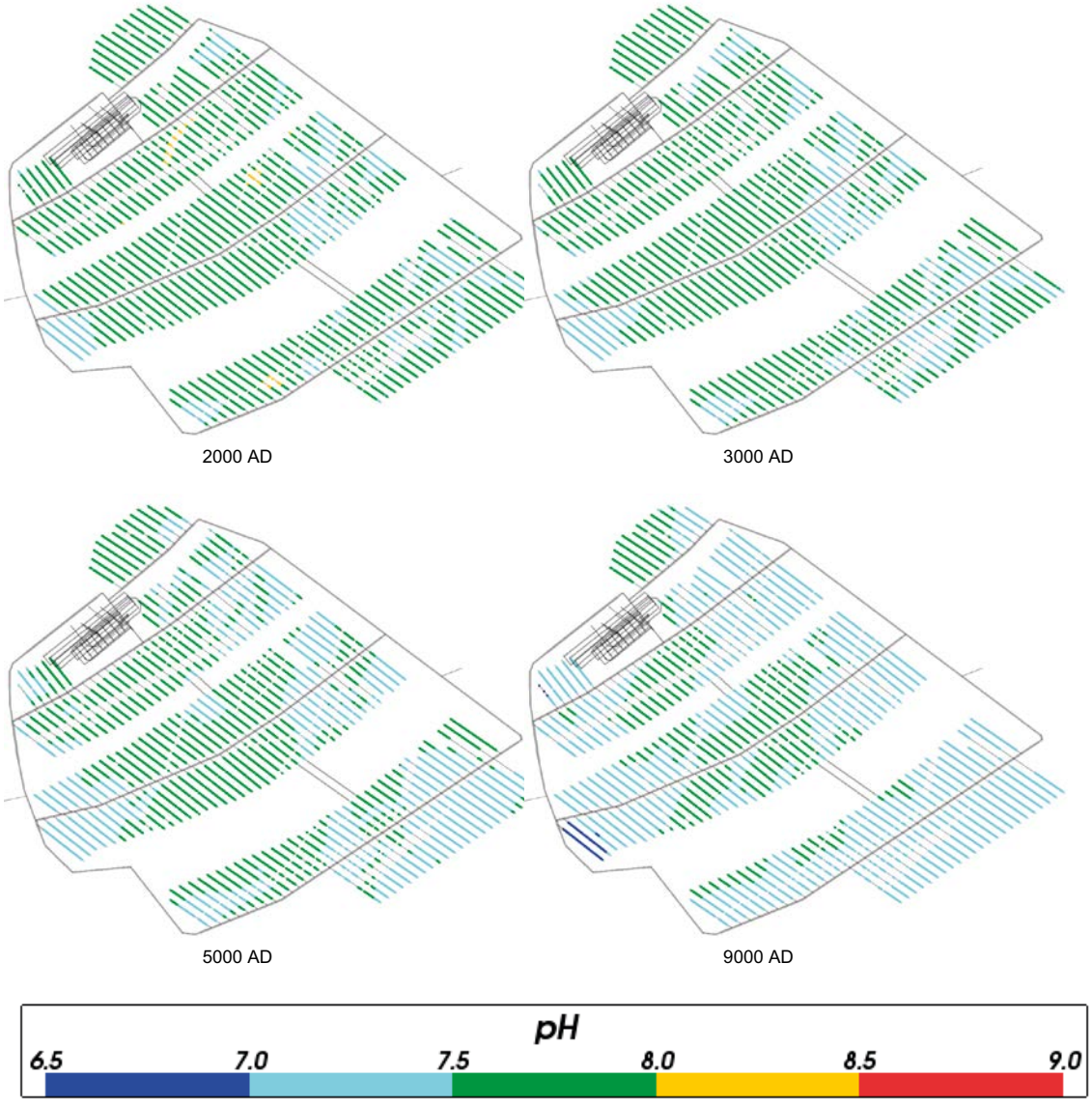


***Figure 4-143.*** *Values of pH for Case 5 at deposition hole locations for time periods 2000 AD to 9000 AD.*

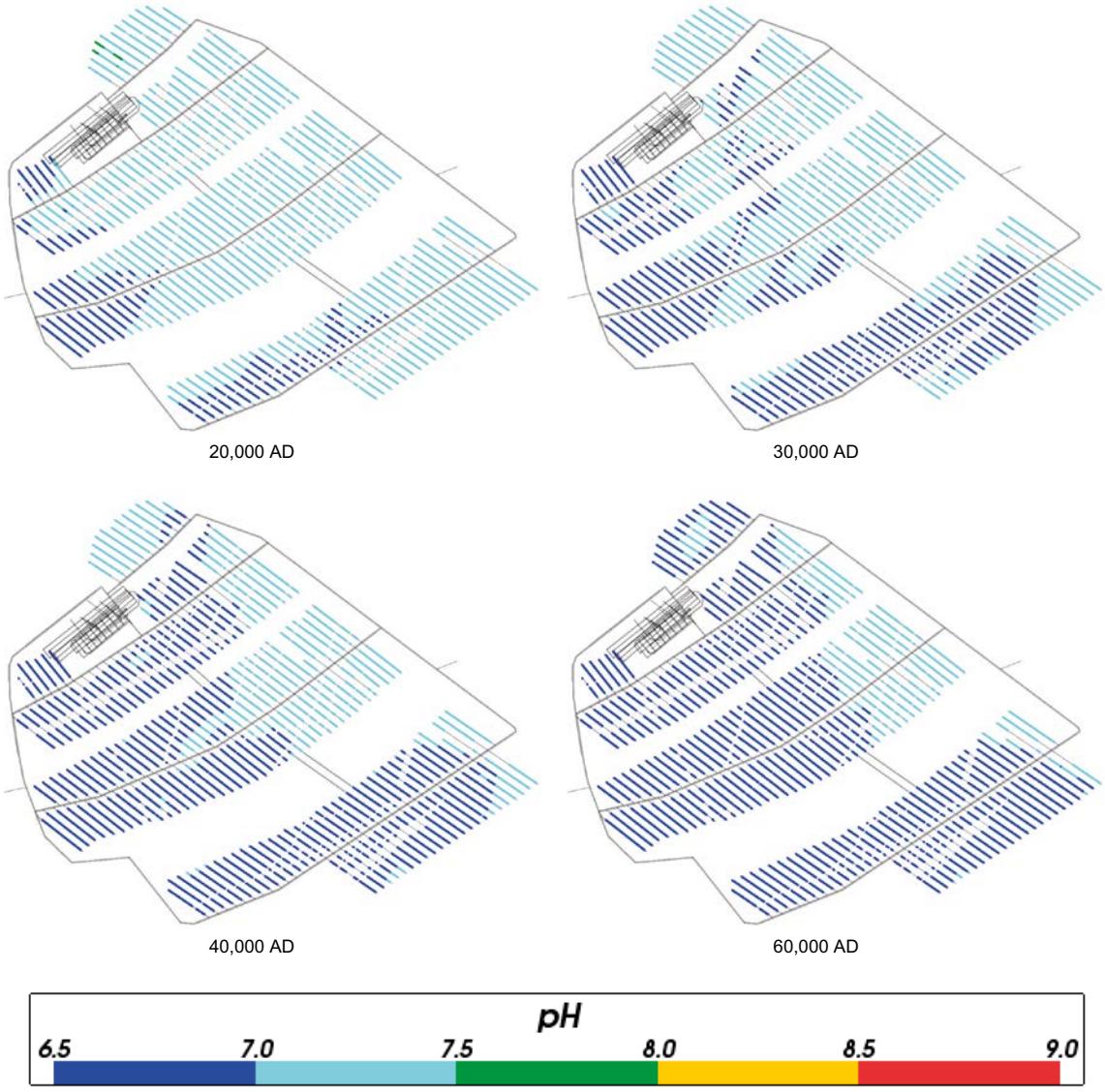


***Figure 4-144.*** *Values of pH for Case 5 at deposition hole locations for time periods 20,000 AD to 60,000 AD.*

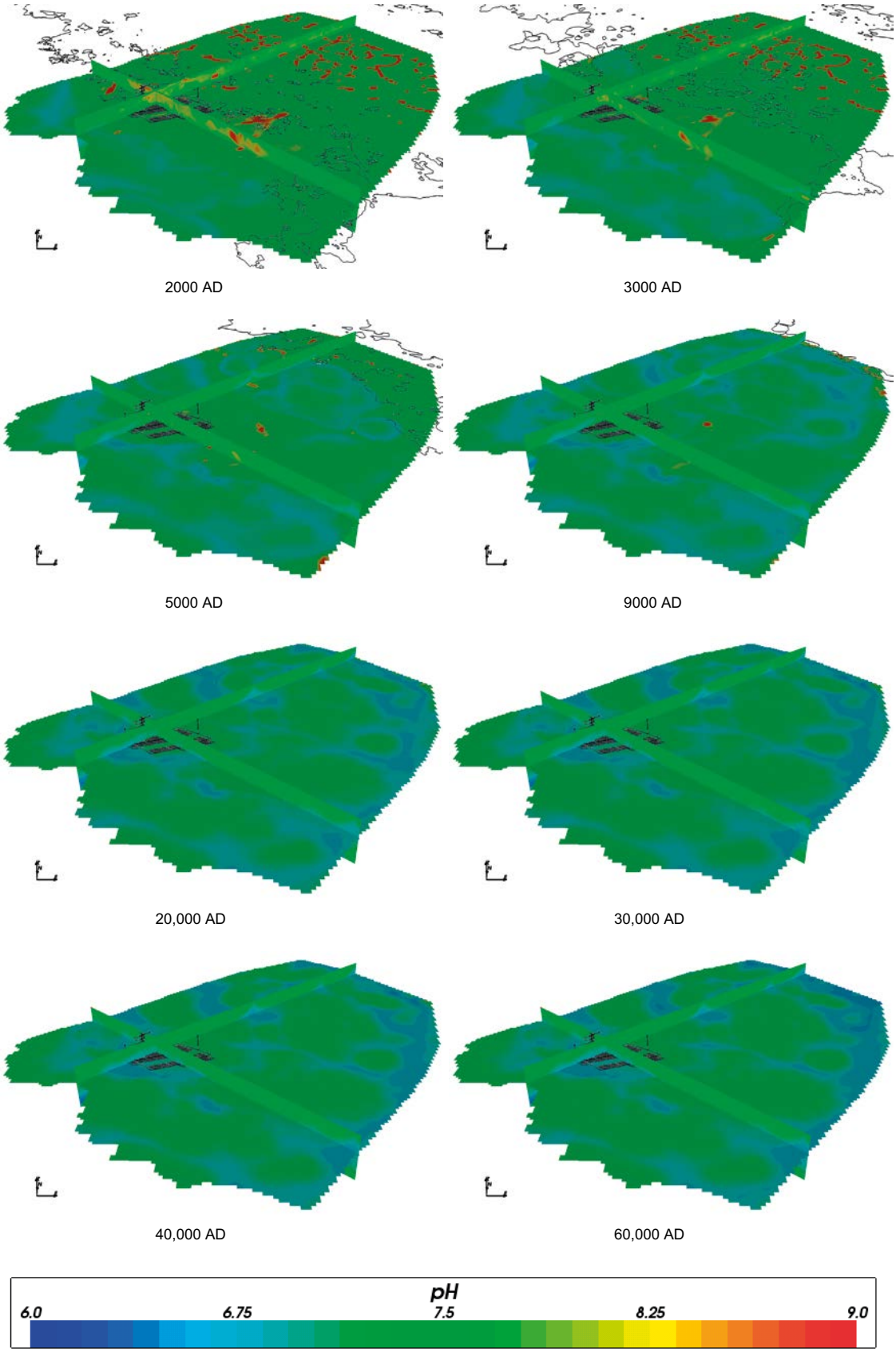


***Figure 4-145.*** *Values of pH on regional scale slices through the repository volume for Case 5 for time periods 2000 AD to 60,000 AD.*

### 4.6.2 Eh (or pe)

Figure 4-146 shows the value of Eh in the repository region and Figure 4-147 and Figure 4-148 show the value of pe at the deposition hole locations for Case 5. These results are very similar to those for Case 2 with only slightly lower mean values and somewhat less spatial variability after 20,000 AD for Case 5.

Figure 4-149 shows the regional slice plots of pe over time for Case 5. As for Case 2, pe is increasing at early times, with larger values being swept in a north easterly direction, and little changes after 20,000 AD.

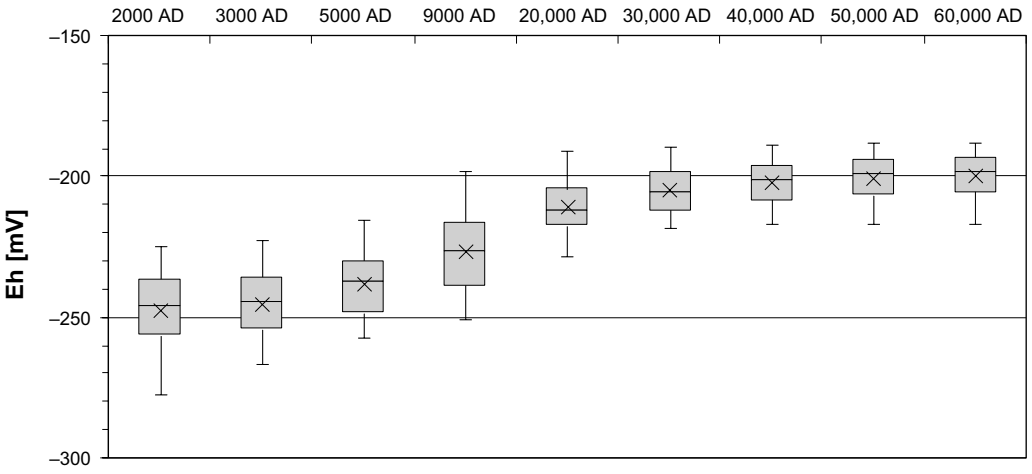


***Figure 4-146.*** *Box and whisker plot showing the statistical distribution of Eh for Case 5 on a regular grid of points within the repository volume between elevations –490 m and –450 m. The statistical measures are the median, the 25$^{th}$ and 75$^{th}$ percentiles (box), the mean (cross) and the 5$^{th}$ and 95$^{th}$ percentiles (whiskers).*

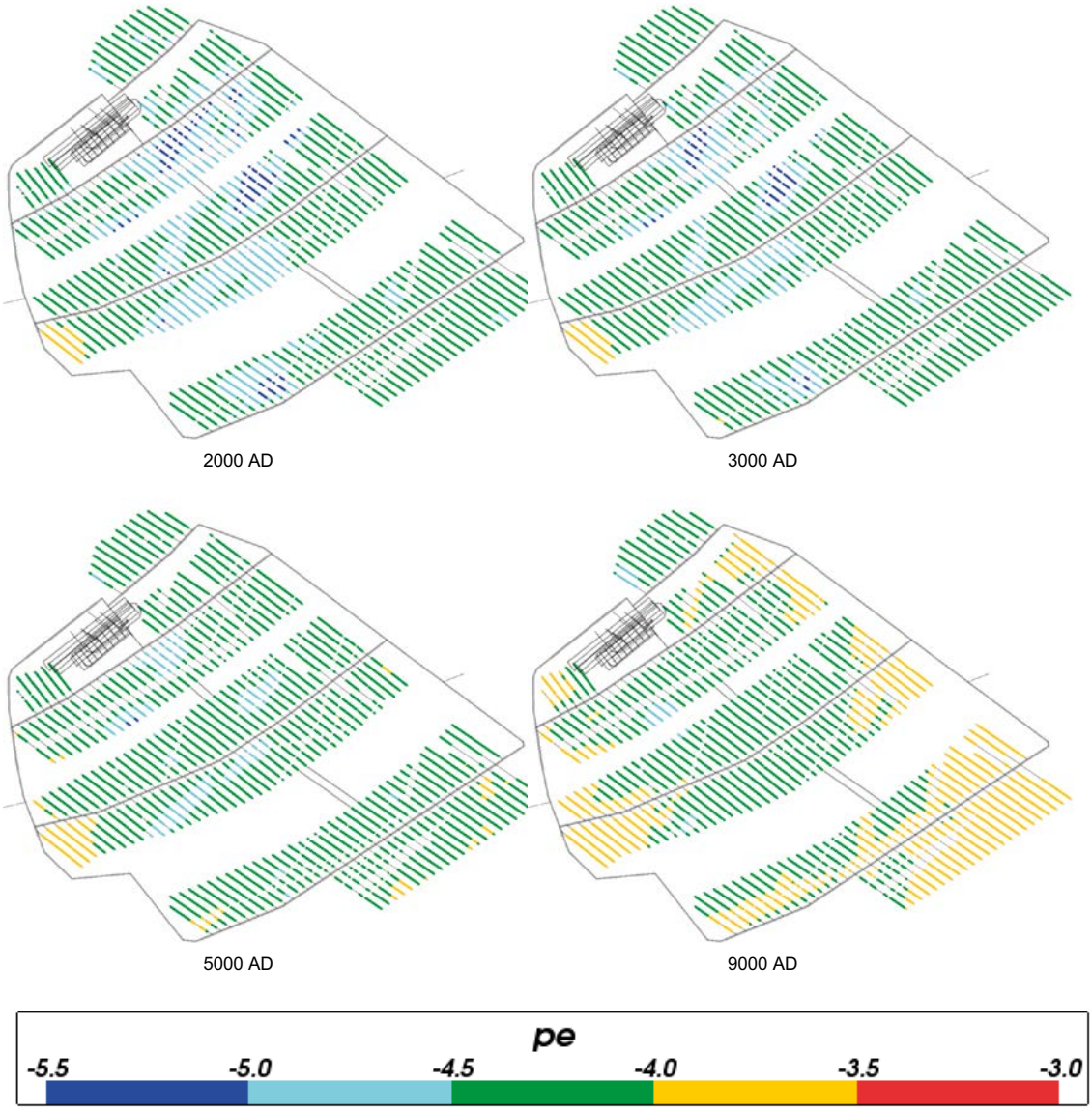


***Figure 4-147.*** *Values of pe for Case 5 at deposition hole locations for time periods 2000 AD to 9000 AD.*

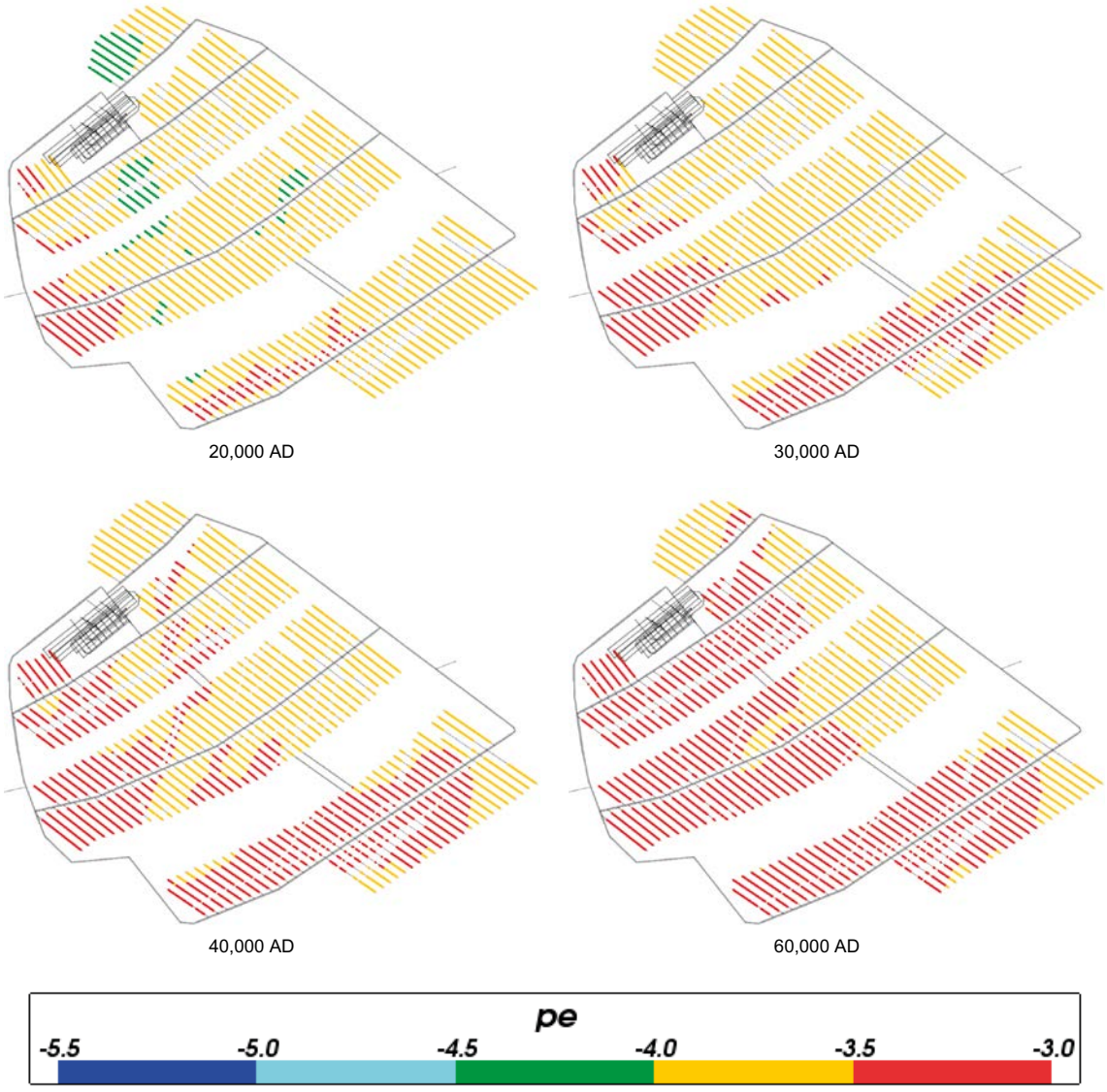


***Figure 4-148.*** *Values of pe for Case 5 at deposition hole locations for time periods 20,000 AD to 60,000 AD.*

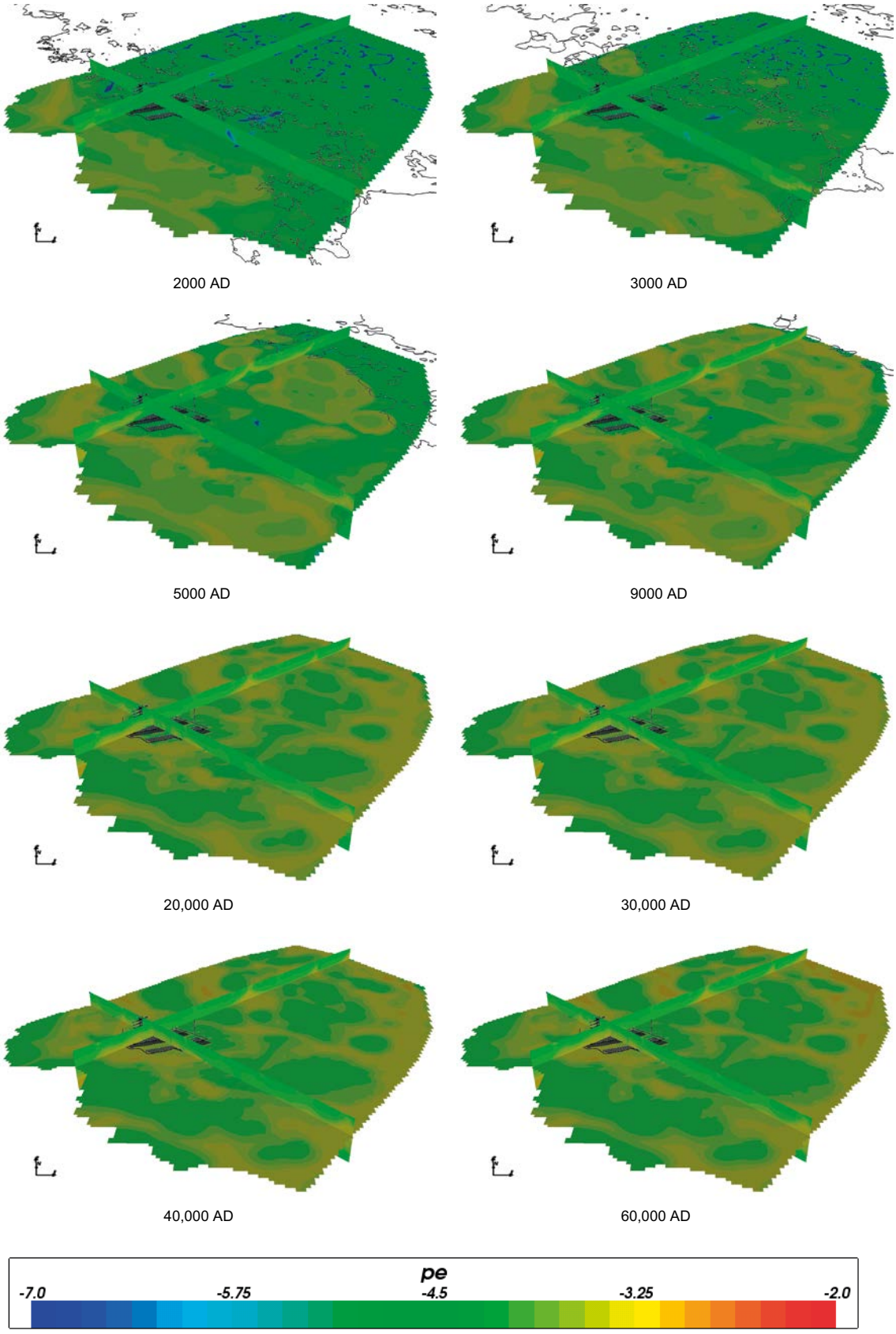


***Figure 4-149.*** *Values of pe on regional scale slices through the repository volume for Case 5 for time periods 2000 AD to 60,000 AD.*

### 4.6.3 TDS and sum of cations

Figure 4-150 and Figure 4-151 show the statistical distribution of TDS and the sum of cation charge molalities in the repository region for Case 5. The evolution with time is very similar to the corresponding results for Cases 1 and 2 with only slightly lower mean values of TDS for Case 5 than for Case 2, a difference that may be due to the more dilute meteoric water infiltrating land areas below sea level in Case 5.

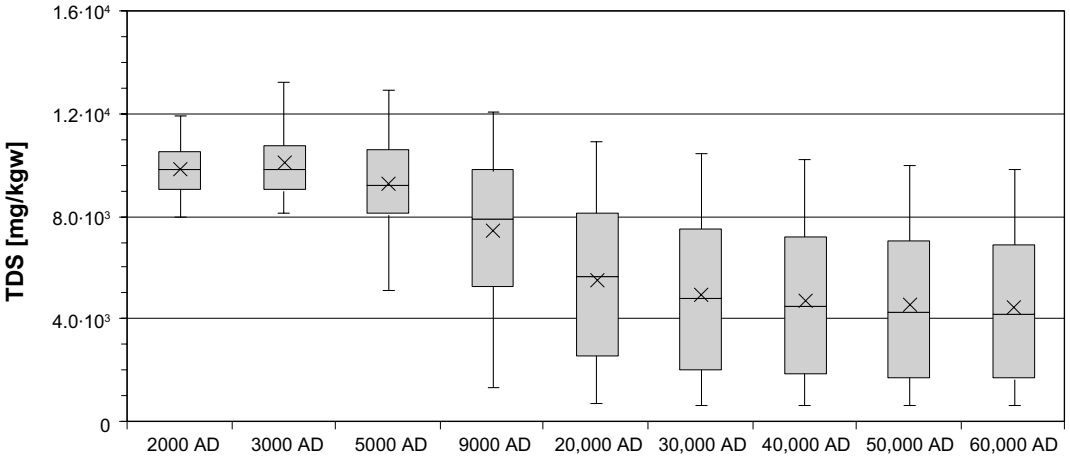


***Figure 4-150.*** *Box and whisker plot showing the statistical distribution of TDS for Case 5 on a regular grid of points within the repository volume between elevations –490 m and –450 m. The statistical measures are the median, the 25th and 75th percentiles (box), the mean (cross) and the 5th and 95th percentiles (whiskers).*

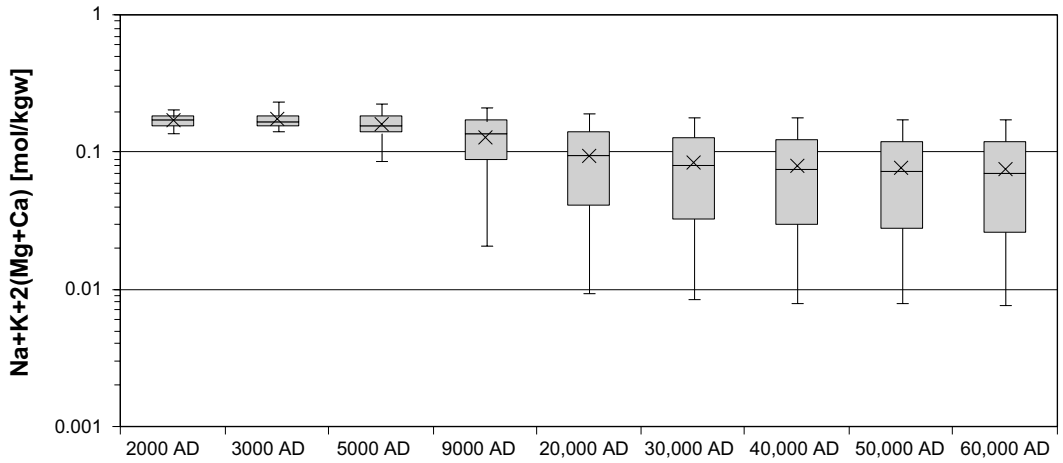


***Figure 4-151.*** *Box and whisker plot showing the statistical distribution of sum of cation charges (Na+K+2(Mg+Ca)) molalities for Case 5 on a regular grid of points within the repository volume between elevations –490 m and –450 m. The statistical measures are the median, the 25th and 75th percentiles (box), the mean (cross) and the 5th and 95th percentiles (whiskers).*

### 4.6.4 Inorganic carbon

Figure 4-152, Figure 4-153, Figure 4-154 and Figure 4-155 show plots of total inorganic carbon for Case 5. At early times up to 3,000 AD the total inorganic carbon concentrations in the repository region, shown in the first three figures, are very similar to that in Case 2. At later times the concentrations are lower in Case 5, as a consequence of the more dilute meteoric water infiltrating in that case. A similar trend, with generally lower concentrations of inorganic carbon on the regional scale in Case 5, can be seen when comparing Figure 4-155 with the corresponding figure for Case 2 (Figure 4-41).

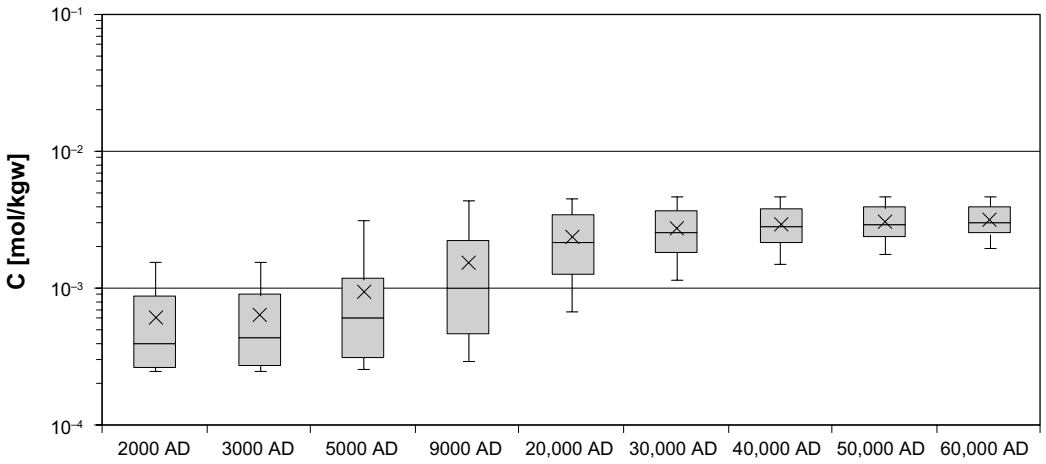


***Figure 4-152.*** *Box and whisker plot showing the statistical distribution of total inorganic carbon molalities for Case 5 on a regular grid of points within the repository volume between elevations –490 m and –450 m. The statistical measures are the median, the 25$^{th}$ and 75$^{th}$ percentiles (box), the mean (cross) and the 5$^{th}$ and 95$^{th}$ percentiles (whiskers).*

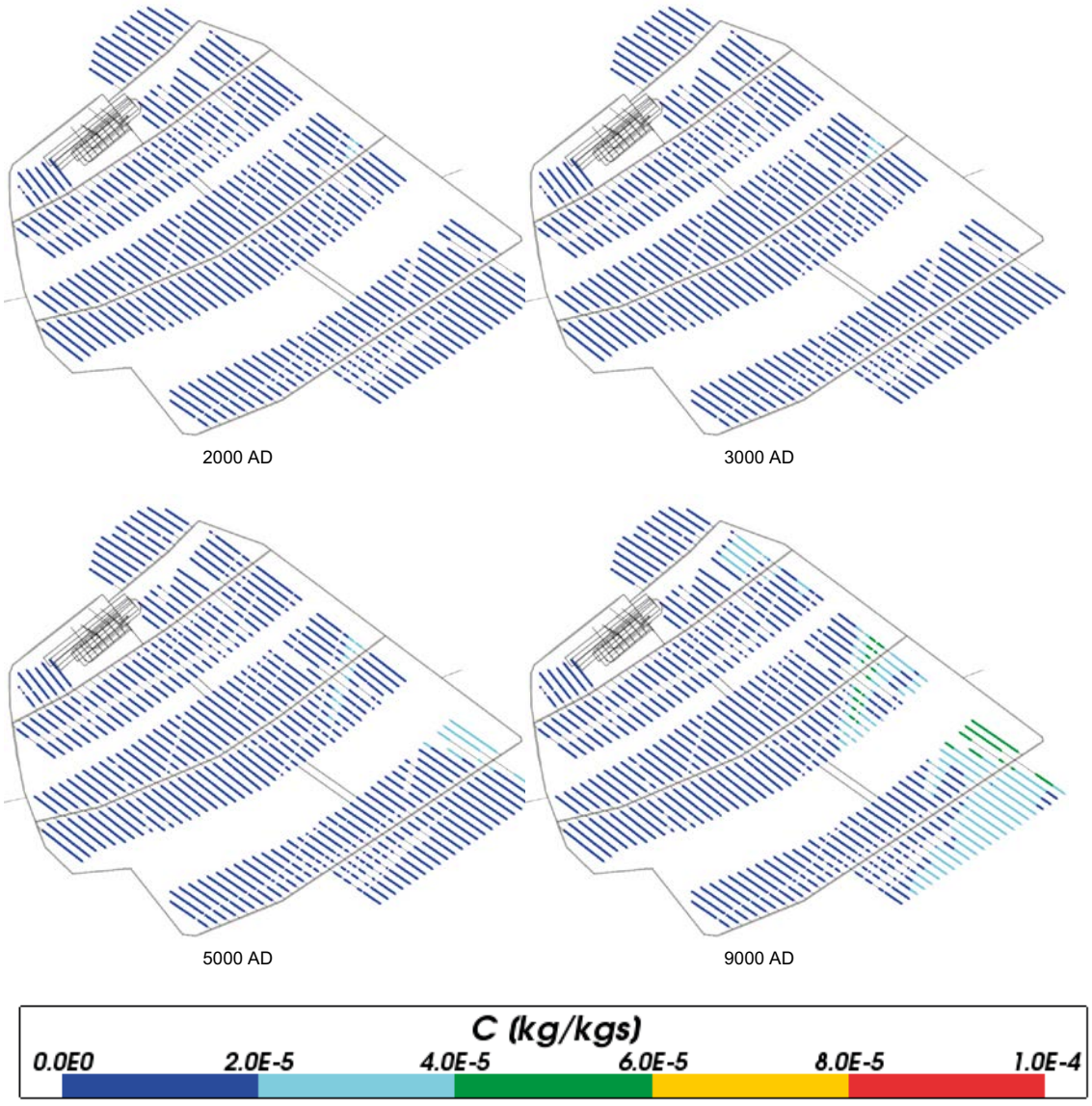


***Figure 4-153.*** *Total inorganic carbon mass fractions for Case 5 at deposition hole locations for time periods 2000 AD to 9000 AD.*

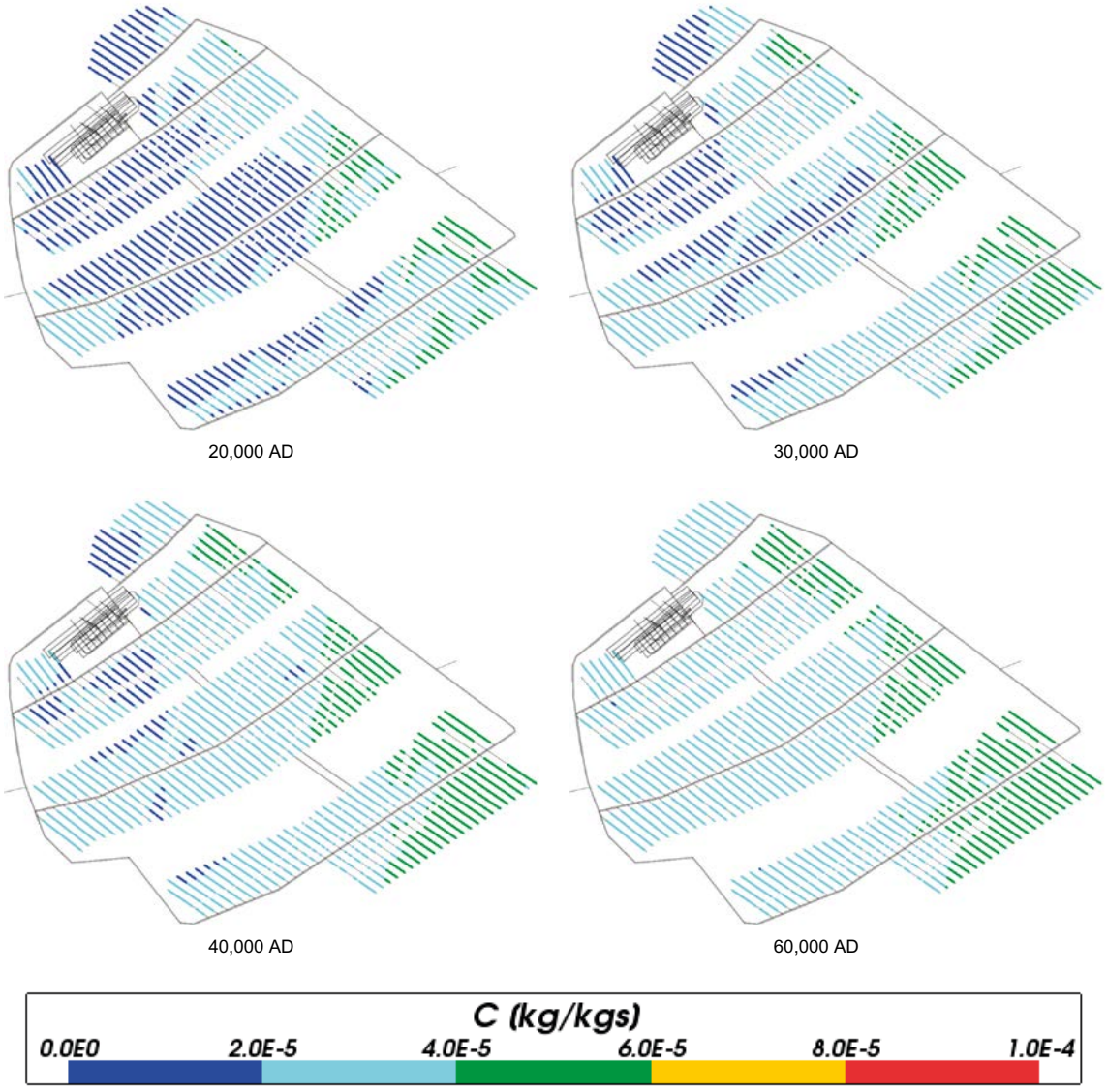


***Figure 4-154.*** *Total inorganic carbon mass fractions for Case 5 at deposition hole locations for time periods 20,000 AD to 60,000 AD.*

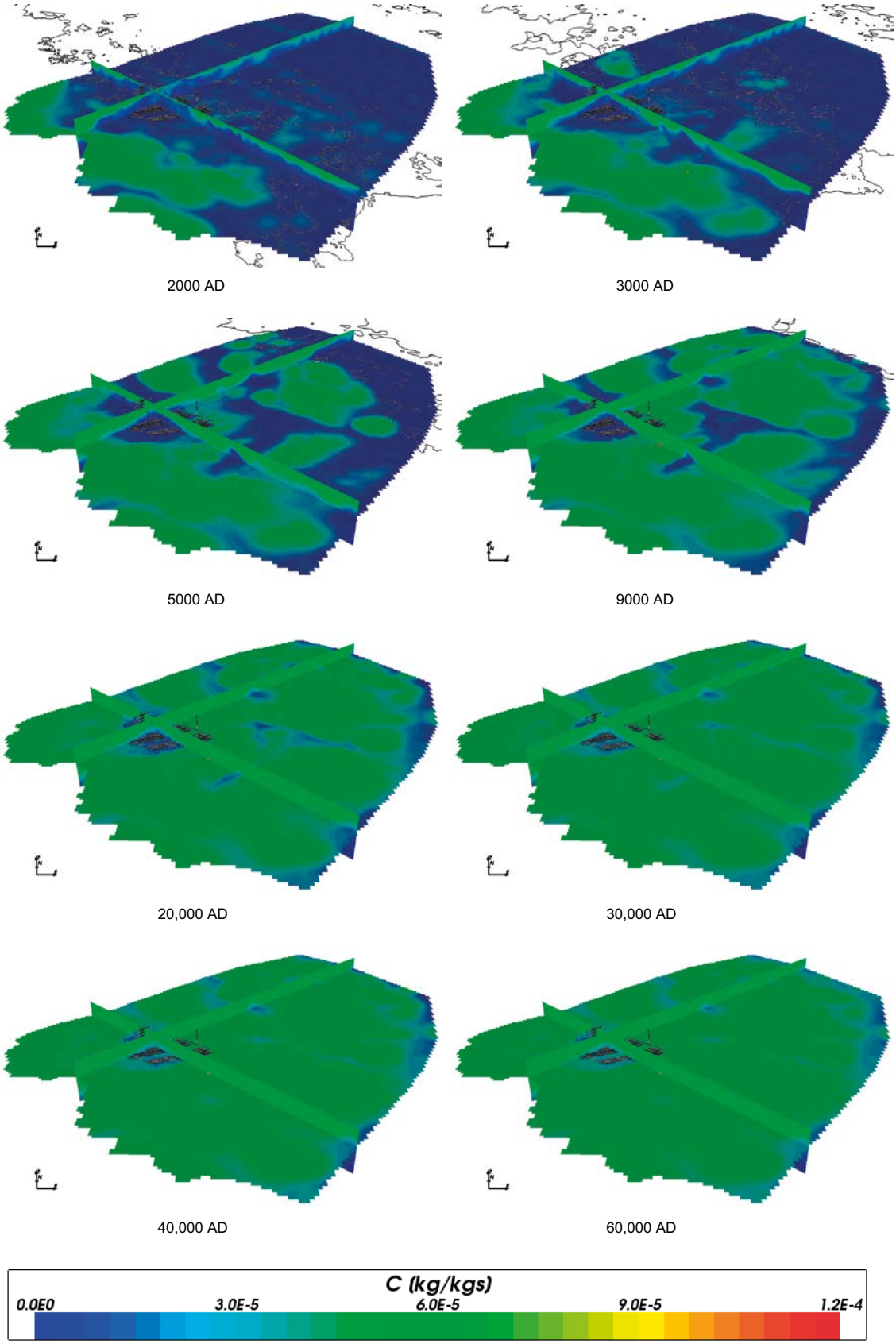


***Figure 4-155.*** *Total inorganic carbon mass fractions on regional scale slices through the repository volume for Case 5 for time periods 2000 AD to 60,000 AD.*

### 4.6.5 Calcium

The concentration of total calcium is very similar to that seen in Case 2, around the repository (shown in Figure 4-156, Figure 4-157 and Figure 4-158) as well as on the regional scale (shown in Figure 4-159). This implies that the more dilute meteoric water is either not penetrating to repository depth or the dissolution of calcite is raising the calcium concentrations to those observed for Case 2.

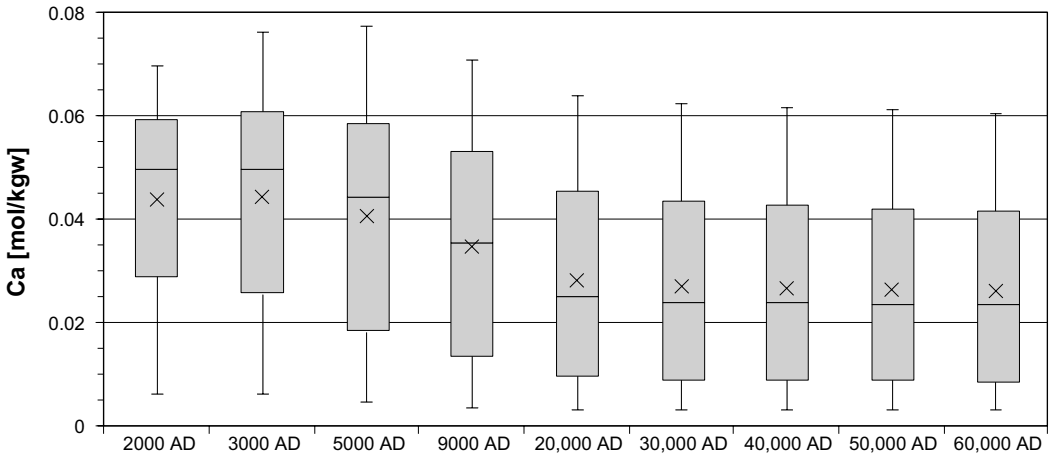


***Figure 4-156.*** *Box and whisker plot showing the statistical distribution of total calcium molalities for Case 5 on a regular grid of points within the repository volume between elevations –490 m and –450 m. The statistical measures are the median, the 25$^{th}$ and 75$^{th}$ percentiles (box), the mean (cross) and the 5$^{th}$ and 95$^{th}$ percentiles (whiskers).*

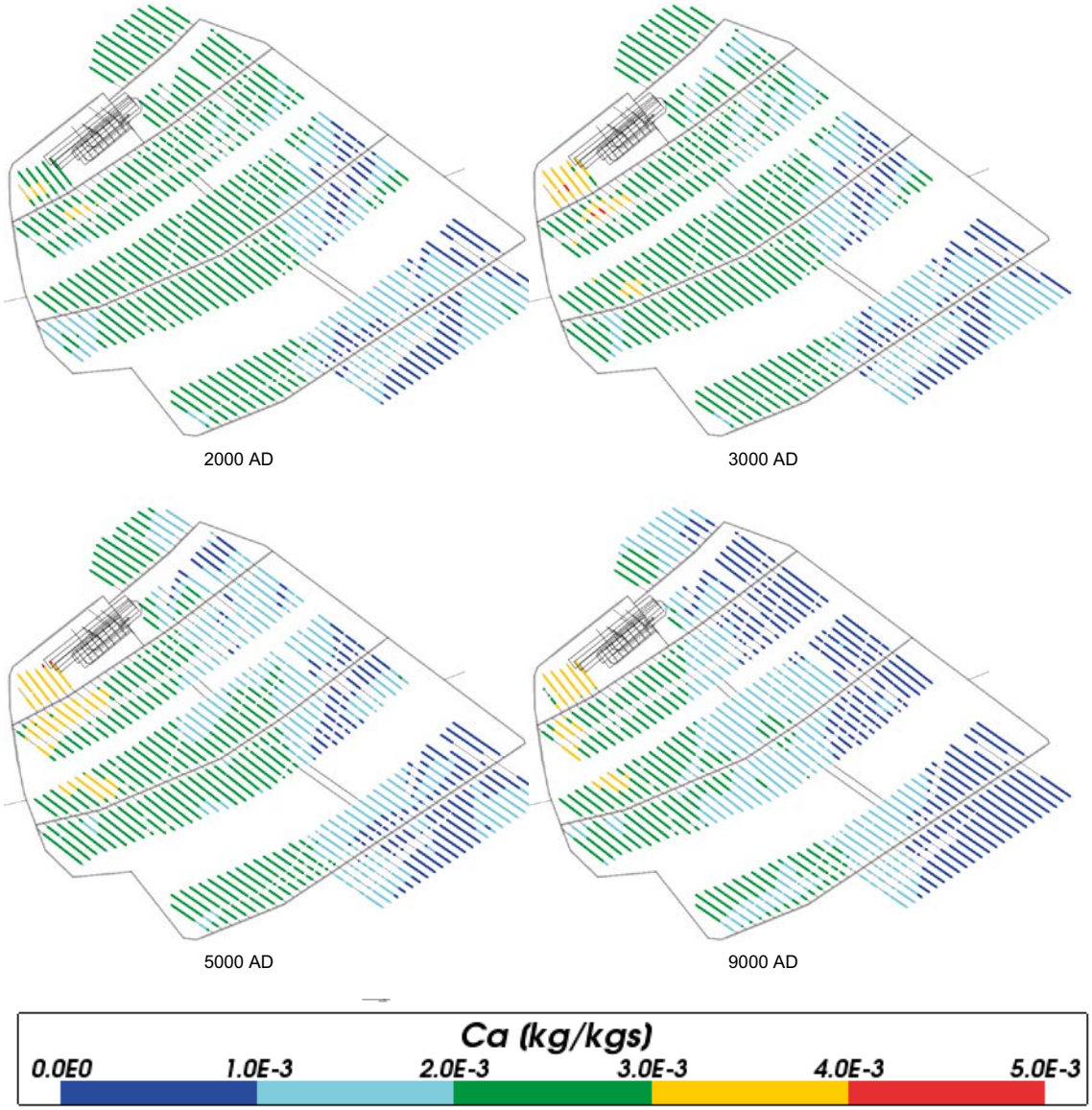


***Figure 4-157.*** *Total calcium mass fractions for Case 5 at deposition hole locations for time periods 2000 AD to 9000 AD.*

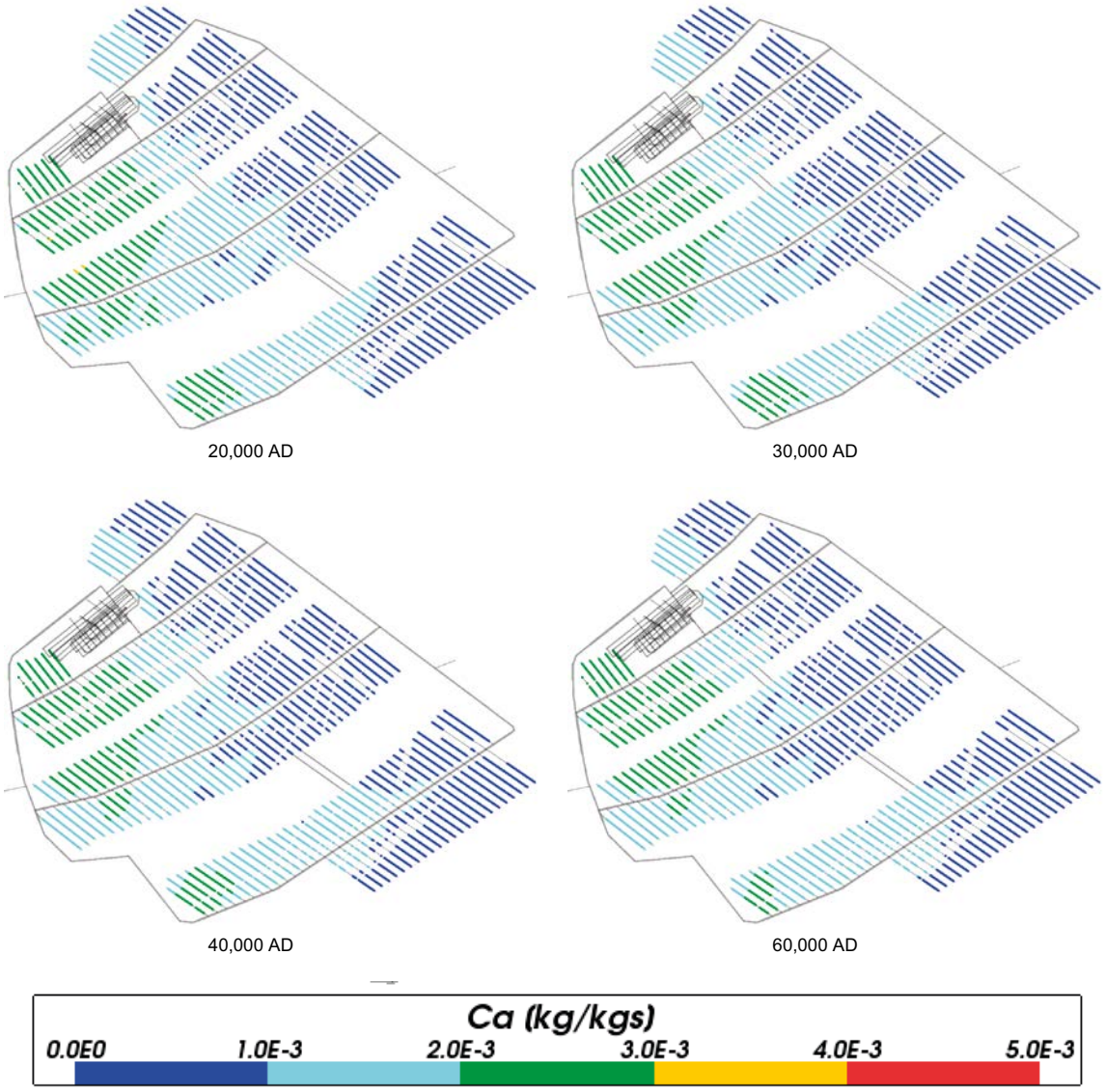


***Figure 4-158.*** *Total calcium mass fractions for Case 5 at deposition hole locations for time periods 20,000 AD to 60,000 AD.*

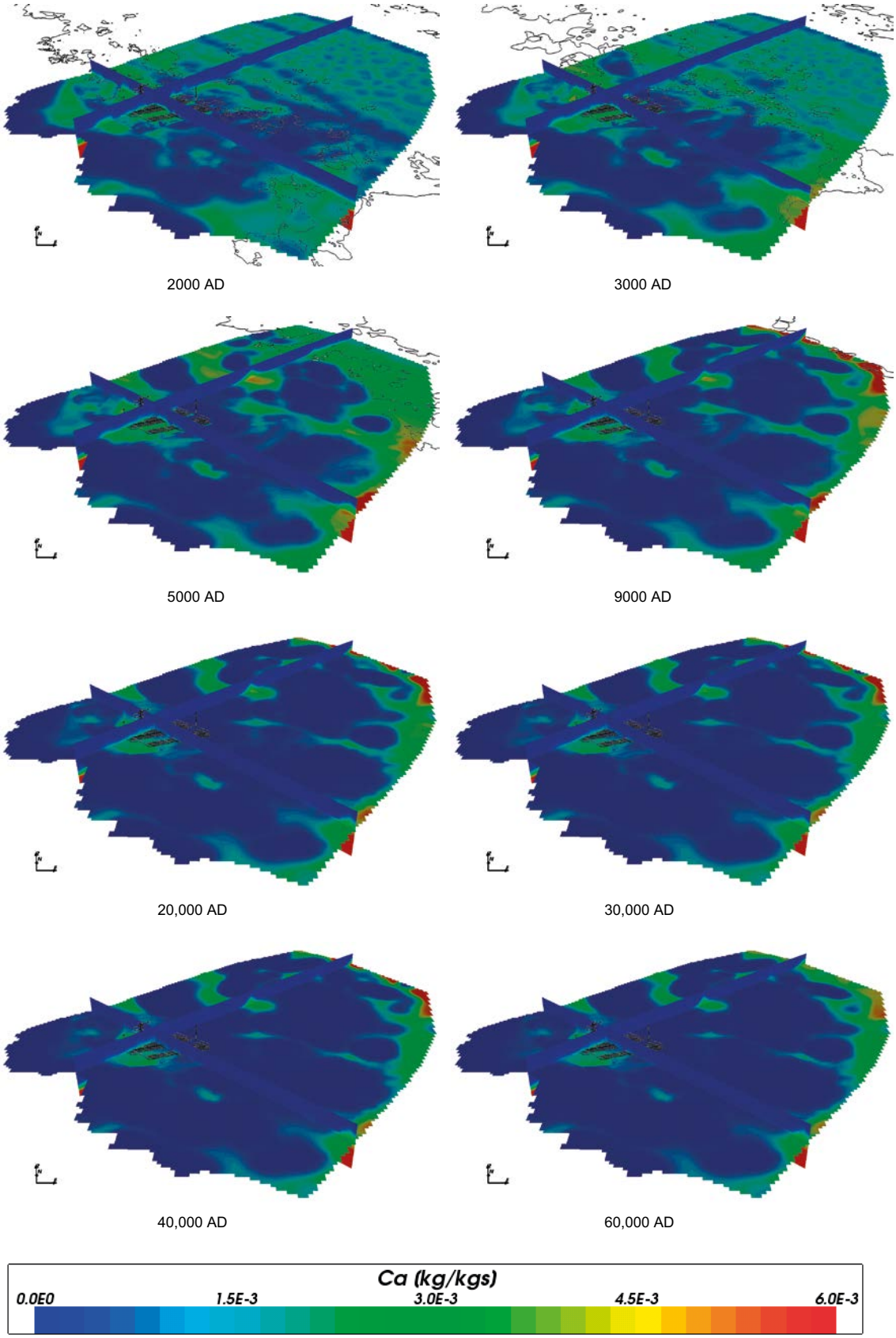


***Figure 4-159.*** *Total calcium mass fractions on regional scale slices through the repository volume for Case 5 for time periods 2000 AD to 60,000 AD.*

### 4.6.6 Chloride

Chloride concentrations in the repository area (shown in Figure 4-160, Figure 4-161 and Figure 4-162) and on the regional scale (shown in Figure 4-163) are similar to those in Case 1, where no chemical reactions are included. The similarities indicate that the more dilute meteoric water in Case 5 is not penetrating into the repository volume during the time period considered.

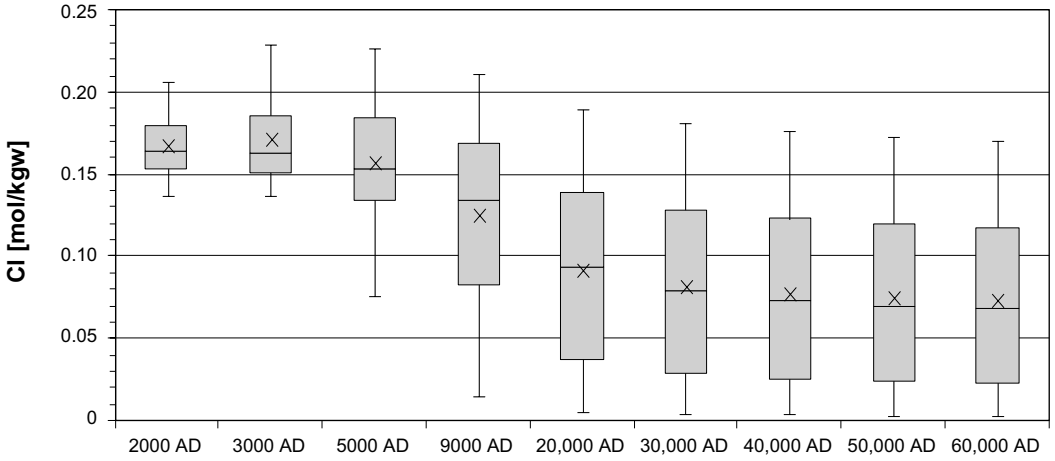


***Figure 4-160.*** *Box and whisker plot showing the statistical distribution of total chloride molalities for Case 5 on a regular grid of points within the repository volume between elevations –490 m and –450 m. The statistical measures are the median, the 25$^{th}$ and 75$^{th}$ percentiles (box), the mean (cross) and the 5$^{th}$ and 95$^{th}$ percentiles (whiskers).*

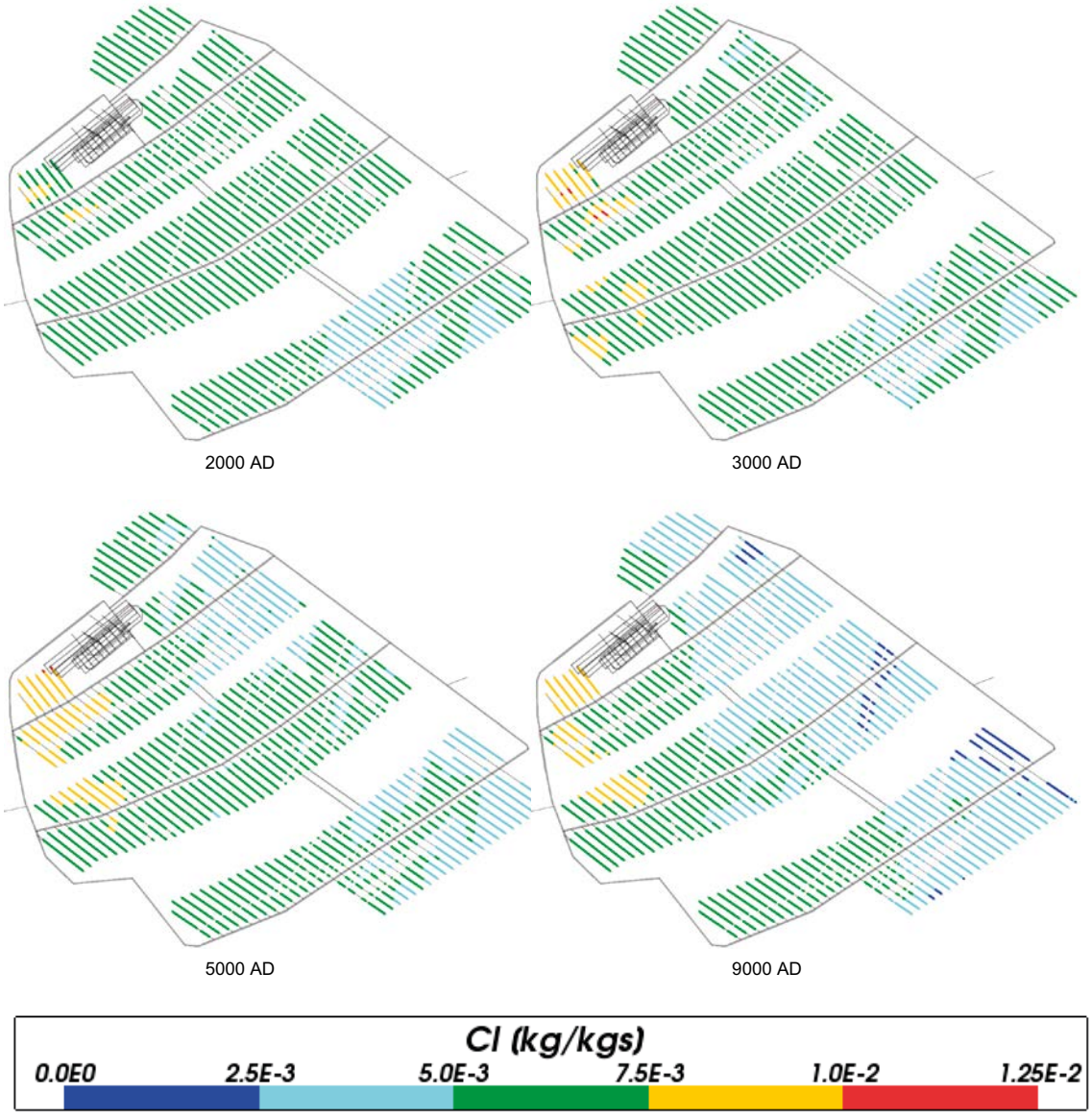


***Figure 4-161.*** *Total chloride mass fractions for Case 5 at deposition hole locations for time periods s 2000 AD to 9000 AD.*

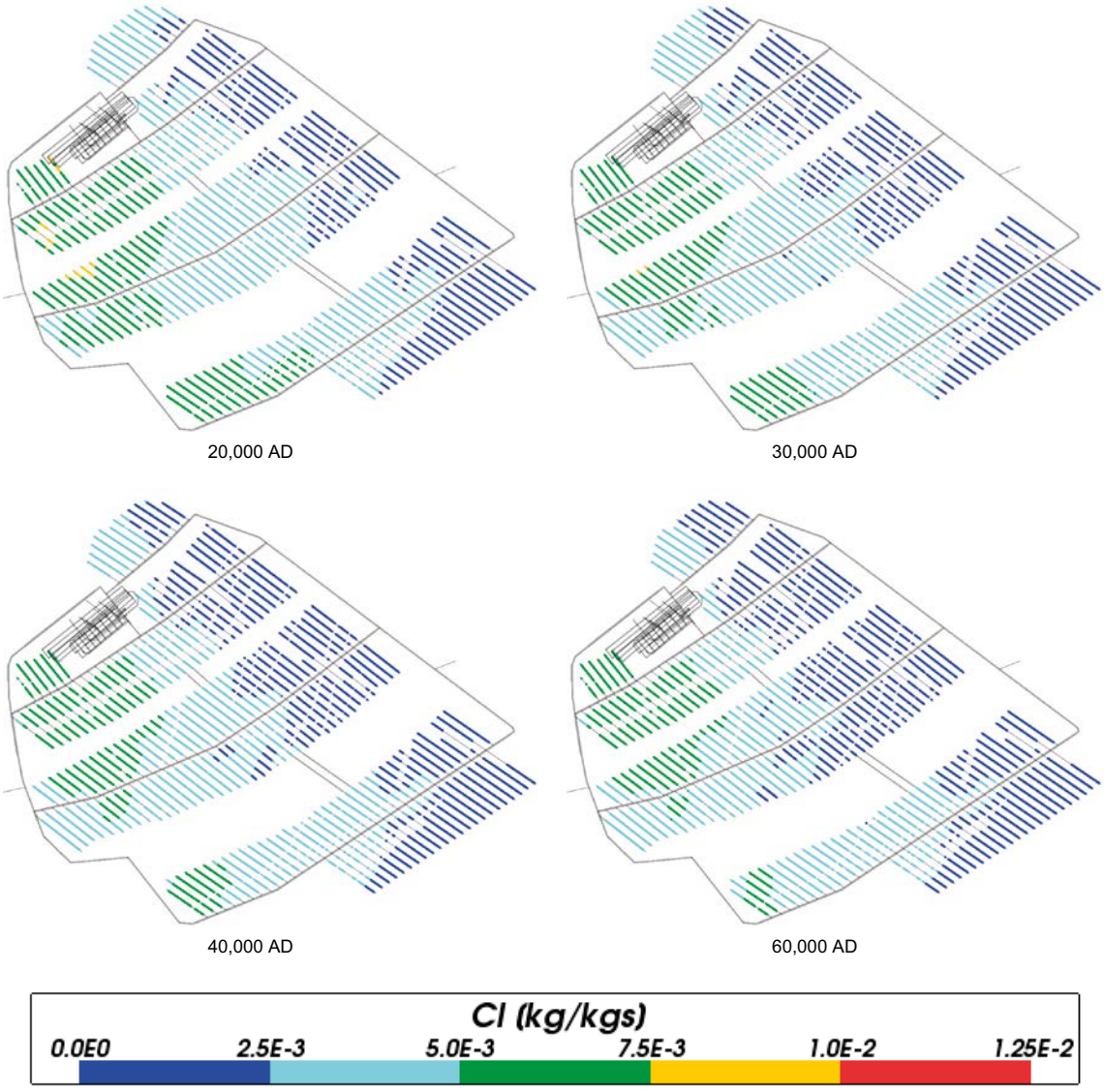


***Figure 4-162.*** *Total chloride mass fractions for Case 5 at deposition hole locations for time periods 20,000 AD to 60,000 AD.*

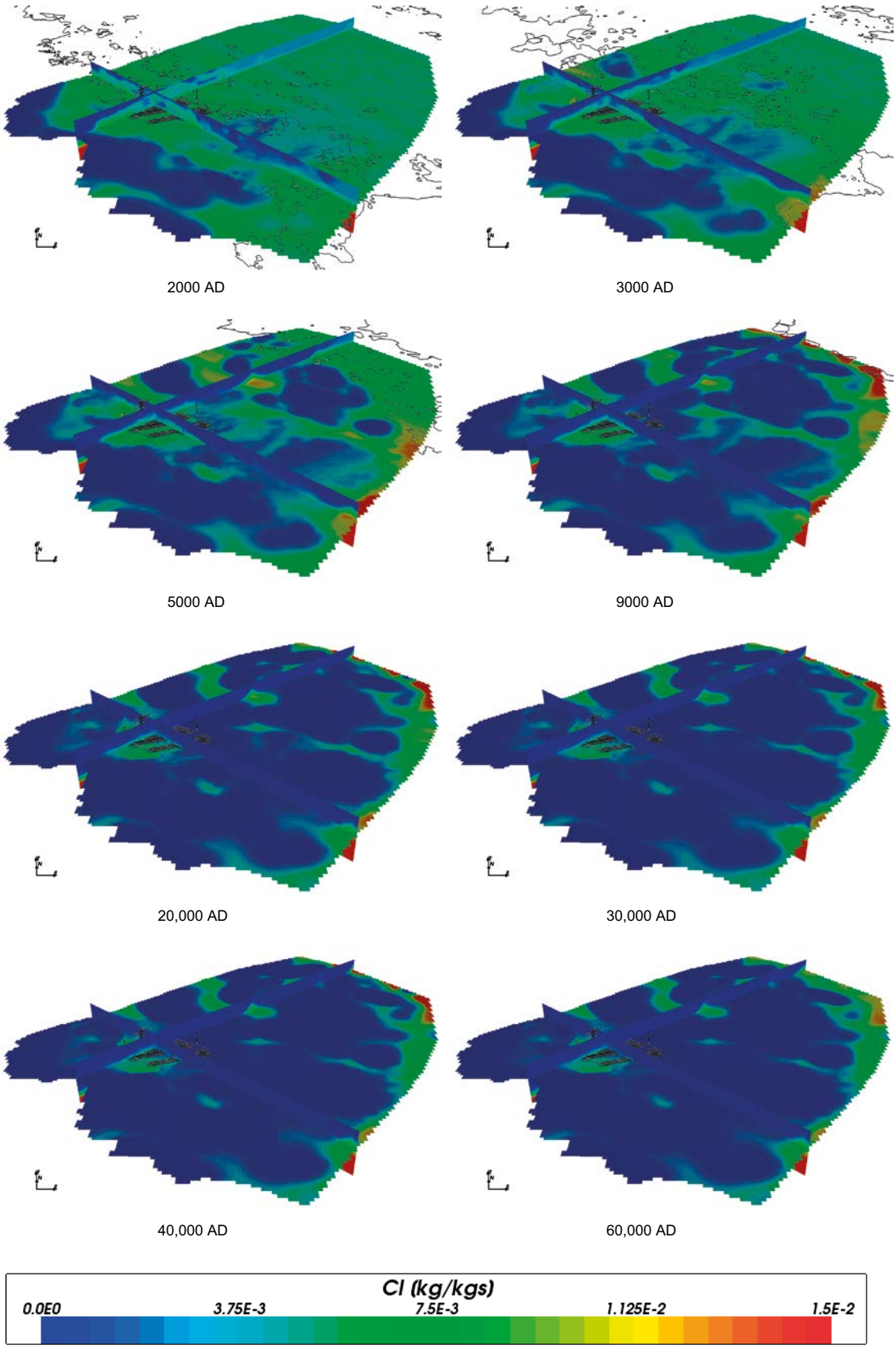


***Figure 4-163.*** *Total chloride mass fractions on regional scale slices through the repository volume for Case 5 for time periods 2000 AD to 60,000 AD.*

### 4.6.7 Iron

The evolution of total iron concentrations in the repository region for Case 5 is shown in Figure 4-164, Figure 4-165 and Figure 4-166 and on the regional scale in Figure 4-167. The results are very similar to Case 2, differing in slightly lower mean concentrations in Case 5. This may be due to the more dilute meteoric water infiltrating land areas above sea level in Case 5.

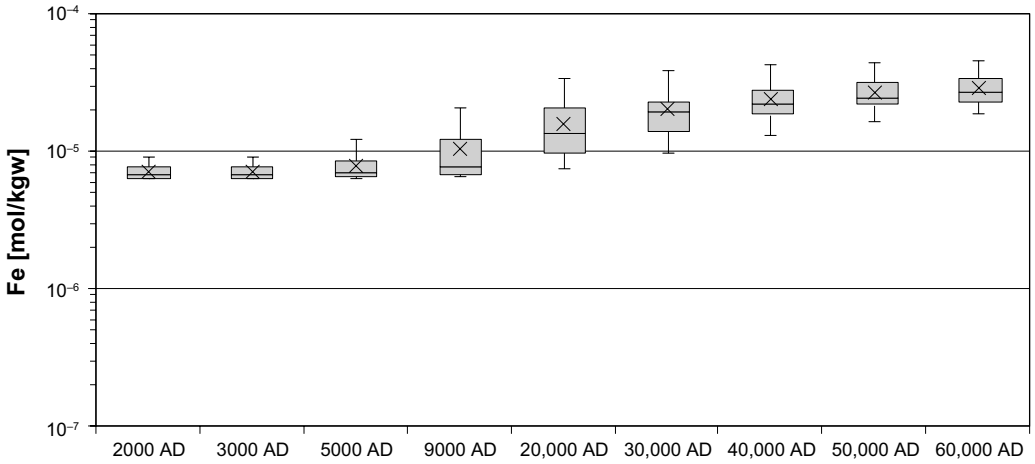


***Figure 4-164.*** *Box and whisker plot showing the statistical distribution of total iron molalities for Case 5 on a regular grid of points within the repository volume between elevations –490 m and –450 m. The statistical measures are the median, the 25$^{th}$ and 75$^{th}$ percentiles (box), the mean (cross) and the 5$^{th}$ and 95$^{th}$ percentiles (whiskers).*

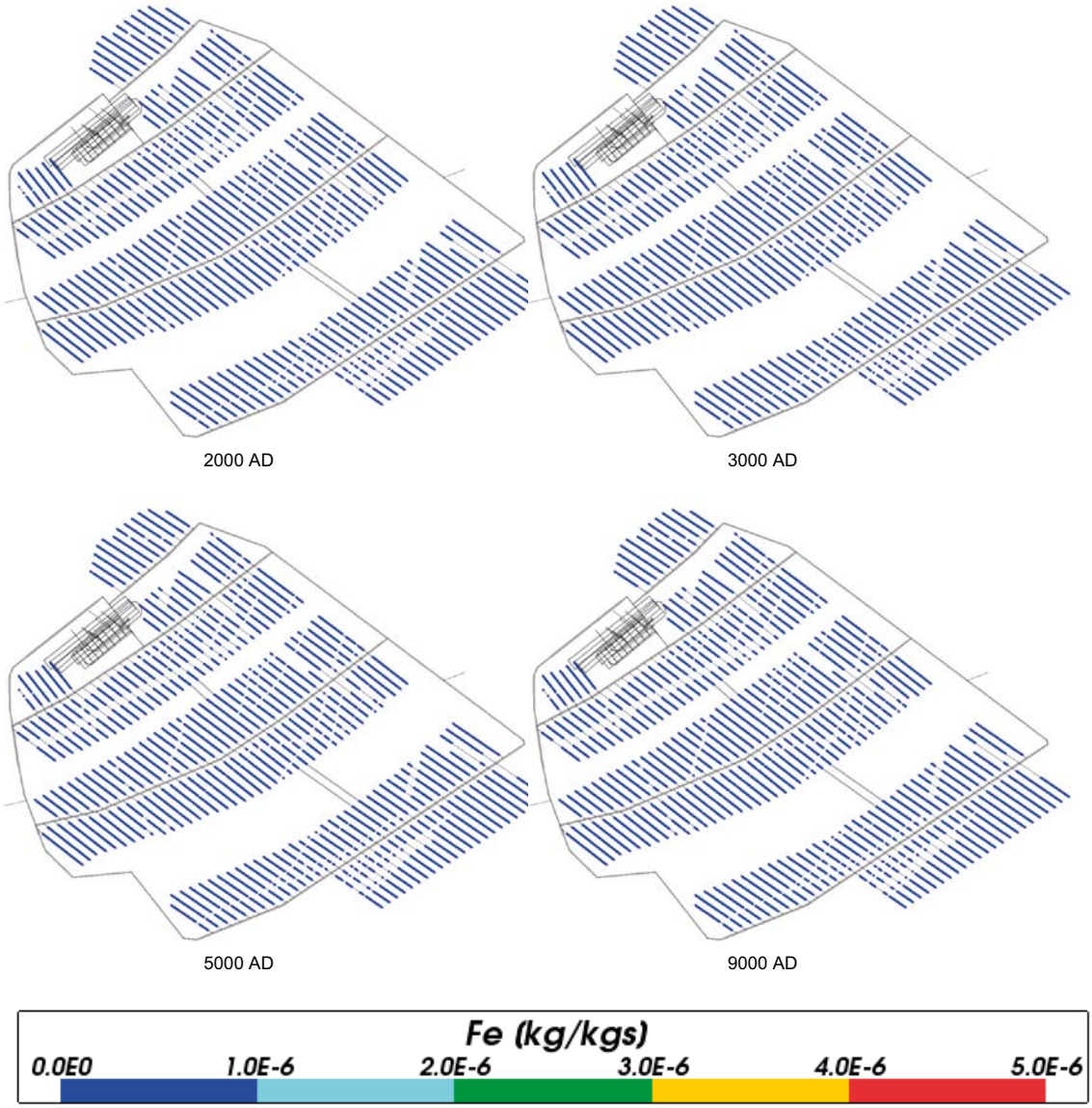


***Figure 4-165.*** *Total iron mass fractions for Case 5 at deposition hole locations for time periods 2000 AD to 9000 AD.*

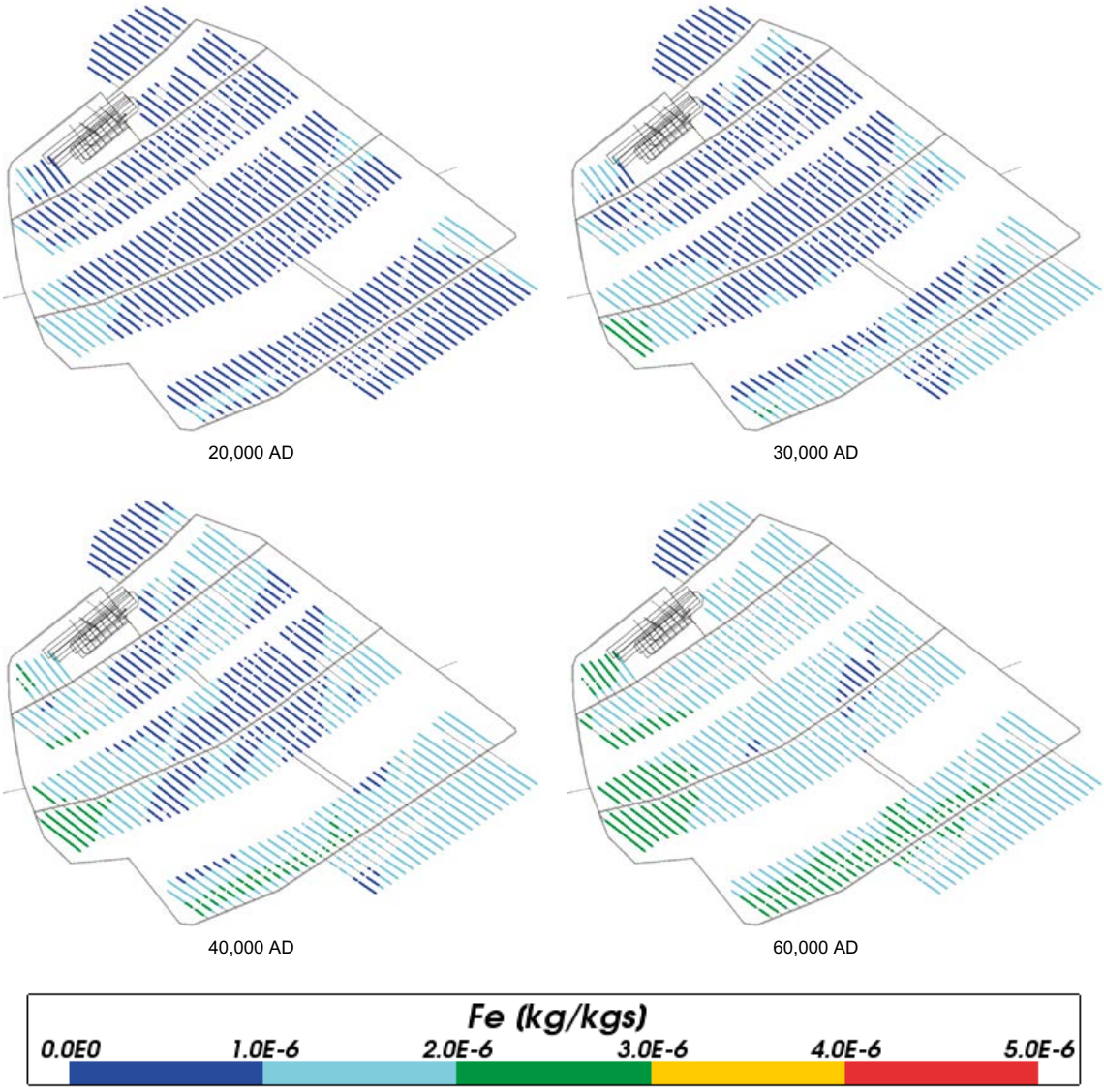


***Figure 4-166.*** *Total iron mass fractions for Case 5 at deposition hole locations for time periods 20,000 AD to 60,000 AD.*

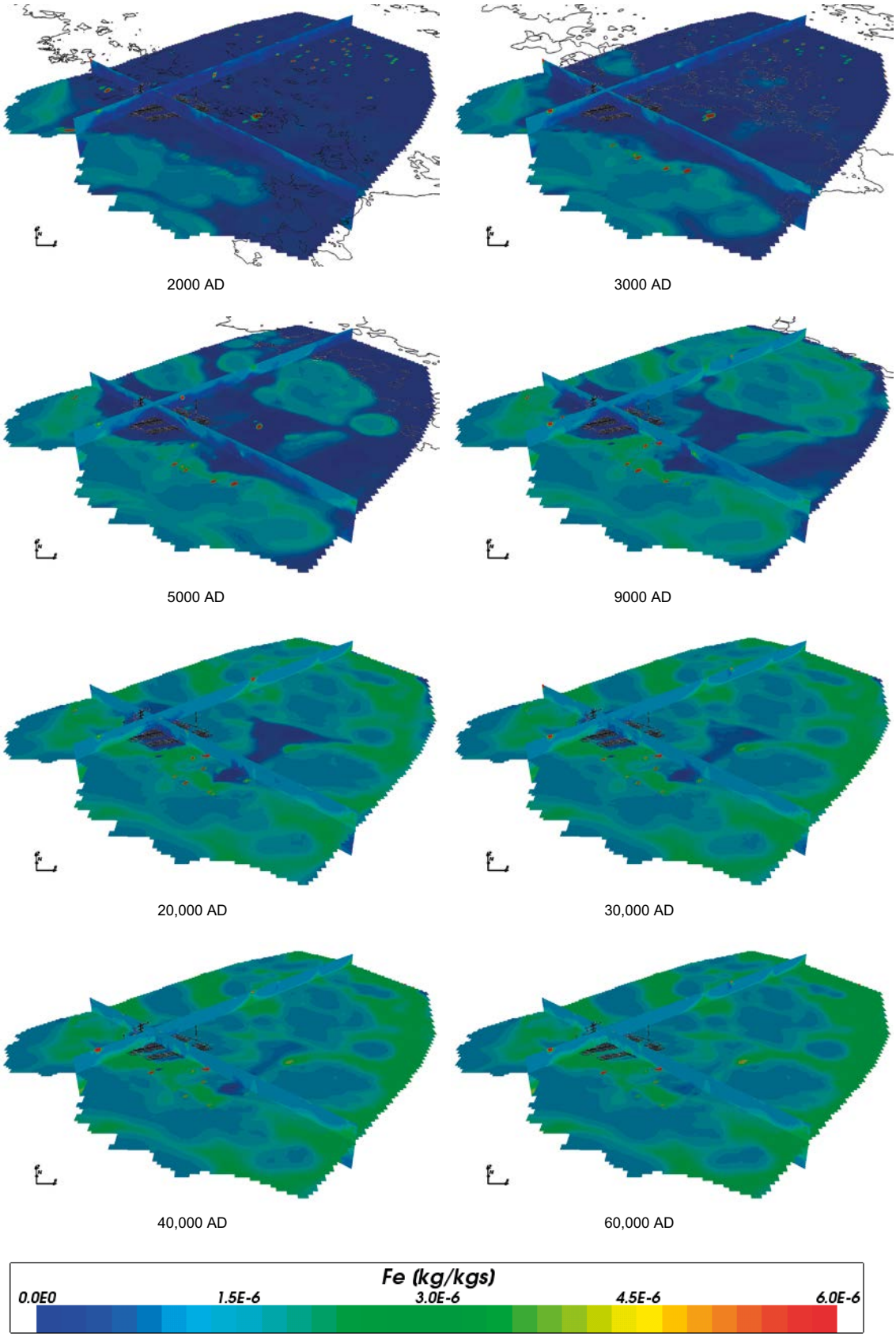


***Figure 4-167.*** *Total iron mass fractions on regional scale slices through the repository volume for Case 5 for time periods 2000 AD to 60,000 AD.*

### 4.6.8 Sodium

The concentration of sodium both in the repository area (shown in Figure 4-168, Figure 4-169 and Figure 4-170) and on the regional scale (shown in Figure 4-171) are similar to Case 1. However, the sodium concentrations are slightly lower in Case 5 than in Case 1. This may partly be due to minor changes in the flow field as a result of chemical reactions affecting groundwater densities and partly due to the more dilute meteoric water infiltrating land areas above sea level in Case 5.

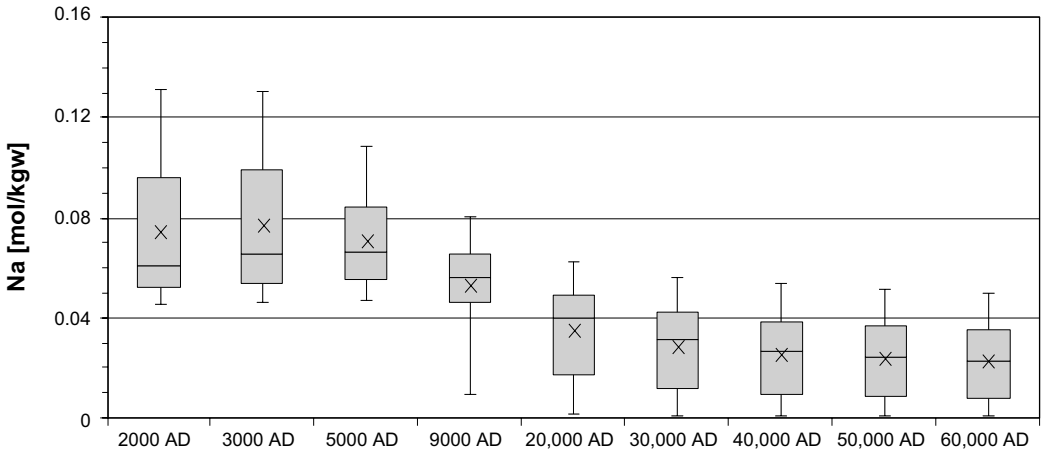


***Figure 4-168.*** *Box and whisker plot showing the statistical distribution of total sodium molalities for Case 5 on a regular grid of points within the repository volume between elevations –490 m and –450 m. The statistical measures are the median, the 25$^{th}$ and 75$^{th}$ percentiles (box), the mean (cross) and the 5$^{th}$ and 95$^{th}$ percentiles (whiskers).*

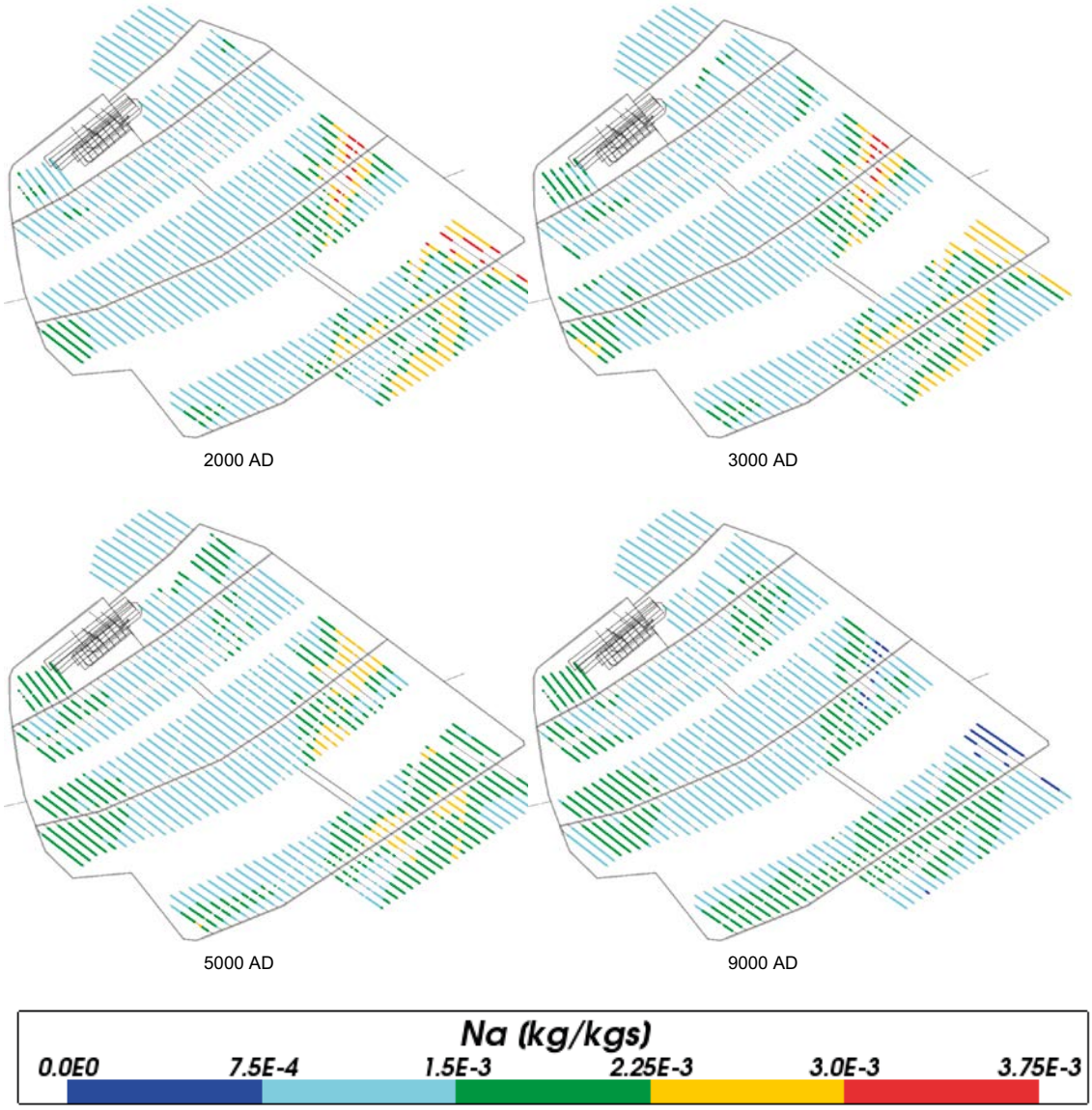


***Figure 4-169.*** *Total sodium mass fractions for Case 5 at deposition hole locations for time periods 2000 AD to 9000 AD.*

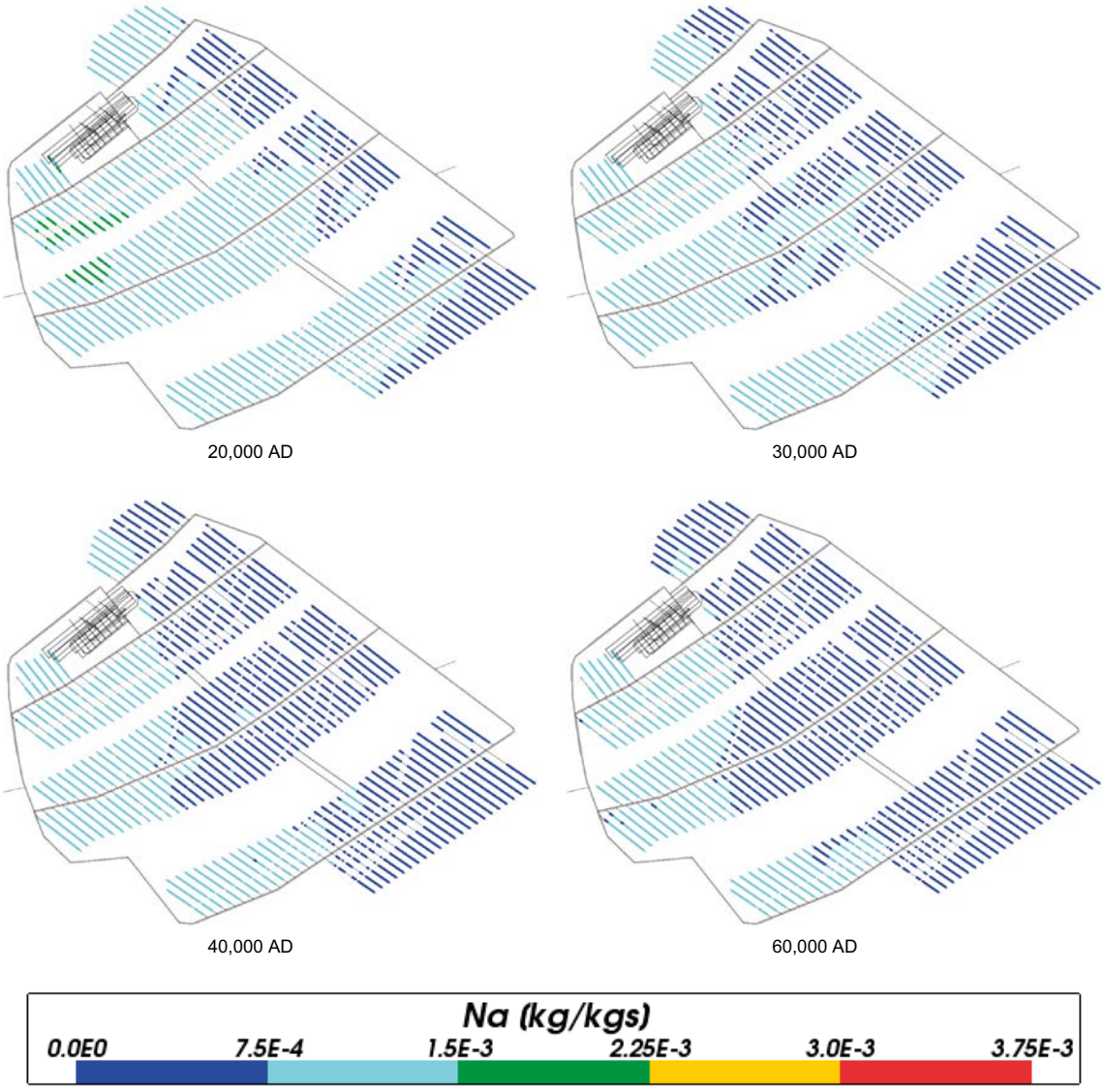


***Figure 4-170.*** *Total sodium mass fractions for Case 5 at deposition hole locations for time periods 20,000 AD to 60,000 AD.*

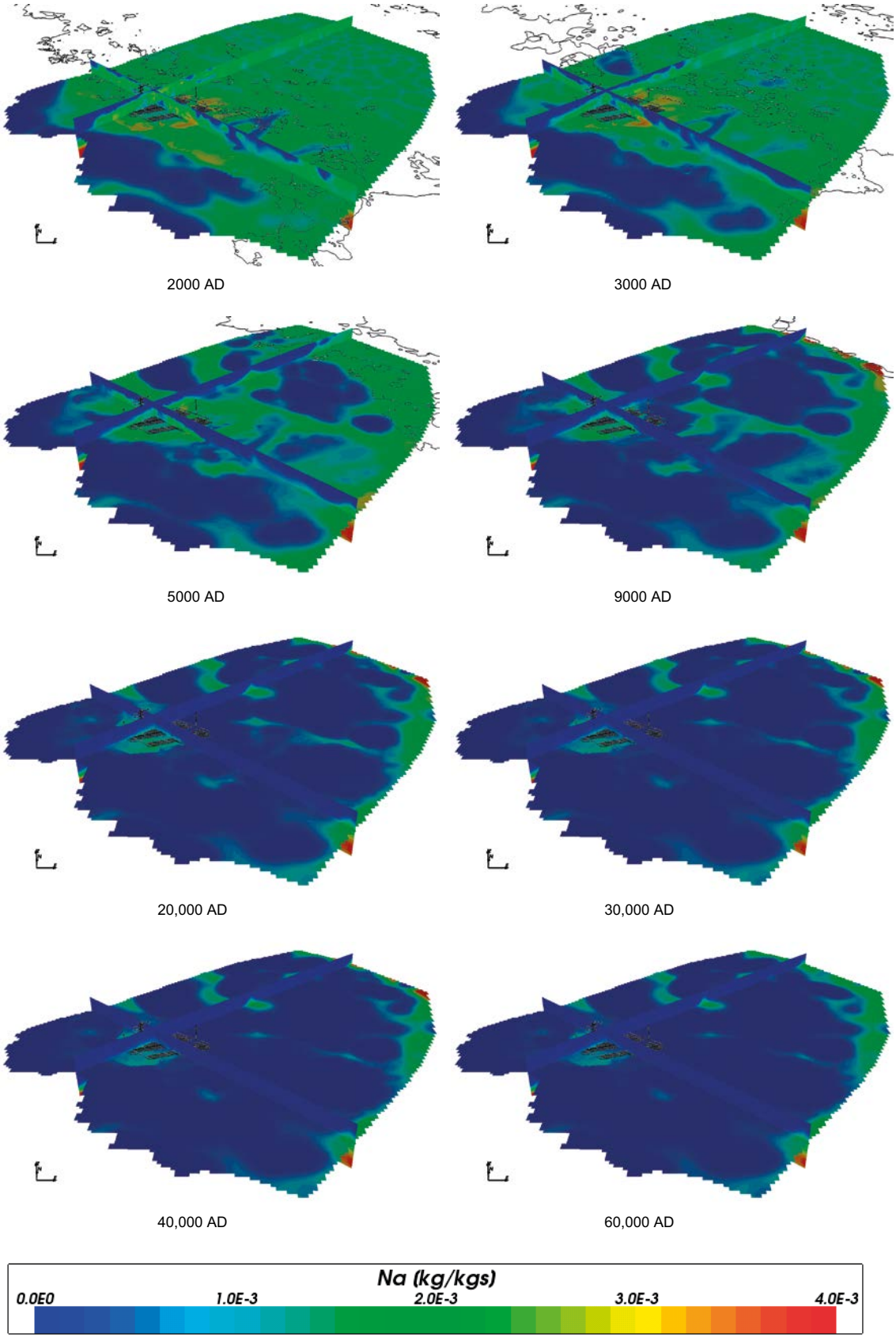


***Figure 4-171.*** *Total sodium mass fractions on regional scale slices through the repository volume for Case 5 for time periods 2000 AD to 60,000 AD.*

### 4.6.9 Potassium

The evolution of potassium concentrations in Case 5 (Figure 4-172 to Figure 4-175) is almost identical to Cases 2 and 3. Again, this indicates that the more dilute meteoric water used in Case 5 has not penetrated to the repository volume in the time period considered.

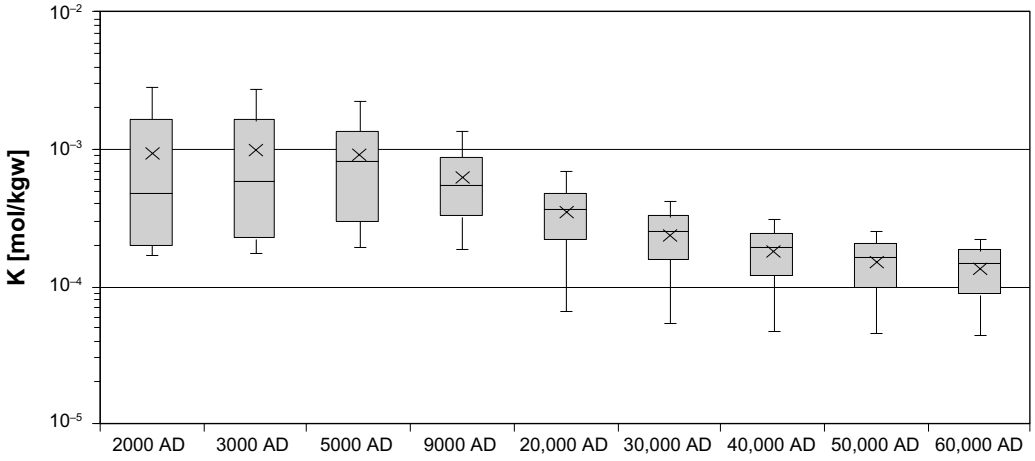


***Figure 4-172.*** *Box and whisker plot showing the statistical distribution of total potassium molalities for Case 5 on a regular grid of points within the repository volume between elevations –490 m and –450 m. The statistical measures are the median, the 25th and 75th percentiles (box), the mean (cross) and the 5th and 95th percentiles (whiskers).*

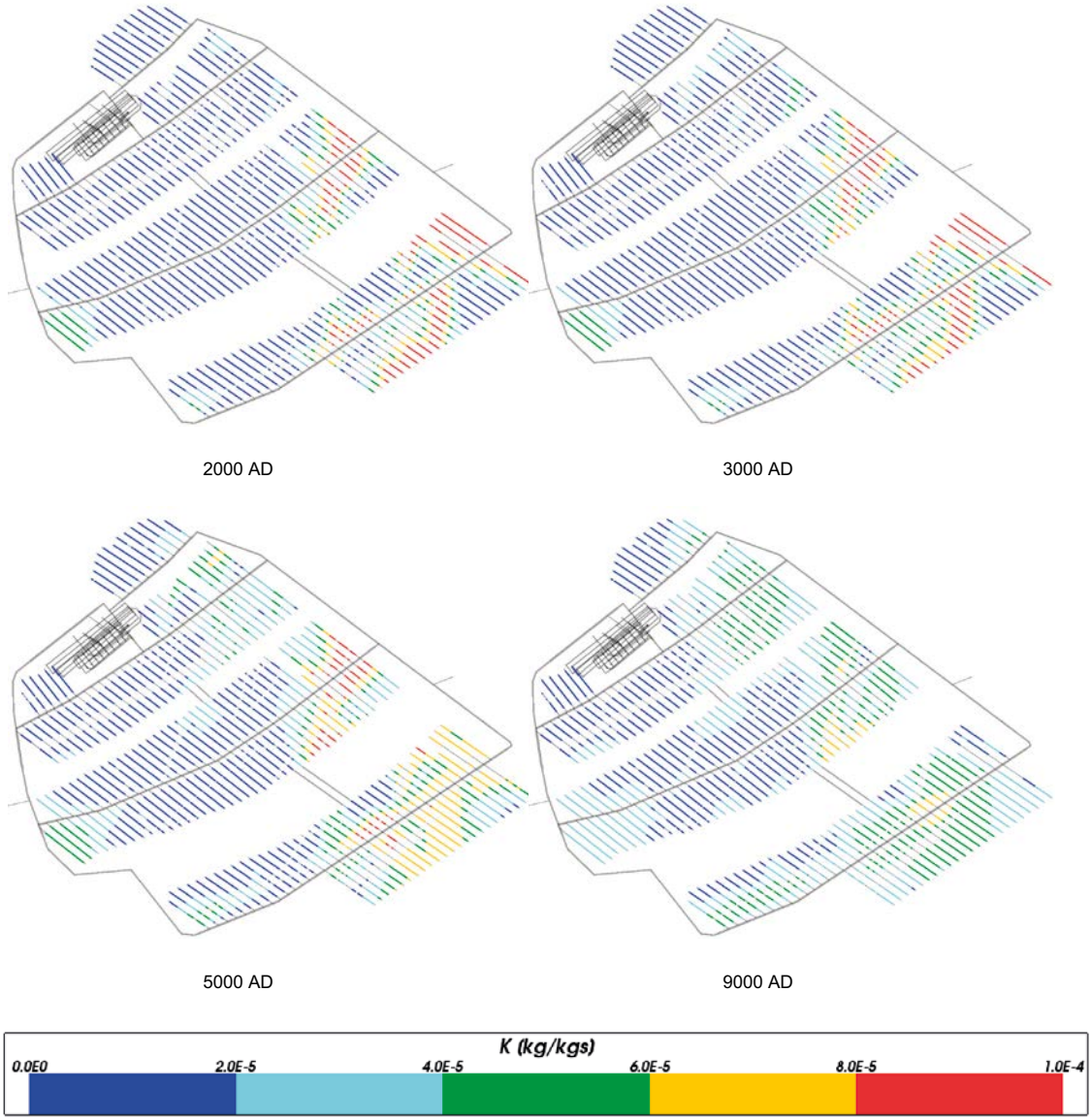


***Figure 4-173.*** *Total potassium mass fractions for Case 5 at deposition hole locations for time periods 2000 AD to 9000 AD.*

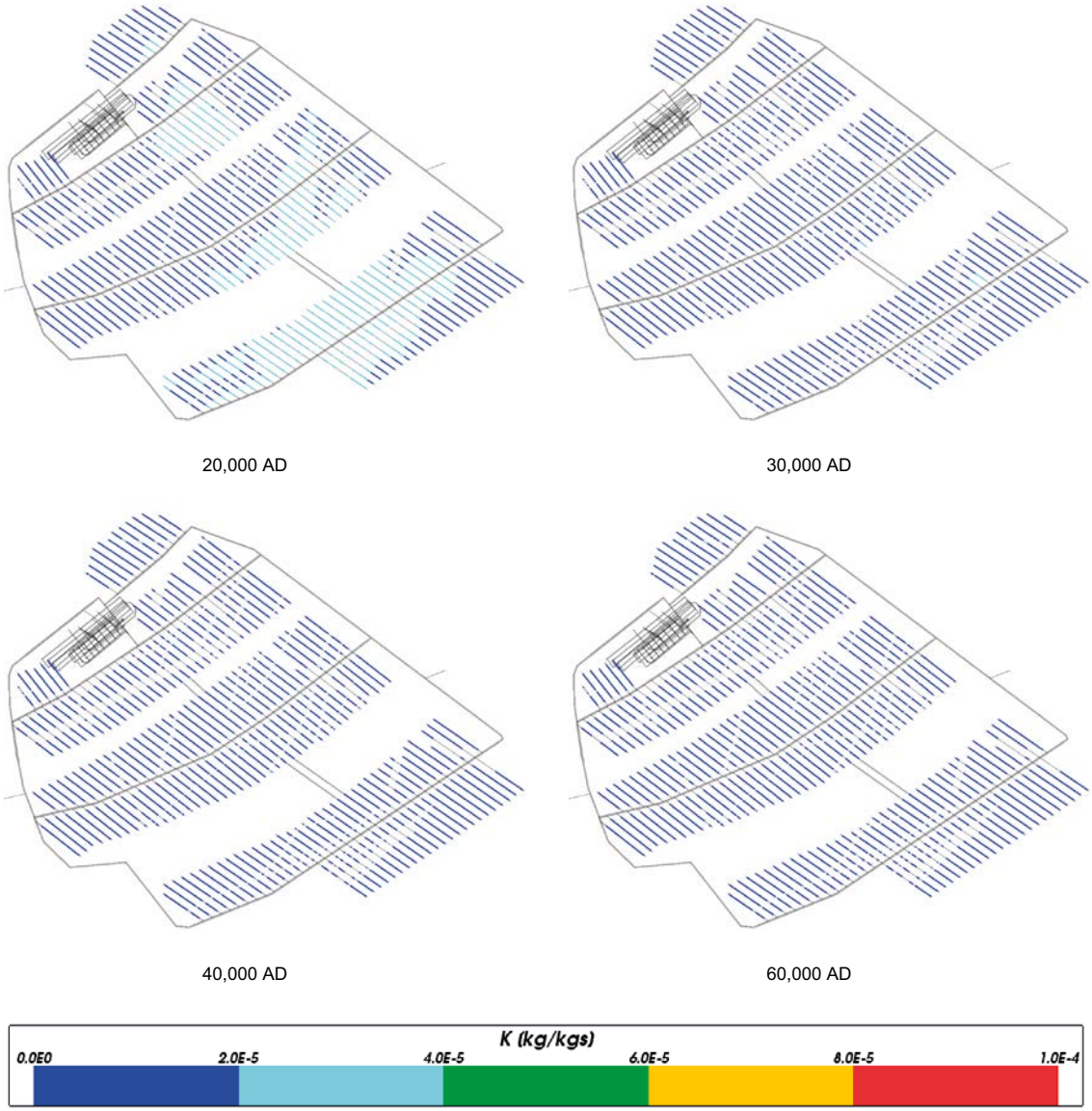


***Figure 4-174.*** *Total potassium mass fractions for Case 5 at deposition hole locations for time periods 20,000 AD to 60,000 AD.*

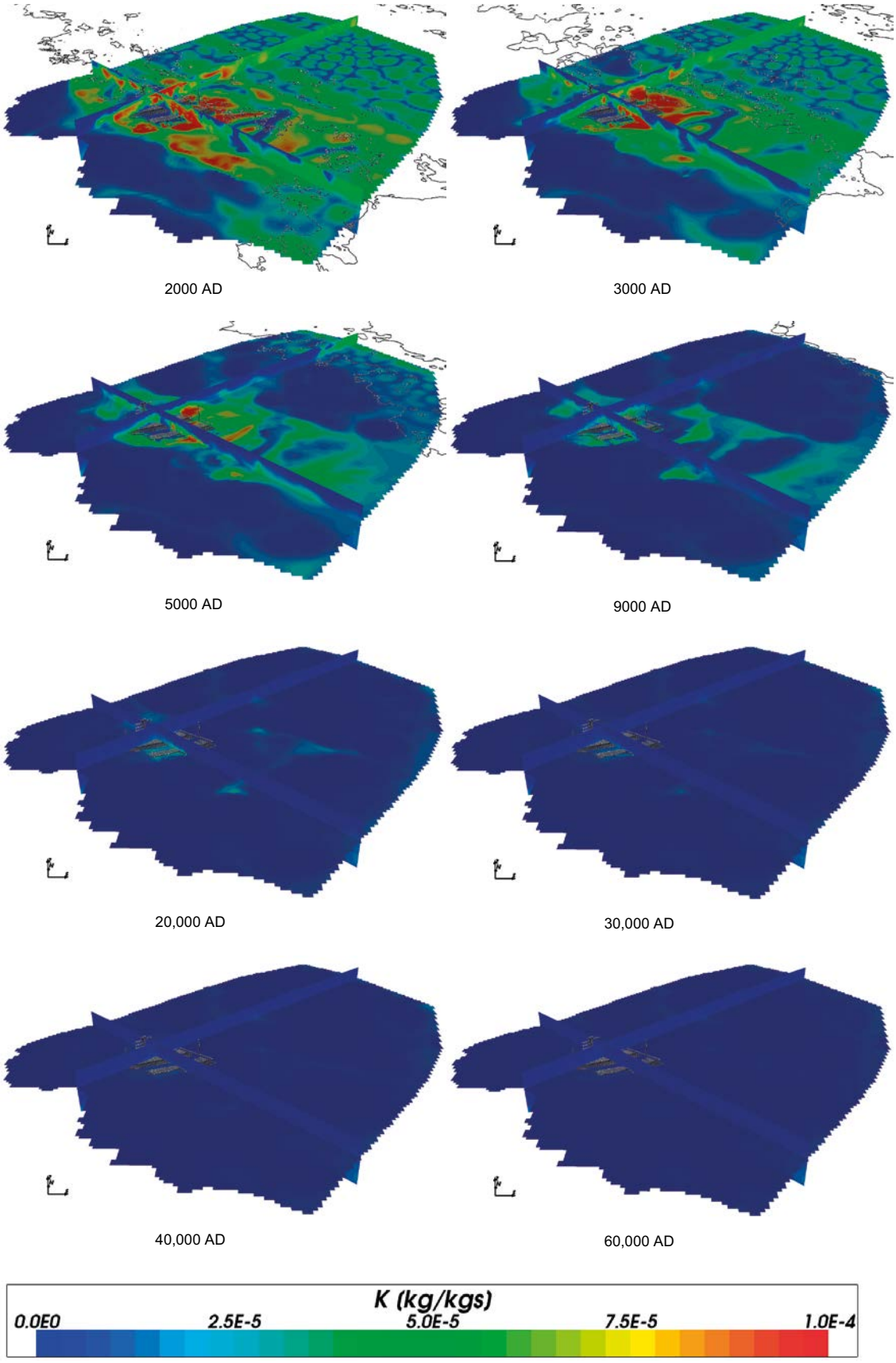


***Figure 4-175.*** *Total potassium mass fractions on regional scale slices through the repository volume for Case 5 for time periods 2000 AD to 60,000 AD.*

### 4.6.10 Sulphate

Figure 4-176, Figure 4-177 and Figure 4-178 show the evolution in sulphate concentrations around the repository in Case 5. The mean values are similar to those in Case 2, but a greater spatial variability is evident at early times in Case 5. This trend is also seen in Case 4.

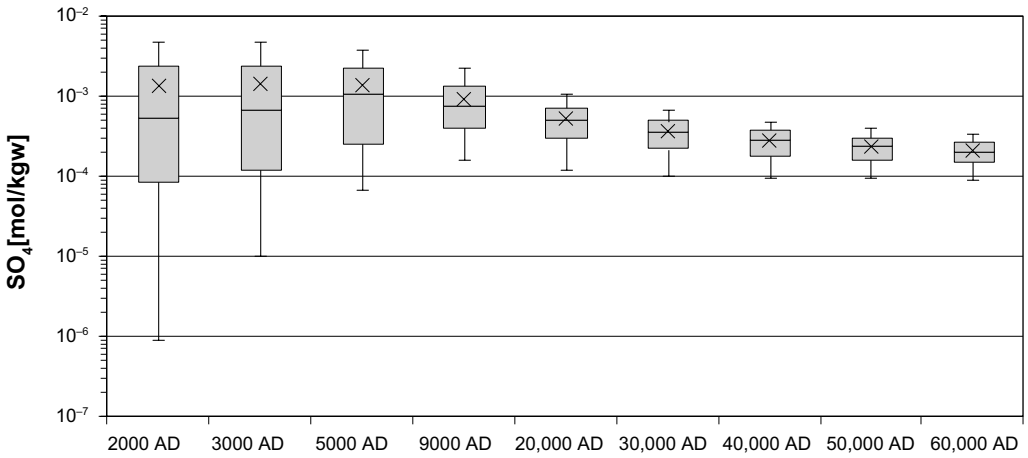


***Figure 4-176.*** *Box and whisker plot showing the statistical distribution of sulphate molalities for Case 5 on a regular grid of points within the repository volume between elevations –490 m and –450 m. The statistical measures are the median, the 25$^{th}$ and 75$^{th}$ percentiles (box), the mean (cross) and the 5$^{th}$ and 95$^{th}$ percentiles (whiskers).*

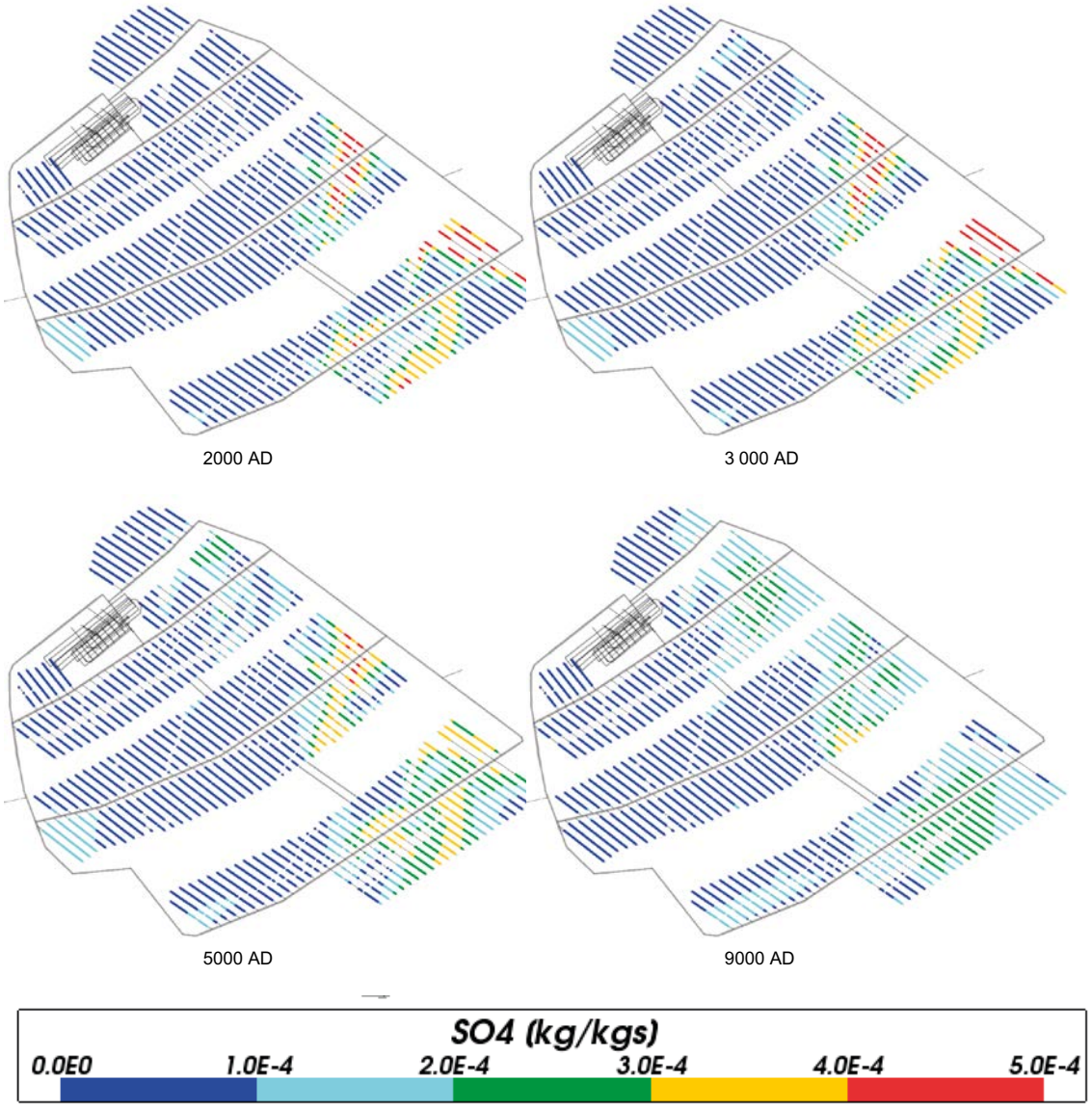


***Figure 4-177.*** *Sulphate mass fractions for Case 5 at deposition hole locations for time periods 2000 AD to 9000 AD.*

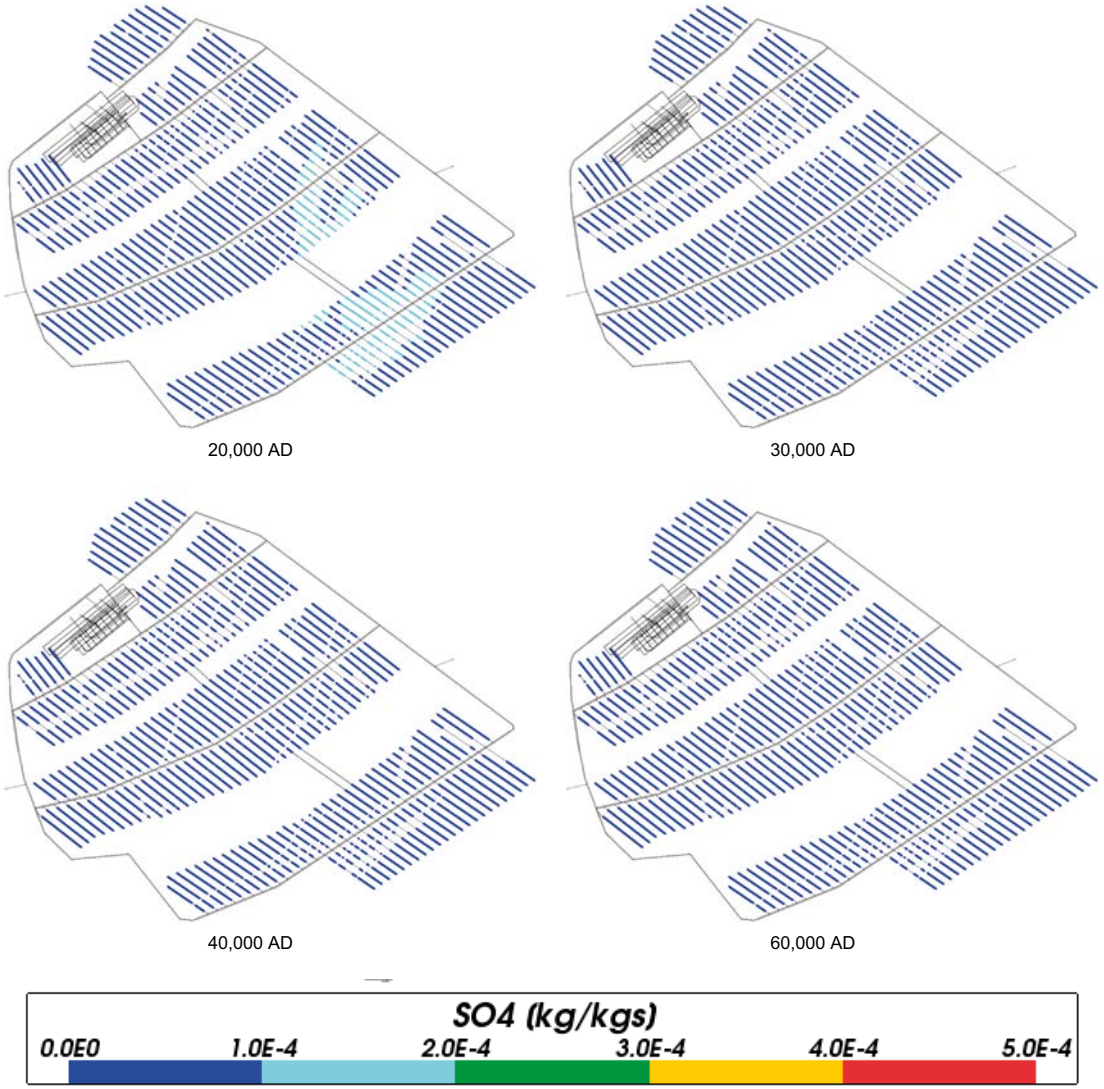


***Figure 4-178.*** *Sulphate mass fractions for Case 5 at deposition hole locations for time periods 20,000 AD to 60,000 AD.*

### 4.6.11 Summary for Case 5

In addition to the groundwater flow and transport processes considered in Case 1, Case 5 includes equilibration of groundwater with calcite, quartz and amorphous iron (II) sulphide as in Case 2. Case 5 differs in that it includes a more dilute meteoric water (Dilute Meteoric water in Table 3-1) as compared to the Case 2, infiltrating at the top boundary for land areas above sea level. The salinity, total cation concentrations, and the concentrations of non-reacting species such as chloride, sodium and potassium were similar to those calculated for Cases 1 and 2, with a slight tendency towards lower concentrations in Case 5 due to the more dilute infiltrating meteoric water. This indicates that the concentrations of the major species are determined primarily by groundwater flow and transport also in Case 5, although the similarity of the results to Case 2 suggests that the more dilute meteoric water used in Case 5 is not penetrating significantly into the repository volume. The results for calcium are almost identical in Case 2 and 5 and only a small effect on the concentrations of total inorganic carbon is seen, with slightly lower concentrations after 20,000 AD in Case 5. Also the total iron concentrations due to the amorphous iron (II) sulphide reactions were very similar to Case 2, showing a significant difference from Case 1 where these reactions are not included. The reactions determine the pH, which fell from a median of around 7.6 at 2000 AD to around 6.9 at 60,000 AD within the repository volume, and the median Eh rose from around –245 mV to –200 mV. These values are very similar as for Case 2, although pH and Eh show a smaller spatial variability within the repository volume in Case 5 in particular after 20,000 AD. Thus the geochemical conditions within the repository volume for this case remained within the bounds required by the safety assessment throughout the simulation period.

# 5 Conclusions

This report describes calculations of the groundwater composition and geochemical conditions in the host rock for a proposed spent nuclear fuel repository at Forsmark for an extended temperate climate period from 8000 BC to 60,000 AD. The results from the calculations are presented from 2000 AD to 60,000 AD. During this period the site would be exposed to an increased duration of infiltrating meteoric water compared to the SR-Site base case, which could have an impact on safety functions related to geochemical conditions. A number of cases were modelled based on different chemical reactions or a different composition for the infiltrating meteoric water.

Case 1 included no chemical reactions and only modelled transient, variable density groundwater flow and transport. This case showed that over time meteoric water could penetrate to repository depth, shown by a reduction in salinity and an increase in the concentration of total inorganic carbon. However, the penetration of meteoric water was limited by the low permeability of the bedrock, the relatively slow and shallow circulation of groundwater and the effects of rock matrix diffusion. The results are consistent with those obtained for SR-Site up to 9,000 AD in Joyce et al. (2010) and with those at 10,000 AD and 60,000 AD for dilute water penetration calculations in Section 10.3.6 of SKB (2011).

Case 2 included equilibration of groundwater with calcite, quartz and amorphous iron (II) sulphide. This case showed similar results to Case 1, but enabled the calculation of pH and Eh. The median pH in the repository volume fell from 7.6 at 2000 AD to 6.8 at 60,000 AD, whilst the median Eh rose from –245 mV to –190 mV. As expected, the salinity, total cation concentrations and the concentrations of non-reacting species such as chloride and sodium were very similar to those calculated for Case 1. There was some effect on the concentrations of calcium and total inorganic carbon as a result of the calcite reactions, which affected the groundwater flow and transport and hence the mixing of waters within the repository volume. The iron concentrations were higher for Case 2 than for Case 1 due to the amorphous iron (II) sulphide reactions. Results were generally consistent with those reported in Salas et al. (2010) between 2000 AD and 9000 AD. The chemical conditions in the repository volume for this case satisfied the SR-Site safety functions during the simulation period.

Case 3 included equilibration of groundwater with calcite, quartz and iron (III) oxyhydroxide. Nearly all the results were almost identical to Case 2, except for the total iron concentrations and Eh. This may be expected since the reaction involving iron is different for the two cases and involves a redox equilibrium. Although some of the Eh values were higher for this case, oxidising conditions did not occur in the repository volume during the simulation period (Eh up to -164 mV for the 95$^{th}$ percentile at 60,000 AD).

Case 4 included equilibration with a few more mineral phases than in previous cases, calcite, quartz, amorphous iron (II) sulphide, kaolinite, albite, and K-feldspar. The thermodynamical data for the additional minerals involve significant uncertainties as described in e.g. Auqué et al. (2006). Furthermore, the aluminosilicates in particular, are known to react slowly under the geochemical conditions considered. The equilibrium assumption of these minerals is likely overly aggressive and the results are considered mainly to illustrate the effect on the safety functions considering thermodynamically permissible yet probably unrealistic geochemical conditions. The difference in mineral phases considered resulted in a lower pH around the repository (less than one pH unit) at early times up to 9,000 AD as compared to Case 2, but increased at later times and levelled off at a slightly higher pH (median around 7.1) than in Case 2. Eh around the repository in Case 4 was fairly constant with a median ranging from –220 to –200 mV throughout the time span modelled. The total inorganic carbon concentrations around the repository showed a greater spatial variability and also higher median values at early times up to 9,000 AD as compared with Case 2. This is due to a sharp vertical concentration gradient with a transition from high to low concentrations that occurred at repository depth as can be seen in Figure 4-118. This is particularly evident for early times up to 3,000 AD, and is due to the equilibrium assumption with the additional mineral phases considered in Case 4 that affects e.g. the pH and Eh. At later times the variability decreased and the mean concentration levelled off at a slightly lower level than in Case 2. As with total inorganic carbon, the iron concentrations showed a greater spatial variability and higher mean values around the repository in Case 4 as compared with Case 2, particularly at early times. The median concentration however,

did not change significantly throughout the simulated time span in Case 4. Also the sulphate concentrations around the repository showed a greater spatial variability as compared with Case 2, but with similar mean values. Potassium concentrations were about one order of magnitude lower as compared to the other cases, where no equilibrium constraints with K-feldspar were considered. Other components showed only minor differences as compared to Case 2.

The model in Case 5 was identical to Case 2 except that the meteoric water, infiltrating at the top boundary in land areas located above the sea level, was more dilute in Case 5. This resulted in very similar pH, Eh and solution species concentrations as in Case 2, but in general with slightly lower concentration values. The similarity of the results to Case 2 indicated that the penetration of the dilute meteoric water into the repository volume was limited.

In terms of the rock safety functions for chemically favourable conditions considered for SR-Site in Section 10.3.16 of SKB (2011), the following conclusions can be drawn from the present study:

a) Reducing conditions; Eh limited.
   As for SR-Site, reducing conditions were maintained within the repository volume for all cases.

b) Salinity; TDS limited.
   The 95$^{th}$ percentile of TDS for all cases was less than $1.3 \cdot 10^{4}$ mg/kg$_w$ at all times, which is consistent with the value of 12 g/L reported in SKB (2011) and is well below the limit of 35 g/L for the repository backfill.

c) Ionic strength; $\sum q[M^{q+}] > 4$ mM charge equivalent.
   The 5$^{th}$ percentile of the cation charge concentration remained higher than $4.0 \cdot 10^{-3}$ mol/kg$_w$ for all cases at all times. For all but case 5 it remained higher than $1.0 \cdot 10^{-2}$ mol/kg$_w$.

d) Concentrations of potassium and iron; limited.
   The 95$^{th}$ percentile for potassium concentration did not rise above $3.0 \cdot 10^{-3}$ mol/kg$_w$ for any case at any time within the repository volume. This is consistent with the maximum value of $4.0 \cdot 10^{-3}$ mol/L reported in SKB (2011). The 95$^{th}$ percentile for iron concentration did not rise above $1.0 \cdot 10^{-4}$ mol/kg$_w$ for any case at any time within the repository volume. This is consistent with the maximum value of $1.0 \cdot 10^{-4}$ mol/L reported in SKB (2011).

e) pH; pH < 11.
   The 95$^{th}$ percentile for pH did not rise above 8.0 within the repository volume for any of the cases at any time.

f) Avoid chloride assisted corrosion; pH > 4 and $[CL^{-}] < 2$ M.
   The 5$^{th}$ percentile for pH did not fall below 6.5 for any of the cases at any time and the 95$^{th}$ percentile for chloride concentration did not rise above $2.3 \cdot 10^{-1}$ mol/kg$_w$.

The results of this work show that the geochemical environment of the site changes little beyond the temperate climate period considered for SR-Site and hardly at all beyond 20,000 AD. The salinity of the groundwater is governed by the low permeability of the bedrock, rock matrix diffusion and the relatively shallow and slow circulation of groundwater. The chemical reactions influence concentrations of reactive species, the calculated pH and redox potential. In particular, the redox reactions considered maintain reducing conditions at repository depth, even with infiltration at the ground surface of meteoric water with a relatively high redox potential. The geochemical safety functions used for SR-Site are met for all of the cases throughout the time period considered.

# References

SKB's (Svensk Kärnbränslehantering AB) publications can be found at www.skb.se/publications. References to SKB's unpublished documents are listed separately at the end of the reference list. Unpublished documents will be submitted upon request to document@skb.se.


**AMEC, 2013a.** CONNECTFLOW Release 10.5 Technical summary document. AMEC/ENV/CONNECTFLOW/15, AMEC, UK.

**AMEC, 2013b.** NAMMU Release 10.5 Technical summary document. AMEC/ENV/CONNECTFLOW/8, AMEC, UK.

**AMEC, 2013c.** NAPSAC Release 10.5 Technical summary document. AMEC/ENV/CONNECTFLOW/12, AMEC, UK.

**Auqué L F, Gimeno M J, Gómez J B, Puigdomenech I, Smellie J, Tullborg E-L, 2006.** Groundwater chemistry around a repository for spent nuclear fuel over a glacial cycle. Evaluation for SR-Can. SKB TR-06-31, Svensk Kärnbränslehantering AB.

**Bosson E, Gustafsson L-G, Sassner M, 2008.** Numerical modelling of surface hydrology and near-surface hydrogeology at Forsmark. Site descriptive modelling, SDM-Site Forsmark. SKB R-08-09, Svensk Kärnbränslehantering AB.

**Charlton S R, Parkhurst D L, 2011.** Modules based on the geochemical model PHREEQC for use in scripting and programming languages. Computers & Geosciences 37, 1653–1663.

**Follin S, 2008.** Bedrock hydrogeology Forsmark. Site descriptive modelling, SDM-Site Forsmark. SKB R-08-95, Svensk Kärnbränslehantering AB.

**Follin S, Johansson P-O, Hartley L, Jackson P, Roberts D, Marsic N, 2007a.** Hydrogeological conceptual model development and numerical modelling using CONNECTFLOW. Forsmark modelling stage 2.2. SKB R-07-49, Svensk Kärnbränslehantering AB.

**Follin S, Levén J, Hartley L, Jackson P, Joyce S, Roberts D, Swift B, 2007b.** Hydrogeological characterisation and modelling of deformation zones and fracture domains, Forsmark modelling stage 2.2. SKB R-07-48, Svensk Kärnbränslehantering AB.

**Hartley L, Joyce S, 2013.** Approaches and algorithms for groundwater flow modeling in support of site investigations and safety assessment of the Forsmark site, Sweden. Journal of Hydrology 500, 200–216.

**Hedenström A, Sohlenius G, Strömgren M, Brydsten L, Nyman H, 2008.** Depth and stratigraphy of regolith at Forsmark. Site desprictive modelling SDM-Site Forsmark. SKB R-08-07, Svensk Kärnbränslehantering AB.

**Jackson C P, Hoch A R, Todman S, 2000.** Self-consistency of a heterogeneous continuum porous medium representation of a fractured medium. Water Resources Research 36, 189–202.

**Joyce S, Simpson T, Hartley L, Applegate D, Hoek J, Jackson P, Swan D, Marsic N, Follin S, 2010.** Groundwater flow modelling of periods with temperate climate conditions – Forsmark. SKB R-09-20, Svensk Kärnbränslehantering AB.

**Joyce S, Applegate D, Appleyard P, Gordon A, Heath T, Hunter F, Hoek J, Jackson P, Swan D, Woollard H, 2015.** Groundwater flow and reactive transport modelling in ConnectFlow. SKB R-14-19, Svensk Kärnbränslehantering AB.

**Laaksoharju M, Smellie J, Tullborg E-L, Gimeno M, Hallbeck L, Molinero J, Waber N, 2008.** Bedrock hydrogeochemistry Forsmark. Site descriptive modelling, SDM-Site Forsmark. SKB R-08-47, Svensk Kärnbränslehantering AB.

**Olofsson I, Simeonov A, Stephens M, Follin S, Nilsson A-C, Röshoff K, Lindberg U, Lanaro F, Fredriksson A, Persson L, 2007.** Site descriptive modelling Forsmark, stage 2.2. A fracture domain concept as a basis for the statistical modelling of fractures and minor deformation zones, and interdisciplinary coordination. SKB R-07-15, Svensk Kärnbränslehantering AB.

**Parkhurst D L, Appelo C A J, 1999.** User's guide to PHREEQC (version 2): a computer program for speciation, batch-reaction, one-dimensional transport, and inverse geochemical calculations. Water-Resources Investigations Report 99-4259, U.S. Geological Survey, Denver, Colorado.

**Rhén I, Follin S, Hermanson J, 2003.** Hydrological Site Descriptive Model – a strategy for its development during Site Investigations. SKB R-03-08, Svensk Kärnbränslehantering AB.

**Salas J, Gimeno M J, Auqué L F, Molinero J, Gómez J, Juárez I, 2010.** SR-Site: Hydro-geochemical evolution of the Forsmark site. SKB TR-10-58, Svensk Kärnbränslehantering AB.

**SKB, 2008.** Site description of Forsmark at completion of the site investigation phase. SDM-Site Forsmark. SKB TR-08-05, Stockholm: Svensk Kärnbränslehantering AB.

**SKB, 2010.** Climate and climate-related issues for the safety assessment SR-Site. SKB TR-10-49, Svensk Kärnbränslehantering AB.

**SKB, 2011.** Long-term safety for the final repository for spent nuclear fuel at Forsmark. Main report of the SR-Site project. SKB TR-11-01, Stockholm: Svensk Kärnbränslehantering AB.

**Smellie J, Tullborg E-L, Nilsson A-C, Sandström B, Waber N, Gimeno M, Gascoyne M, 2008.** Explorative analysis of major components and isotopes. SDM-Site Forsmark. SKB R-08-84, Svensk Kärnbränslehantering AB.

**Svensson U, Follin S, 2010.** Groundwater flow modelling of the excavation and operational phases – Forsmark. SKB R-09-19, Svensk Kärnbränslehantering AB.

**Vidstrand P, Follin S, Zugec N, 2010.** Groundwater flow modelling of periods with periglacial and glacial climate conditions – Forsmark. SKB R-09-21, Svensk Kärnbränslehantering AB.

**Unpublished documents**



| SKBdoc id, version | Title | Issuer, year |
|---|---|---|
| SKBdoc 1261302 ver 3.0 | Thermodynamic database_TDB_SKB-2009_Amphos21, Svensk Kärnbränsle-hantering AB. | SKB, 2013 |